Institut für Physik und Astronomie
H. E. S. S. Gruppe

Pulsar Wind Nebulae At High Energies:
A Diverse Population and Exceptional Twins

Dissertation

zur Erlangung des akademischen Grades
"doctor rerum naturalium"
(Dr. rer. nat.)
in der Wissenschaftsdisziplin "Astroteilchenphysik"

eingereicht an der
Mathematisch-Naturwissenschaftlichen Fakultät
der Universität Potsdam

von

Michael Mayer

Potsdam, den 25. Juni 2014

Kurzfassung

Pulsarwindnebel (PWN) sind im Bereich der TeV Gammastrahlung die am häufigsten vorkommende Quellklasse. Die vorliegende Arbeit präsentiert eine detaillierte Studie der Population von gammastrahlungsemittierenden PWNn. Um ihre Entwicklung zu untersuchen, wird ein zeitabhängiges Modell vorgestellt und mit Messdaten verglichen. Der Fokus dieser Arbeit liegt des Weiteren auf zwei außergewöhnlichen PWNn, die aus der übrigen Population hervorstechen: der Krebsnebel und N 157B. Diese beiden PWN werden von Pulsaren mit ähnlich hohen Rotationsenergieverlustraten gespeist. Daher werden die beiden Pulsare auch oft als "energetische Zwillinge" bezeichnet.

Im Rahmen dieser Arbeit wird die Breitbandemission von N 157B modelliert. Dies ermöglicht es, spezielle Eigenschaften dieses PWNs abzuschätzen. Diese sind im Vergleich zum Krebsnebel sehr unterschiedlich, obwohl sich die jeweiligen Energiequellen stark ähneln. Es werden verschiedene Möglichkeiten für die unterschiedliche Erscheinung dieser beiden Quellen diskutiert.

Auf Grund kürzlich gemessener MeV Gammastrahlungsausbrüche wird die Einzigartigkeit des Krebsnebels in diesem Energiebereich verdeutlicht. Die auf Zeitskalen von Tagen bis Wochen variierende Helligkeit ist nach dem gegenwärtigen Verständnis von PWNn unerwartet. In dieser Arbeit wird die zeitliche Variabilität des Krebsnebels mit Daten vom *Fermi* Large Area Telescope (*Fermi*-LAT) analysiert. Die vorgestellte Datenanalyse basiert auf einer neuen Rekonstruktionsmethode von Gammastrahlen, welche zu einer höheren Empfindlichkeit und einer niedrigeren Energieschwelle führt. Die Lichtkurve des Krebsnebels in Gammastrahlung wird auf Periodizität und Variabilität untersucht. Des Weiteren werden die nachgewiesenen Strahlungsausbrüche hinsichtlich ihrer Energiespektren ausgewertet und miteinander auf Gemeinsamkeiten und Unterschiede verglichen. Zusätzlich wird eine detaillierte Analyse der starken Flusserhöhung vom März 2013 vorgestellt. Die hierbei bestimmte Kurzzeitvariabilität von ca. sechs Stunden lässt vermuten, dass eine sehr kleine Region innerhalb des Krebsnebels für die Strahlungsausbrüche verantwortlich ist. Die vielversprechendsten Theorien zu diesem Phänomen werden vorgestellt und diskutiert.

Im technischen Teil dieser Arbeit wird eine neue Analyseumgebung vorgestellt, die derzeit für das zukünftige CTA Observatorium entwickelt wird. Diese Software wird intensiven Analysetests mit Daten des H. E. S. S. Experiments unterzogen. Für die angemessene Durchführung von H. E. S. S. Datenanalysen wird ein Modell vorgestellt, das die Verteilung der Untergrundereignisse in H. E. S. S. Daten beschreibt. Des Weiteren erlaubt die Analyseumgebung die Kombination von Daten mehrerer Instrumente. Diese einzigartige Option wird genutzt, um die beschriebene PWN Population genauer zu studieren. Zu diesem Zweck werden Daten von *Fermi*-LAT und H. E. S. S. gemeinsam analysiert. Von besonderem Interesse ist hierbei das spektrale Maximum von PWN, welches meist im energetischen Überlappbereich der beiden Instrumente liegt. Die Ergebnisse der gemeinsamen Analyse werden mit dem zeitabhängigen Modell für PWN verglichen. Die daraus gewonnenen Resultate verdeutlichen unter anderem die breite Vielfalt von PWNn.

Abstract

Pulsar wind nebulae (PWNe) are the most abundant TeV γ-ray emitters in the Milky Way. The radiative emission of these objects is powered by fast-rotating pulsars, which donate parts of their rotational energy into winds of relativistic particles. This thesis presents an in-depth study of the detected population of PWNe at high energies. To outline general trends regarding their evolutionary behaviour, a time-dependent model is introduced and compared to the available data. In particular, this work presents two exceptional PWNe which protrude from the rest of the population, namely the Crab Nebula and N 157B. Both objects are driven by pulsars with extremely high rotational energy loss rates. Accordingly, they are often referred to as energetic twins. Modelling the non-thermal multi-wavelength emission of N 157B gives access to specific properties of this object, like the magnetic field inside the nebula. Comparing the derived parameters to those of the Crab Nebula reveals large intrinsic differences between the two PWNe. Possible origins of these differences are discussed in context of the resembling pulsars.

Compared to the TeV γ-ray regime, the number of detected PWNe is much smaller in the MeV-GeV γ-ray range. In the latter range, the Crab Nebula stands out by the recent detection of γ-ray flares. In general, the measured flux enhancements on short time scales of days to weeks were not expected in the theoretical understanding of PWNe. In this thesis, the variability of the Crab Nebula is analysed using data from the *Fermi* Large Area Telescope (*Fermi*-LAT). For the presented analysis, a new γ-ray reconstruction method is used, providing a higher sensitivity and a lower energy threshold compared to previous analyses. The derived γ-ray light curve of the Crab Nebula is investigated for flares and periodicity. The detected flares are analysed regarding their energy spectra, and their variety and commonalities are discussed. In addition, a dedicated analysis of the flare which occurred in March 2013 is performed. The derived short-term variability time scale is roughly 6 h, implying a small region inside the Crab Nebula to be responsible for the enigmatic flares. The most promising theories explaining the origins of the flux eruptions and γ-ray variability are discussed in detail.

In the technical part of this work, a new analysis framework is presented. The introduced software, called GAMMALIB/CTOOLS, is currently being developed for the future CTA observatory. The analysis framework is extensively tested using data from the H. E. S. S. experiment. To conduct proper data analysis in the likelihood framework of GAMMALIB/CTOOLS, a model describing the distribution of background events in H. E. S. S. data is presented. The software provides the infrastructure to combine data from several instruments in one analysis. To study the γ-ray emitting PWN population, data from *Fermi*-LAT and H. E. S. S. are combined in the likelihood framework of GAMMALIB/CTOOLS. In particular, the spectral peak, which usually lies in the overlap energy regime between these two instruments, is determined with the presented analysis framework. The derived measurements are compared to the predictions from the time-dependent model. The combined analysis supports the conclusion of a diverse population of γ-ray emitting PWNe.

Contents

1. Introduction

During the last decades, well-established fields of radio, optical and X-ray astronomy were complemented by the research of more energetic photons, i.e. astrophysical γ rays up to $100\,\mathrm{TeV}$. These γ rays are the products of violent phenomena in our Milky Way and other close-by galaxies. Before then, the solitary messengers of this most energetic part of our Universe were charged cosmic rays. In contrast to these energetic particles, which get deflected in interstellar magnetic fields, γ rays directly point back to their origin. Spatially resolving the regions of γ-ray emission in the sky therefore provides particular insights where particles get accelerated to the highest energies and where they subsequently interact with their surrounding. Consequently, the new field of γ-ray astronomy offers the possibility to trace back powerful cosmic accelerators.

State-of-the-art γ-ray telescopes have angular resolutions improving from $5°$ at $100\,\mathrm{MeV}$ to roughly $0.1°$ at $1\,\mathrm{TeV}$. However, the complete energy range above $100\,\mathrm{MeV}$ is not covered by a single instrument alone. The space-born *Fermi* Large Area Telescope (*Fermi*-LAT) on board the Fermi satellite e.g. is sensitive to an energy range from $100\,\mathrm{MeV}$ to $300\,\mathrm{GeV}$, while ground-based systems like H. E. S. S., MAGIC or VERITAS cover energies above $30\,\mathrm{GeV}$ to roughly $100\,\mathrm{TeV}$. Together, these experiments provide a combined sensitivity over more than five decades of energy. Up to now, more than 1800 objects emitting high-energy γ rays, (HE, $100\,\mathrm{MeV} < E < 100\,\mathrm{GeV}$) have been detected by *Fermi*-LAT (Nolan et al. 2012). At very high energies (VHE, $E > 100\,\mathrm{GeV}$), however, the amount of known sources shrinks dramatically to roughly 150. Around half of these VHE γ-ray sources are detected along the Galactic plane by the H. E. S. S. experiment (Aharonian et al. 2005a, 2006d; Carrigan et al. 2013). Benefiting from its location in the southern hemisphere in Namibia, H. E. S. S. provides an exclusive view into the central part of our Milky Way in the light of the most energetic radiation.

Many of the γ-ray sources within our Galaxy are attributed to remnants of massive supernova explosions. Due to the sensitivity of γ-ray instruments, it is possible to detect and resolve a large population of these kind of energetic objects. The population of supernova remnants (SNRs) can be subdivided into shell-type and centrally filled objects. While the former type is thought to be caused by the interaction of the supernova shock wave with its surrounding, the latter is driven by the remainder of the progenitor star of the explosion − a fast-rotating neutron star. The existence of neutron stars was postulated by Baade & Zwicky (1934) and confirmed by the measurement of Hewish et al. (1968)[1]. These neutron stars (also called pulsars), power winds of relativistic particles which emit radiation all across the electromagnetic spectrum. Such a system is called pulsar wind nebula (PWN). In particular in the VHE γ-ray domain, the majority of discovered sources within our Galaxy can be associated with PWNe. Additionally, there is a large fraction of VHE γ-ray sources which remains unidentified due to a missing or unclear association to objects at other wavelengths (see, e.g., Aharonian et al. 2008). Some of these unidentified sources are possibly related to the abundant source class of

---

[1]In fact, Hewish's student J. Bell discovered this first neutron star. It was Hewish however, who received the Nobel prize for this ground-breaking discovery.
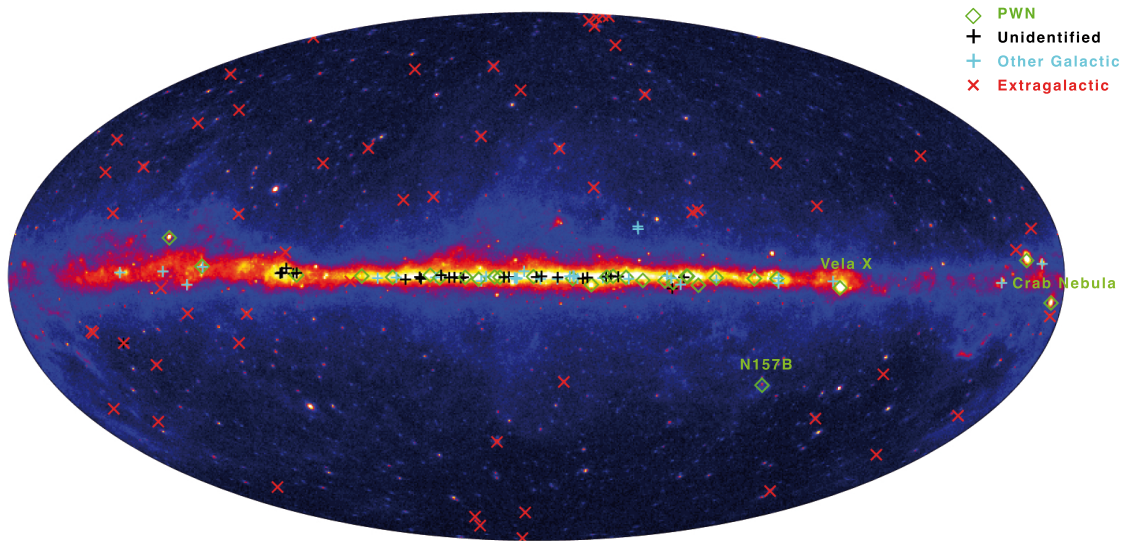
Figure 1.1.: The Milky Way in the γ-ray regime. The map is depicted in Galactic coordinates using a Hammer-Aitoff projection. The image represents a map of *Fermi*-LAT counts above $1\,\mathrm{GeV}$ using five years of observations. The colour scale is logarithmically stretched, while dark blue colours indicate regions with few counts and red colours denote intense γ-ray emission. Overlaid are all currently detected VHE γ-ray sources above $100\,\mathrm{GeV}$. Different symbols are drawn to distinguish between the source types.

PWNe (see, e.g., de Jager & Djannati-Ataï 2009; de Jager et al. 2009). The understanding of these objects as γ-ray emitters therefore becomes more and more important to get a clearer picture of the population of VHE γ-ray sources in our Galaxy. In order to illustrate the spatial distribution of γ-ray emission regions in the sky, Fig. 1.1 depicts a map of the HE sky seen with *Fermi*-LAT, superimposed with all currently known VHE γ-ray sources, compiled from several experiments[2]. In both energy ranges, the Galactic plane is very pronounced. In the HE domain the Milky Way is dominated by diffuse γ-ray emission and unresolved sources, while the detected VHE γ-ray emission is mainly attributed to resolved sources. To emphasis their abundance along the Galactic plane, VHE γ-ray emitting PWNe and unidentified sources are highlighted in Fig. 1.1. Additionally labelled are PWNe of which more detailed studies are presented later in this work.

Investigating the population of well-known PWNe, it is possible to draw conclusions about their evolution and their characteristics. Of general interest is the process of efficient particle acceleration which is an ongoing matter of debate. The detection of VHE γ rays from PWNe suggests that particles above $100\,\mathrm{TeV}$ can be produced inside these objects. In general, it is assumed that the energetic particle population inside PWNe mainly consist of electrons and positrons (see, e.g., Gaensler & Slane 2006, and references therein). Therefore, such systems are well-suited to study leptonic acceleration processes up to the highest energies. Characterising the present particle population which emits the most energetic γ rays has become a very important means to probe current acceleration theories for PWNe. The abundance of PWNe in the VHE γ-ray range provides the possibility to study theoretical approaches in

---

[2]http://tevcat.uchicago.edu

the context of several representatives from this source class.

In contrast to the numerous PWNe at VHEs, there was a lack of detections in the HE domain. Recently, however, the *Fermi*-LAT collaboration reported several detections above $10\,\text{GeV}$ (Acero et al. 2013) which can be associated to a corresponding VHE PWN. Their energy spectra suggest an intrinsic peak between the HE and VHE domain. Combining the information of both instruments, also the non-detections of *Fermi*-LAT, helps to determine this spectral peak, which in turn complements the study of the underlying particle distribution. The energetics of PWNe and of their particle content can be linked to the respective pulsar, which is the energy source of these systems.

This thesis derives PWN properties in order to draw conclusions about the variety and commonalities of PWNe at high energies. In addition, the work puts a special emphasis on PWNe which seem to violate the general scheme. Chapter 2 summarises the current conceptional understanding of PWNe. It further introduces the population of the most energetic PWNe to outline general trends, e.g. regarding their spectral evolution, which can be compared to model predictions. At this point, data from γ-ray experiments are used. However, to make it a comprehensible overview, a broad introduction into the respective data analysis procedure is omitted. Chapters 3 and 4 highlight two PWNe protruding from the population, namely N 157B and the Crab Nebula. Although the corresponding pulsars of these two objects are considered energetic twins, their nebulae are rather different. While N 157B has the highest intrinsic VHE γ-ray luminosity of all detected PWNe, the Crab Nebula challenges current PWN models due to the detection of timely variable emission above $100\,\text{MeV}$. The respective Chapter presents the data analysis of this variability. For this purpose, the *Fermi*-LAT instrument and the respective analysis procedure is introduced in more detail. The dedicated data analysis of the Crab Nebula puts a specific focus on the major flares, which have been detected in the last years. In addition, theories explaining the origin of these flares are summarised.

Conducting a unified analysis of γ-ray emitting PWNe, Chapter 5 introduces a new approach to combine data from several instruments. The presented framework is currently being developed to meet future analysis challenges with more sensitive instruments in the VHE γ-ray regime. Complementing the descriptions of γ-ray detectors which are used for data analysis in this work, the Chapter gives an overview of the H. E. S. S. experiment and the corresponding data analysis approaches. In addition, the technical efforts undertaken to analyse H. E. S. S. data in the new analysis framework are explained in detail. Subsequently, its advantages over the well-established methods are discussed. The new approach is then applied to derive PWNe properties, using data from H. E. S. S. and *Fermi*-LAT. The obtained results are put into context to the PWN population presented in Chapter 2. The thesis finally closes with conclusions, which are based on the presented findings.

Most results presented in this thesis are derived in a collaborative work. Significant own contributions are indicated by in-depths descriptions of analyses procedures and results.

2. Pulsar Wind Nebulae at High Energies

2.1. Historical Introduction

In 1054, Chinese astronomers observed a new appearing bright star in the Taurus region, which disappeared again after 21 months (see, e.g. Duyvendak 1942; Mayall & Oort 1942; Clark & Stephenson 1977; Stephenson & Green 2002, and references therein). Today, it is known they sighted a supernova explosion of which the remnant, a PWN, is called Crab Nebula (Collins et al. 1999). Short after the detection of the first pulsar (Hewish et al. 1968), optical and radio pulses were found from the Crab Nebula, too (Staelin & Reifenstein 1968; Cocke et al. 1969). The pulse profile reappeared periodically every 33 ms with a slowing rate of 13 μs per year, giving rise to the energetics of the central energy source in the Crab Nebula. These observations implied that rotational energy from the pulsar is dissipated at a rate of roughly $5 \cdot 10^{38}\,\mathrm{erg\,s^{-1}}$. A small fraction of this energy output producing non-thermal particles is sufficient to explain the observed photon emission. Today, the Crab Nebula is one of the best studied objects in astrophysics (see Fig. 2.1 for detailed view). In particular, it belongs to the brightest sources in γ rays which indicates efficient acceleration of energetic particles. Therefore, the Crab Nebula is one of the best laboratories to study particle acceleration inside PWNe despite several more γ-ray emitting PWNe having been discovered in the past decades.

2.2. Theoretical Aspects

With the advent of numerous observatories, sensitive to various wavelengths, the number of known PWNe has steadily increased. At the same time, theories providing detailed explanations for the detected emission have developed accordingly. This Section is intended to broadly summarise the current conceptional understanding of PWNe. Comprehensive overviews which serve as foundation of in particular Sect. 2.2.1 can be found in Gaensler & Slane (2006); Hester (2008); Arons (2012); Bühler & Blandford (2014). The following summary commences by introducing the acceleration processes which are believed to produce the most energetic particles inside PWNe. Subsequently, the dominant interaction processes of these particles with their surroundings, creating the detectable non-thermal radiation are explained. This Section closes with presenting a model for the time evolution of PWNe (Sect. 2.2.3). The model is applied and tested with the population of VHE γ-ray emitting PWN (Sect. 2.3).

2.2.1. Particle Acceleration

The process of particle acceleration in PWNe up to the highest energies is still under scientific debate. It represents the least understood part in the theoretical modelling of PWNe. Nevertheless, there is a consensus that the non-thermal emission of PWNe is assumed to originate from electrons and positrons (hereafter electrons). For hadron-induced emission, a
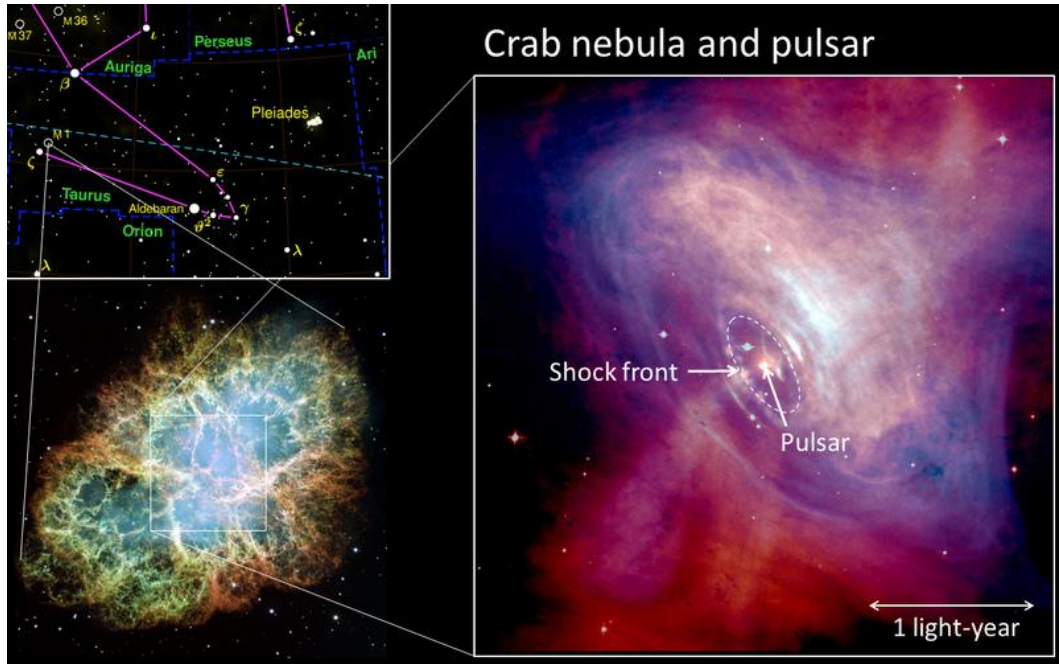
Figure 2.1.: Several views on the Crab Nebula. *Top left:* The position of the Crab Nebula with respect to other bright stars in the Taurus region. *Lower left:* The Crab Nebula in optical wavelengths imaged by the Hubble Space Telescope. *Right:* The X-ray emission from the central region, measured by the Chandra X-ray Observatory. The Crab pulsar can be clearly recognised as bright point source in the image center. Image credit: Composition: MPIK, Pictures: NASA

dense target material such as a nearby molecular cloud would be required. The precedent supernova explosion, however, has swept away most of the denser material, which is why most theories consider electron dominated nebulae. The current understanding of accelerated electrons forming the nebula is mostly based on observations of the Crab Nebula and the knowledge of pulsar properties in general.

In first order, pulsars can be approximated as a perfectly rotating dipole. They are assumed to have very large surface magnetic fields in the order of 10^{12} G (e.g. Gaensler & Slane 2006). The origin of this dense field is simple: during the supernova explosion, the progenitor's core collapses to a size of roughly 10 km. Due to magnetic flux conservation, the field of the progenitor star is compressed to high magnetic densities. Similarly, the conservation of the moment of inertia causes extremely high rotation periods, e.g. 30 Hz for the Crab pulsar (Cocke et al. 1969). Generally, the axis of the magnetic dipole is not aligned with its rotational axis. Radiation emitted along the magnetic axis therefore appears as pulses to a distant observer, similar to a lighthouse. These pulses are observed if the light cone sweeps across the line of sight. The electromagnetic pulses from the Crab pulsar can be measured up to several hundred GeV (VERITAS Collaboration et al. 2011; Aleksić et al. 2012). Although this is the only known pulsar emitting pulsed VHE γ rays above 100 GeV, there are many pulsars powering HE γ-ray emission (Abdo et al. 2013).

The fast-rotating magnetic field induces strong electric potentials ($\Phi > 10^{16}$ V for the Crab pulsar), in which charged particles can be accelerated up to high energies. The present

electric forces are strong enough to remove gravitationally bound particles from the pulsar surface. Hence, the magnetosphere gets filled with charged plasma. The charges immediately get separated due to the strong electric potential (Goldreich & Julian 1969). Pair creation within the pulsar magnetosphere further increases the particle density (e.g. Sturrock 1971). In the past years, many simulations of pulsar magnetospheres using force-free electrodynamics and/or magnetohydrodynamics (MHD) have been performed (see, e.g., Spitkovsky 2006; Kalapotharakos & Contopoulos 2009; Bai & Spitkovsky 2010; Li et al. 2012; Kalapotharakos et al. 2012a,b; Tchekhovskoy et al. 2013, and references therein for further details). Along magnetic field lines, the charge separated plasma flows out from the pulsar magnetosphere and forms the pulsar wind (e.g. Kennel & Coroniti 1984; Bucciantini et al. 2011, and references therein). The emerging positive and negative currents follow magnetic fields of anti-parallel polarity. The left panel of Fig. 2.2 depicts the outflowing current and the corresponding direction of magnetic field lines.
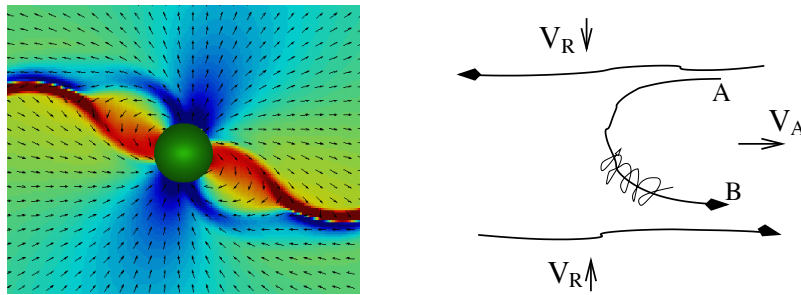

Figure 2.2.: *Left*: Sketch of a pulsar magnetosphere. This image, adopted from Bai & Spitkovsky (2010), illustrates a pulsar (dark green sphere) where the magnetic dipole axis is tilted by 30° with respect to the rotational axis of the pulsar. Black arrows indicate the polarity of magnetic field lines, while the colour scale depicts the charge density. Deep blue represents negatively charged plasma whereas dark red colours mean strongly positive charge densities. Greenish colours stand for electrically neutral regions. *Right*: Simplistic sketch illustrating magnetic reconnection adopted from Lazarian (2005). Magnetised plasma with opposite polarity approach each other with velocity V_R. Particles captured in reconnecting magnetic field lines experience strong acceleration. Along the created reconnection layer the particle outflow is depicted as V_A.

Further away from the pulsar, magnetic field lines can be approximated as being radial and axial (Michel 1974). Following Blumenthal & Gould (1970, Eq. 4.4), the strongly magnetised pulsar wind outflow is not radiating while moving parallel to magnetic field lines (cold pulsar wind, see, e.g., Kennel & Coroniti 1984; Bogovalov 1999). This radiationless flow, however, is terminated when the outflow pressure is balanced by the ambient nebula ram pressure. At the surface of the so-called termination shock, particles and magnetic field lines are randomized, causing particle re-acceleration and synchrotron emission. The termination of the pulsar wind is believed to be strongly relativistic (Sironi & Spitkovsky 2011b). Therefore it is an unlikely site for diffusive shock acceleration, which was long thought to be the dominating acceleration process (Fermi 1949). More compelling ideas emerge from particle-in-cell simulations (e.g. Lyubarsky 2003; Komissarov & Lyubarsky 2004; Bucciantini et al. 2006; Lyutikov 2010; Sironi & Spitkovsky 2011a): especially in the equatorial plane of the magnetic dipole, magnetised plasma currents of different charge approach each other, increasing the probability of magnetic

reconnection (see sketch in right panel of Fig. 2.2 and Lazarian (2005); Lazarian et al. (2011) for more details on magnetic reconnection). Three-dimensional MHD simulations from the past years shed further light onto the reconnection sites (Mizuno et al. 2011; Porth et al. 2014). Since magnetic reconnection is a very efficient process to convert magnetic into kinetic energy, the magnetisation of the pulsar wind suddenly drops after its termination, implying a particle dominated wind. This phenomenon is nicely depicted in Fig. 2.1 (labeled *Shock front* on the right panel), which was taken by the *Chandra* - X-ray observatory. According to e.g. Spitkovsky (2008); Sironi et al. (2013), this acceleration process produces a power-law distribution of the most energetic electrons with a predicted spectral index around 2.4. This power law, however, has a more complex structure at lower energies and cuts off exponentially at high energies. Behind the termination shock, the relativistic electron plasma is subject to interaction with ambient magnetic and radiation fields. The interaction processes cause these electrons to lose their energy by emitting radiation across the electromagnetic spectrum. In the following, these processes with their characteristics are briefly introduced.

2.2.2. Radiation Processes

The electromagnetic radiation observed from PWNe is thought to originate from energetic electrons losing their energy via different processes. In general, energetic electrons are subject to two main radiation processes which produce photons in different energy regimes. Multi-wavelength (MWL) observations of PWNe therefore provide access to the same present underlying electron population emitting broad photon spectra. The present Section therefore focuses on these two, most relevant radiation processes occurring in PWNe.

Synchrotron Radiation

The nebulae of energetic pulsars were primarily observed in radio, optical and X-ray wavelengths. The origin of these photons can be reduced to one dominant process, which is synchrotron radiation. It occurs when charged and relativistic particles get deflected in magnetic fields. As described in the previous Section, the particles within a nebula are believed to consist of relativistic electrons carrying the elementary charge e. Randomised magnetic fields behind the wind termination shock cause these electrons to lose their energy by radiating synchrotron photons. In general, the energy loss of an electron moving through a magnetic field is dependent on the pitch angle between field line and electron momentum (Blumenthal & Gould 1970, Eq. 4.5). Behind the wind termination shock, however, the pitch angle distribution is assumed to be flat. The average energy loss of an energetic electron is hence only dependent on its energy E and the magnetic field density B:

$$\frac{\partial E}{\partial t} \propto E^2 B^2.$$ (2.1)

More specific, the emitted synchrotron power P of an electron at a photon frequency ν can be averaged to (Blumenthal & Gould 1970, Eq. 4.31)

$$P(\nu) = \frac{\sqrt{3}e^3 B}{mc^2} \cdot \frac{\nu}{\nu_c} \int_{\nu/\nu_c}^{\infty} \mathrm{d}\xi K_{5/3}(\xi),$$ (2.2)

with mc^2 being the electron mass and $K_{5/3}$ the modified Bessel function of the order 5/3. The critical frequency ν_c is defined as $\nu_c = 3eB\gamma^2/4\pi mc$, where γ is the Lorentz factor of

the radiating electron.

The observed synchrotron emission from PWNe gives insights into the spectral shape of the electron distribution and the present magnetic field inside these objects. To explain MWL data, the absolute number of electrons and their energy distribution is however strongly correlated with the magnetic field strength. Accordingly, if the electron population and its energy content could be derived independently, the magnetic field could be determined without ambiguity. In the subsequent Section another radiation process revealing an independent view on the electron distribution is therefore introduced.

Inverse Compton Radiation

The same electron population suffering energy losses by emitting synchrotron radiation within magnetic fields is subject to interactions with ambient photon fields, like e.g. the cosmic microwave background (CMB, Penzias & Wilson 1965; Dicke et al. 1965). The original Compton scattering process (Compton 1923) describes the momentum transfer from photon to electron. The inverse process, namely a relativistic electron up-scattering a low energy photon, called *Inverse Compton process* (IC) is believed to be responsible for the most energetic photon emission from PWNe. The IC emission spectrum of an electron traveling through photon fields was derived by Blumenthal & Gould (1970, Eq. 2.48)

$$\frac{\mathrm{d}N_{\gamma,\epsilon}}{\mathrm{d}t \mathrm{d}E_1} = \frac{2\pi r_\mathrm{e}^2 m_\mathrm{e} c^3}{\gamma} \cdot \frac{n(\epsilon)\mathrm{d}\epsilon}{\epsilon} \left[2q \ln q + (1+2q)(1-q) + \frac{(\Gamma_\epsilon q)^2}{2(1+\Gamma_\epsilon q)}(1-q) \right]. \tag{2.3}$$

In this equation, ϵ is the (unscattered) photon energy, $n(\epsilon)$ the ambient radiation field density and E_1 the ratio of the up-scattered photon energy ϵ_1 and the electron energy $\gamma m_\mathrm{e} c^2$ ($E_1 = \epsilon_1/\gamma m_\mathrm{e} c^2$). Furthermore, the dimensionless quantities Γ_ϵ and q are defined as

$$\Gamma_\epsilon = \frac{4\epsilon\gamma}{m_\mathrm{e} c^2}, \tag{2.4}$$

$$q = \frac{E_1}{\Gamma_\epsilon(1-E_1)}. \tag{2.5}$$

To obtain the total emissivity per up-scattered photon frequency, Eq. 2.3 has to be integrated over the electron distribution $\mathrm{d}N(\gamma) = N(\gamma)\mathrm{d}\gamma$ and ϵ. Eq. 2.3 also takes into account the relative decrease of the electron-photon cross section in case of increasing center of mass energies ($\Gamma_\epsilon \gg 1$), the so-called Klein-Nishina regime (Klein & Nishina 1929). Because of this effect, the most energetic electrons ($E > 1\,\mathrm{TeV}$) mainly interact with very low energy photons. As described in e.g. Bennett et al. (2003), the distribution of CMB photons follows a black-body function with temperature $T = 2.73\,\mathrm{K}$, which can be assumed constant in any region of the Universe. Other photon fields are subject to strong local variations. Examples for these fields are thermal radiation from dust, nearby stars, or in extreme cases also the synchrotron emission from the same electron population (synchrotron-self Compton, SSC). The latter e.g. is a very dominant component in the Crab Nebula (de Jager & Harding 1992; Meyer et al. 2010). In sum, tracing back the electron population using IC emission only, requires adequate knowledge of the locally present radiation fields. Nevertheless, the spectrum of the most energetic electrons can be derived by assuming CMB only due to the decreasing cross section in the Klein-Nishina regime. Fortunately, these most energetic electrons are the same producing synchrotron emission which is visible in the X-ray regime. Combining the information from synchrotron and IC emission is discussed and illustrated in the following.

Multi-Wavelength Picture

Synchrotron and IC radiation are the two dominant processes responsible for photon emission from PWNe. Generally, it is assumed that synchrotron and IC emission originate from the same electron population. Accordingly, both discussed processes provide independent access to the present electron distribution inside a PWN. Fig. 2.3 shows two exemplary spectral energy distributions (SEDs) of photon emission, produced by energetic electrons. Here, the spectrum of these electrons follows a power law in energy:

$$\frac{\mathrm{d}N}{\mathrm{d}E} \propto E^{-p}, \tag{2.6}$$

with a spectral index of $p = 2.4$ as predicted from acceleration processes (see Sect. 2.2.1). The spectrum is defined within the energy boundaries $E_{\min} = 100\,\mathrm{GeV}$ and $E_{\max} = 1\,\mathrm{PeV}$. To illustrate the influence of ambient parameters, two different sets of magnetic fields and radiation fields are applied on the given electron spectrum. For the solid line in Fig. 2.3, a magnetic field of $5\,\mu\mathrm{G}$ and CMB as sole target radiation field are used. For the dashed line, the target radiation fields from the Earth position, derived from the GALPROP code (Porter & Strong 2005), and a stronger magnetic field of $10\,\mu\mathrm{G}$ is added. The Figure shows the two
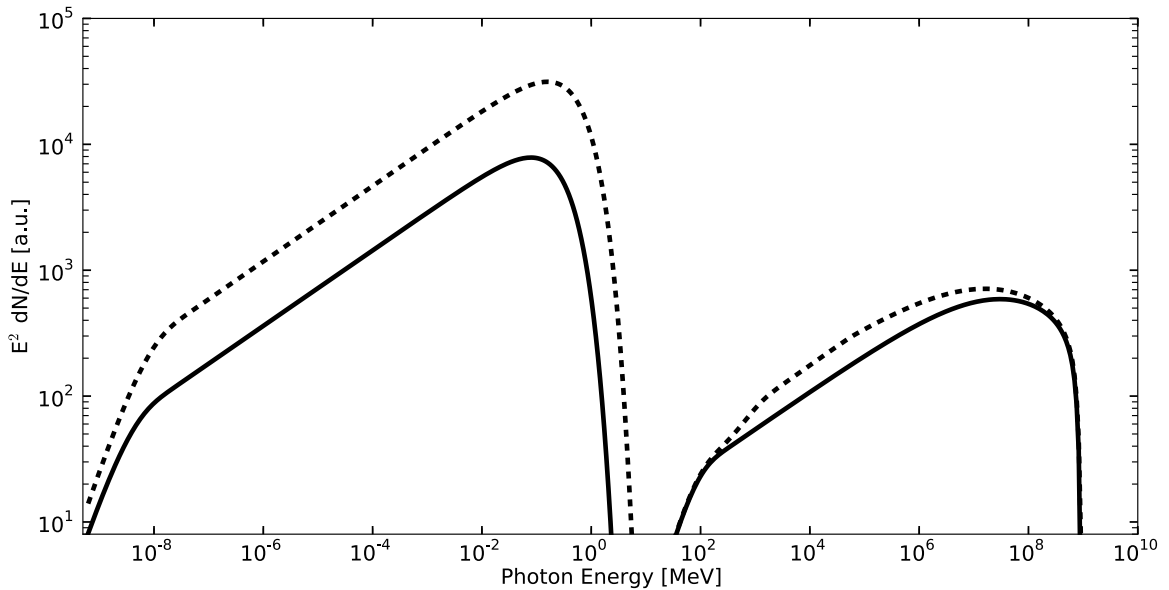
Figure 2.3.: Spectral energy distributions of photons produced by an electron spectrum following a power law. Dashed and solid lines denote two different ambient conditions.

distinct peaks in the SEDs: at lower energies, the nebula emits only synchrotron radiation, while above a few hundred MeV the spectrum is dominated by IC emission. The dashed line, representing the higher magnetic field and denser ambient radiation fields, corresponds to a brighter photon emission from the same electron spectrum. Above 100 TeV, however, the differences are marginal since the main target field for the most energetic electrons is the CMB due the above-described Klein-Nishina regime. The SEDs underline the importance of a MWL view on PWNe. Observations in energy ranges covering both, synchrotron and IC emission, provides two independent insights to the underlying electron spectrum. Under

the assumption of one electron population being responsible for the detectable radiation, many quantities, e.g. the magnetic field inside the nebula can be derived almost model independent. Under the assumption of present radiation fields, this can be achieved by fixing the electron spectrum with data taken in the IC energy range, leaving the magnetic field as exclusive free parameter to model the synchrotron emission. Applying this rather simplified approach, the SEDs of many PWNe can be reproduced quite well. This is quite surprising because the magnetic field strength and the spatial distribution of energetic electrons inside a PWN is probably far from being homogeneous. This type of stationary modelling, however, already provides good estimates for the averaged conditions inside PWNe. With a similar approach, Meyer et al. (2010) determined the energy distribution of electrons inside the Crab Nebula as well as the average magnetic field. Since this prototype PWN is visible all across the electromagnetic spectrum, the present electron spectrum can be derived based on many MWL data from synchrotron and IC emission. The authors found an average magnetic field inside the nebula of $B_{\mathrm{Crab}} = 124 \pm 6\,\mu\mathrm{G}$ presuming CMB, SSC and close-by thermal emission from dust and filaments as dominant radiation fields for IC emission. A maximum electron energy of $3\,\mathrm{PeV}$ inside the nebula is required to match the data. This implies the Crab Nebula to be a Galactic pevatron. In general, the hereby determined electron distribution, however, reflects only the present conditions inside the nebula. The snapshot of today's emission is probably a product of the complex history of the PWN. By investigating the evolution of PWNe, a more general view on PWNe can be obtained. To compare PWN of different ages, their evolution has to be taken into account. The next Section is intended to discuss the evolution of PWNe by means of a time-dependent model.

2.2.3. Evolution

As described in Sect. 2.2.1, the compact pulsar is the central energy source of the much larger nebula. The Crab Nebula has a radius of $3\,\mathrm{pc}$ ($\approx 10\,\mathrm{ly}$), but PWNe can extend up to $40\,\mathrm{pc}$ (see, e.g., Aharonian et al. 2006f). Due to causal reasons, a PWN is hence insensitive to rapid changes in the pulsar's proximity. Although it is not linked directly with its surrounding nebula, the pulsar heavily affects the particle wind and the nebula over a larger time scale. Pulsars slow down their rotation significantly over time (e.g. $13\,\mu\mathrm{s}$ per year for the Crab pulsar). The lost rotational energy is partly carried away by energetic electrons and magnetic energy. The provided amount of energy (*spin-down luminosity*, $\dot{E}$) can be estimated using measurements of the pulsar period P and its first derivative, i.e. the slowing rate $\dot{P}$:

$$\dot{E} = 4\pi^2 I \frac{\dot{P}}{P^3}, \tag{2.7}$$

with the assumption of $I \approx 10^{45}\,\mathrm{g\,cm^{-2}}$ being the moment of inertia of a rotating sphere with $1.4\,M_\odot$ and a radius of $10\,\mathrm{km}$. Following Pacini & Salvati (1973), $\dot{E}$ evolves with time as

$$\dot{E}(t) = \dot{E}_0 \cdot \left(1 + \frac{t}{\tau_0}\right)^{-\frac{n+1}{n-1}}, \tag{2.8}$$

where $\dot{E}_0$ depicts the spin-down luminosity at the birth of the pulsar ($t = 0$), τ_0 is the spin-down time scale and n is called braking index. The latter derives from the pulsar braking $\dot{\Omega} \propto \Omega^n$ ($\Omega = 2\pi/P$) and is assumed to be $n = 3$ in case of a rotating pure magnetic dipole (see Magalhaes et al. 2012, and references therein for further details), while τ_0 is defined as

(see, e.g., Gaensler & Slane 2006)

$$\tau_0 = \frac{P}{(n-1)\dot{P}} \left(\frac{P_0}{P} \right)^{n-1}, \tag{2.9}$$

where P_0 is the pulsar birth period, i.e. $P(t=0)$. Furthermore, solving the pulsar braking equation leads to the age of a pulsar, derived by Manchester & Taylor (1977):

$$T = \frac{P}{(n-1)\dot{P}} \left(1 - \left(\frac{P_0}{P} \right)^{n-1} \right). \tag{2.10}$$

In most cases, P_0 and n are unknown, which is why the real age of a pulsar cannot be estimated via Eq. 2.10. Accordingly, the so called *characteristic age* τ_c, presuming $P_0 \ll P$ and $n=3$, is the most common approximation for the age of a pulsar:

$$\tau_c = \frac{P}{2\dot{P}}. \tag{2.11}$$

This estimate of the pulsar age is challenged in many cases: for the Crab Pulsar $\tau_c = 1.25\,\mathrm{kyr}$ while the historical supernova of 1054 implies a true age of $T = 960\,\mathrm{yr}$. Another example is PSR B1951+32, where the characteristic age is overestimating the true age by almost a factor of 2 (Migliazzo et al. 2002). On the other hand, Gvaramadze (2001) describes the case of MSH15−5*2*, where τ_c is more than one order of magnitude smaller than the inferred true age. Estimating the proper age of the pulsar is however essential for the modelling of the PWN evolution. To investigate and discuss the evolution of PWNe in the following, the work documented in Mayer et al. (2012) is reflected and summarised with some extensions and additions.

To obtain the present electron distribution considering the PWN evolution, the constantly changing energy output as well as other time-dependent properties of the PWN such as magnetic field or size has to be taken into account. Subsequently, the interplay between energetic electron injection into the pulsar wind and their energy losses can be calculated in discrete time steps δt. Independent of time, this work assumes a braking index of $n = 3$. In addition, it is inferred that 100% of the spin-down luminosity is converted into relativistic electrons ($\eta = 1.0$). The choice of this value is motivated by the strong correlation with the initial spin-down power $\dot{E}_0$ (Eq. 2.8). The energy content in fresh electrons, injected between t and $t + \delta t$, can be written as

$$\Delta E_\mathrm{p}(t) = \eta \int_t^{t+\delta t} \dot{E}(t')\mathrm{d}t'. \tag{2.12}$$

In addition, the energy distribution of the injected electrons is assumed to follow a power law

$$\frac{\mathrm{d}N_\mathrm{inj}}{\mathrm{d}E}(E,t) = \Phi_0(t) \left(\frac{E}{1\,\mathrm{TeV}} \right)^{-p}, \tag{2.13}$$

where p is the spectral index. The normalisation $\Phi_0(t)$ is adjusted to match the respective energy output:

$$\Delta E_\mathrm{p}(t) \overset{!}{=} \int_{E_\mathrm{min}}^{E_\mathrm{max}} \frac{\mathrm{d}N_\mathrm{inj}}{\mathrm{d}E}(E,t)\,\mathrm{d}E. \tag{2.14}$$

The considered energy interval ranges from $E_{\min} = 100\,\text{GeV}$ to $E_{\max} = 1\,\text{PeV}$, optimised to reproduce the most energetic photon emission. The energy losses are approximated by an exponential function adopted from Zhang et al. (2008):

$$\frac{\mathrm{d}N_{\text{cooled}}}{\mathrm{d}E}(E,t) = \frac{\mathrm{d}N}{\mathrm{d}E}(E,t-\delta t) \cdot \exp\left(-\frac{\delta t}{\tau_{\text{eff}}(E,t)}\right), \tag{2.15}$$

where as an effective time scale for energy losses, the so-called cooling time scale is given as $\tau_{\text{eff}}^{-1} = \tau_{\text{syn}}^{-1} + \tau_{\text{esc}}^{-1} + \tau_{\text{ad}}^{-1}$. This approach takes into account energy losses due to synchrotron radiation, electrons escaping the nebula and adiabatic cooling of the electron plasma. Energy losses attributed to IC emission are generally assumed to be negligible compared to the aforementioned processes. Under specific circumstances, e.g. if the PWN is located in a strongly radiative region, IC cooling could become important and should be taken into account. For the purpose of a qualitative description of the PWN evolution in general, however, the average IC cooling time scale is much larger compared to the other time scales. The first two terms of the cooling time scale τ_{eff}^{-1} are adopted from Zhang et al. (2008):

$$\tau_{\text{syn}}(E,t) = 12.5 \cdot \left[\frac{B(t)}{10\,\mu\text{G}}\right]^{-2} \cdot \left[\frac{E}{10\,\text{TeV}}\right]^{-1}\,\text{kyr} \tag{2.16}$$

$$\tau_{\text{esc}}(E,t) = 34 \cdot \left[\frac{B(t)}{10\,\mu\text{G}}\right] \cdot \left[\frac{E}{10\,\text{TeV}}\right]^{-1} \cdot \left[\frac{R(t)}{1\,\text{pc}}\right]^{2}\,\text{kyr}, \tag{2.17}$$

where $R(t)$ and $B(t)$ denote the time-dependent PWN radius and the magnetic field evolution, respectively. For the radius evolution, the model is based on analytical studies of PWNe evolving inside their SNR environment (e.g. Chevalier 1977; Reynolds & Chevalier 1984), taking into account the interaction with the SNR reverse shock (see, e.g., Blondin et al. 2001; van der Swaluw et al. 2001, 2004). The functional time evolution of the nebula radius includes three phases, depending on the pulsar spin-down time scale τ_0 and the time of the reverse shock interaction t_{rs}. The moment of the reverse-shock interaction is usually assumed to occur when $t_{\text{rs}} > \tau_0$. For this case, the following piecewise power law is compiled from the above-mentioned works:

$$R(t) \quad \propto \quad \begin{cases} t^{6/5} & \text{for } t \leq \tau_0 \\ t & \text{for } \tau_0 < t \leq t_{\text{rs}} \\ t^{3/10} & \text{for } t > t_{\text{rs}}. \end{cases} \tag{2.18}$$

In the case of $t_{\text{rs}} < \tau_0$, the PWN radius evolves slightly different:

$$R(t) \quad \propto \quad \begin{cases} t^{6/5} & \text{for } t \leq t_{\text{rs}} \\ t^{11/15} & \text{for } t_{\text{rs}} < t \leq \tau_0 \\ t^{3/10} & \text{for } t > \tau_0. \end{cases} \tag{2.19}$$

According to de Jager & Harding (1992) the radius evolution can be used to calculate the time scale for adiabatic energy losses as

$$\frac{\mathrm{d}E_{\text{ad}}}{\mathrm{d}t} = -\frac{E}{3}\nabla\vec{v}_{\perp}(R) = \dot{E}_{\text{p}} \tag{2.20}$$

where $\vec{v}_\perp(R)$ depicts the radial component of the particle outflow velocity. In general, its divergence can be calculated to

$$\nabla\vec{v}_\perp(R) = \frac{1}{R^2} \cdot \frac{\partial(R^2\vec{v}_\perp)}{\partial R} \tag{2.21}$$

$$= \frac{1}{R(t)^2} \cdot \frac{\partial(R(t)^2\vec{v}_\perp(t))}{\partial t} \cdot \frac{\partial t}{\partial R}. \tag{2.22}$$

Evaluating Eq. 2.20 for the assumed radius evolution, the time scale for adiabatic energy losses can be derived:

$$\Rightarrow \tau_{\mathrm{ad}} = -\frac{E}{\dot{E}_{\mathrm{p}}} = \left\{ \begin{array}{lll} 15/13 \cdot t & \text{for} & t \leq \tau_0 \\ 3/2 \cdot t & \text{for} & \tau_0 < t \leq t_{\mathrm{rs}} \\ -30 \cdot t & \text{for} & t > t_{\mathrm{rs}}. \end{array} \right. \tag{2.23}$$

In case $t_{\mathrm{rs}} < \tau_0$, the second segment ($3/2 \cdot t$) changes to $45/18 \cdot t$. Eq. 2.23 leads to an adiabatic energy gain of electrons in older PWNe. Compared to the much shorter time scale of other processes, this energy gain, however, can be considered negligible. To likewise feed Eq. 2.16, the magnetic field evolution is adapted from Zhang et al. (2008) as

$$B(t) = \frac{B_0}{1 + \left(\frac{t}{\tau_0}\right)^\alpha} + B_{\mathrm{ISM}}, \tag{2.24}$$

with the addition to assume a constant contribution from the interstellar medium (ISM) of $B_{\mathrm{ISM}} = 3\,\mu\mathrm{G}$. An index of $\alpha = 0.6$ is required to conserve the magnetic flux in old PWNe. The presented framework for electron injection and subsequent cooling processes can be applied to calculate the yield of electrons with energy E present in the nebula at a time $t + \delta t$. This number is composed of electrons injected and cooled until time t on top of freshly injected electrons between t and $t + \delta t$:

$$\frac{\mathrm{d}N}{\mathrm{d}E}(E, t + \delta t) = \frac{\mathrm{d}N_{\mathrm{cooled}}}{\mathrm{d}E}(E, t) + \frac{\mathrm{d}N_{\mathrm{inj}}}{\mathrm{d}E}(E, t + \delta t). \tag{2.25}$$

Evaluating Eq. 2.25 in small steps δt yields the spectral energy distribution of electrons inside a PWN at any time. For details about the model performance and the ideal time and energy binning, the reader is referred to Mayer (2010). Based on the resulting electron distribution, the corresponding photon emission can be determined. The two processes considered here are, as presented in Sect. 2.2.2, synchrotron and IC emission. Note that the calculations of the synchrotron spectrum makes use of an approximation derived by Schoeck (2010), where the integrated Bessel function of the order 5/3 from Eq. 2.2 is simplified to:

$$\frac{\nu}{\nu_{\mathrm{c}}} \int_{\nu/\nu_{\mathrm{c}}}^{\infty} \mathrm{d}\xi K_{5/3}(\xi) \approx 1.7826 \left(\frac{\nu}{\nu_{\mathrm{c}}}\right)^{0.3005} \cdot \exp\left(\frac{\nu}{\nu_{\mathrm{c}}}\right) \tag{2.26}$$

For the sake of simplicity and computational speed, the SSC component in the IC spectrum is considered sub-dominant in most cases. Table 2.1 summarises all model parameters. The parameters denoted in column "mean model" are used to illustrate the model predictions for a generic PWN in Fig. 2.4. The parameter ranges given in the latter column are used later on for the specific modelling of the PWN population. Note that for the modelling of individual objects, the radiation fields have to be derived on a case-by-case basis. For

Table 2.1.: Overview of parameters used for modelling.

Parameter description			Parameter values	
			Mean Model	Scatter range
Braking index	n		3.0	2.5 ... 3.5
Initial spin-down power	$\dot{E}_0$	$(10^{39}\,\mathrm{erg\,s^{-1}})$	3.0	0.5 ... 6.0
Initial spin-down timescale	τ_0	(kyr)	0.5	0.23 ... 1.1
Initial magn. field strength	B_0	$(\mu\mathrm{G})$	50.0	20.0 ... 110.0
Reverse shock interaction timescale	t_{rs}	(kyr)	5.0	5.0 ... 20.0
PWN radius at $t = 10\,\mathrm{kyr}$	R_{10}	(pc)	7.5	3.8 ... 15.0
Adopted const. ISM magn. field strength	B_{ISM}	$(\mu\mathrm{G})$	3.0	3.0
Lepton conversion efficiency	η		1.0	1.0
Index of magn. field evolution	α		0.6	0.6
Index of lepton injection spectrum	p		2.0	2.0
Lower bound of lepton energy distribution	E_{min}	(TeV)	0.1	0.1
Upper bound of lepton energy distribution	E_{max}	(PeV)	1.0	0.1 ... 1.0

Notes. The parameters listed in the column "mean model" are used to illustrate the evolution of a generic PWN (see text). The column "scatter range" gives the parameter range which is used to mimic the intrinsic scatter of the PWN population (see next Section).
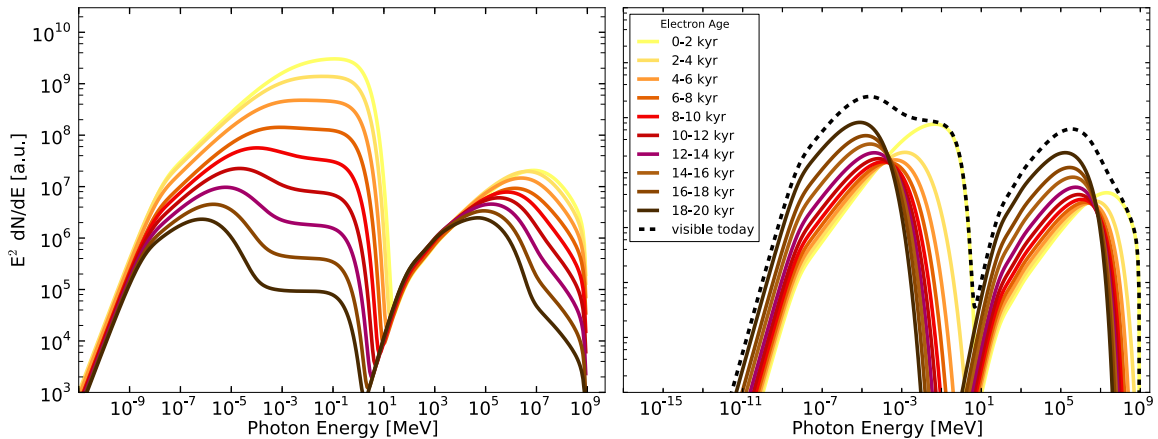

Figure 2.4.: SED evolution and composition of a generic PWN as predicted by the model. The used parameters follow the column "mean model" in Table 2.1. *Left*: Time evolution of the SED, ranging from a young (0.5 kyr, yellow) to an old (150 kyr, dark red) PWN. *Right*: The SED of a 20 kyr old PWN shown as black-dashed line. Coloured lines denote a decomposition of the SED into contributions by electrons from different injection epochs.

this purpose, the GALPROP code (Porter & Strong 2005) provides estimates on the dust and starlight components dependent on the position in our Galaxy. To visualise the time evolution predicted by the model, the left panel of Fig. 2.4 shows sample SEDs tracing several evolutionary stages of the exemplary PWN. The model curves represent the radiative output between 0.5 kyr and 150 kyr, derived in equidistant logarithmic time steps. In the picture of an evolving PWN, the synchrotron and IC emission change with increasing age of the generic system. Due to the rapidly decaying magnetic field (see Eq. 2.24), the synchrotron component fades much faster than the IC radiation. In the latter energy range, the losses of the electrons are reflected in a more slowly declining luminosity and a pronounced shift of the spectral peak towards lower energies. In this context, evolved PWNe of sufficient

age become strong γ-ray emitters with a weak X-ray counterpart which complicates their MWL identification. This scenario offers a potential explanation for the large amount of unidentified sources at VHE γ rays (Aharonian et al. 2008): old systems could produce IC dominated γ-ray sources without a detectable synchrotron counterpart, e.g. at X-rays. The right panel of Fig. 2.4 depicts a snapshot of the generic system at an age of 20 kyr. The SED is decomposed into contributions from the past live time epochs. On the one hand the photon emission from the population of freshly injected electrons (bright yellow line) is responsible for the most energetic synchrotron (in particular X-ray) and IC emission. On the other hand, the peak of IC emission is powered by a superposition of electrons from various injection epochs. This Figure further implies that investigations of the X-rays emission only provides insights on the most recently injected electrons. A study targeted on γ rays, however, is subject to a different electron population which is influenced by the past evolution of the PWN.

The evolutionary model suggests that PWNe change their appearance with age. Focused on the highest energies, this work studies measured PWN properties in the VHE regime and compares them to characteristics of their corresponding pulsar in the next Section. It is additionally discussed whether the investigated parameter trends are expected in the context of the presented model.

2.3. PWN Population at Very High Energies

In the past years, several efforts were made to comprehensively investigate the population of VHE detected PWNe, either by performing a uniform analysis (Carrigan 2007; Carrigan et al. 2008; Marandon 2010; Mayer 2010), or by compiling and collecting data from individual publications and archival data (e.g. Mattana et al. 2009; Kargaltsev & Pavlov 2010; Kargaltsev et al. 2013). More recently, an extensive study of PWNe at HE γ rays correlated with the public VHE data has been conducted by Acero et al. (2013). The present Section is following Klepser et al. (2013) which is based on the most recent analysis of the H. E. S. S. Galactic Plane Survey (HGPS, version 1, H.E.S.S. internal[1]). For this study, the presented, time-dependent model is applied to the population of VHE γ-ray emitting PWNe.

The HGPS has accumulated over ten times more data than presented in Aharonian et al. (2006d), resulting in a major sensitivity gain which leads to a large amount of newly discovered sources in the VHE regime. Table 2.3 shows a detailed list of the considered PWNe including objects outside the HGPS, or observed by other Cherenkov telescopes. The list is a composition of VHE γ-ray sources flagged as PWNe[2] with the additional requirement that the corresponding pulsar has a spin-down luminosity of at least $\dot{E} > 10^{35}\,\mathrm{erg\,s^{-1}}$. This value was chosen to reduce the PWN sample to firm associations. The spectral and morphological results were taken from the HGPS where possible. For sources which are located outside the HGPS range, the published values are used instead. In the following, properties of PWNe are plotted versus observables of their associated pulsar. Throughout Fig. 2.5 and 2.6, two PWNe are marked in particular, which are discussed in more detail later in this thesis.

The most reliable and unambiguous measurements of pulsar properties are the pulsar period and its time derivative. To illustrate the fraction of pulsars producing nebulae at VHE γ rays, they are highlighted in a $P - \dot{P}-$diagram (Fig. 2.5). All pulsars with their properties are

---

[1]https://hess-confluence.desy.de/confluence/display/HESS/HGPS+Paper+-+Source+catalog+version+1

[2]http://tevcat.uchicago.edu

Table 2.2.: List of all considered PWNe

Name	Pulsar	Ra [°]	Dec [°]	D [kpc]	Size [°]	L_γ [erg s^{-1}]	Γ
CTA 1	J0007+7303	1.61	72.98	1.40	0.27 ± 0.02	$(7.07 \pm 1.01) \cdot 10^{32}$	2.20 ± 0.20
Crab Nebula	J0534+2200	83.63	22.01	2.00	< 0.10	$(3.21 \pm 0.07) \cdot 10^{34}$	2.63 ± 0.02
N 157B	J0537−6910	84.43	-69.17	53.70	< 0.12	$(4.77 \pm 0.91) \cdot 10^{35}$	2.80 ± 0.20
Vela X	J0835−4510	128.72	-45.74	0.28	0.55 ± 0.01	$(3.78 \pm 0.30) \cdot 10^{32}$	2.04 ± 0.06
HESS J1026−582	J1028−5819	156.66	-58.20	2.33	0.14 ± 0.03	$(2.54 \pm 1.06) \cdot 10^{33}$	1.94 ± 0.20
G292.2−0.5	J1119−6127	169.76	-61.46	8.40	0.12 ± 0.02	$(2.26 \pm 0.33) \cdot 10^{34}$	2.67 ± 0.14
HESS J1303−631	J1301−6305	195.77	-63.21	6.65	0.22 ± 0.00	$(9.21 \pm 0.22) \cdot 10^{34}$	2.35 ± 0.02
HESS J1356−645	J1357−6429	208.98	-64.53	2.50	0.21 ± 0.02	$(8.25 \pm 0.79) \cdot 10^{33}$	2.34 ± 0.09
Kookaburra (Rabbit)	J1418−6058	214.50	-60.99	5.60	0.10 ± 0.01	$(2.72 \pm 0.16) \cdot 10^{34}$	2.32 ± 0.05
Kookaburra (PWN)	J1420−6048	215.07	-60.76	5.61	0.08 ± 0.01	$(2.91 \pm 0.16) \cdot 10^{34}$	2.23 ± 0.05
HESS J1458−608	J1459−6053	225.01	-60.82	−	0.37 ± 0.04	−	1.88 ± 0.41
MSH 15−52	J1513−5908	228.53	-59.17	4.40	0.11 ± 0.00	$(3.25 \pm 0.13) \cdot 10^{34}$	2.34 ± 0.03
HESS J1616−508	J1617−5055	244.14	-50.90	6.82	0.21 ± 0.01	$(1.28 \pm 0.09) \cdot 10^{35}$	2.41 ± 0.05
HESS J1708−443	J1709−4429	257.03	-44.28	2.60	0.30 ± 0.04	$(1.05 \pm 0.15) \cdot 10^{34}$	1.96 ± 0.09
HESS J1718−385	J1718−3825	259.55	-38.55	3.60	0.13 ± 0.02	$(3.61 \pm 0.51) \cdot 10^{33}$	1.76 ± 0.08
G0.9+0.1	J1747−2809	266.85	-28.16	13.31	< 0.03	$(3.95 \pm 0.26) \cdot 10^{34}$	2.38 ± 0.05
HESS J1809−193	J1809−1917	272.54	-19.35	3.55	0.43 ± 0.01	$(3.31 \pm 0.28) \cdot 10^{34}$	2.23 ± 0.07
HESS J1813−178	J1813−1749	273.42	-17.85	4.70	0.08 ± 0.01	$(2.03 \pm 0.13) \cdot 10^{34}$	2.21 ± 0.05
HESS J1825−137	J1826−1334	276.29	-13.87	3.93	0.49 ± 0.01	$(7.85 \pm 0.25) \cdot 10^{34}$	2.43 ± 0.02
HESS J1831−098	J1831−0952	277.78	-9.87	4.05	0.58 ± 0.13	$(2.52 \pm 0.36) \cdot 10^{34}$	2.28 ± 0.13
HESS J1833−105	J1833−1034	278.41	-10.60	4.10	< 0.04	$(1.81 \pm 0.44) \cdot 10^{33}$	2.39 ± 0.18
HESS J1846−029	J1846−0258	281.60	-2.98	5.80	0.03 ± 0.01	$(6.08 \pm 0.82) \cdot 10^{33}$	2.32 ± 0.10
IGR J18490−0000	J1849−0001	282.25	-0.01	−	0.05 ± 0.02	−	1.94 ± 0.09
HESS J1912+101	J1913+1011	288.26	10.11	4.76	0.33 ± 0.02	$(2.07 \pm 0.23) \cdot 10^{34}$	2.46 ± 0.08
G54.1+0.3	J1930+1852	292.55	18.79	7.00	0.13 ± 0.03	$(1.38 \pm 0.32) \cdot 10^{34}$	2.70 ± 0.27

Notes. The columns "Ra" and "Dec" denote position of the VHE centroid in equatorial coordinates. The column "D" lists the distances to the pulsars (Manchester et al. 2005), while "Size" depicts the Gaussian extension (1σ) of the VHE γ-ray source derived in the HGPS. In case of an asymmetric morphology, the given size is the equivalent radius ($\sigma = \sqrt{\sigma_1 \sigma_2}$). Upper limits on the extension are given in case the fitted value is smaller than the nominal systematic of the instrument angular resolution. L_γ and Γ are the intrinsic luminosity within $1 - 10 \, \text{TeV}$ and the spectral index of the HGPS analysis, respectively. The luminosity of objects without a distance measure, namely HESS J1458-608 and IGR J18490-0000, cannot be derived. Four PWNe in this list are not in the range of the HGPS. The values are taken from the following references:
CTA 1: Aliu et al. (2013).
Crab Nebula: 3σ extension limit from Aharonian et al. (2004a), spectrum from Aharonian et al. (2006a).
N 157B: H.E.S.S. Collaboration et al. (2012a), extension limit derives from conservative PSF estimate.
HESS J1026−582: H.E.S.S. Collaboration et al. (2011).

taken from the ATNF pulsar database[3] (Manchester et al. 2005, version 1.49), comprising 2311 objects to date. It can be recognised that all pulsars with a detectable VHE PWN are on the upper left of the bulge in Fig. 2.5, implying them to have a small period combined with a high period derivative. Applying Eq. 2.7 rephrases this statement into requiring a high pulsar spin-down luminosity to form a detectable VHE PWN (Fig. 2.5, right panel). The Figure highlights in particular the two most energetic pulsars since they both power VHE γ-ray emission. Their respective PWNe are discussed in detail later in this thesis. It has to be noted that less energetic pulsars may produce nebulae which are just too dim to detect with current instruments. The depicted and discussed population hence cannot be fully representative, only for those with similar energetics in our Galactic environment.

In the following, the characteristic age of a pulsar is assumed to be a reasonable approximation for its real age. This assumption, along with Eq. 2.18, allows for a comparison of the
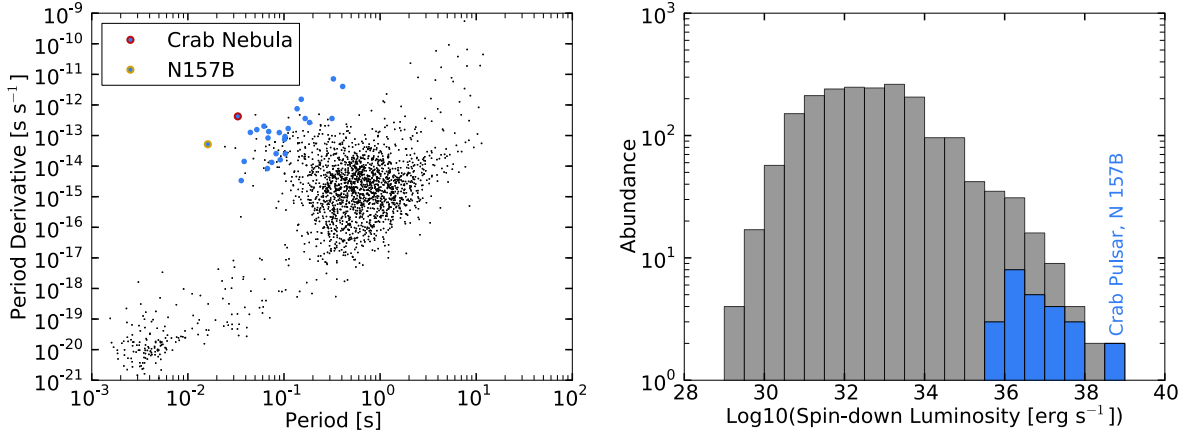
---
[3]http://www.atnf.csiro.au/people/pulsar/psrcat/

Figure 2.5.: *Left*: All pulsars depicted as black dots in a $P - \dot{P}-$diagram. Highlighted in blue are those producing VHE γ-ray emitting PWNe. Two PWNe are highlighted which are discussed individually in this thesis. *Right*: Distribution of all measured spin-down luminosities on a double logarithmic scale. The fraction of pulsars producing VHE PWNe are overlayed in blue. Further noted are the two most energetic pulsars, namely the Crab pulsar and the pulsar in the SNR N 157B (PSR J0537−6910).
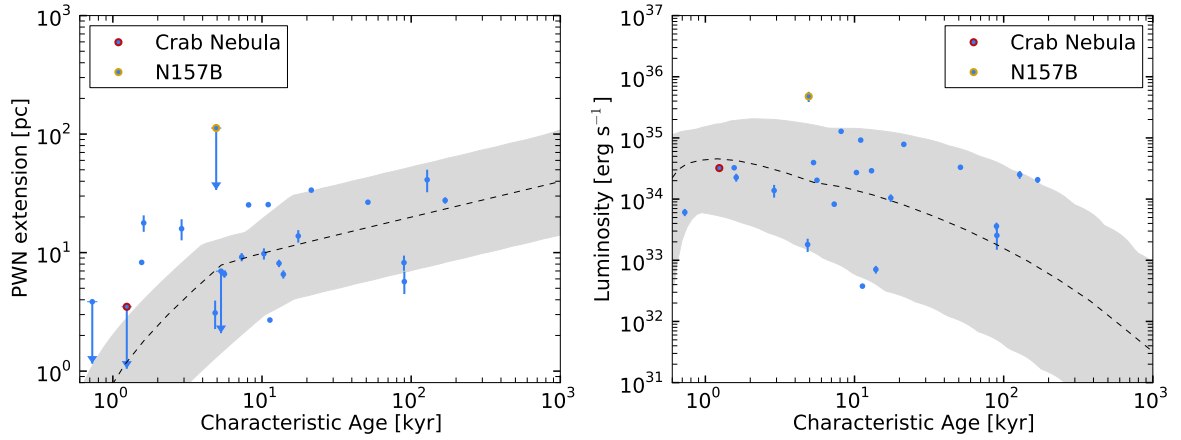
Figure 2.6.: *Left*: The intrinsic size of the considered PWNe (blue points) plotted versus the characteristic age of the associated pulsar. Overlaid as grey-shaded area is the model prediction from Eq. 2.18 with the artificial spread listed in Table 2.1. The black-dashed line denotes the "mean model". *Right*: Intrinsic PWN luminosity between $1 - 10 \, \mathrm{TeV}$ also shown against the characteristic age. The modelled solid line is also based on the predicted evolution by the "mean model", while the grey-shaded area mimics an intrinsic scatter.

radius evolution of PWNe to that of the model prediction. It should be mentioned that the size, as well as other intrinsic PWN properties, are also subject to uncertainties in the distance measurement of the corresponding pulsar. Due to the strong dependence on the applied method to derive the pulsar distance, these uncertainties are not considered here. The mea-

sured extensions of PWNe, plotted against the characteristic age, is shown in Fig. 2.6 (left). In this Figure, the model presented in Sect. 2.2.3 is also overlaid, using the parameter spread given in Table 2.1 to mimic an intrinsic scatter. Note that upper limits in Fig. 2.6 are drawn if the determined value is smaller than $0°03$, which is the H. E. S. S. systematics of the angular resolution. The trend of an expanding PWN as predicted by Eq. 2.18 can be confirmed though there is a large spread in the measured extensions, which could be attributed to a real intrinsic spread plus the uncertainties in the characteristic age and distance estimate. The dynamical expansion of an individual PWN is furthermore affected by its surrounding. A density gradient in the surrounding medium may cause an asymmetrically expanding PWN (see, e.g., Aharonian et al. 2006f). The interaction with the SNR reverse shock might also cause extensions which vary on much shorter time scales compared to the predicted long-term radius evolution (Gelfand et al. 2009). The snapshots of the PWN extension may therefore be affected by radius instabilities producing a larger scatter for middle-aged ($10 - 20\,\mathrm{kyr}$) PWNe.

In terms of spectral evolution, the right panel of Fig. 2.6 shows the evolution of the PWN luminosity in the interval $1 - 10\,\mathrm{TeV}$. Again, this observable is plotted versus the characteristic age as an approximation for the real age. Due to the large spread in intrinsic luminosities, the very slow trend of dimming PWNe with progressing age, predicted by the model can neither be confirmed nor rejected. By construction, the luminosity spread is well reproduced with the parameter range resulting in the model band. The PWN standing out of both plots in Fig. 2.6 by the lowest luminosity and the smallest measured extension is Vela X. Located only $290\,\mathrm{pc}$ from Earth (e.g. Caraveo et al. 2001), the proximity of Vela X provides unique insights into the structure and morphology of a PWN. Estimates for its age range from $5\,\mathrm{kyr}$ to $50\,\mathrm{kyr}$, (Stothers 1980, and references therein), while most of them converge at $11\,\mathrm{kyr}$ which is close to its characteristic age ($\tau_c = 11.3\,\mathrm{kyr}$). Dedicated analyses of Vela X at VHE γ rays (Aharonian et al. 2006b; Abramowski et al. 2012) are conducted in the innermost $4\,\mathrm{pc}$ which however corresponds to a large angular size of $1°2$. Since the hypothetical tails of Vela X are probably diluted over a much larger solid angle range, its complete detection might be impossible due to its very low surface brightness which may fall under the detection threshold of current γ-ray instruments. This scenario, leading to an underestimation of the extension and photon flux, is also proposed for other VHE γ-ray sources (Vernetto 2014). Consequently, if Vela X was further away, the derived extension and luminosity would possibly be higher, moving it into the grey-shaded model band of "ordinary" PWNe.

Another aspect which supports the strong diversity of the observed PWN population are the case-by-case locally varying radiation fields. The density of these fields strongly affect the IC emission (compare Fig. 2.3). The modelling of the PWN luminosity shown in Fig. 2.6, however, does not account for an intrinsic scatter of radiation field densities. For the Crab Nebula, an important radiation field component is SSC. Other PWNe might have intense close-by radiation fields which affect their VHE γ-ray appearance. Highlighted throughout the plots, the PWN in N 157B seems to have an exceptionally high luminosity compared to other systems of this sample. The spin-down luminosity of the pulsar associated with N 157B is comparable to the Crab pulsar, which is why it is often referred to as "Crab-like". As shown in Fig. 2.6, however, their nebulae are quite different regarding the intrinsic luminosity. The following Chapter puts a special emphasis on N 157B. The non-thermal radiation of this system is modelled and compared to the Crab Nebula. Accordingly, conclusions about the intrinsic differences of these two objects can be derived.

3. N 157B - An Energetic Twin of the Crab Nebula

Since the Crab Nebula is one of the best studied astrophysical objects, the abundant MWL data provides the unique opportunity to characterise many quantities of this source. Usually, a comparably strong magnetic field combined with electrons up to some PeV are required to explain the observational data. Since these key properties differ for other PWNe, the Crab Nebula is commonly assumed to be a rather special representative of the PWN population. Generally, the uniqueness of the Crab Nebula is thought to be linked to the high spin-down luminosity of the Crab pulsar ($\dot{E}_{\mathrm{C}} = 4.6 \cdot 10^{38}\,\mathrm{erg\,s^{-1}}$), which is why most PWNe are not expected to be of similar nature. Apart from the Crab pulsar, the pulsar with the highest observed spin-down luminosity is PSR J0537$-$6910 inside the SNR N 157B which also drives an energetic PWN (see Fig. 3.1). In this Chapter, the basic properties, like the magnetic field of this PWN are derived using a stationary modelling. These characteristics are compared to the ones of the Crab Nebula. Subsequently, the connection between these properties and the energy output of the pulsar is investigated.

Located within the LMC at a distance of roughly 48 kpc (Macri et al. 2006), PSR J0537$-$6910 was detected with *ROSAT* (Marshall et al. 1998; Wang & Gotthelf 1998). The spin period of the pulsar was measured to be $P_{\mathrm{N}} = 16\,\mathrm{ms}$, which, combined with the period derivative of $\dot{P}_{\mathrm{N}} = 5.14 \cdot 10^{-14}\,\mathrm{s\,s^{-1}}$, implies a remarkably high spin-down luminosity of $\dot{E}_{\mathrm{N}} = 4.9 \cdot 10^{38}\,\mathrm{erg\,s^{-1}}$ (see Eq. 2.7). In terms of energetics, this pulsar therefore strongly
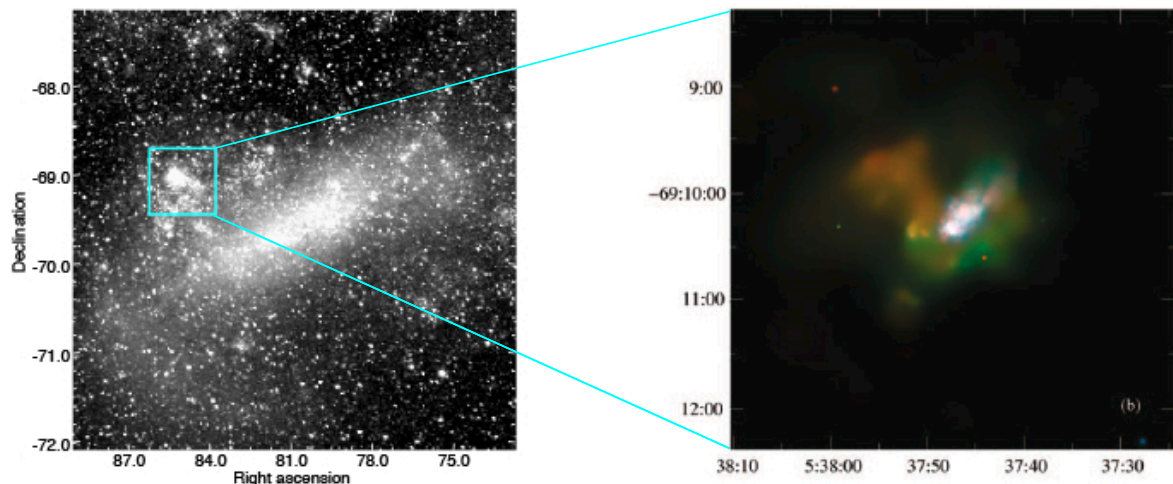

Figure 3.1.: *Left*: Optical image of the LMC adapted from Mellinger (2009). The cyan box represents the frame of the right image of N 157B. *Right*: X-ray intensity map of N 157B adopted from Chen et al. (2006). The image is colour-coded to illustrate the energy dependence of the emission. Colours represent the following energy bands: $0.3 - 0.7\,\mathrm{keV}$ (red), $0.7 - 1.5\,\mathrm{keV}$ (green), and $1.5 - 7\,\mathrm{keV}$ (blue).

resembles the Crab pulsar which is why these objects can be referred to as energetic twins. The characteristic age of PSR J0537−6910, is around 5 kyr which was also derived independently for its surrounding SNR (Wang & Gotthelf 1998). Marshall et al. (2004), however found P_N and $\dot{P}_N$ to be very unstable which complicates age estimates of the pulsar. The inferred braking index of $n \approx 7$ is far from the usually assumed canonical value of $n = 3$. In case of a constant braking index and assuming a birth period of 11 ms, the pulsar has be younger than 1.7 kyr. In contrast, Chu et al. (1992) constrained the age of the SNR to be around 24 kyr. Besides the present age uncertainties, PSR J0537−6910 is surrounded by an extended, non-thermal X-ray nebula (Wang & Gotthelf 1998; Chen et al. 2006), indicating energetic electron acceleration (Fig. 3.1, right). Additionally, the detection of VHE γ rays from this PWN was recently reported by the H.E.S.S. Collaboration et al. (2012a). In this energy range, it is the first discovery of a PWN outside of our Galaxy.

The PWN in N 157B and the Crab Nebula are driven by pulsars which are similar in terms of spin-down luminosity. This provides the opportunity to compare these two objects in order to evaluate whether the Crab Nebula and its counterpart in the LMC have commonalities. In particular, investigating the magnetic fields inside these nebulae might indicate a possible link of spin-down luminosity and pulsar wind magnetisation. Therefore, the non-thermal MWL emission of N 157B is modelled in the following. The derived properties, like the magnetic field, are subsequently compared to the Crab Nebula.

3.1. MWL situation

For the purpose of deriving the present electron spectrum and magnetic field within N 157B, the existing MWL information is collected. Since this work is focused on the most energetic fraction of electrons, only the non-thermal X-ray and VHE γ-ray data are used for the modelling. Accordingly, available radio data (Lazendic et al. 2000), originating from low energy electrons with long cooling time scales are neglected.

Chen et al. (2006) determined the non-thermal X-ray spectrum of N 157B as a power law (Eq. 2.13) with an integral energy flux of $1.4 \cdot 10^{-11} \, \mathrm{erg \, cm^{-2} \, s^{-1}}$ and a spectral index of $2.29^{+0.05}_{-0.06}$ within an energy range of $0.5 - 10 \, \mathrm{keV}$. For the IC luminosity at VHE γ rays, it is possible to make use of the most recent H. E. S. S. data set. Since the LMC was intensely observed by H. E. S. S. in the past years, the exposure on N 157B has increased by more than a factor of four compared to the first publication on this source (H.E.S.S. Collaboration et al. 2012a). The corresponding H. E. S. S. data analysis is not part of this work, which is why the derived energy spectrum is used without further introduction. The conducted spectral analysis of the larger dataset yields a power law with a flux normalisation at 1 TeV of $(1.32 \pm 0.1) \cdot 10^{-12} \, \mathrm{TeV^{-1} \, cm^{-2} \, s^{-1}}$ and a spectral index of 2.8 ± 0.1. For further details on this analysis, the reader is referred to an upcoming publication (H.E.S.S. Collaboration, in prep.). To complement the IC emission, the HE γ-ray range is also checked for data. Abdo et al. (2010b) presented an analysis of *Fermi*-LAT data from the LMC. The analysis indeed revealed a bright source close to the pulsar position but its association with N 157B is uncertain. The authors argue that the source is likely associated with the massive close-by star forming region 30 Doradus. This object is also important for the modelling which, among others, is discussed in the following.

The major missing ingredient for the model to derive the electron spectrum inside the nebula of N 157B is the composition of present radiation fields. An adequate estimate of these fields is required to determine the IC emission. The known part is the omnipresent CMB following

a black-body function with a temperature $T = 2.7$ K. In contrast to the Crab Nebula (e.g. Meyer et al. 2010), the SSC component is considered negligible since the detected X-ray emission from N 157B is intrinsically dimmer than from the Crab Nebula by about one order of magnitude. To estimate other prominent radiation components, the cosmic neighbourhood of N 157B has to be investigated. Within a few arc minutes of PSR J0537$-$6910 there are two very strong thermal radiators in the LMC, namely the OB association LH 99 and the aforementioned massive star forming region 30 Doradus. Since the exact distance to either of these objects is unknown, two extreme scenarios are assumed:

1. N 157B is located in front of or behind these two infra-red emission regions. Therefore these radiation fields do not contribute as target for IC scattering and CMB is the only relevant ambient radiation field.

2. N 157B, 30 Doradus and LH 99 are at the same projected distance implying very strong radiation fields at the PWN position.

The first scenario depicts the case of the minimum radiation fields, while the second case gives an upper limit on the radiation field energy density. The thermal component of 30 Doradus was measured by the *Spitzer* telescope. Indebetouw et al. (2009) determined that the isotropic emission follows a black body function with temperature $T_{30\mathrm{Dor}} = 88$ K and an energy density of $2.7\,\mathrm{eV\,cm}^{-3}$. Micelotta et al. (2009) analysed data on LH 99 from the same telescope. They modelled the radiation intensity as a superposition of two modified black body functions $I_{LH99}(\nu) = C_1 I_1(\nu, T_1, \beta_1) + C_2 I_1(\nu, T_2, \beta_2)$, where:

$$I(\nu, T, \beta) = \nu^{\beta} \cdot B(\nu, T), \tag{3.1}$$

with ν being the photon frequency and

$$B(\nu, T) = \frac{1}{\exp(\frac{h\nu}{k_b T}) - 1} \tag{3.2}$$

is the black body function. The best-fit parameters reported in Micelotta et al. (2009) are $T_1 = 29$ K, $T_2 = 230$ K and $\beta_1 = \beta_2 = 2$, corresponding to a cold and hot dust component, respectively. The energy densities for both components are $\rho_1 = 12.7\,\mathrm{eV\,cm}^{-3}$ and $\rho_2 = 5.7\,\mathrm{eV\,cm}^{-3}$ from which the coefficients C_1 and C_2 can be derived. Note that in case of scenario 2, N 157B is potentially inside the intensely emitting LH 99 region. The derived energy densities are therefore up-scaled by a factor of 1.5, as it is expected for an object close to edge of a homogeneously emitting sphere (Atoyan & Aharonian 1996). For illustration, the energy spectra of the described radiation fields are shown in Fig. 3.2.

3.2. Modelling

After assembling the required MWL data and having derived the radiation fields, the present electron spectrum along with the magnetic field inside N 157B can be inferred for the two scenarios. Since the available MWL data are rather sparse, the modelling is restricted to small energy range in which the electron spectrum is assumed to follow a simple power law (Eq. 2.13). To explain the considered data, the smallest possible energy range is between $E_{\min} = 2$ TeV and $E_{\max} = 200$ TeV. A higher $E_{\min}$ would not allow for properly reproducing the photon emission at around 1 TeV. At the same time, a lower $E_{\max}$ would result in a
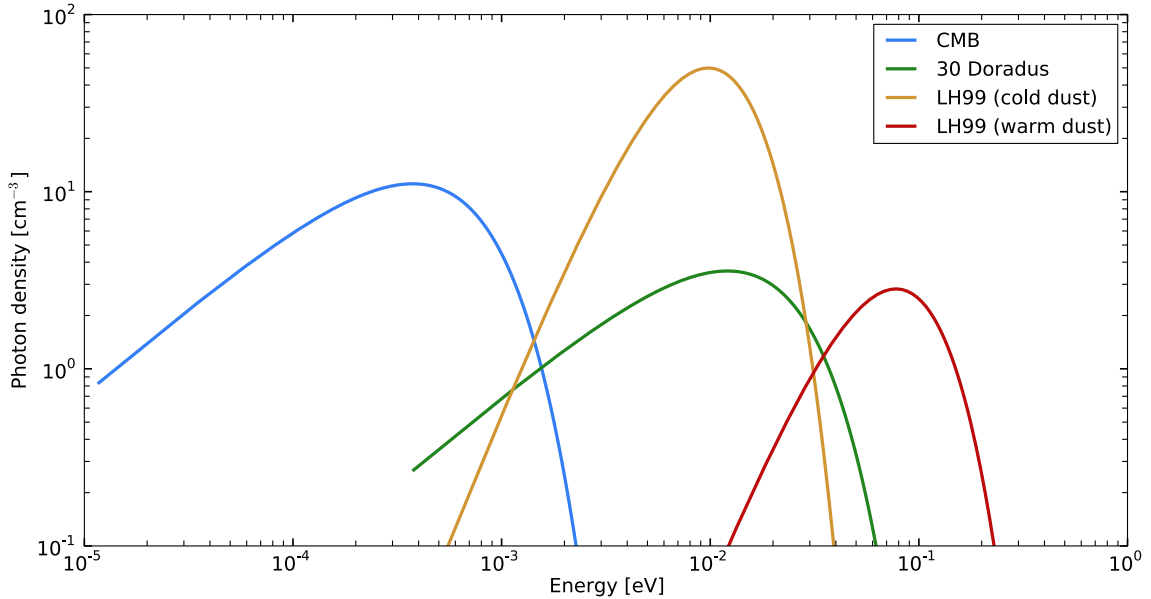
Figure 3.2.: Assumed radiation fields for N 157B. The blue line, depicting the CMB, is assumed for both scenarios. While the other shown radiation fields are exclusively used for scenario 2 (see text).

spectral mismatch with the X-ray data. To optimise the model parameters, a χ^2 fit is applied, using the MINUIT minimisation package (James & Roos 1975). Note that since errors on the measured X-ray flux are not provided in Chen et al. (2006), an artificial uncertainty of 10% is added to that value, which is realistic for a source with comparable flux. This uncertainty was further chosen such that the X-ray and VHE γ-ray data have a comparable weight in the χ^2 optimisation. The fitted parameters of the two scenarios are summarised in Table 3.1.

Table 3.1.: Modeling results of N 157B and the Crab Nebula

	Scenario 1	Scenario 2	Crab Nebula
Energy in electrons [10^{47} erg]	722.1	6.0	1.6
Spectral index	3.9	3.5	3.23
B-field [μG]	8.0	45.8	124

Notes. Parameters from the Crab Nebula are taken from Meyer et al. (2010, "constant B-field model for the pulsar wind"). The particle energy content of the Crab Nebula is determined by an energy weighted integral over the function provided in this reference. The integration range is the same as used for N 157B ($2-200$ TeV). Note that the spectral index of the Crab Nebula of 3.23 is only valid up to 150 TeV. Above this break energy, the authors found a value 3.76 to better match the data.

Statistical errors on the bets-fit parameters are in the order of 5%, which is negligible compared to the uncertainties introduced by the assumption on the radiation fields described above. For comparison, the same specific properties of the Crab Nebula, which where derived by Meyer et al. (2010) in an analogous approach, are also listed in Table 3.1. The energy content in electrons for the Crab Nebula is adapted for the considered energy range
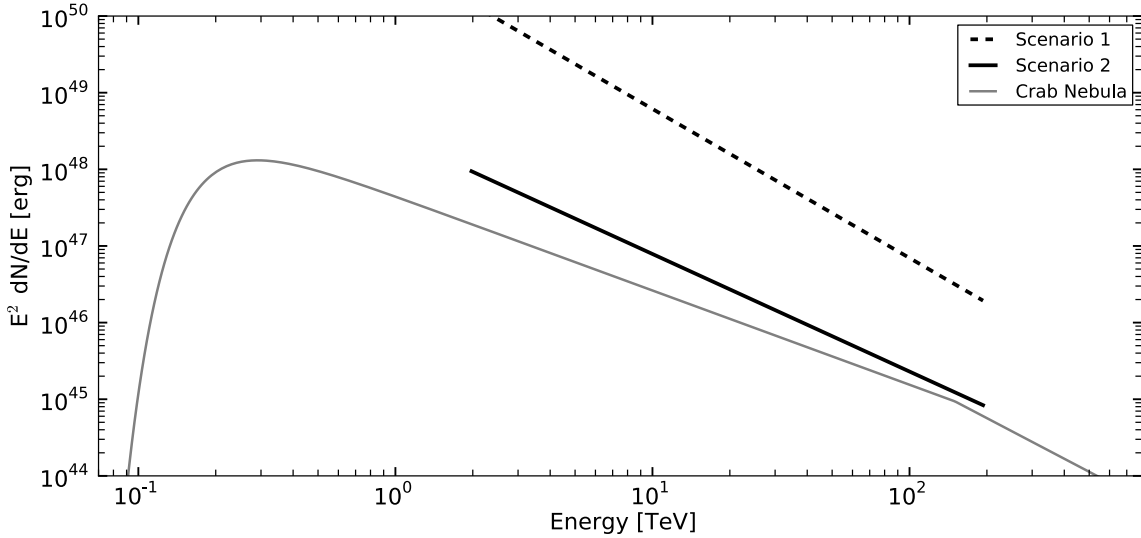
Figure 3.3.: Spectral energy distribution of the electrons for the different scenarios within N 157B (this work) and the Crab Nebula (Meyer et al. 2010).

of $2 - 200$ TeV. Despite the intense radiation fields in case of scenario 2, the energy content in electrons between $2 - 200$ TeV is higher for N 157B than in the Crab Nebula. Enlarging the considered energy range to e.g. $0.5 - 200$ TeV further increases this difference. This can be ascribed to the larger spectral index of N 157B which forms a slightly steeper spectrum than the Crab Nebula. Since the considered energy range is subject to efficient synchrotron cooling, the spectrum is much steeper than the commonly assumed injection spectra with indices between $2.0 - 2.5$ (see Sect. 2.2.1). Visualising the spectral differences, the derived energy spectra of electrons are illustrated in Fig. 3.3.

Regarding the magnetic fields inside the nebulae, the "twins" differ quite substantially. This statement is underlined by the fact that the field strength derived for the second scenario of N 157B represents an upper limit on its value. This is due to the assumption of intense radiation fields which results in a high IC luminosity. The parameter fit therefore requires less energy stored in particles to match the VHE γ-ray data. The lower energy content in relativistic electrons, in turn, implies a higher magnetic field required to match the X-ray data. Along with the X-ray and VHE γ-ray data, the modelled SEDs of N 157B are shown in Fig. 3.4. To have a better comparison, the data from the Crab Nebula are scaled to the distance of N 157B and overlayed in this Figure. The intrinsic differences between the "twins" are nicely illustrated: while the Crab Nebula has a much brighter synchrotron component, N 157B exceeds the intrinsic IC luminosity of the Crab Nebula by roughly one order of magnitude. Comparing the derived energy contents and magnetic fields of N 157B to the Crab Nebula allows to draw the following conclusion: as listed in Table 3.1, N 157B has more energy stored in particles than the Crab Nebula, even in the more conservative scenario 2. The Crab Nebula, however, stands out by its intense magnetic field which causes the strong synchrotron emission. In the subsequent Section, further implications of these derived results are discussed.
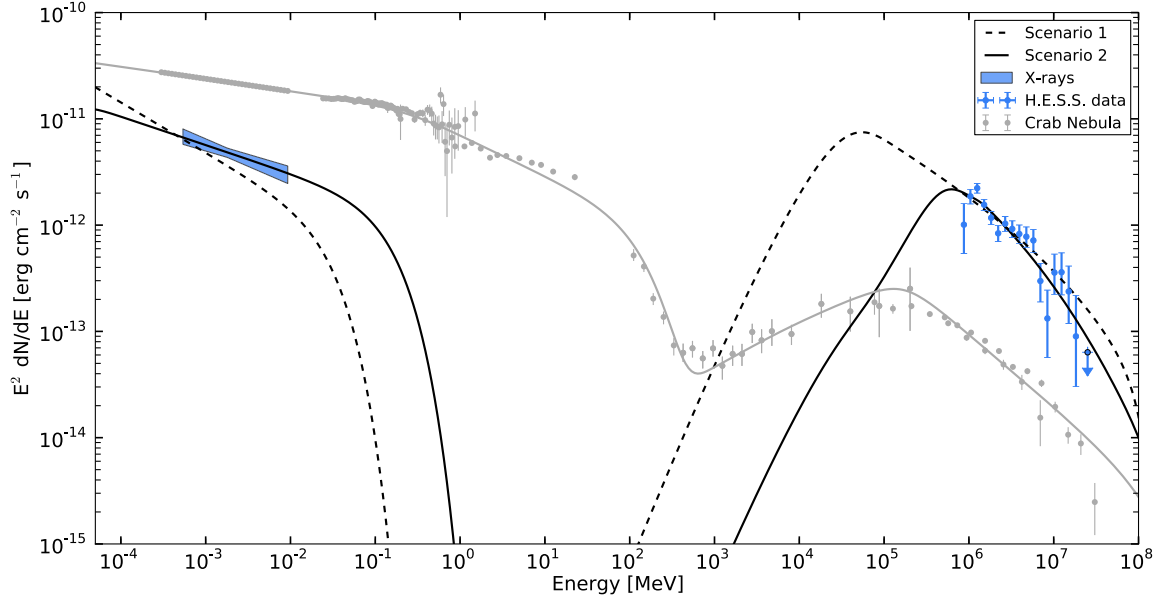
Figure 3.4.: SED of N 157B. Black lines denote models for the two different scenarios described in the text. The data to which the model parameters were adjusted to are depicted in blue. For comparison to the Crab Nebula (grey), the model from Meyer et al. (2010) is recalculated. The numbers of the Crab Nebula are scaled to the N 157B distance to allow for a better comparison.

3.3. Discussion

In the following, the derived parameters are linked to the respective pulsar To discuss implications on the acceleration efficiencies of the Crab pulsar and PSR J0537−6910. Based on the modelling of scenario 2, an upper limit on the magnetic field within N 157B of $B_N = 45\,\mu$G is derived. The energy content of the electrons of $W_N = 6 \cdot 10^{47}$ erg is a lower limit since less dense radiation fields would require an even higher energy content. In the considered energy range of $2 - 200\,$TeV, this fitted value is nevertheless more than a factor of three higher than that of the Crab Nebula. Due to the derived magnetic fields, the energetic electrons which produce the measured radiation are subject to efficient synchrotron cooling. In general, the cooling time of an electron with kinetic energy E moving through a magnetic field B can be approximated as

$$t_{\rm cool} \approx \frac{3 \cdot 10^5\,{\rm yr}}{\left(B/5\,\mu{\rm G}\right)^2 \cdot \left(E/1\,{\rm TeV}\right)^2}. \tag{3.3}$$

In case the cooling time scale is small compared to the timely change of the spin-down luminosity of a pulsar, the energy content in the most energetic electrons W can be simplified to

$$W = \eta \int_{T-t_{\rm cool}}^{T} \dot{E}(t){\rm d}t \tag{3.4}$$

$$\approx \eta \dot{E} t_{\rm cool}, \tag{3.5}$$

with η being the conversion efficiency from spin-down luminosity to energetic electrons. Accordingly, the unknown true age T can be eliminated. Applying Eq. 3.3 to the low energy end of the considered electron spectrum in N 157B leads to a mean life time for a 2 TeV electron of $t_{\mathrm{cool,N}} \approx 920\,\mathrm{yr}$. Since the current estimated braking index of $n \approx 7$ (Marshall et al. 2004) implies a presently rather slow change in the spin-down luminosity with time (Eq. 2.8), Eq. 3.5 is assumed to be a reasonable approximation in this case. For the Crab Nebula an electron with 2 TeV cools in $t_{\mathrm{cool,C}} = 120\,\mathrm{yr}$. Since the Crab pulsar has been monitored for almost 50 yr and no major changes regarding its energy output were reported up to now, Eq. 3.5 is also assumed to be valid here. The energy contents of N 157B, W_{N}, and the Crab Nebula ,W_{C}, can therefore provide an approximate measure of the ratio of particle acceleration efficiency $\eta_{\mathrm{N}}/\eta_{\mathrm{C}}$. Forming the ratio of the energy contents gives

$$\frac{W_{\mathrm{C}}}{W_{\mathrm{N}}} = \frac{\eta_{\mathrm{C}} \cdot \dot{E}_{\mathrm{C}} \cdot t_{\mathrm{cool,C}}}{\eta_{\mathrm{N}} \cdot \dot{E}_{\mathrm{N}} \cdot t_{\mathrm{cool,N}}}. \tag{3.6}$$

Since $t_{\mathrm{cool,N}} \propto B_{\mathrm{N}}^{-2}$ and $t_{\mathrm{cool,C}} \propto B_{\mathrm{C}}^{-2}$ (see Eq. 3.3) the ratio of energy contents can be written as

$$\frac{W_{\mathrm{C}}}{W_{\mathrm{N}}} = \frac{\eta_{\mathrm{C}} \cdot \dot{E}_{\mathrm{C}}}{\eta_{\mathrm{N}} \cdot \dot{E}_{\mathrm{N}}} \cdot \left(\frac{B_{\mathrm{N}}}{B_{\mathrm{C}}} \right)^2. \tag{3.7}$$

Accordingly the ratio of acceleration efficiencies can be derived by the following equation:

$$\frac{\eta_{\mathrm{N}}}{\eta_{\mathrm{C}}} = \frac{\dot{E}_{\mathrm{C}} \cdot W_{\mathrm{N}}}{\dot{E}_{\mathrm{N}} \cdot W_{\mathrm{C}}} \cdot \left(\frac{B_{\mathrm{N}}}{B_{\mathrm{C}}} \right)^2, \tag{3.8}$$

with $\dot{E}_{\mathrm{C}} = 4.6 \cdot 10^{38}\,\mathrm{erg\,s^{-1}}$ and $\dot{E}_{\mathrm{N}} = 4.9 \cdot 10^{38}\,\mathrm{erg\,s^{-1}}$. Taking into account the modelled energy contents and magnetic fields of Table 3.1, Eq. 3.8 implies $\eta_{\mathrm{N}}/\eta_{\mathrm{C}} = 0.46$ for scenario 2 and $\eta_{\mathrm{N}}/\eta_{\mathrm{C}} = 1.7$ in case of scenario 1. These values represent a lower and upper limit, respectively. Accordingly, at least during last few hundred years, the Crab pulsar and its energetic twin PSR J0537-6910 seem to accelerate energetic electrons with efficiencies of similar magnitude.

3.4. Conclusion

Using the latest H. E. S. S. data, it is possible to compare specific properties of the Crab Nebula to its energetic counterpart in the LMC. Based on the modelling of N 157B some basic but interesting conclusions can be drawn. In case of scenario 2, an upper limit on the magnetic field within N 157B of $45\,\mu\mathrm{G}$ and a minimal energy stored in relativistic electrons of $6 \cdot 10^{47}\,\mathrm{erg}$ between $2 - 200\,\mathrm{TeV}$ is derived. Comparing these findings to the Crab Nebula implies that these nebulae can be considered non-identical twins. Since the age of N 157B can not be determined unambiguously, conclusions related to the possible age difference between both PWNe should be taken with care. Accordingly, the following conclusions are based on the stationary modelling. Although in terms of spin-down luminosity both pulsars are quite similar, their nebulae exhibit large differences. While the pulsar wind of N 157B seems to be particle dominated, the Crab Nebula is much more magnetised causing strong synchrotron emission which in turn reduces the number of very energetic electrons. This could be explained by the diverse environments in which these nebulae evolve. While the Crab Nebula expands into a rather quiet environment at the outer region of our Galaxy, N 157B is probably

located in an intensely radiative region within the LMC. These different settings may affect the evolution and non-thermal appearance of these two objects. The modelling of N 157B therefore indicates that the distinct environments of the Crab Nebula and N 157B may play an important role regarding the present ratio between magnetic and kinetic particle energy inside these nebulae.

Another explanatory approach for different magnetisations of pulsar winds is given in Komissarov (2013). The author argues that the inclination angle of the magnetic dipole with respect to the pulsar rotational axis influences the wind magnetisation. Large inclination angles could support particle-dominated nebulae, while smaller angles would lead to more magnetic energy injected into the pulsar wind.

4. The Crab Nebula and Its γ-ray Flares

This Chapter deals with an impressive peculiarity of the Crab Nebula. It is the only known PWN whose synchrotron component extends to the HE γ-ray regime (Nolan et al. 1993; van der Meulen et al. 1998; Abdo et al. 2010a). This observational fact is thought to be most certainly linked to the powerful energetics of the Crab pulsar and the very strong magnetic field inside the nebula (see, e.g., Meyer et al. 2010).

Most surprisingly, the synchrotron component was found to be variable over time at HE γ rays. Tavani et al. (2011) and Abdo et al. (2011) reported on enhanced γ-ray fluxes from the direction of the Crab pulsar and Nebula system (hereafter referred to as Crab), lasting a few days. These flares were detected by the space-born instruments *Fermi*-LAT and *AGILE* in February 2009 and September 2010. Subsequent pulse-phase resolved analyses could rule out the energetic pulsar as possible origin of the flares. Due to the observed variability time scale of less than 4 days, causalities implies that a small region inside the Crab Nebula is responsible for the flux eruptions. A dense MWL campaign was therefore initiated in order to spot the origin of these enigmatic flares with the best angular resolutions. The Crab Nebula, however, kept its mystery alive by not revealing any variability at other wavelengths. In April 2011, the next HE γ-ray flare was detected by *Fermi*-LAT (Buehler et al. 2012) and *AGILE* (Striani et al. 2011). That time, the synchrotron component exceeded its average luminosity up to a factor of 30, which depicts the highest flux enhancement up to date. In addition, Buehler et al. (2012) determined the flux doubling time scale to $\sim 8\,\mathrm{h}$. Besides regular monitoring of the Crab, the instruments *Chandra* (X-rays), Keck (near infrared) and VLA (radio) paid special attention during the flaring period. Again, the flare origin could not be pinned down unambiguously (Weisskopf et al. 2013). Nevertheless, the authors reported on contemporaneous infrared activity of the so-called "inner knot", a bright structure located $0\overset{''}{.}65$ South-East of the pulsar (Hester et al. 1995). However, the luminosity of this knot is known to regularly vary by a factor of two (Sandberg & Sollerman 2009). A significant correlation could therefore not be established. Again, in July 2012, the flux increased significantly (Ojha et al. 2012) although only for a short time. In March 2013, the Crab provided yet another opportunity to expose the origin of the flares. For a two week period, the γ-ray flux increased significantly, unveiling the rapid variability of the synchrotron component. In the scope of this thesis, the flux variability time scale was determined to less than 6 h. In addition, a 20 fold flux increase of the synchrotron component was measured during the flare maximum (Mayer et al. 2013).

To study the flares and the long-term variability of the synchrotron component in a homogeneous way, a uniform analysis of *Fermi*-LAT data of the Crab Nebula is conducted and presented in this Chapter. The first Section describes the *Fermi*-LAT instrument and the applied analysis methods. Subsequently, the spectral composition of the Crab is analysed, disentangling the pulsar and nebula spectrum. Investigating the variability of the synchrotron component of the Crab, a long-term light curve is calculated. This light curve is generated with the most sensitive analysis method using a low energy threshold of 50 MeV. The light curve is studied to characterise the flares and search for periodicity and long-term variability time scales. To investigate the short but intense flux peaks, spectra are obtained for each

Figure 4.1.: *Left*: Artist impression of the Fermi Satellite. *Right*: A sketch of a vertical profile through the LAT, highlighting the most important subsystems. Further illustrated is the path of an incident HE γ-ray.

detected flare. These spectra are compared to each other in order to find commonalities and differences. Studying the short-term variabilities during the flare, the light curve of the March 2013 flare is re-analysed to quantify the rapid spectral change during the flaring periods. The final Section of this Chapter summarises the presented findings and discusses implications in the context of current theoretical models.

4.1. The Fermi Large Area Telescope

The *Fermi* Large Area Telescope (*Fermi*-LAT) on-board the *Fermi* Satellite was launched in June 2008. After some weeks of commissioning, routine science operation was initiated in the beginning of August 2008. The LAT is designed to measure astrophysical γ rays between 20 MeV and roughly 300 GeV. Photons enter the LAT through the so-called tracker which consists of silicon strips and tungsten foils. This environment triggers the creation of e^+e^- pairs from the incident photon:

$$\gamma \longrightarrow e^+ + e^-. \tag{4.1}$$

The recorded tracks of the e^+e^- pairs are used to determine the direction of the incoming photon, resulting in a point-spread function (PSF, 68% containment radius) of roughly $3°\!\!.3$ at around 100 MeV, improving to about $0°\!\!.2$ at 10 GeV (Atwood et al. 2007, 2009; Ackermann et al. 2012a). The charged electrons and positrons further interact in the calorimeter, which consists of scintillation crystals. In this part of the LAT, the γ-ray energy is determined with an accuracy of 15% at low energies shrinking to approximately 8% at 10 GeV (Ackermann et al. 2012a). An artistic image of the Fermi Satellite along with a profile of the LAT is depicted in Fig. 4.1. The collecting area of the LAT is $\approx 1\,\mathrm{m}^2$. Since γ-ray sources usually have steep energy spectra, the photon statistics, especially at high energies, is a limiting factor of *Fermi*-LAT analyses. The Fermi Satellite is orbiting the Earth at an altitude of 525 km above sea level and an inclination angle of 25° with respect to the equator. Furthermore, the instrument is rocking alternately North and South with a usual rocking range of $\pm 52°$. With this observing strategy, called *survey* mode, along with the large field of view (FoV) of 2.4 sr, the full sky can be imaged roughly every three hours. Most of the time, *Fermi*-LAT operates in survey mode. Interesting astrophysical events, such as bright flares from the Crab Nebula, can trigger a target of opportunity (ToO) observation, where the LAT switches to pointed observations in order to maximise the exposure on the sky region of interest. In the

following, the *Fermi*-LAT analysis procedure, which is used for the analyses of the Crab, is described in detail.

4.1.1. Data Analysis Procedure

The analysis of *Fermi*-LAT data is conducted via a likelihood framework. The emission inside the region of interest (hereafter RoI) is fully parametrised by the superposition of models describing the different sources of γ-ray emission. In this approach, each γ-ray source in the RoI is modelled by a spatial and spectral component. The best-fitting model parameters, e.g. the normalisation and spectral index of a power law function are obtained using a maximum likelihood optimisation. The likelihood method is described in Cash (1979), while its application to γ-ray data from *EGRET* was presented in Mattox et al. (1996). Calculating the likelihood $\mathcal{L}$ for a set of models describing the given data requires the product of the likelihoods $\mathcal{L}_i$ for all n individual events

$$\mathcal{L} = \prod_{i=0}^{n} \mathcal{L}_i. \tag{4.2}$$

For computational reasons, it is common to rephrase Eq. 4.2 into the sum of the natural logarithms, implying to calculate the log-likelihood

$$\log \mathcal{L} = \sum_{i=0}^{n} \log \mathcal{L}_i. \tag{4.3}$$

Maximising this log-likelihood gives the most probable realisation of the model parameters for the given data set. Since the given models $\mathcal{M}$ are intended to reflect the true energy spectra and positions, the instrument response functions (IRFs), which describe the probability to reconstruct an event p_i' from a certain incoming photon p_i, have to be taken into account. The main attributes of an event p_i' are the measured energy E_i', and reconstructed direction (x_i', y_i'). Note that the IRFs are mainly dependent on the detector coordinates, while the models are represented in sky coordinates. Taking into account the LAT pointing direction, these values can easily be converted from one system to the other. For the sake of simplicity, the coordinates (x, y) represent both systems in the following. In addition, only the most important dependencies are depicted in the following.

Since there is no calibration source with perfectly known attributes in the sky, the IRFs are usually derived from Monte Carlo simulations and consist of three components:

- the PSF, describing the probability to reconstruct a photon from the true direction (x_i, y_i) at the position (x_i', y_i').

- the energy resolution (ER), which gives the probability to reconstruct an event energy E_i' of a photon with true energy E.

- the effective area (A_{eff}), giving the detection probability for a certain photon p_i, in units of physical collection area (e.g. [cm^2] for *Fermi*-LAT).

All of the described IRFs further depend on observational attributes and properties of the measured event, e.g. its offset angle from the LAT pointing direction. To calculate the likelihood for a single event, all its properties are taken into account and reflected in p_i'. The

log-likelihood $\log \mathcal{L}_i$ can thus be computed by the sum over the set of models $\mathcal{M}$, evaluated for p_i:

$$\log \mathcal{L}_i = \sum_{j=0}^{m} \log \mathcal{M}_j(p_i'). \tag{4.4}$$

The probability to detect the event p_i' originating from a source which is parametrised by $\mathcal{M}_j$ is defined by convolving the model components with the IRFs. Accordingly, integrals over the true photon attributes have to be solved

$$\mathcal{M}_j(p_i') = \int \mathrm{d}x \int \mathrm{d}y \int \mathrm{d}E \; \mathcal{S}(E, x, y) \times \mathrm{IRF}(p, p_i'), \tag{4.5}$$

where $\mathcal{S}(E, x, y)$ represents the source model, which is usually decomposed into a spatial and spectral part. To compare the number of predicted events, N_{pred}, to the absolute number of measured events N_{obs}, $\mathcal{M}_j$ needs to be multiplied by the dead-time-corrected observation time. The mean dead time of the LAT is roughly $100\,\mu\mathrm{s}$ after each detected event, corresponding to roughly 8% of the observation time. While maximising the likelihood to find the best-fitting parameters, the condition $N_{\mathrm{pred}} = N_{\mathrm{obs}}$ is required to match at the same time.

The described likelihood framework takes into account single photon events, implying expensive computations in case of a large dataset. Therefore, the framework is flexible to evaluate the likelihood for binned events, too. In this case, an event p_i' can be replaced by an event bin b_i' containing a certain number of events. Such a bin typically consists of three dimensions, namely the energy and the sky coordinates. Accordingly, the IRFs for the binned analysis are averaged and precomputed for each bin.

Fermi-LAT analyses, conducted in the described likelihood frameworks, can make use of several optimisation methods. The *Fermi*-LAT analyses in this Section make use of the MINUIT optimisation package, which was also used for the modelling of N 157B (Sect. 3.2). Defining the input for the likelihood analysis, the data selection and considered RoI models are described in the following.

4.1.2. Data Selection

Since the launch of *Fermi*-LAT, the understanding of the instrument and the data calibration has steadily improved. The *Fermi*-LAT Collaboration hence regularly updates the public data using more and more sophisticated reconstruction techniques. The IRFs are renewed accordingly. The most recent set of data and IRFs available from the Fermi data server[1] is called Pass 7 reprocessed (P7Rep). Details on this type of reconstruction are given in Ackermann et al. (2012a). Currently the *Fermi*-LAT Collaboration is working on a major revision of the reconstruction and the corresponding IRFs, called Pass 8 (P8, Atwood et al. 2013). The newly introduced reconstruction scheme leads to a substantial increase of γ-ray acceptance, i.e. the photon detection probability. Fig. 4.2 illustrates the strong improvement in effective area of P8 compared to P7Rep. P8 is currently in preparation to be released to the public. To be most sensitive in the analyses, this work makes already use of P8. In the following, the applied event selection criteria are described.

In contrast to the usually applied energy threshold of $100\,\mathrm{MeV}$ in P7Rep, P8 provides the possibility to reduce this threshold to roughly $50\,\mathrm{MeV}$. Therefore events are selected, which were reconstructed between $50\,\mathrm{MeV}$ and $300\,\mathrm{GeV}$. Since the PSF of *Fermi*-LAT at low energies is rather poor, a large RoI around the Crab position is defined. To account for the tails of

---

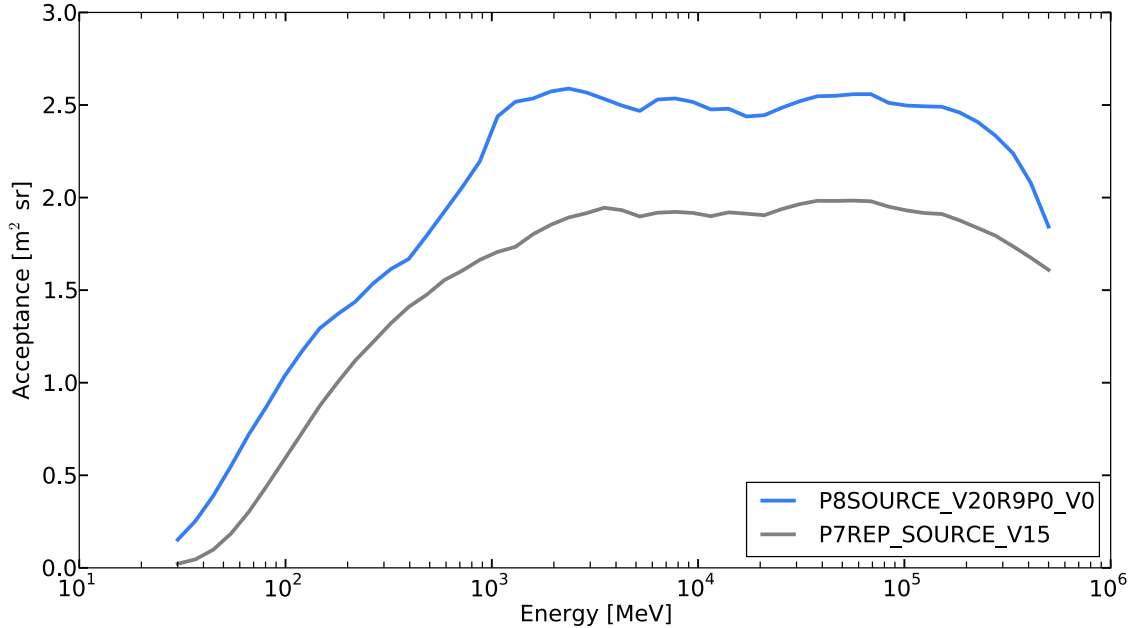[1]`http://fermi.gsfc.nasa.gov/ssc/data/access/lat/`

Figure 4.2.: Comparison of the γ-ray acceptance from P8 (blue) against P7REP (grey). The full names of the used reconstruction versions are indicated in the legend on the lower right.

the PSF and further ensure enough photon statistics to determine the background level, the chosen RoI radius is 15° from where photons are selected for the analysis. The used dataset comprises events arriving between MJD 54682.7 and 56456.8 which corresponds to almost 5 yr of observations. The analysis is conducted in the equatorial system where astrophysical objects are stationary in the sky. Due to interactions of cosmic-rays in the atmosphere, the brightest source of HE γ rays is however the Earth itself (Abdo et al. 2009). This γ-ray emission creates a complex pattern in the sky coordinate system according to the orbital movement and observing strategy of the LAT. Accordingly, the dataset is further reduced by requiring γ rays to arrive within 95° of zenith, i.e. 18° away from the nominal Earth limb at 113° zenith. In addition, events passing the LAT reconstruction chain are flagged with a quality factor. This analyses uses *SOURCE* events, which is the standard criterion for the analysis of Galactic sources[2]. The described selections reduce the dataset to around $4.6 \cdot 10^6$ events. The following Section describes the set of models, used to parametrise this dataset.

4.1.3. Model Generation

Generating an appropriate source model describing the RoI is essential for the analysis of *Fermi*-LAT data in the likelihood framework. In case of the presented data selection, all known sources which are closer than 20° to the Crab are included in the RoI model. This region is larger than the chosen RoI to account for spill-over events, caused by PSF tails from sources close to the edge of the RoI. The second catalogue of *Fermi*-LAT sources (2FGL, Nolan et al. 2012) generated after two years of observations is usually used to compile known

---

[2]http://fermi.gsfc.nasa.gov/ssc/data/analysis/documentation/Cicerone/Cicerone_Data_
Exploration/Data_preparation.html

sources inside the RoI. After currently 5 years of observation, however, the 2FGL might be outdated due to more data and the higher sensitivity which comes along with P7Rep or P8 data. This work therefore makes use of a preliminary list of sources compiled by the *Fermi*-LAT catalogue team using 4 years of observations[3]. The source model for the RoI created from this list consists of 68 point sources and two extended sources, namely the SNRs IC 443 and S 147. The spatial components of these extended sources are modelled by map templates parametrising the complex intrinsic morphologies. These templates are also provided in the 4 yr cataloque. Apart from HE γ-ray sources, *Fermi*-LAT measures astrophysical background photons. As already shown in Fig. 1.1, the Galactic plane in this energy range is dominated by diffuse emission with complex structures (see also Ackermann et al. 2012b). Further away from the plane, the background is dominated by an isotropic emission which can be well-described by a spatially constant function (Abdo et al. 2010c; Bechtol et al. 2014). These two diffuse components are also included in the RoI model. The Galactic diffuse model is represented via a three-dimensional template, i.e. a set of energy dependent sky maps, which are already scaled to the expected intensity. The spectrum of the isotropic diffuse model is likewise described by a template without spatial information making it a function dependent on energy only. In general, the latest diffuse models can be retrieved from the *Fermi* Science Support Center[4]. For the analysis with increased sensitivity and an extended energy range, the most recent diffuse models are used, which are created with 4 yr of data[5].

The analysis of the Crab in the HE γ-ray regime conducted by Abdo et al. (2010a) and Buehler et al. (2012) revealed that the spectrum consists of three physically independent components: the pulsed emission from the Crab pulsar as well as the synchrotron and IC component of the Crab Nebula. Since the Crab is a rather compact object with an apparent size in γ rays of $< 0°03$ on the sky (Aharonian et al. 2000), these components cannot be spatially resolved by *Fermi*-LAT due to the PSF of ideally $0°1$. Accordingly, the spatial parts of the Crab components are modelled point sources.

4.2. Time-Averaged Spectra of the Crab

The time-averaged spectra of the Crab pulsar and IC nebula are re-analysed with P8. These components, assumed to be temporally constant, are subsequently needed for the variability studies of the synchrotron component. Fig. 4.3 gives an overview of the current MWL spectrum of the Crab. The nebula and pulsar are visualised separately. The red box shows the energy range which is used for subsequent analyses.

To analyse the time-averaged IC and synchrotron component, the Crab Nebula emission has to be separated from the pulsar emission. In contrast to the nebula emission, the pulsar periodically emits pulsed radiation, similar to a lighthouse (see Sect. 2.2.1). The time distance between the main pulses reflects the spin period, which is 33 ms (Cocke et al. 1969). By means of the exact photon arrival times, the precise pulse phase can be assigned to each individual event. The pulse phase ϕ is defined as the fractional time within one pulsar period, i.e. every γ-ray is tagged with a value $0 < \phi < 1$. The calculation of pulse phases over a longer time span requires detailed knowledge of the rotation frequency of the pulsar as well as frequency

---

[3]Internal docoumentation: `gll_psc4year_v12.xml`
[4]`http://fermi.gsfc.nasa.gov/ssc/data/access/lat/BackgroundModels.html`
[5]Internal documentation:
  Isotropic: `p8_p300x_isotropic_source_p8v1_zmax100_4years`
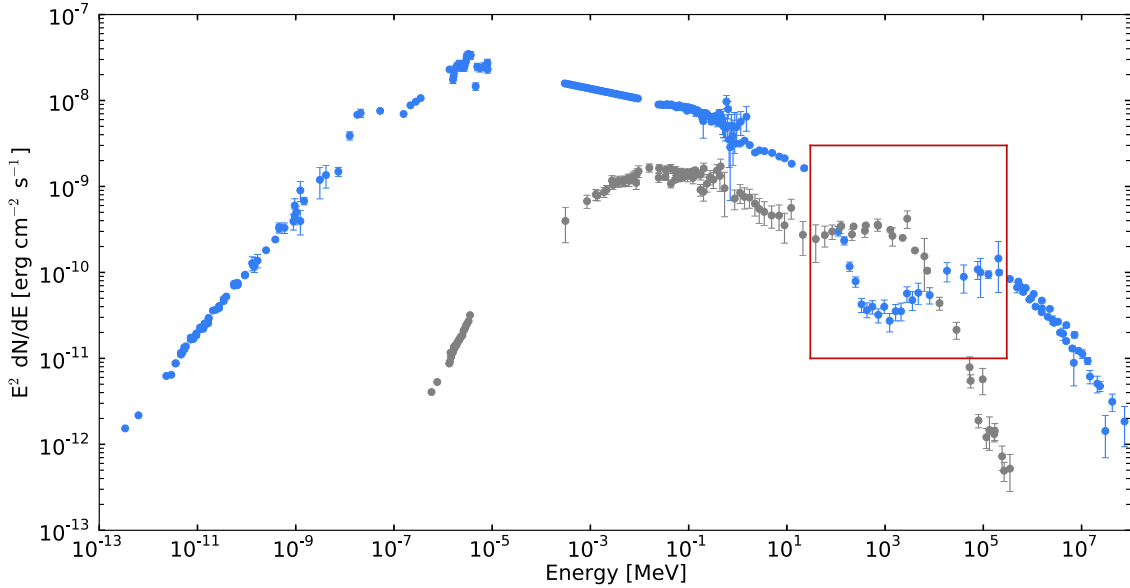 Galactic: `template_4years_P7_v15_repro_v3`

Figure 4.3.: MWL SED of the Crab Nebula and pulsar. The blue data points represent the emission from radio to VHE γ rays of the Crab Nebula. The energy spectrum of pulsar is represented by grey points. The red box denotes the energy range of interest in this Section. All data points are compiled from Bühler & Blandford (2014).

derivatives of several orders. In addition to the time evolution of the spin period, several correction terms are necessary to properly describe the time-dependent rotation period with microsecond accuracy (Smith et al. 2008).

This work makes use of the timing solution for the Crab pulsar derived by Abdo et al. (2013). The corresponding parameters (ephemerides) are publicly available[6]. These ephemerides, however, are only valid for the first three years of *Fermi*-LAT observations. The analysis of the pulsar and IC nebula is therefore restricted to this time window. The pulse phases are calculated and assigned to the events using `TEMPO2` (Hobbs et al. 2006; Edwards et al. 2006) for *Fermi*-LAT data (Ray et al. 2011). The resulting pulse phase distribution is shown in Fig. 4.4. To simplify the identification of the peaks, the dataset in this Figure is restricted to a small region of 3° around the pulsar, reducing the background contamination. From this diagram, the phase range where the pulsar contribution is negligible can be determined. The chosen cut values on the pulse phase are $0.65 < \phi < 0.95$ (off-pulse), marked by vertical red lines in Fig. 4.4. Despite sacrificing statistics, this cut enables to exclusively measure the Crab Nebula spectrum independently from the pulsar. To obtain correct flux measurements, the exposure needs to be scaled according to the chosen phase cut by a factor $0.95 - 0.65 = 0.3$.

4.2.1. Crab Nebula

Following Abdo et al. (2010a) and Buehler et al. (2012), the time-averaged spectrum of synchrotron component can be parametrised as a power law which takes the integrated photon flux F_{syn} between $E_{min} = 100\,\text{MeV}$ and $E_{max} = 100\,\text{GeV}$ and the spectral index Γ as free

---

[6]`http://fermi.gsfc.nasa.gov/ssc/data/access/lat/2nd_PSR_catalog/`
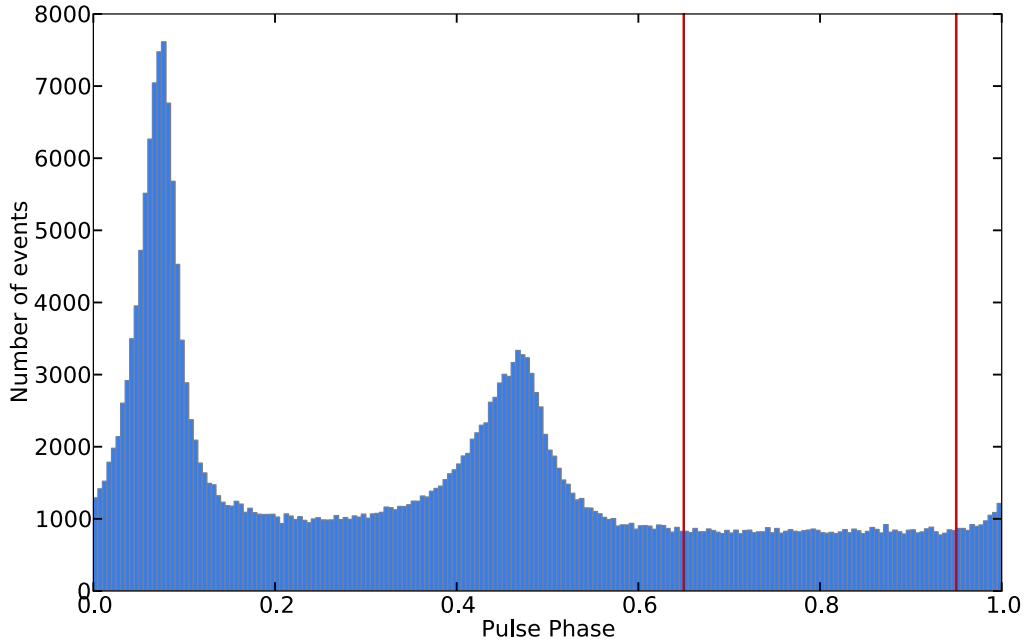
Figure 4.4.: Pulse phase distribution of events within $3°$ around the Crab. The two peaks caused by the pulsar are very pronounced. The phase cut values which are chosen to safely remove the pulsar from the dataset are marked by vertical red lines.

parameters:

$$\frac{\mathrm{d}N}{\mathrm{d}E} = F_{\mathrm{syn}} \frac{\Gamma + 1}{E_{\max}^{\Gamma+1} - E_{\min}^{\Gamma+1}} \cdot E^{\Gamma}. \tag{4.6}$$

As indicated in Buehler et al. (2012), the IC spectrum significantly deviates from a power law at higher energies. This component is therefore modelled by a log-parabola

$$\frac{\mathrm{d}N}{\mathrm{d}E} = \Phi_{\mathrm{IC}} \left(\frac{E}{E_0} \right)^{-\alpha - \beta \log(E/E_0)}, \tag{4.7}$$

allowing for a curvature in the spectrum. The reference energy E_0 is fixed to $1\,\mathrm{GeV}$ in the analysis. All other parameters from sources listed in the $4\,\mathrm{yr}$ catalogue are fixed to the provided values. The only free parameters left are the ones describing the average synchrotron emission, the IC emission as well as spectral components which scale the Galactic and isotropic diffuse models. The former is commonly scaled by a power law with the normalisation Φ_{gal} and spectral index Γ_{gal}. Since the template for the Galactic diffuse emission already contains the absolute values, $\Phi_{\mathrm{gal}} \approx 1$ and $\Gamma_{\mathrm{gal}} \approx 0$ is expected. The isotropic diffuse model, also given in absolute flux values, is adjusted by a normalisation factor N_{iso}. This value is also expected to be in the order of 1.

Having defined the spectral model for the off-pulse emission, all events after cuts (including the pulse phase cut) are binned into 40 sky maps, corresponding to equally spaced logarithmic energy bins. The maps comprise $10° \times 10°$ on the sky. Each spatial bin has a width of $0°.1$ resulting in 100×100 bins per map. In total, this choice results in $4 \cdot 10^5$ three-dimensional

bins to be use in the analysis. Using these binned events, the analysis is conducted with binned `gtlike` (*Fermi* Science Tools version 09-32-05)[7]. The best-fit values for the free parameters are listed in Table 4.1 in the "Off-pulse" section. Subsequently, a model map

Table 4.1.: Fit results of *Fermi*-LAT analyses.

Fit	Symbol	Fitted Value	Unit
Off-pulse	F_{syn}	$(7.46 \pm 0.04) \cdot 10^{-7}$	$\mathrm{cm}^{-2}\,\mathrm{s}^{-1}$
	Γ	$-(3.49 \pm 0.03)$	–
	Φ_{IC}	$(1.48 \pm 0.28) \cdot 10^{-11}$	$\mathrm{MeV}^{-1}\,\mathrm{cm}^{-2}\,\mathrm{s}^{-1}$
	α	1.21 ± 0.07	–
	β	0.11 ± 0.02	–
	Φ_{gal}	0.929 ± 0.004	–
	Γ_{gal}	9.8 ± 6.5	10^{-3}
	N_{iso}	0.95 ± 0.01	–
On-pulse	Φ_{psr}	$(2.67 \pm 0.02) \cdot 10^{-9}$	$\mathrm{MeV}^{-1}\,\mathrm{cm}^{-2}\,\mathrm{s}^{-1}$
	p_1	1.91 ± 0.02	–
	p_2	2.90 ± 0.13	–
	E_b	1.99 ± 0.37	GeV
	s	0.55 ± 0.19	–
	Φ_{gal}	0.941 ± 0.006	–
	Γ_{gal}	5.2 ± 4.4	10^{-3}
	N_{iso}	0.93 ± 0.02	–

Notes. See text for explanation of all parameters.

is computed, showing the predicted number of counts in each spatial bin according to the best-fit model and taking into account the exposure information. All events, binned in an energy-integrated count map C and the corresponding model map M are presented in Fig. 4.5. The Crab Nebula in the image center is very pronounced compared to the other components. Also visible is the close-by source 2FGL J0521.7+2113 towards East of the Crab. Since this source is listed in the 4 yr catalogue it also appears on the model map. Subtracting these maps bin by bin results in a residual map which is inspected to point out badly modelled sources. Comparing the residuals to statistical significance, each bin of the subtracted map is further divided by the square root of the bin entry of the corresponding model map. Accordingly, an entry in the bin (i, j) in the residual map X is calculated by

$$X_{ij} = \frac{C_{ij} - M_{ij}}{\sqrt{M_{ij}}}. \tag{4.8}$$

The resulting map is presented in the left panel of Fig. 4.6. To enhance the visibility of possible structures, the map is smoothed by a Gaussian with a width of $0°\!.3$. If all γ-ray emission was modelled properly, the residual significance distribution should follow a normal distribution with a mean and width of $(\mu, \sigma) = (0, 1)$. The right panel of Fig. 4.6 shows the residual significance distribution compared to the expected curve. In general, the applied

---

[7]Available from the *Fermi* Science Support Center: `http://fermi.gsfc.nasa.gov/ssc/`
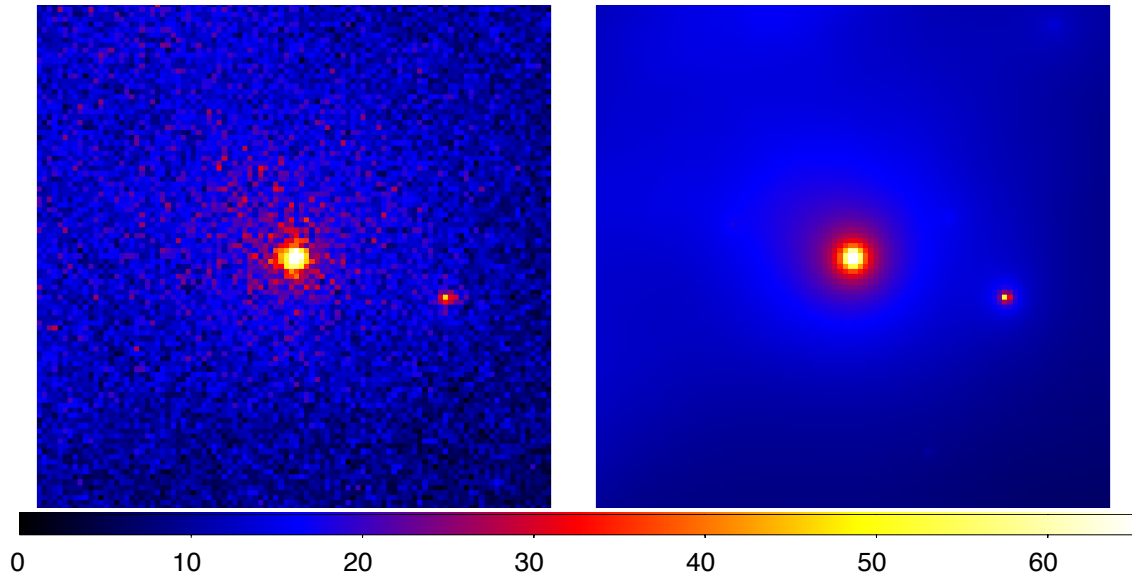
Figure 4.5.: Count map (*left*) and model map (*right*) of the RoI around the Crab. The Crab Nebula stands out in the image centre due to its brightness. Right of the Crab, the *Fermi*-LAT source 2FGL J0521.7+2113 is visible. The colour scale indicates the number of counts per bin.
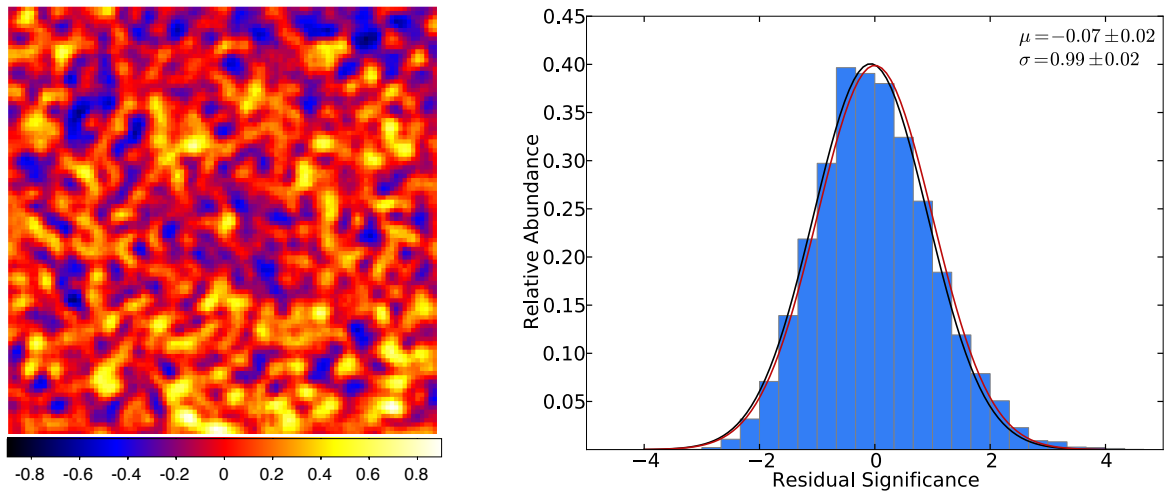

Figure 4.6.: *Left*: Residual significance map calculated from the data and best-fit model. The map is smoothed with a Gaussian to visualise possible structures. The colour scale indicates the smoothed residuals, where reddish colours stand for residuals close to zero. *Right*: Significance distribution of the unsmoothed residuals. The expected curve is a standard normal distribution as depicted by the red line. The solid black line indicates fit with a Gaussian function. The corresponding fit results are indicated top right.
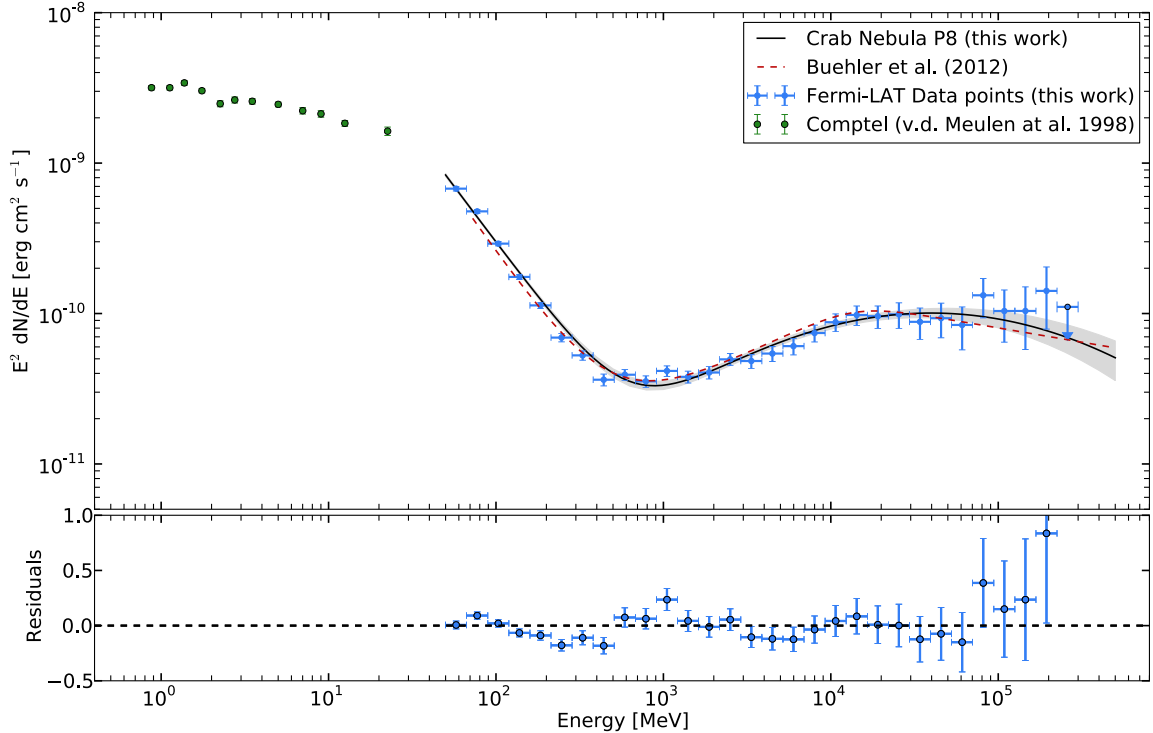
Figure 4.7.: SED of the Crab Nebula. Blue data points result from a flux measure in each energy bin (see text). The black line denotes the best-fit model in the off-pulse window, while the red-dashed line is a comparison to the best-fit model of Buehler et al. (2012). The grey band denotes the 68% confidence band of the fit. Illustrating the spectral connection to lower energies, data from *Comptel* are also shown in green (van der Meulen et al. 1998). The lower panel presents the residuals of the fitted data points to the best-fit model.

model describes the data within the RoI quite well. A Gaussian fit (black solid line) leads to a mean $\mu = -0.07 \pm 0.02$ and $\sigma = 0.99 \pm 0.01$.

As a next step, an SED of the Crab Nebula is produced to reveal possible spectral features which where not considered in the modelling. For this purpose, the dataset is subdivided into 30 bins of equal size in the logarithm of energy. The above-described analysis is repeated in each energy bin using binned `gtlike` with the addition of fixing all spectral parameters to their best-fit values, except the flux normalisation of the Crab Nebula. To account for systematic uncertainties in the diffuse models, their normalisation parameters are also left free to optimise. The fitted normalisations of the Crab Nebula in each bin are scaled by the square of the respective energy bin center resulting in the SED shown in Fig. 4.7. For a better comparison to the best-fit model, the lower panel of Fig. 4.7 presents fit residuals, which depict the relative deviation of each data point from the fitted model. The test statistics (TS, Mattox et al. 1996), which is a measure for the statistical significance of the detection, is computed in each bin. If the Crab Nebula cannot be detected with TS > 4 within one energy bin, an upper limit is drawn instead of the data point. The upper limits, corresponding to 95% confidence, are computed via a standard Bayesian approach (Helene 1983). The limit is derived by integrating the likelihood function along the normalisation parameter up to a

point which contains 95% of the total probability. Such a limit, represented by a downwards arrow in the SED, is drawn for the highest energy data point of the Crab Nebula for which the TS value is close to zero. The presented data points and upper limit are in good agreement with the best-fit model.

4.2.2. Crab Pulsar

The spectral components of the Crab Nebula, determined in the previous Section, are a constant background for the pulsar analysis. Although the synchrotron component is known to vary, its time-averaged spectrum can be used to calculate the timely constant pulsar emission. For the purpose of computing a long-term light curve, the HE γ-ray spectrum of the pulsar is determined as a steady component. Therefore, events which are considered "on-pulse" ($0 < \phi < 0.65$ or $0.95 < \phi < 1.0$) are select events for the analysis. Accordingly, the model describing the RoI has to be adjusted. As shown in Abdo et al. (2013) and Buehler et al. (2012), the pulsar spectrum can be parametrised by a power law which cuts off exponentially. The recent detection of VHE γ-ray emission from the Crab pulsar (VERITAS Collaboration et al. 2011; Aleksić et al. 2012) indicates a spectral break rather than a cut-off. Accordingly, the pulsar emission is modelled by a smoothly broken power law

$$\frac{\mathrm{d}N}{\mathrm{d}E} = \Phi_{\mathrm{psr}} \left(\frac{E}{100\,\mathrm{MeV}} \right)^{-p_1} \left(1 + \left(\frac{E}{E_b} \right)^{\frac{p2-p1}{s}} \right)^{-s} , \tag{4.9}$$

where $p_{1,2}$ denote the spectral index before and after the break energy E_b, respectively. The parameter s represents the sharpness of the transition between the two slopes. The pulsar is added to the RoI model leaving the parameters Φ_{psr}, p_1, p_2, E_b and s free. The IC nebula and synchrotron component are fixed to the previously derived values. The RoI
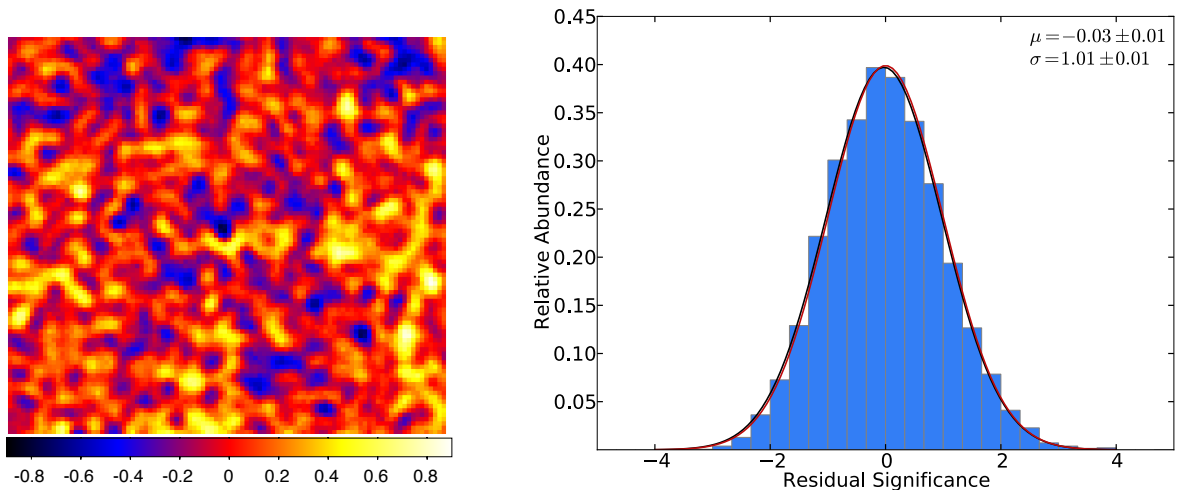
Figure 4.8.: *Left*: Smoothed residual significance map, analogous to Fig. 4.7. *Right*: Distribution of the unsmoothed residual significances are shown in blue. The expected curve from a normal distribution is depicted by the red line. A Gaussian fit is indicated by the black line, while the resulting parameters are presented in the top right.
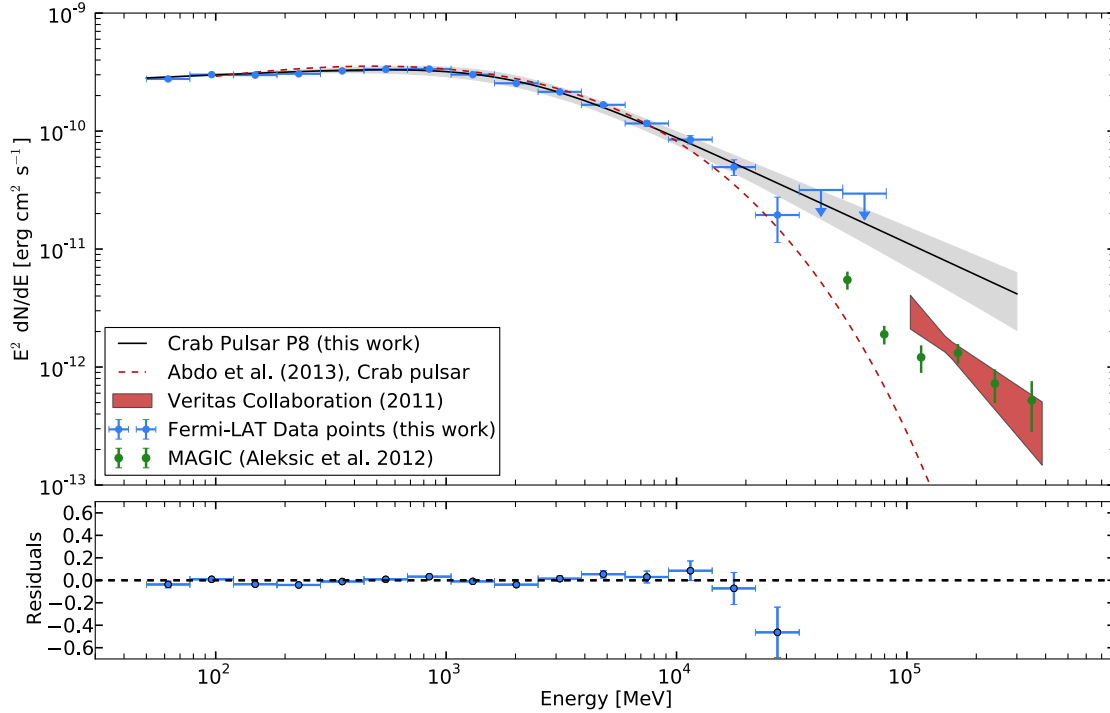
Figure 4.9.: SED of the Crab Pulsar. The colour scheme is the same as in Fig. 4.7. The red-dashed line is a comparison to the best-fit model of Abdo et al. (2013). Illustrating the spectral connection to higher energies, data from MAGIC and VERITAS are shown as green points and red confidence area, respectively. The lower panel presents the residuals, i.e the relative deviation of the fitted data points from the best-fit model.

model is subsequently optimised in the likelihood framework of binned `gtlike`. The best-fit parameters of the on-pulse analysis are also listed in Table 4.1. To trace back possible errors in the fit, a residual significance map is created and shown in Fig. 4.8. Similar to the Crab Nebula, the RoI model sufficiently describes the emission. As cross-check, the analysis of the pulsar is repeated for the full time interval without phase selection, leading to compatible results.

In the same way as for the nebula, an additional analysis in energy bins is performed. Since the pulsar dims out quite rapidly at high energies, only 20 bins are used, which are equally spaced in the logarithm of energy. The resulting SED is shown in Fig. 4.9. For comparison, the best-fit model from Abdo et al. (2013) and the recent VHE γ-ray detections (VERITAS Collaboration et al. 2011; Aleksić et al. 2012) are also shown. Upper limits are derived and drawn with the same procedure and criterion as for the Crab Nebula. The residuals between the data points and derived model are depicted in the lower panel. In general, the SED of the pulsar is well-described by the best-fit model.

4.3. Long-Term Variability

In the previous Section, the constant components in the spectrum of the Crab, i.e. the pulsar and IC emission, were determined. The fitted photon fluxes above $100\,\mathrm{MeV}$ are $F_{\mathrm{psr}} = (1.9 \pm 0.1) \cdot 10^{-6}\,\mathrm{cm}^{-2}\,\mathrm{s}^{-1}$ and $F_{\mathrm{IC}} = (6.5 \pm 0.6) \cdot 10^{-8}\,\mathrm{cm}^{-2}\,\mathrm{s}^{-1}$, respectively. Verified in previous works, these two components are steady underneath the varying synchrotron component. To obtain time-dependent flux measurements, the dataset is subdivided into time intervals of $12\,\mathrm{h}$ length. The choice of this duration represents a trade-off between being sensitive to variability and enough statistics to significantly detect the Crab in the majority of the intervals. The shortest variability time scales during flaring periods of $\sim 6\,\mathrm{h}$ (see, e.g., Mayer et al. 2013), however, cannot be detected with this binning. Therefore, the light curve is more suitable to investigate variabilities and periodicities on larger time scales. The time binning definition of the dataset results in roughly 4600 time intervals. Since the photon statistics in each individual bin are rather limited, the analysis is conducted with unbinned `gtlike`, taking into account every single photon event in the likelihood optimisation. The spectral composition of the Crab cannot be resolved within $12\,\mathrm{h}$ of data. Therefore, the Crab spectrum is modelled as a single power law (Eq. 4.6). As the Galactic diffuse model is expected to be time-independent, its scaling parameters are fixed. The values are set to the means of the parameters listed in Table 4.1, i.e. $\Phi_{\mathrm{gal}} = 0.935$ and $\Gamma_{\mathrm{gal}} = 7.5 \cdot 10^{-3}$. The isotropic diffuse component is left free to account for variations in the hadron-induced background of *Fermi*-LAT, which depends on the orbiting and pointing position of the instrument. Accordingly, there are three free parameters in each time bin: the two parameters modelling the Crab spectrum (F_{crab}, Γ_{crab}) and the isotropic diffuse normalisation N_{iso}. The fitted HE γ-ray flux F_{Crab}, plotted against time, is presented in the long-term light curve in Fig. 4.10. The light curve shows that the Crab flux is varying on various time scales. In addition to the five previously known flares, the analysis of P8 data above $50\,\mathrm{MeV}$ reveals a few more short-lasting flux peaks (e.g. MJD 54990 and MJD 55300) on top of a slowly varying continuum. The Crab flux does not reveal a real quiescent state in the light curve. In contrast to the long periods of increased flux compared to the average (e.g. after the March 2013 flare between MJD $56350 - 56450$), there are intervals in the light curve where the Crab flux is compatible with pulsar and IC flux only (e.g. around MJD 55535 or MJD 55900). The five major flares, mentioned at the beginning of this Chapter are highlighted and labelled in the light curve.

To characterise the variability and flux peaks, an adaptive time binning is applied. For this purpose, "Bayesian blocks" (BBs) (Scargle 1998; Jackson et al. 2003) are created, which provide an unbiased time binning by statistically merging consecutive periods of compatible flux levels. The algorithm decomposes the $12\,\mathrm{h}$ light curve in as few BBs as possible. At the same time, the statistical compatibility of the BBs with the provided flux points is ensured. The durations of the derived blocks provide enough statistics to disentangle the synchrotron component from the constant components. Accordingly, the model to describe the emission within the BBs is adjusted: the pulsar and IC spectra derived in Sect. 4.2 are considered as fixed background components, while the synchrotron component, modelled as a power law (Eq. 4.6), is left free to during the fit. To compare the derived fluxes within the BBs to the $12\,\mathrm{h}$ time bins, the constant pulsar and IC fluxes are added to the fitted synchrotron flux in each bin. The resulting fluxes, fitted within the BB time intervals, are overlaid in red in Fig. 4.10. The duration of the BB time intervals provides a measure for the long-term variability time scale. The longest block has a duration of $\approx 28\,\mathrm{days}$, depicting the longest time scale for which the synchrotron flux is statistically compatible with being constant.
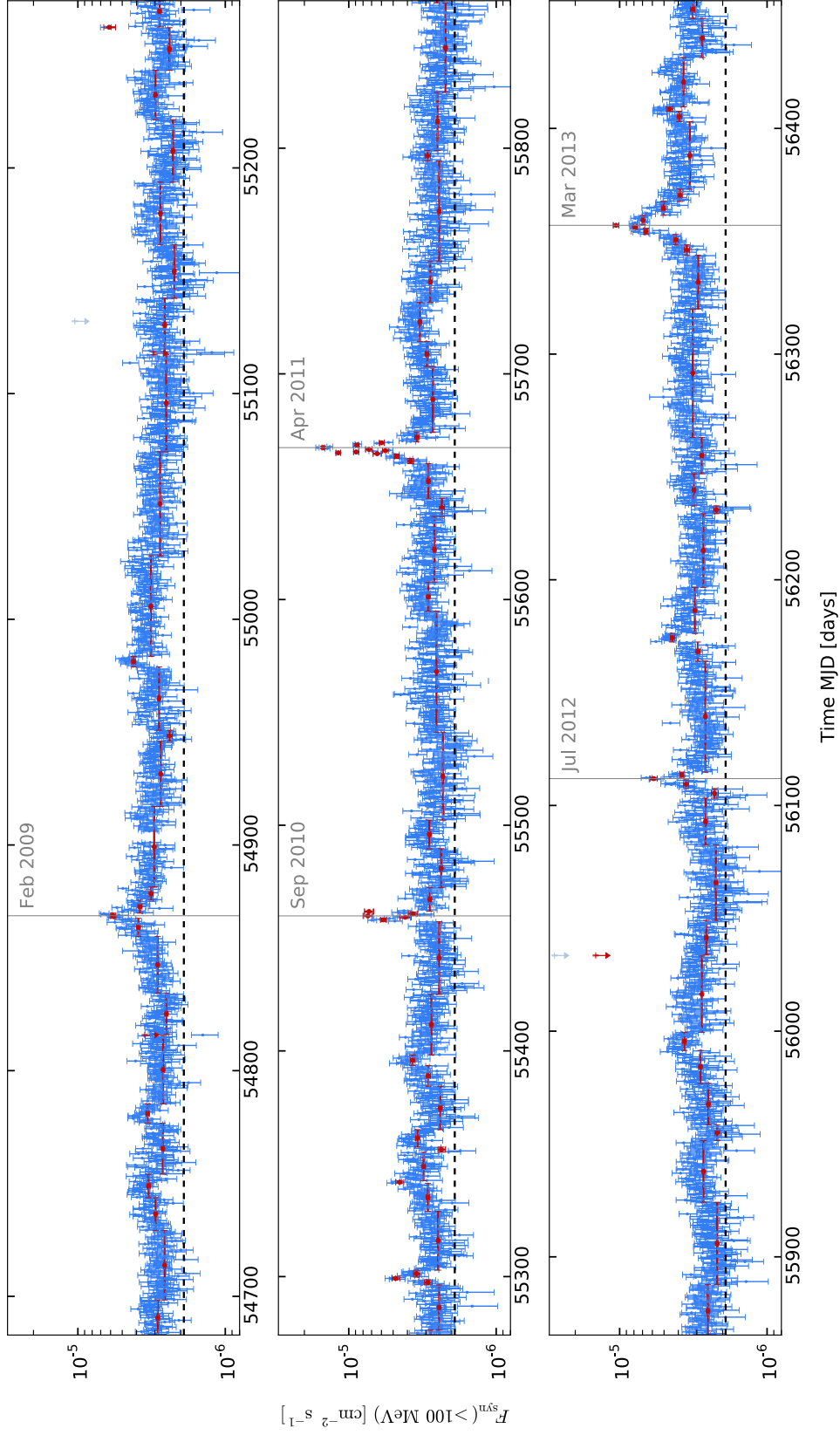
Figure 4.10.: Long-term light curve of the Crab binned into time intervals of 12 h length. The blue points denote the Crab flux above 100 MeV in each time bin. The black dashed line represents the sum of the time-averaged spectra of the pulsar and IC component derived in this work. Red data points represent the analysis of the synchrotron component in the derived Bayesian blocks.
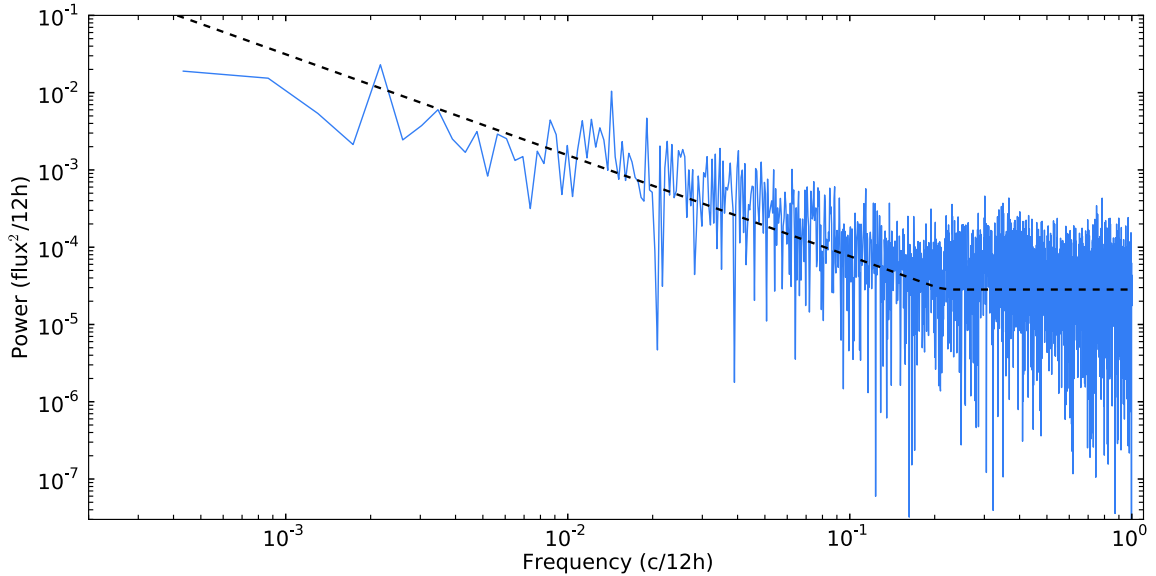
Figure 4.11.: Power density spectrum of the Crab derived from almost 5 yr of *Fermi*-LAT observations. The blue line denotes the emitted power against the wave frequency. The latter is described in the number of cycles per 12 h. The black-dashed line shows the best-fit power law plus a constant value to describe the white noise.

There is variability on many different time scales. The mean BB time window lasts 7.5 days with a large standard deviation of 6.8 days. Due to their rapid bursts, the identified flares significantly reduce the mean variability time scale. Therefore the mean duration is also calculated excluding the flaring periods. For this purpose, all time intervals which overlap with two weeks before or after one of the five flare maxima are dropped. The mean duration of the Bayesian blocks apart from the flares increases to 9.3 days with a standard deviation of 6.7 days. This mean value is in agreement with Striani et al. (2013), who inferred a $1-2$ week average as duration for periodically reoccurring waves.

Probing the light curve for periodic behaviour, a Fourier analysis of the measured fluxes in the 12 h time bins is performed. By means of a fast Fourier transformation, the fluxes of the 12 h time bins are transformed into the wave frequency space. Since this approach is only suited for evenly spaced data, small periods without available flux measurement (e.g. around MJD 54900) filled by interpolation. For this interpolation, a Gaussian scatter according to the error of the last and next real flux point is used. In total, only 14 flux points are added to the light curve. This small number does not affect the result of the transformation. The resulting Fourier power density spectrum (PDS) of the Crab, presented in Fig. 4.11, shows power on all time scales. Measured variabilities above the noise level last from several days to years. The PDS can be well described by a power law which terminates in a constant white noise level at short wavelengths. This noise level is found at less than ≈ 0.23 cycles per 12 h corresponding to a wave duration of ≈ 2.2 days. The index of the fitted power law is 1.2, which is slightly steeper than the value of 0.9 found in Buehler et al. (2012) for 33 months of *Fermi*-LAT observations. Apart from the broad distribution of variability time scales, no peak in the PDS can be detected. This implies that the variability is not subject to a periodically reoccurring process and that the observed long-term variations do not follow any
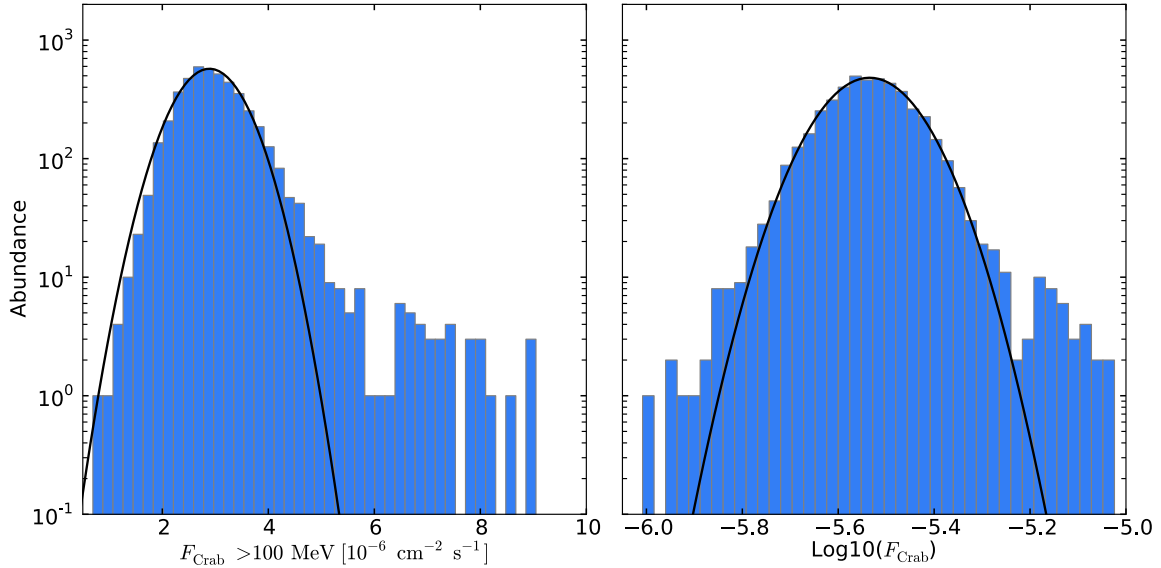
Figure 4.12.: *Left*: Distribution of Crab fluxes measured in 12 h time intervals. The distribution is fitted by a Gaussian (black solid line). *Right*: Log-normal distribution of the Crab fluxes. The blue histogram depicts the abundance of the logarithm of Crab fluxes. The black line (solid an dashed) is the result of a Gaussian fit as described for the left panel.

obvious patterns.

Investigating the origin of the variability, the light curve is analysed further. The 12 h time intervals provide enough independent flux measurements to investigate the flux distribution. In case the variability is originating from a random state of the synchrotron component with unknown scatter amplitude, the fluxes are expected to be normally distributed. The left panel of Fig. 4.12 accordingly shows the distribution of Crab fluxes measured in the 12 h time binning. To illustrate the comparison to a normal distribution, a fit with a Gaussian is performed and denoted by the black line. The fit converges on the peak of the distribution. A significant deviation from a normal distribution can be seen at higher fluxes. Therefore, the active states of the Crab, especially during the flares, cannot be attributed to a luminosity outburst from the same random process that is dominant in the rather quiet states.

The flares and flux peaks are further investigated regarding a self-amplifying, multiplicative process. The fluxes from such a process are not expected to follow a normal distribution. As shown in Aitchinson & Brown (1963), however, the logarithms of the fluxes should be described by a Gaussian function. The so-called "log-normal" distribution of fluxes is shown in the right panel of Fig. 4.12. Again, a the fit with a Gaussian function is denoted by the black line. At least around the peak of the distribution there is a good agreement with a normal distribution. Nevertheless, the measured fluxes seem not statistically compatible with a multiplicative process, either. The tail of the flux distribution towards high fluxes is significantly deviating from a single Gaussian. Consequently, at least during the flaring periods, an independent spectral component should emerge from the Crab. A connection between the flares and the long-term variability is therefore unclear.

4.4. Flare Spectra

To compare and study the spectral properties of the different flares, spectral analyses of the synchrotron component for each flaring period are conducted. Since the flares exhibit flux increases of different durations, a uniform way to define the peak flare time window is applied. The BBs, presented in Sect. 4.3 provide a statistically unbiased approach to define the time window of the flux peak during each flaring epoch. For the spectral analysis of each flare, the respective Bayesian block with the highest flux is selected. A dedicated analysis is performed in each of the five time windows. Besides the optimised power law models to describe the synchrotron component, the flare spectra are further tested for a power law which cuts off exponentially

$$\frac{\mathrm{d}N}{\mathrm{d}E} = \Phi_{\mathrm{cut}} \left(\frac{E}{100\,\mathrm{MeV}} \right)^{\Gamma_{\mathrm{cut}}} \cdot \exp\left(-\frac{E}{E_{\mathrm{cut}}} \right), \qquad (4.10)$$

with E_{cut} being the cut-off energy. For three out of five flares, the latter model is significantly preferred ($\Delta \mathrm{TS} > 9$) over the simpler power law. The derived spectral parameters for each flare are listed in Table 4.2. Spectral data points are calculated for each flare within ten energy bins, which range from $50\,\mathrm{MeV}$ and $1\,\mathrm{GeV}$. Together with the time-averaged nebula
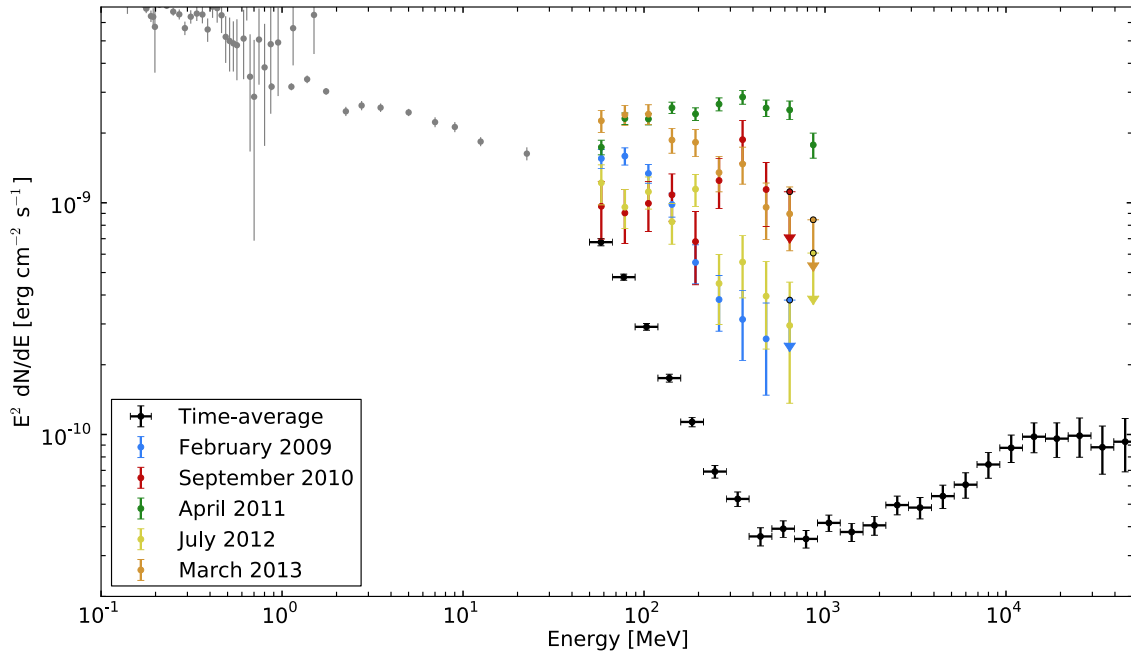
Figure 4.13.: SED of the Crab Nebula focusing on the energy regime of the flares. The black points denote the time-averaged spectrum of the nebula, derived in Sect. 4.2. The grey points represent the nebula spectrum continuing at lower energies (compiled from Meyer et al. 2010). In colour, the spectral points of the different flares are superimposed.

spectrum, the SEDs of the flares are presented in Fig. 4.13. For reasons of visibility, the superposition of each respective best-fit model is omitted.

Each detected flare seems to have a different spectral appearance. While the flares in February 2009 and July 2012 are well described by a power law, the other flares show evidence

Table 4.2.: The synchrotron component during the flares

Time binning			Power law (Eq. 4.6)		Exponential cut-off (Eq. 4.10)			
Flare	Start	Stop	$F_{\mathrm{syn}}{}^{\star}$	Γ	$\Phi_{\mathrm{cut}}{}^{\dagger}$	Γ_{cut}	$E_{\mathrm{cut}}{}^{\ddagger}$	$\Delta\mathrm{TS}$
February 2009	54867.48	54869.79	$3.85^{+0.24}_{-0.23}$	$-2.88^{+0.07}_{-0.08}$	–	–	–	–
September 2010	55459.63	55460.01	$5.51^{+0.53}_{-0.51}$	$-2.23^{+0.08}_{-0.08}$	$0.73^{+0.11}_{-0.10}$	$1.5^{+0.3}_{-0.3}$	$562.0^{+258.3}_{-258.3}$	13.0
April 2011	55666.74	55667.90	$13.01^{+0.30}_{-0.29}$	$-2.19^{+0.02}_{-0.02}$	$1.67^{+0.05}_{-0.05}$	$1.5^{+0.1}_{-0.1}$	$623.4^{+70.4}_{-63.2}$	224.0
July 2012	56111.33	56112.48	$3.98^{+0.33}_{-0.32}$	$-2.62^{+0.09}_{-0.09}$	–	–	–	–
March 2013	56356.87	56357.26	$8.67^{+0.46}_{-0.45}$	$-2.55^{+0.05}_{-0.06}$	$1.72^{+0.18}_{-0.14}$	$2.0^{+0.1}_{-0.2}$	$453.0^{+179.5}_{-114.3}$	23.7

Notes. The columns "Start" and "Stop" denote the time bin edges of the Bayesian block time binning for the selected flaring periods. The values are in days (MJD). The results of a power law fit (Eq. 4.6) of the synchrotron component are listed for each block. In addition, the best-fit values for the exponential cut-off power law (Eq. 4.10) are also listed, if that model is preferred with at least $\Delta\mathrm{TS} > 9$ compared to a power law model. Units of parameters are given in the following
$\star$ in units of $[10^{-6}\,\mathrm{cm}^{-2}\,\mathrm{s}^{-1}]$.
$\dagger$ in units of $[10^{-7}\,\mathrm{cm}^{-2}\,\mathrm{s}^{-1}\,\mathrm{MeV}^{-1}]$.
$\ddagger$ in MeV.

for an exponential cut-off in the spectra. The flare in July 2012, has a slightly harder spectrum compared to February 2009. Despite the statistical uncertainties, the flux eruptions in September 2010 and April 2011 significantly have the hardest spectra with a compatible exponential cut-off energy. In these two time windows, the spectral peak of the flaring synchrotron component in the *Fermi*-LAT energy range can be detected. In contrast, such a detection is not possible for data from March 2013. Although this flare is the second brightest, its spectrum is steeper compared to the dimmer September 2010 flare. Consequently, there is no clear correlation between flare brightness and the respective spectral shape.

Having investigated the long-term variability and the short pronounced flux peaks in the light curve, the March 2013 flare is analysed in the following.

4.5. March 2013 Flare

The most recent flare in March 2013 showed the second highest flux increase of the synchrotron component of the Crab Nebula ever measured. After the Crab flux passed the respective trigger threshold on March 3rd, 2013 (Ojha et al. 2013), a ToO was requested which triggered pointed observations with *Fermi*-LAT to maximise the exposure on the Crab. The deeper exposure, combined with the increased flux of the Crab, allows for a significant decrease of the time interval length compared to the long-term light curve. The shorter time bins, in turn, provide the possibility to measure the flare variability time scale. The analyses presented in Mayer et al. (2013) is repeated with the difference of using the updated reconstruction P8 instead of `P7SOURCE_V6`.

4.5.1. Orbit Bins

The March 2013 flare was detected by the automated science processing of the LAT data (Atwood et al. 2009; Chiang 2012) which uses a time binning of 6 h. The flux level of the Crab during this flare provides enough statistics to even further shorten the time bins. To access shorter variability time scales, a different binning is applied in the following. Following Buehler et al. (2012) and Mayer et al. (2013), one orbit of the Fermi Satellite is defined as one time bin. In each orbit, *Fermi*-LAT has continuous exposure on the Crab for about 45 min.
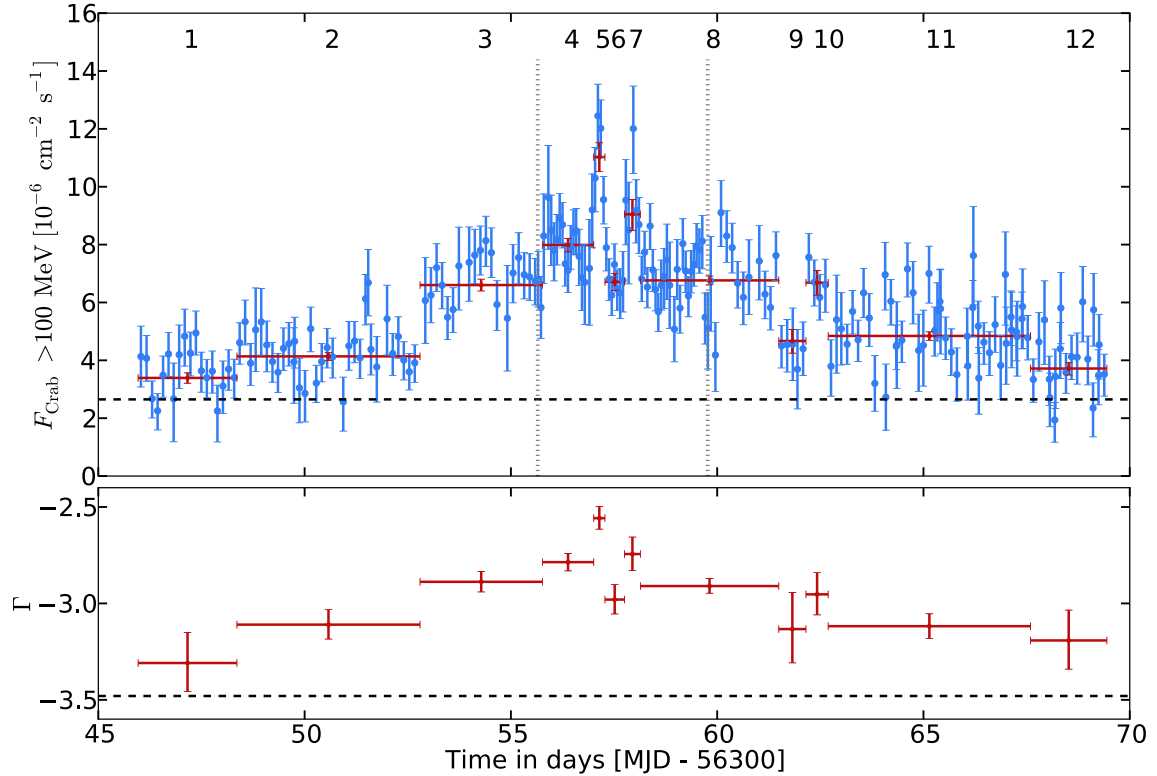
Figure 4.14.: *Top:* The light curve of the Crab during the flaring period in March 2013. The blue points denote the flux measurements in the orbit-wise time binning definition. The dashed black line represents the time-averaged flux level of the Crab. The ToO time window of pointed observations is enclosed by the vertical, grey-dotted lines. Red data points represent the flux of the synchrotron component during the BB time intervals (see text). For later reference, the BBs are consecutively numbered on top of the panel. *Bottom:* The spectral index of the synchrotron component derived in each BB. For comparison, the time-averaged spectral index is depicted by a dashed black line.

Due to the complex orbital movement of the satellite, this duration varies from bin to bin. Each orbit provides enough photon statistics to conduct the analysis with unbinned `gtlike` and significantly detect the Crab. Within every time bin, the same model as for the 12 h light curve (see Sect. 4.3) is applied. The time-dependent flux of the Crab, determined in the orbital light curve, is shown in Fig. 4.14 (blue points). The time window during which the LAT switched to pointed observations due to the triggered ToO is enclosed by dotted grey lines. In this interval, more orbits than usual have exposure on the Crab, leading to more frequent flux points. During the ToO campaign, there are two distinct flux peaks which are roughly one day apart. These peaks are on top of a strongly increased flux continuum compared to the time-averaged flux. This indicates that the Crab was already in an active state before and after the flare.

In the same way as in the long-term light curve, the BB procedure is applied to find an optimal time binning. Within the hereby obtained time intervals, the synchrotron component

is analysed separately from the pulsar and IC emission. For this purpose the time-averaged spectra of the IC and the pulsar component are used as fixed underlying background. To compare the fitted fluxes to the orbit-binned light curve, the red points in Fig. 4.14 denote the sum of the varying synchrotron component and the constant components of the Crab. The smallest time window, derived by the BB algorithm, is a measure for shortest significant variability time scale during the flare. This time scale is defined by the 5th BB which is approximately 6.5 h long. This value is slightly larger but still compatible with the variability time scale of 6 h, derived in Mayer et al. (2013).

During the shortest BB, the γ-ray flux reaches it maximum. The peak flux of the synchrotron component during the March 2013 flare, determined in this time window, is $(9.1 \pm 0.5) \cdot 10^{-6}\,\mathrm{cm}^{-2}\,\mathrm{s}^{-1}$. This value is in agreement with the previous analysis, where the peak flux of the synchrotron component was determined to $(10.2 \pm 0.8) \cdot 10^{-6}\,\mathrm{cm}^{-2}\,\mathrm{s}^{-1}$. To study the spectral behaviour during the flare, Fig. 4.14 additionally shows the spectral index of the synchrotron component in the lower panel. It can be seen that a flux increase is strongly correlated with a contemporaneous spectral hardening of the synchrotron component. This
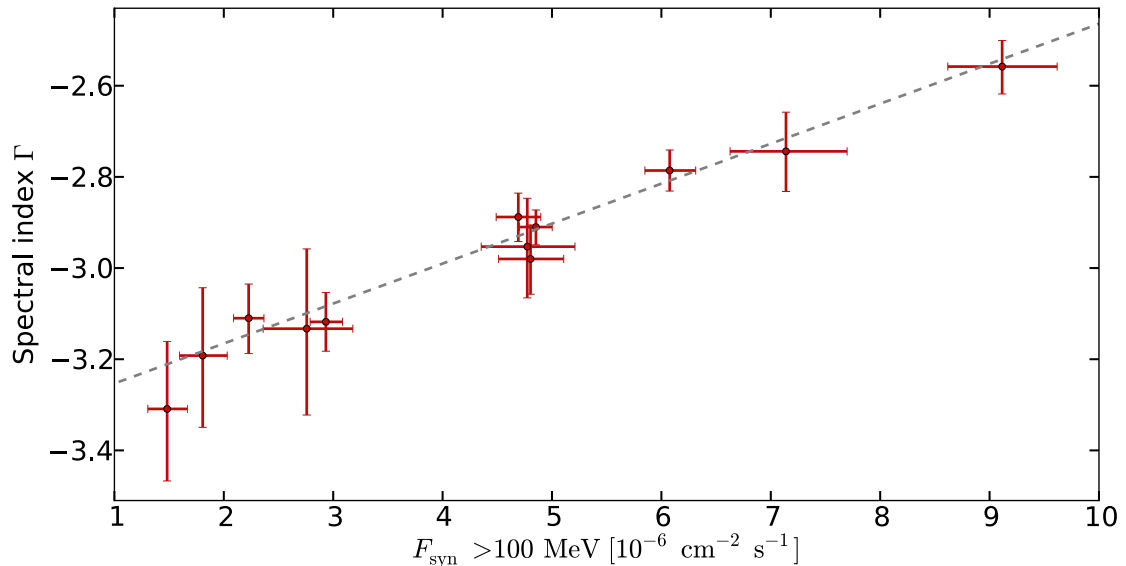
Figure 4.15.: Spectral index of each BB, plotted against the flux of the synchrotron component. Each red data point belongs to the measurement in one Bayesian block. The dashed grey line indicates the best-fit of the data by a linear function.

correlation is well described by a linear function. The best-fit function of a first-order polynomial is

$$\Gamma(F_{\mathrm{syn}}) = (8.8 \pm 0.5) \cdot 10^{-2} \cdot F_{\mathrm{syn}} - (3.34 \pm 0.03). \tag{4.11}$$

The flux-index correlation, along with the linear fit, is shown in Fig. 4.15. Generally, as shown in the 2FGL catalogue (Nolan et al. 2012), the detected source flux is dependent on the corresponding spectral index. This is mainly due to the energy-dependent sensitivity of *Fermi*-LAT. Since the flux of the Crab, however, is far above the detection threshold, the observed correlation is considered real. The flux increases are consequently related to simultaneous spectral changes. Such a behaviour was also reported for previous flares. In the following, the spectral evolution during the March 2013 flare is investigated in more detail.
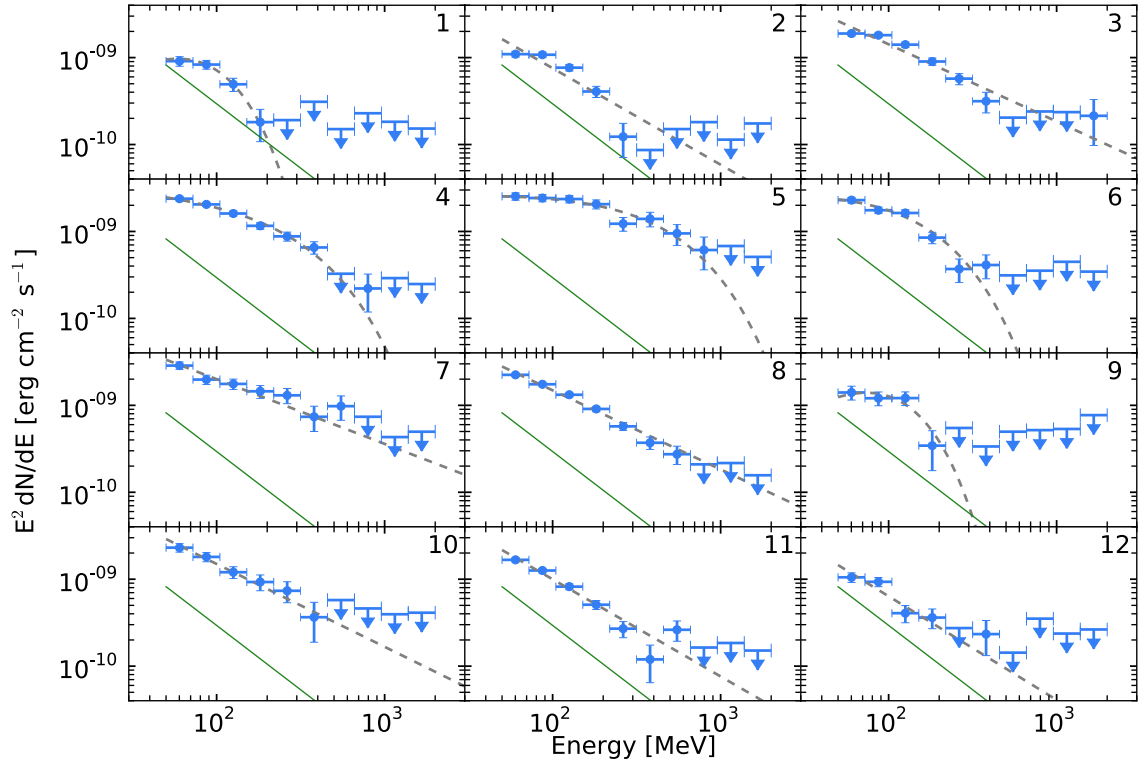
Figure 4.16.: SEDs derived for each Bayesian block. On the top right, each panel is numbered according to its respective Bayesian time bin. The blue data points are result of the flux measurements in each energy bin. The dashed grey lines denote the respective best-fit model, while the green line represents the time-average synchrotron spectrum derived in Sect. 4.2.

4.5.2. Spectral Analysis

To visualise the spectral changes of the synchrotron component during the flare, SEDs with data points are created for each BB. The spectral points are calculated for ten energy bins which are equally distributed on a logarithmic scale between 50 MeV and 2 GeV. As shown in Mayer et al. (2013), the synchrotron spectra determined during BBs close to the flux peaks differ significantly from a simple power law description. The hypothesis of a power law which cuts off exponentially (Eq. 4.10) is therefore tested in each block. The increased sensitivity of P8, combined with the lower energy threshold, provides higher photon statistics for the spectrum determination compared to the previously used reconstruction. Accordingly, more Bayesian blocks are found within which a power law with exponential cut-off is statistically preferred (ΔTS > 9) over a simple power law. A detailed list of the Bayesian block time intervals and the respective best-fit spectral models can be found in Table 4.3. The twelve spectra measured during these time intervals of compatible flux level are shown in Fig. 4.16. For comparison, the time-averaged spectrum of the synchrotron component, derived in Sect. 4.2, is also shown in each panel. It seems that during intervals with strongly increased flux levels, the synchrotron emission is dominated by a newly emerging spectral component. The emission of this component is shifted towards higher energies with respect to the time-averaged spectrum. The time intervals with the highest flux levels show significant evidence for a

Table 4.3.: Spectra within the Bayesian blocks during the March 2013 flare

	Time binning		Power law (Eq. 4.6)		Exponential cut-off (Eq. 4.10)			
Block	Start	Stop	$F_{\mathrm{syn}}^{\mathrm{a}}$	Γ	$\Phi_{\mathrm{cut}}^{\mathrm{b}}$	Γ_{cut}	$E_{\mathrm{c}}^{\mathrm{cut}}$	ΔTS
1	56345.96	56348.36	$1.48^{+0.18}_{-0.18}$	$-3.31^{+0.15}_{-0.16}$	$9.51^{+2.46}_{-2.46}$	$0.20^{+0.06}_{-0.06}$	$32.7^{+2.9}_{-2.9}$	14.0
2	56348.36	56352.80	$2.23^{+0.14}_{-0.14}$	$-3.11^{+0.07}_{-0.08}$	–	–	–	–
3	56352.80	56355.76	$4.69^{+0.21}_{-0.20}$	$-2.89^{+0.05}_{-0.05}$	–	–	–	–
4	56355.76	56357.01	$6.08^{+0.24}_{-0.23}$	$-2.79^{+0.05}_{-0.05}$	$1.70^{+0.23}_{-0.18}$	$2.13^{+0.16}_{-0.16}$	$266.8^{+73.1}_{-73.1}$	28.0
5	56357.01	56357.28	$9.12^{+0.50}_{-0.50}$	$-2.56^{+0.06}_{-0.06}$	$1.88^{+0.22}_{-0.18}$	$1.93^{+0.17}_{-0.17}$	$397.9^{+128.2}_{-128.2}$	22.8
6	56357.28	56357.75	$4.80^{+0.30}_{-0.29}$	$-2.98^{+0.07}_{-0.08}$	$2.51^{+0.96}_{-0.96}$	$1.82^{+0.36}_{-0.49}$	$119.6^{+63.4}_{-40.1}$	16.7
7	56357.75	56358.14	$7.14^{+0.56}_{-0.51}$	$-2.74^{+0.09}_{-0.09}$	–	–	–	–
8	56358.14	56361.49	$4.85^{+0.15}_{-0.15}$	$-2.91^{+0.04}_{-0.04}$	–	–	–	–
9	56361.49	56362.15	$2.76^{+0.42}_{-0.40}$	$-3.13^{+0.17}_{-0.19}$	$9.05^{+3.72}_{-3.72}$	$0.21^{+0.28}_{-0.28}$	$41.1^{+6.3}_{-6.3}$	11.7
10	56362.15	56362.69	$4.77^{+0.44}_{-0.42}$	$-2.95^{+0.11}_{-0.11}$	–	–	–	–
11	56362.69	56367.60	$2.93^{+0.15}_{-0.14}$	$-3.12^{+0.06}_{-0.06}$	–	–	–	–
12	56367.60	56369.45	$1.81^{+0.22}_{-0.21}$	$-3.19^{+0.15}_{-0.16}$	–	–	–	–

Notes. The parameter units and scales are the same as in Table 4.2

spectral hardening. Corresponding spectra show evidence for an exponential cut-off. The peak flare spectrum during the 5th Bayesian block is measured up to 800 MeV. This value, together with the cut-off energy $E_{\mathrm{cut}} = 398 \pm 128$ MeV, is in agreement with Mayer et al. (2013), where a maximum energy of ~ 700 MeV and a cut-off energy of 484^{+409}_{166} MeV was derived.

Time-resolved analyses of data from *Fermi*-LAT reveal a varying synchrotron component of the Crab Nebula. The long-term behaviour of the synchrotron light curve indicates variability on the time scales from years down to a few hours. A Fourier analysis, however, does not reveal any periodicity and shows power on all time scales. The distribution of measured fluxes indicates that the variability and strong flares of the synchrotron component of the Crab can not be attributed to a random state of a single process. A multiplicative process can likewise be excluded to be exclusively responsible for the flares and the long-term variability. Accordingly, the flares might originate from a distinct, randomly occurring process. Compared to the time-averaged emission, the flares have harder spectra in addition to the increased fluxes.

4.6. Discussion

The variability time scales of the flares vary from case to case. The shortest variability time scale is around 6.5 h, determined during the March 2013 flare. Causality implies that the flaring region is smaller than $2.2 \cdot 10^{-4}$ pc or 47 AU[8]. Assuming a distance of 2 kpc to the Crab, the apparent size of this region is roughly $0\farcs024$. Consequently, this region is hard to resolve directly, even for instruments observing with the best angular resolutions at other

---

[8]1 AU $= 1.5 \cdot 10^{8}$ km, i.e. the mean distance from Sun to Earth.

wavelengths. Due to the short cooling time scales of very energetic electrons in the magnetised nebula, the flaring regions must be very close to their acceleration site.

During the flaring epochs, many telescopes conducted deep observations of the Crab Nebula to find indications for the origins of the flares. The used instruments cover a large energy range from radio to VHE γ rays. Up to now, no significant contemporaneous activities at other wavelengths could be detected from the Crab (Morii et al. 2011; Lobanov et al. 2011; Balbo et al. 2011; Weisskopf et al. 2013; Aliu et al. 2014; H. E. S. S. Collaboration et al. 2014). These non-detections constrain the flare spectra (Weisskopf et al. 2013).

The emitted isotropic power during the brightest flare in April 2011 reaches 1% of the spin-down power of the pulsar (Buehler et al. 2012). In terms of causality and energetics, it is hard to explain that such a strong emission originates from the small flaring region. A more reasonable assumption is that the emission is relativistically boosted towards the Earth. This could also explain why the synchrotron emission during the flares is detected up to $\sim 1\,\mathrm{GeV}$ which is much higher than the maximum expected synchrotron energy of $160\,\mathrm{MeV}$, derived from MHD simulations (Guilbert et al. 1983; Uzdensky et al. 2011). In the following, recent theories explaining the origin of the synchrotron variability are summarised.

The variability could be subject to the interactions of the termination shock with magnetosonic waves producing Doppler-boosted post-shock flows (Lyutikov et al. 2012). A weak termination shock in the polar region is also proposed as the origin of the flares (Lyubarsky 2012): the post shock flow could still be strongly magnetised and relativistic, triggering sudden magnetic dissipation into electrons causing variable synchrotron emission. In contrast, Yuan et al. (2011) propose series of knots of relativistic particles moving outwards from the inner nebula with a power law distribution of Doppler factors. These knots can raise strong stochastic instabilities of magnetic fields causing rapid bursts of synchrotron emission (Bykov et al. 2012).

In the context of magnetic reconnection (see also Sect. 2.2.1), relativistic beaming of electrons is expected. The layer of reconnecting plasmas with different polarity functions similar to a linear accelerator. Strong electric fields can emerge within magnetic reconnection layers (Sironi & Spitkovsky 2011a, 2014). These fields accelerate electrons to PeV energies, such that magnetic instabilities of the reconnection layer are negligible due to the large electron gyration radii (Kirk 2004; Uzdensky et al. 2011). This acceleration mechanism can form minijets, which appear as flares when they sweep across the line of sight (Clausen-Brown & Lyutikov 2012). These particles are subsequently deflected in the comparably strong magnetic field inside the nebula, producing intense synchrotron emission (Bednarek & Idec 2011). From particle-in-cell simulations, Cerutti et al. (2012) found that mono-energetic electrons pile up at the end of the reconnection layer. Their synchrotron emission in a $\sim 0.1\,\mathrm{mG}$ magnetic field describes the flare spectra quite accurately. The observed rapid variability can be explained by these simulations, too. Beams of accelerated particles cross the line of sight and cause rapid jumps in the synchrotron luminosity and spectrum (Cerutti et al. 2013, 2014a,b). The simulated PDS is in very good agreement with the observed variability time scales.

In summary, magnetic reconnection events accumulating mono-energetic electrons in a small region seem to be a plausible explanation for the observed variability. Such electron distributions could also explain the absence of MWL counterparts.

Komissarov & Lyutikov (2011) argue that the inclination angle of the Crab with respect to the line of sight supports the observed HE γ-ray variability. The inner knot of the Crab, briefly mentioned in the introduction of this Chapter (also often referred to as "arch shock" or "knot 1"), could be the origin of the variability. Fig. 4.17 (left) presents the line of sight
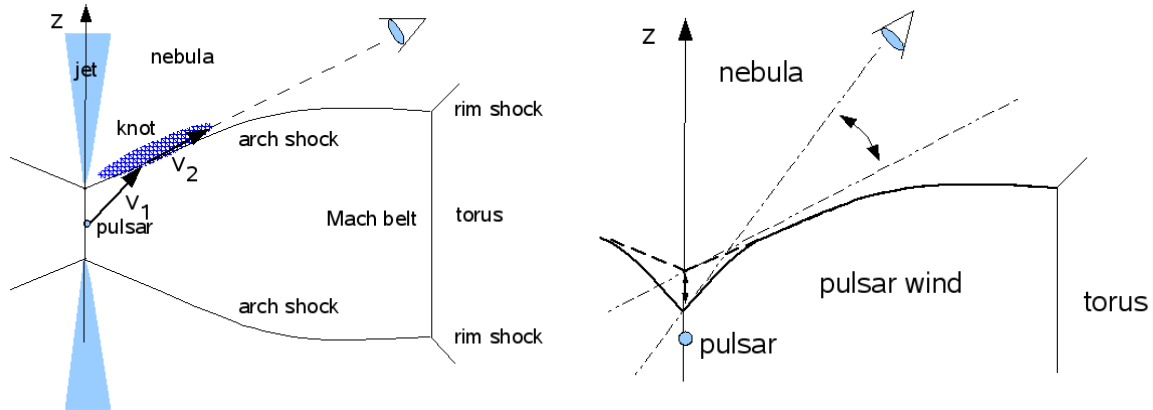
Figure 4.17.: *Left*: Schematic illustration of the geometry of the inner knot compared to the line of sight, which is depicted as a black-dashed line. *Right*: Visualisation of the possible knot movement, crossing the line of sight. Both images are adopted from Komissarov & Lyutikov (2011).

with respect to the geometry of the Crab Nebula. Three-dimensional MHD simulations indicate that the inner knot is a projection along the oblique termination shock (Komissarov & Lyubarsky 2004; Porth et al. 2014). It could therefore be a strong source of HE γ rays, boosting particles in our direction via magnetic reconnection. Additionally, the magnetic field close to the knot could be much higher than the surrounding average (Komissarov & Lyutikov 2011), which further supports the hypothesis of strong γ-ray emission from this structure.

Optical observations revealed the inner knot to be a persistent feature in the structure of the inner nebula of the Crab (Hester et al. 2002). Its position with respect to the pulsar is known to randomly vary on small scales (e.g. Sollerman 2003), which is also expected from simulations (Camus et al. 2009; Porth et al. 2014). Such slight movements of the arch shock caused by possible flow instabilities could produce the observed long-term variability of γ rays (see Fig. 4.17, right). Until now, however, no clear correlation of the knot movement with the HE γ-ray flux level could be found. For detailed and updated MWL investigations of the inner knot, the reader is referred to an upcoming publication (Rudy et al. in prep.). In this paper, the knot position is analysed from a larger dataset to further study a putative correlation with the HE γ-ray flux level of the Crab. This will further constrain the nature of the flares and long-term variability of the synchrotron component of the Crab Nebula.

Despite many comprehensive theories, these phenomena remain puzzling. Future flares might provide more insights to pinpoint their origin unambiguously.

Having studied two extreme cases of the PWN population, namely the energetic twins N 157B and the Crab Nebula, the peculiarity of these two objects is apparent. While N 157B stands out by its intense IC emission in the VHE γ-ray range, the Crab Nebula shows unexpected and surprising variability at HE γ rays. The distance of N 157B makes it unlikely to detect similar flares: a flux eruption as bright as the April 2011 flare of the Crab would still be too dim by a factor of ~ 5 to be detected by the *Fermi*-LAT all sky variability detection procedure (Ackermann et al. 2013). Both objects are rather special cases of the diverse PWN population presented in Sect. 2.3. In the following, the population of these γ-ray emitting

objects is investigated, using a uniform analysis framework, which provides the possibility to combine data from *Fermi*-LAT and ground-based VHE γ-ray detectors.

5. A Uniform Likelihood Analysis for PWNe

The study of the PWN population presented in Sect. 2.3 is exclusively targeted on VHE γ rays. Extending the analysed energy range could provide more insights into important PWN properties, such as the peak of the IC emission. Evaluating all available γ-ray data in one analysis framework leads to a complete description of the IC emission from PWNe. In this Chapter, an approach to combine γ-ray data from *Fermi*-LAT and H. E. S. S. is presented. The major challenge in this is to unify the completely different analysis approaches which are applied in the HE and VHE regime. In the following, the H. E. S. S. experiment and the current analysis approach of VHE γ-ray data is presented. Subsequently, the analysis framework, which can combine the data from several instruments is introduced. Its advantages and limitations compared to single instrument analyses are discussed. The main focus of the presented work is the technical realisation of a combined data analysis in the new framework. This framework is used to analyse the γ-ray emitting PWN population.

5.1. The H. E. S. S. Experiment and VHE γ-ray Data Analysis

The High Energy Stereoscopic System (H. E. S. S.) is a current-generation, ground-based γ-ray detector. It consists of five so-called *Imaging Atmospheric Cherenkov Telescopes* (IACTs). Located in the Khomas Highland in Namibia ($23°16'18''$ S, $16°30'00''$ E), it can regularly observe the inner Galactic plane. Since most of the PWNe are detected within our Galaxy, this system is well suited to study the majority of the PWN population. In the following, the measuring technique of H. E. S. S. and IACTs is described. A particular emphasis is put on the spectral and morphological analysis procedure, which starts from reconstructed VHE γ rays. This so-called high-level analysis is discussed regarding its advantages and limitations.

5.1.1. Imaging Atmospheric Cherenkov Technique

IACTs use the atmosphere of the Earth as detector material and calorimeter. The basic principles of this approach are described in the following.

Air Showers

The atmosphere of the Earth is constantly hit by cosmic radiation. The idea of detecting this radiation from the ground can be attributed to Auger et al. (1939) and Galbraith & Jelley (1953). The latter found short light pulses as result of cosmic ray interactions in the atmosphere. These interactions induce cascades of secondary particles. Such cascades are called extensive air showers (EAS). An electromagnetic EAS for instance, induced by an energetic photon or cosmic-ray electron, is driven by two alternating processes: bremsstrahlung and pair creation. An incoming γ-ray creates an electron-positron pair in the presence of an atomic nucleus. These charged particles, in turn, produce photons via bremsstrahlung in electric fields of atomic nuclei while propagating through the atmosphere. Subsequently,
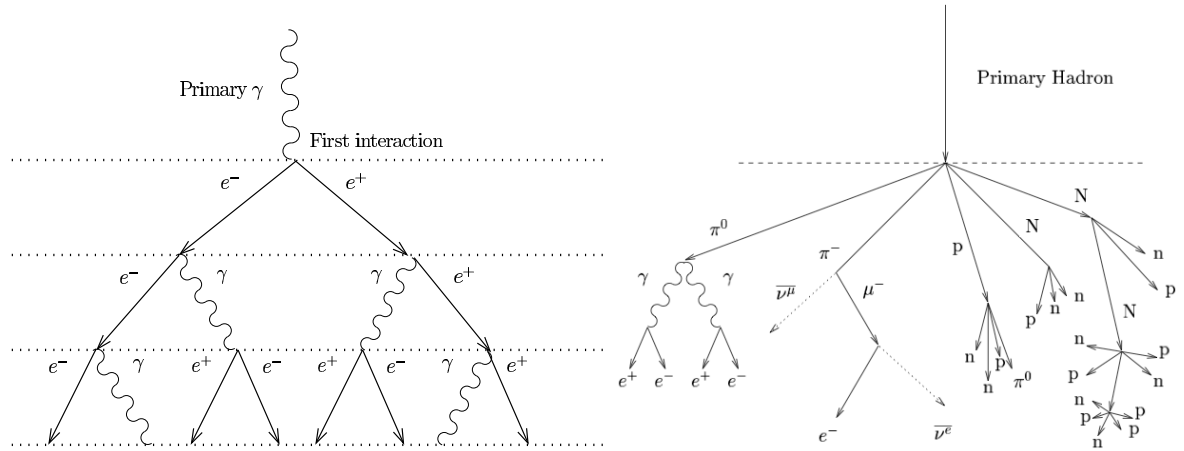
Figure 5.1.: *Left*: Schematic illustration of an air shower, induced by a γ-ray hitting the atmosphere. The distances between the horizontal dotted lines represent one radiation length. *Right*: Scheme of a hadron-induced air shower, showing several sub-showers, among others an electromagnetic one on the very left. The particles p and n represent nucleons created in hadronic interactions, while N stands for an energetic atomic nucleus. Further shown are pions ($\pi^{\pm,0}$), neutrinos (ν) and muons (μ). Both images are adopted from Funk (2005).

the process restarts with pair creation from the bremsstrahlung induced photons. Accordingly, the number of particles in an EAS doubles within one radiation length X_0. This cascade continues until the mean energy of the particles has dropped such that ionisation of molecules becomes dominant. At this point, no new particles are created and the shower fades quite rapidly. Fig. 5.1 (left) schematically illustrates the development of such an electromagnetic air shower induced by an astrophysical γ-ray. In contrast to electromagnetic showers, hadron-induced cascades appear much more frequently. Most of the cosmic-ray particles are protons or heavier atomic nuclei ($\sim 99\%$). Such air showers look more complex due to several distinct branches, which again consist of electromagnetic and hadronic sub-showers. Accordingly, hadron-induced EAS are much more scattered than electromagnetic ones (see right panel of Fig. 5.1).

Cherenkov Light

As measured by Galbraith & Jelley (1953), EAS produce faint and short pulses of visible and ultra-violet light, so-called Cherenkov light. These electromagnetic waves are emitted when a charged particle exceeds the speed of light of the medium it travels in (Čerenkov 1937). Along its path through the atmosphere, such a charged particle polarises the surrounding molecules. Consequently, these molecules emit radiation with constructive interference. Cherenkov light is emitted in a cone with the opening angle θ

$$\cos\theta = \frac{1}{\beta n}, \tag{5.1}$$

where β is the particle velocity with respect to the speed of light in the vacuum and n is the refraction index of the medium. Cherenkov light is radiated if $\beta n > 1$. Since in the atmosphere, n is strongly dependent on density and therefore on altitude, the emitted

Figure 5.2.: The H. E. S. S. array. Image taken in during the inauguration of the fifth telescope in September 2012.

Cherenkov light is a superposition of radiation emitted from different heights. Around an altitude of $10\,\mathrm{km}$, at the approximate shower maximum, the refraction index is $n \approx 1.0002$, leading to an opening angle of $\sim 1°$ (for $\beta \approx 1$). Accordingly, from this point, the ground is illuminated in an area of roughly $150\,\mathrm{m}$ radius. The spectrum of the emitted Cherenkov radiation peaks at roughly $330\,\mathrm{nm}$ (see, e.g., Doering et al. 2001; Bouvier et al. 2013). The short Cherenkov pulses of roughly $10\,\mathrm{ns}$ exceed the luminosity of night sky for this short time[1]. The emitted amount of Cherenkov light is proportional to the energy of the primary particle which hit the atmosphere. A large collection area therefore leads to more collected photons which in turn improves the sensitivity to fainter air showers of low energy cosmic rays.

The H. E. S. S. Telescopes

The H. E. S. S. array consists of five IACTs. Four equally sized telescopes, operational since 2004, which are arranged in a square of $120\,\mathrm{m}$ length. The fifth telescope, inaugurated in 2012, is placed in the square center. The latter exceeds the other telescopes in size, weight and mirror surface by far (see Fig. 5.2). After a commissioning phase, the large telescope started routine data taking in 2013. For the analysis of the entire PWN population, a large uniform dataset is required. Therefore, the analyses presented in this work makes use of data from the smaller telescopes exclusively. Each of the four telescopes is equipped with 382 mirror facets, forming a collecting surface of $108\,\mathrm{m}^2$ per telescope (see Fig. 5.3, left). The mirrors are designed to particularly reflect blue and ultra-violet light from $300-600\,\mathrm{nm}$ wavelength. In the focal plane of the telescope, $15\,\mathrm{m}$ away from the mirror-holding dish, a camera is installed to record the Cherenkov light pulses (see Fig. 5.3, right). Such a camera consists of 960 photomultiplier tubes (PMTs), which amplify the light pulses and convert them into electronic signals. The camera electronics, which digitise these pulses, have a fixed signal integration window of $16\,\mathrm{ns}$. This value is optimised to separate Cherenkov light pulses from the night sky background light (for details about the camera readout and calibration, see Vincent et al. 2003; Aharonian et al. 2004b). Since the cameras of the telescopes are

---

[1]Note that the human eye integrates light over few milliseconds, which is why the short Cherenkov pulses cannot be recognised by the naked eye.
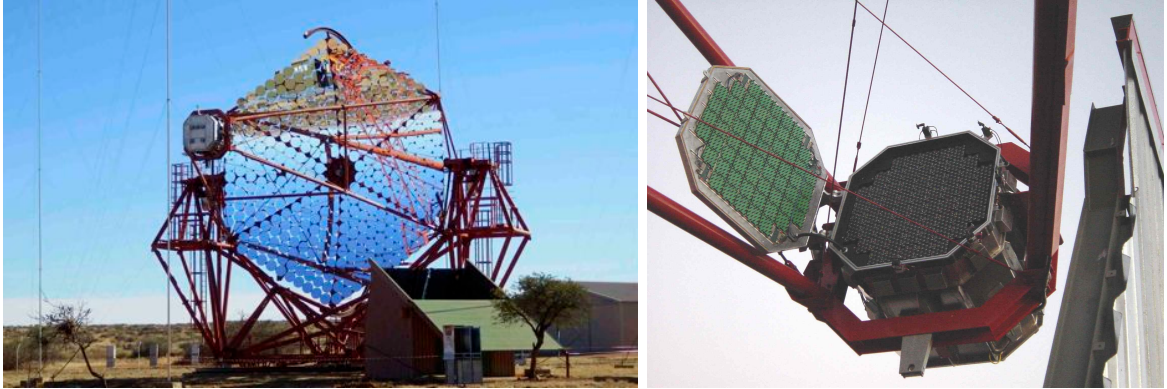
Figure 5.3.: *Left*: A H. E. S. S. telescope during the day. The mirrors reflect the inverted Namibian landscape. The steel structure holds the camera in the the focal plane. *Right*: Front view of a H. E. S. S. camera, installed in the telescope showing the 960 PMTs. The camera has a diameter of 1.6 m and a weight of 800 kg. Image Credit: H. E. S. S. Collaboration

optically very sensitive, observations are exclusively conducted during moonless times of the night. Together with periods of bad weather (rain, clouds, etc.), which prevent data-taking, the available observation time is limited to roughly 1000 h per year. The FoV of H. E. S. S. is $\sim 5°$, and therefore much more limited compared to *Fermi*-LAT. In general, H. E. S. S. observations are therefore targeted on individual objects. Observations are usually subdivided into units of 28 min duration (so-called runs). The choice of this time window is subject to the common *wobble* observing strategy (see Fomin et al. 1994, for further details). In the analysis, each run can be handled separately to avoid problems with observation conditions varying over a larger time scale.

While data-taking, if at least two telescopes report coinciding signals, the central trigger system (Funk et al. 2005) induces a readout of the triggered cameras. During routine observations, the trigger rate is around $150 - 300$ Hz, depending on atmospheric conditions and the night sky brightness of the pointing position. From the recorded intensities in the PMTs, camera images can be obtained to investigate the origin of the triggered signal. Many signals derive from electronic noise and night sky background (NSB) variations. Most of them can already be dropped by image selection algorithms. In the remainder images of cosmic-ray air showers, the fraction of images induced by VHE γ rays is only about 0.1%. For subsequent analyses, the selection of VHE γ rays, therefore, has to very efficient. The analysis of camera images needs powerful identification criteria to separate γ rays from the mainly hadronic background.

5.1.2. Reconstruction and γ-Hadron Separation

Air showers induced by γ rays differ from those originating from hadrons (Fig. 5.1). Accordingly, the emitted Cherenkov light has slightly different profiles. The recorded camera images can therefore indicate the type of the incident primary particle. Probing the geometry of the shower image, it is possible to distinguish between γ rays and hadrons. Hillas (1985a,b) showed that air showers, initiated by VHE γ rays, leave an elliptical signature in
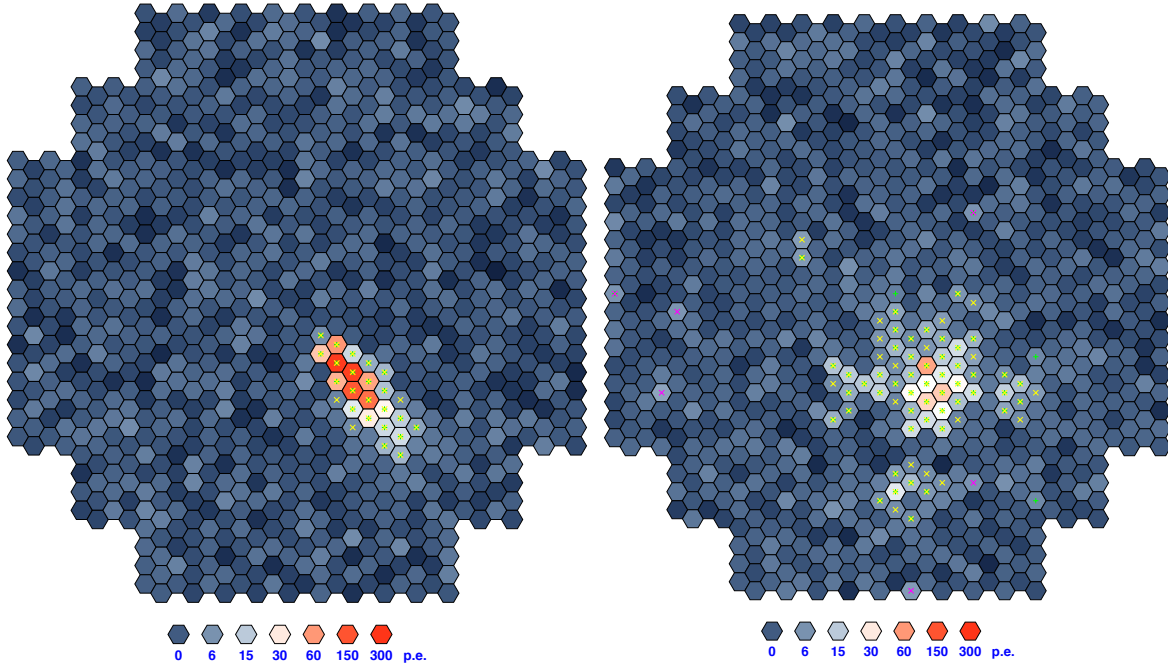
Figure 5.4.: *Left*: MC simulated camera image, induced by a 1 TeV photon. Crossed pixels are taken into account to compute the elliptical parameters. *Right*: MC simulation of a hadron-induced air shower, imaged with the H. E. S. S. camera. The colour scale in each image represents the measured charges (photo electrons, p.e.) in each PMT. Image credit: K. Bernlöhr

the camera. Monte Carlo (MC) simulations can give a relation between the energy of the primary VHE γ-ray and the size of the recorded ellipse. From the orientation of the ellipse, the incoming direction of the VHE γ-ray can be determined. Images of the same shower, recorded by several telescopes provide a stereoscopic view on the shower. The reconstruction of the VHE γ-ray direction can therefore be substantially improved. Combined with a better cosmic-ray rejection capability, this is why the H. E. S. S. trigger system always requires at least two telescopes to detect an EAS. Such an analysis, based on the image geometry, is called classical Hillas approach. Fig. 5.4 shows the distribution of photoelectrons (p.e.) in the camera induced by a VHE γ-ray (left) and a cosmic-ray proton (right). The proton image looks more scattered, while the pixel amplitudes of the γ-ray image indicate an elliptical shape. To determine important primary photon attributes, such as energy and direction, the momenta of the charge distributions are compared to lookup tables derived from extensive MC simulations. Cutting on the calculated ellipse parameters, it is possible to reject a large fraction of 90% of all hadron-induced EAS.

This work makes use of a more advanced photon reconstruction framework (de Naurois & Rolland 2009). From extensive simulations of EAS, a semi-analytical model describing the Cherenkov light distribution inside the camera is derived. The model of the shower image depends on the attributes of the incident photon. A likelihood optimisation of this model with respect to the recorded shower image, taking into account each pixel amplitude in the camera, leads to estimates of the properties of a putative incoming VHE γ-ray. The optimi-

sation procedure takes the Hillas-based estimates as start parameters. From the likelihood analysis, the goodness of fit can be retrieved for each camera image. This value has proven to be a very efficient variable to distinguish between VHE γ rays and cosmic rays. This type of analysis, so-called Model analysis, can reject roughly 95% of cosmic ray events, implying a doubled sensitivity compared to the Hillas-based analysis. The free parameters of the image fit are, among others, the energy and direction of the incoming photon and the atmospheric depth of the first interaction. The latter parameter provides a further rejection variable, especially for cosmic-ray electrons, which tend to emit Cherenkov light slightly earlier than primary γ rays (see Fig. 22 in de Naurois & Rolland 2009). To select VHE γ rays for the usage in this work, a set of cuts is applied on the camera images and the subsequent fit parameters. The applied cuts, hereafter referred to as *standard* Model analysis are listed in de Naurois & Rolland (2009). Though the applied selection cuts effectively reject cosmic rays, the sample of candidate VHE γ rays is still contaminated with events originating from cosmic-ray air showers (hadrons and electrons) by more than 50%. This fraction is typical for sources like the Crab Nebula. The fraction strongly increases for weak sources. The irreducible background has to be estimated to properly analyse sources of VHE γ rays.

5.1.3. High-Level Analysis of IACTs

The high-level analysis in VHE γ-ray astronomy is quite different from the *Fermi*-LAT analysis presented in Chap. 4. Many small observation units, with independent IRFs have to be combined to detect and measure sources of VHE γ rays. The IRFs of IACTs depend e.g. on the distance of the VHE γ-ray source from the pointing position, on the opacity of the atmosphere and on the telescope pointing position in the horizon system. The latter is the stationary sphere in zenith and azimuth. The zenith angle dependency e.g. originates in the decreasing atmospheric depth when approaching zenith. Since the Cherenkov light dims on a longer path through the atmosphere, observations conducted at low zenith angles are limited in detecting faint air showers induced by low energy particles. The Earth magnetic field also has an influence on the shower evolution, which is reflected in the azimuthal dependence of the IRFs (Commichau et al. 2008; Homola et al. 2014). In contrast to *Fermi*-LAT analyses, morphological analyses are strictly separated from spectral analyses in VHE γ-ray astronomy. In the following, the morphology analysis is briefly described before this work focuses on the derivation of spectra.

Morphology Analysis

To obtain the intrinsic morphology of the measured γ-ray excess, a two-dimensional analysis of the excess sky map is performed. For this purpose, the background is usually being determined and subtracted via the *ring background model* (Berge et al. 2007). The resulting excess map is then fitted with a two-dimensional (2D) function, e.g. a Gaussian. This function is convolved with an average PSF, which is the exposure-weighted mean over all observational runs. The optimisation of the parameters of a 2D Gaussian function leads to a position and intrinsic extension estimate. Further details about the morphology analysis procedure are given in de Naurois (2012).

Spectral Analysis

To derive spectra for VHE γ-ray sources, the background emission has to be determined and subtracted. This background mostly consists of reconstructed cosmic rays, passing the γ-hadron selections. The acceptance of the detector for this cosmic-ray background also depends on many quantities. A huge amount of MC simulations of cosmic rays would therefore be necessary to study this background. The currently most common approach circumvents this large computational effort by determining the background from the observation itself.

In contrast to *Fermi*-LAT analyses, where the RoI is fully modelled, it is common to conduct region-based analyses in VHE γ-ray astronomy (e.g. Berge et al. 2007). Extracting the spectrum of a source requires to define a region in the sky which contains the emission (on-region). For a point-like source, the usual region is a circle with radius $\theta = 0°1$ around the center of gravity of the emission. This value is optimised to maximise the ratio of signal to background in that region without losing too much statistics. Due to the PSF, which has a similar width, the derived fluxes have to be corrected for events leaking out of that region. This in turn requires adequate knowledge of the PSF and its tails.

To determine the background level, which is present in the on-region, one has to define so-called off-regions. In the aforementioned *wobble* observation mode, the telescopes point slightly offset from the source of interest ($0°5 - 0°7$). Assuming radial symmetry of the background acceptance in the camera, the off-regions are of the same size as the on-region and are arranged on a circle around the pointing position (see Fig. 5.5). The VHE γ-ray excess within the on-region is then calculated to

$$N_{\mathrm{exc}} = N_{\mathrm{on}} - \alpha N_{\mathrm{off}}, \tag{5.2}$$

where N_{on} and N_{off} are the number of detected events in the on-region and in all off-regions, respectively. The correction factor α takes into account the differences between the on-region and off-regions, e.g. deviating exposure. In the case shown in Fig. 5.5, $\alpha = 1/8$, due to the eight off-regions. With the quantities N_{on}, N_{off} and α, the statistical significance of a source detection can be calculated following Li & Ma (1983, Eq. 17). Conducting a spectral analysis, the excess is converted into a flux measurement by taking into account the effective area and the observation time. The analysis is subdivided into fine energy bins to measure an energy-dependent flux, i.e. a spectrum. Usually, ER is also taken into account here.

The above method is well-suited to account for systematic differences in the acceptance for each run. The approach also gives a solid estimate of the significance of the source detection. For the spectral analysis of VHE γ-ray sources with small extensions in otherwise empty FoVs, the reflected region method depicts a very stable procedure to determine the background level.

Regarding more complex regions in the sky with several source components, the reflected region method reaches its limits. Known regions of VHE γ-ray emission have to be excluded from the off-regions in order to not contaminate them with source emission. This problem is enhanced if the source of interest is largely extended leading to the requirement of large off-regions. At a certain region size, the FoV is a limiting factor for these kind of analysis. In case the FoV is further contaminated by a large diffuse structure, like for the Galactic center region (Aharonian et al. 2006e), the off-regions might not reflect the true background rate for the chosen on-region. Sources with overlapping tails are hard to separate since the on-region definition has to exclude the other close-by source without losing statistics from the source of interest. An example with an extended source, overlapping with a point source on top of a diffuse component is shown in Fig. 5.5 (right). The definition of an on-region is difficult due
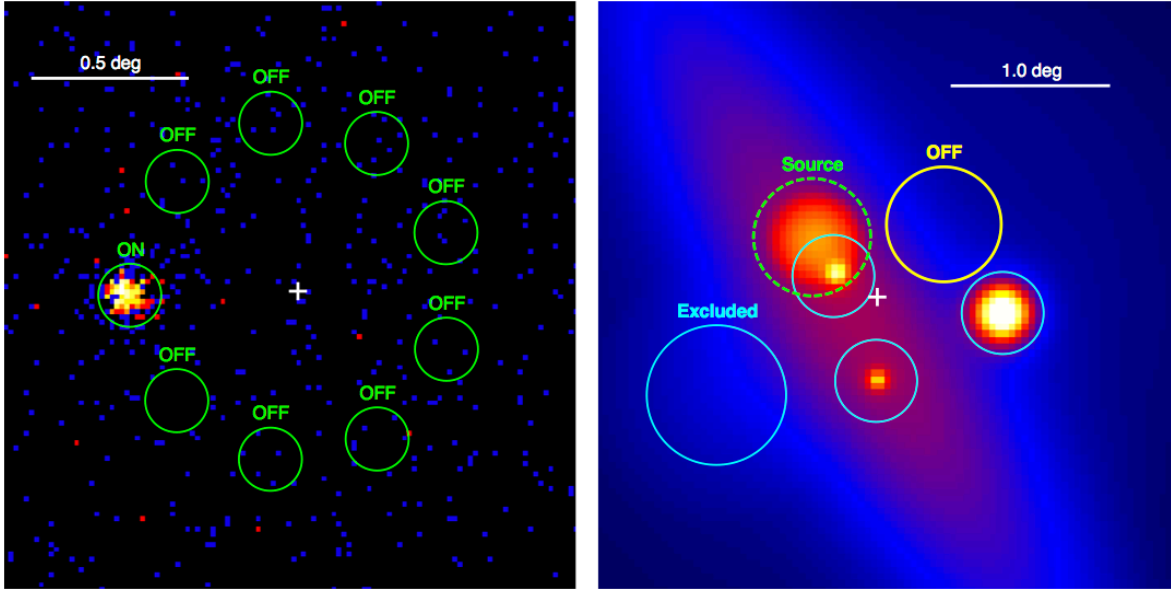
Figure 5.5.: Two sky maps, illustrating the reflected region method. The telescope pointing position is marked by a white cross in both frames. The colour scale represents the number of counts per bin in arbitrary units. *Left*: Count map of one run on Crab Nebula (# 23544), pointing 0°.5 offset from the source position. The on-region is at the Crab position with a radius of 0°.1. Equidistant from the pointing position, the off-regions reflect the on-region in size. *Right*: Simulated crowded FoV. Cyan circles show excluded regions at the positions of known sources. The source of interest is marked in green. This extended source is located on top of a diffuse continuum (light red colours) that could represent e.g. the Galactic diffuse emission close to the Galactic Center. Indicated in yellow is the only possible off-region for the source of interest.

to the overlapping source which needs to be excluded. The only possible off-region, shown in yellow, however, is not representative for the background level at the source position. Using such a run with the indicated off-region would falsify the background level at the source position.

In conclusion, the reflected region method provides a solid approach to detect and analyse compact sources in the FoV. In contrast, regions in the sky with VHE γ-ray emission from several, also extended sources, or even with diffuse components, cause difficulties in finding suitable off-regions which are representative for the background level in the defined on-region. The analyses in this work are targeted on PWNe, which are mainly located along the Galactic plane with possible diffuse emission (Egberts et al. 2013). The increasing number of detected sources in the recent years (Carrigan et al. 2013) also increases the number of excluded regions which have to be taken into account. Accordingly, it is more and more challenging to find suitable off-regions to determine the background level. In the following, an analysis method which does not rely on region definitions is therefore introduced.

5.2. From Standard H. E. S. S. Analysis to GAMMALIB/CTOOLS

With the advent of the future VHE γ-ray observatory *Cherenkov Telescope Array* (CTA)[2], the number of detectable sources in our Galaxy is expected to increase by roughly a factor of ten (see Dubus et al. 2013). This is due to the much higher sensitivity which comes along with the numerous telescopes planned for CTA. Accordingly, crowded sky regions, including overlapping sources and diffuse components are expected to be found. Meeting this new challenge, a currently very promising analysis framework for the CTA high-level analysis is GAMMALIB/CTOOLS.

5.2.1. Introducing GAMMALIB and CTOOLS

GAMMALIB[3] is "a self-contained, instrument independent, open source, multi-platform `C++` library that implements all code required for high-level science analysis of astronomical gamma-ray data" (Knödlseder 2012). This framework is currently prepared to specifically analyse data from CTA. In GAMMALIB, the γ-ray data is analysed in a likelihood framework, analogous to *Fermi*-LAT analyses (see Chap. 4). Accordingly, the RoI is fully parametrised by means of simple analytical models. On top of GAMMALIB, there are the CTOOLS[4], which are a set of executables, conducting individual analysis steps by making use of the GAMMALIB library. This philosophy is based on the FTOOLS, which are commonly used in e.g. X-ray astronomy (Pence et al. 1993). All functionality of GAMMALIB and CTOOLS is interfaced into PYTHON using SWIG[5]. Accordingly, dependent on the user preference, analyses can be executed via the command line or a PYTHON-based script.

For data input/output (I/O), GAMMALIB and CTOOLS make use of the Flexible Image Transport System (FITS, Pence et al. 2010), which is also widely used throughout astronomy. The data and IRFs of any instrument have to be provided in this FITS format. Reading them into GAMMALIB, a likelihood analysis can be performed, optimising a given RoI model (see Sect. 4.1.1 for a detailed description of the likelihood function). In one likelihood analysis, it is possible to consider data from several instruments. Such a combined analysis, is exemplarily presented in (Knödlseder et al. 2013). In this analysis, a log-parabola model (Eq. 4.7) was fitted over five decades in energy to the IC emission of the Crab Nebula using a small dataset from H. E. S. S. and *Fermi*-LAT. The first step towards a combined analysis of PWNe is the data preparation for the use in GAMMALIB.

5.2.2. Exporting H. E. S. S. Data into FITS

Data analysis and data storage in VHE γ-ray astronomy is currently based on the ROOT package[6]. H. E. S. S. data and corresponding simulations are stored in so-called data storage tables (DSTs), which are readable with the H. E. S. S. internal software only. Using this ROOT-based software, the information in these DSTs are exported to the proper FITS format for GAMMALIB. For the high-level analysis, only good quality data, i.e. runs which are taken under sufficient observation conditions are used. Further details about the standard criteria defining this quality are described in Aharonian et al. (2006a). Additionally, the exact choice of run selection parameters are listed in the Appendix (A.1) of this work.

---

[2] `www.cta-observatory.org`
[3] `http://gammalib.sourceforge.net`
[4] `http://cta.irap.omp.eu/ctools/`
[5] `http://www.swig.org/`
[6] `http://root.cern.ch`

Export of Event Lists

The data provided to GAMMALIB is portioned in event lists. Each event list comprises VHE
γ-ray events from one observational run. The information in each DST ia analysed to obtain
the properties of each individual event. The conducted Model analysis reveals the goodness of
fit, the primary depth and few more discriminating variables. Since the analysis in GAMMALIB
should be conducted for VHE γ-ray candidates only, *standard* cuts are applied on these
variables to effectively discriminate hadrons and triggers induced by the NSB (see de Naurois
& Rolland 2009, for a detailed description of these cuts). These cuts imply a rate of VHE
γ-ray candidates of $\sim 1\,\mathrm{Hz}$ within an observational run. Compared to the average run trigger
rate, only $\sim 0.5\%$ of all events are kept for later analyses. For the likelihood approach, the
fundamental attributes of each photon which are stored in the FITS event lists are:

- The event arrival time

- The event energy

- The event direction in
    - sky coordinates (Right Ascension, Declination) in J2000
    - detector coordinates (x, y)
    - horizon system (zenith, azimuth)

In addition, several more event specifications are written into the resulting event list file. Most
of them are intended to be used in future analyses, like the uncertainty of the event energy
and direction. The directional information in different coordinate systems are necessary to
determine the corresponding IRFs in the horizon system and, at the same time, evaluate the
given models in the sky coordinate system. In the near future, this might be simplified by
providing a FITS table listing the exact telescope pointing for every time[7]. In addition to the
event list stored in the FITS table, observational attributes of the respective run are written
in the corresponding FITS file header.
Having agreed on the event list FITS format, all available H. E. S. S. DSTs as of January 2014
are exported. The amount of data comprises 16145 observation runs passing the standard
run selection criteria. Together all runs accumulate a total observation time of 7150 h. All
processed event lists require a total hard disk space of 4 GB. Accordingly, they can be quickly
redistributed as intended for the CTA observatory. The H. E. S. S. DSTs, containing more
in-depth information about the events (e.g. pixel amplitudes of each PMT), occupy $\sim 16\,\mathrm{TB}$
of disk space.

Export of IRFs

Similar as in *Fermi*-LAT analyses, the likelihood framework requires IRFs corresponding to
the given data set. In standard H. E. S. S. analysis, the IRFs are derived from extensive MC
simulations and are stored in multi-dimensional lookup tables. First, the IRFs scheme for
H. E. S. S. analysis is explained, before the export to a GAMMALIB compliant format is de-
scribed.
To create the proper set of IRFs for a H. E. S. S. analysis, the same shower reconstruction
algorithm and subsequent γ-ray selection procedure is applied on simulated air showers trig-
gering a simulated telescope array. In this work, the high-level data is derived by the Model

---

[7]https://cta-redmine.irap.omp.eu/issues/1113

analysis with *standard* cuts, which is why these cuts are also applied on the MC simulations. Mimicking realistic data-taking, the shower simulations are available for diverse observational conditions and different energies and directions of the incoming VHE γ rays. The parameters on which the MC simulations depend are listed in the following. In brackets, the simulated spacing for each parameter is given.

- True photon energy (20, equally spaced in the natural logarithm of the energy between 10 GeV and 80 TeV)

- Offset angle of the photon from camera center, i.e. from the pointing position (6, linearly spaced between $0°\!.0$ and $2°\!.5$)

- Zenith of telescope pointing (14, equally spaced in the cosine space between $0°$ and $70°$)

- Azimuth of telescope pointing (2, namely North and South, corresponding to $0°$ and $180°$)

- Muon efficiency (6, linearly spaced between 50% and 100%), a run-wise varying parameter reflecting the opacity of the atmosphere and the detector efficiency. The latter includes the mirror reflectivity and the optical efficiency of the PMTs (Chalme-Calvet et al. 2014)

- Number of active telescopes (2, only runs with 3 or 4 operational telescopes are considered)

In total, this implies more than 40000 sets of simulations, one set for each combination of the above variables. The analysis of all these MC simulation, leading to the computation of the IRFs, is condensed in three lookup tables. These tables are divided into effective area (A_{eff}), point-spread function (PSF) and energy resolution (ER). For the PSF, the true energy is replaced by the source spectral index. For this purpose MC simulations providing γ-ray spectra instead of fixed energies are used. This approach leads to an average PSF for the derived sky map, which is used in morphological analyses (see Sect. 5.1.3). The resulting tables contain all needed information to perform high-level H. E. S. S. analyses. Since the MC simulations are conducted for fixed sets of variables, a multi-dimensional interpolation is performed to determine the IRFs for an arbitrary set of parameters.

The likelihood framework of GAMMALIB makes use of individual events, combining spectral and morphological information. Therefore, the PSF table has to be converted to an energy-dependent table, removing the spectral index dependency. For this purpose, all MC simulation of fixed energy VHE γ rays are re-analysed. The reconstructed directions for each set of MC variables are filled in a θ^2-histogram, representing the squared offset from the true source position. To simplify the storage and in particular to speed-up the computation in GAMMALIB, the PSF is parametrised with an analytical function. A simple but sufficient description of the PSF can be achieved by a King profile (King 1962), which is e.g. also used to parametrise the *Fermi*-LAT PSF. The probability density function of the radially symmetric King profile is defined as follows:

$$P(r|\sigma,\gamma) = \frac{1}{2\pi\sigma^2}\left(1-\frac{1}{\gamma}\right)\left(1+\frac{1}{2\gamma}\frac{r^2}{\sigma^2}\right)^{-\gamma}, \tag{5.3}$$

where r describes the distance from the true source position. The parameters σ and γ are adjustable to match the core and the tails of the PSF. The left panel of Fig. 5.6 shows the
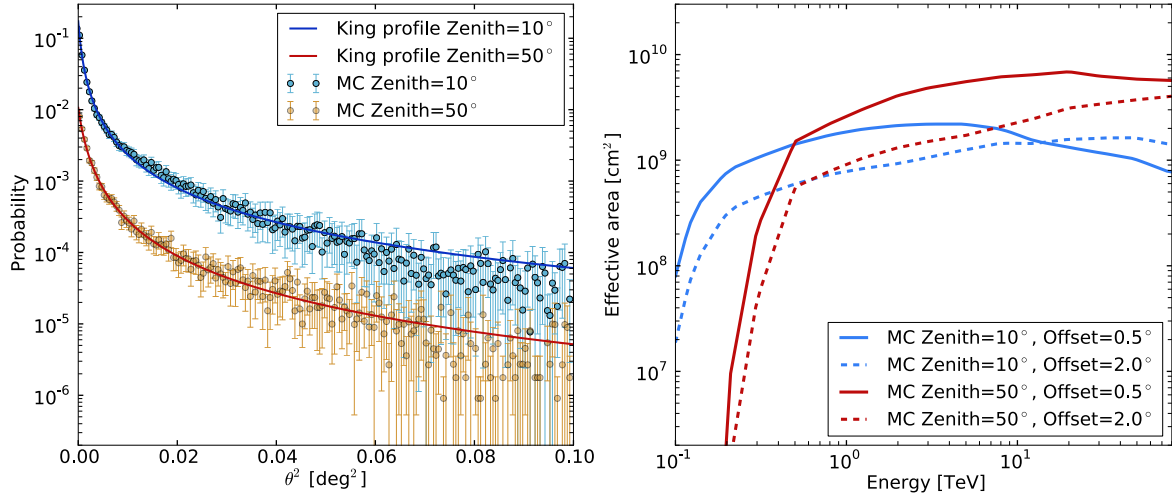
Figure 5.6.: PSF and A_{eff} for H.E.S.S., derived for a fixed azimuth of 0° and muon efficiency of 100%. *Left*: Shape of the PSF with squared offset from the true source position, which is simulated at an offset of 0°.5 from the telescope pointing position. The data points correspond to the respective MC simulation, while the lines present the fit of a King profile (Eq. 5.3) to the data. Note that the distributions for the zenith angle of 50° (orange/red) are scaled down by a factor of ten for improved visibility. *Right*: The H.E.S.S. effective area as a function of energy. As indicated in the legend on the lower right, the different curves represent four setting of MC simulations.

θ^2-distributions of reconstructed events of a fixed MC source, located 0°.5 offset from the pointing position and emitting mono-energetic photons with 1 TeV. The fit of a King profile to the θ^2-distribution is depicted for two different zenith angles. The increasing errors with larger values of θ^2 depict the lack of MC statistics to further constrain the tails of the PSF. For a 50° zenith angle, the King profile represents a slightly better description than for 10°. Nevertheless, Eq. 5.3 depicts a sufficient parametrisation of the MC simulated PSF. For each MC setup, the stored values from the complete histogram are reduced to two parameters, namely σ and γ.

The right panel of Fig. 5.6 shows the effective area as function of the true photon energy. The functional dependence is presented for two different set of zenith angles and offsets. As mentioned above, the effective area decreases rapidly for low energies in case of high zenith angles. For an analysis targeted at the low energy part of a VHE γ-ray source, observations close to zenith provide the best conditions. In contrast, high energy photons are better reconstructed for larger zenith angles. This effect can be explained by the increasing size of the shower image with energy: high-energy photons are rejected by the reconstruction chain since they appear similar to cosmic rays. In addition, images where parts of the shower lie outside of the camera are also rejected in the analysis. The offset dependency of the effective area has a similar origin. For low zenith angle observations, the effective area increases with offset at high energies, since the shower requires a longer path through the atmosphere. This implies slightly fainter shower images supporting the reconstruction in this case.

For most analyses, only a small subset of these IRFs are used. Handling the large tables is neither practicable nor necessary in GAMMALIB. Accordingly, the necessary IRFs are

derived for each run individually, reducing time consuming I/O operations to an absolute minimum. There are variables changing for each event (energy, offset) and variables which can be assumed constant during one run (zenith, azimuth, muon efficiency). Due to the rotation of the Earth, the telescopes needs to track sources across the sky. Since the H. E. S. S. runs are limited to 28 min duration, the mean values of zenith and azimuth for each run provide a sufficient approximation to compute the respective IRFs. Fixing these values, combined with the run-specific muon efficiency, the run-wise IRFs can be reduced to two dependencies: true energy of the photon and it offset from the camera center. The other variables are fixed to the observational parameters when reading the lookup table.

Since the data format of the IRFs for CTA is not settled yet, a preliminary working format for current analyses is defined. This format has enough flexibility and can host enough details to conduct proper and competitive H. E. S. S. analyses. The A_{eff} is stored as a two dimensional function, depending on the MC energy and offset angle. Accordingly, each A_{eff} file contains only $20 \times 6 = 120$ values. For the PSF, the parameters γ and σ of the king profile also depend on energy and offset. This implies twice as many stored values as for the A_{eff} in each PSF file. Both file types are readable from GAMMALIB via the implemented class `GCTAResponseTable`. Most recently, the use of ER was implemented in GAMMALIB. The analysis with ER is still in a testing phase and not optimised for the use with a large amount of data, yet. Therefore, ER is neglected for the H. E. S. S. analyses with GAMMALIB in this thesis. To minimise the hereby introduced uncertainties, the analysis is restricted to a conservative energy range, where the energy bias can be assumed close to zero (see, e.g., Aharonian et al. 2006a, for the definition of the energy bias). The choice of the considered energy range is described in the next Section.

Together, the exported IRF files of A_{eff} and PSF require a disk space of 12 kB per run. Therefore, for the total exported dataset, only 194 MB are necessary to store all IRFs. For the CTA philosophy of a quick and easy data distribution, the defined formats provide a good possibility to condense the necessary IRFs. Applying the IRFs to determine the considered energy range for each individual run is described in the following.

5.2.3. Energy Threshold

Since in this work high-level analyses in GAMMALIB are not corrected for ER, the range of reconstructed energies has to be restricted. The energy bias, i.e. the mean shift of reconstructed energies with respect to the true photon energy is defined as $(E_{\mathrm{reco}} - E_{\mathrm{true}})/E_{\mathrm{true}}$ (Aharonian et al. 2006a). The use of ER is important for energy ranges, where the bias significantly deviates from zero. This is typically the case for the low and the high energy end of reconstructed energies. In the Model analysis framework, the low energy threshold E_{th} is estimated according to the effective area:

$$E_{\mathrm{th}} = \lambda E_{\mathrm{A}_{\mathrm{eff}}, \mathrm{max}}, \tag{5.4}$$

where $E_{\mathrm{A}_{\mathrm{eff}}, \mathrm{max}}$ depicts the energy where the effective area reaches its maximum. In past analyses, the fraction λ is commonly set to 0.1. A more recent study[8], however revealed that the systematic uncertainty in the effective area can be significantly reduced by requiring $\lambda = 0.15$. Accordingly, this value is used in the following. The resulting energy threshold shows the same dependencies as the effective area.

To reduce the systematic uncertainties of the IRFs at higher energies, the energy range

---

[8]G. Giavitto, private communication

is restricted to a maximum ($E_{\max}$), too. In the Model analysis, the event distribution in the off-regions is commonly used to determine $E_{\max}$. Since no off-regions are used in the likelihood approach of GAMMALIB, the maximum energy is derived from the available MC statistics. For each run configuration, a certain number of corresponding MC events passing the selection cuts is required. If, above a certain true photon energy, the number of MC events drops below 25, the statistical errors on the IRFs induce uncertainties in measured source attributes. Therefore, a run with the corresponding observational configuration is limited to that energy. Since the MC energy binning is rather coarse, the exact maximum energy is determined via an interpolation between the fixed MC energies. This interpolation is performed in the natural logarithm of the MC energy. For following analyses, every event which was reconstructed outside of the run-specific range $[E_{\mathrm{th}}, E_{\max}]$ is rejected.

5.2.4. Background Modelling

Compared to *Fermi*-LAT analyses, the residual hadronic background needs to be modelled on a run-wise basis. Such a model should describe the cosmic-ray background flagged as VHE γ-ray candidates (hereafter γ-like background). Parametrising the γ-like background in the FoV is the major obstacle in conducting likelihood analyses of the RoI in VHE γ-ray astronomy. The rate of such background events depends on many quantities, similar as the IRFs. Accordingly, a model describing the γ-like event distribution in multiple dimensions has to take into account all these dependencies. Deriving the γ-like background by means of MC simulations requires an extraordinary high computational effort. This can be attributed to the sensitive reconstruction chains, which reject $\sim 95\%$ of all cosmic ray events. Since it is not possible to exclusively simulate γ-like cosmic rays, the accumulation of enough MC statistics to study the γ-like background implies a heavy increase of necessary simulations. To circumvent this problem, this work presents a method to derive the background from available observations. With this approach it is possible to sufficiently model the γ-like background in each run. In addition, the technical implementation of this procedure in GAMMALIB is summarised.

The likelihood framework in GAMMALIB is flexible enough to handle models which do not represent a source in the sky but describe the distribution of reconstructed events in the detector (`GModelData` class). A simplistic realisation of an analytical model describing the spatial γ-like background distribution in the camera is a symmetrical 2D Gaussian. The distribution of reconstructed energies can, for instance, be modelled by a power law. Such an approach does not account for a possible change in the spatial shape of the background with energy. Fig. 5.7, illustrates the event distribution of an observational run, where no VHE γ-ray source is present in the FoV. Therefore, it is assumed to detect γ-like background events, exclusively. The two panels on the left and in the middle show the spatial event distribution for two energy bands, adjoining at $600\,\mathrm{GeV}$. The left panel sky map is filled with lower energy events, which are far more numerous due to the steep energy spectrum of cosmic rays. The map shows the broad distribution, distributed symmetrically around image center. In contrast, the sky map in the middle depicts the fewer reconstructed high energy events. The distribution, looks slightly flatter across the FoV. Accordingly, the energy-dependence of the spatial distribution of γ-like events should be taken into account for the background modelling. All events of this run, regardless their reconstructed position are used to create the data in the right panel. This plot shows the energy dependence of the background rate. The functional relation of the data deviates quite significantly from a simple power law in energy.
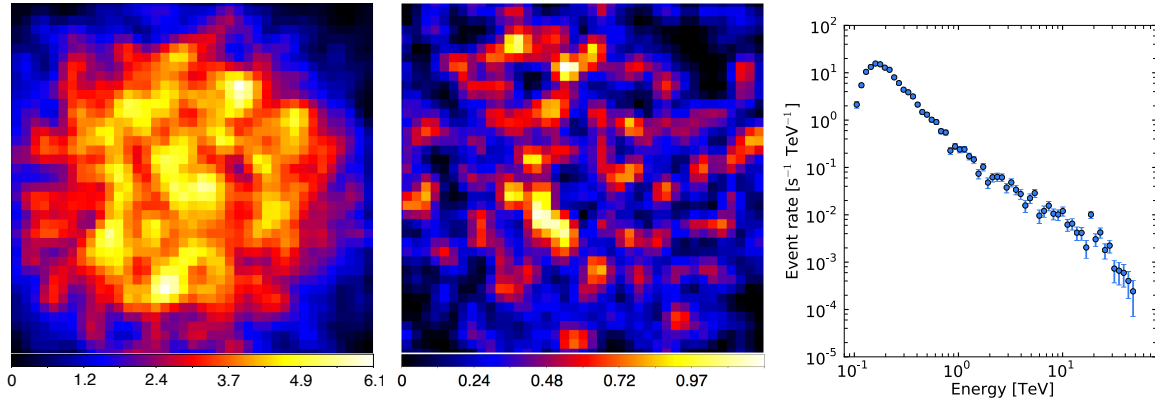
Figure 5.7.: Event distribution of an off-run (Run #21835). The two sky maps (left and middle) show a $4° × 4°$ region on the sky. Each bin has a width of $0°.1$. The sky map in the left panel is filled with events of which the reconstructed energies are below 600 GeV, while the middle panel shows only events above 600 GeV. Both maps are smoothed to illustrate the shape of the background distribution. Note that the colour scale therefore does not represent true count values. The right panel illustrates the rate of $γ$-like background as a function of reconstructed energy.

Building the Background Model

Similar to the IRFs, the $γ$-like background depends on many observational attributes. A full, multi-dimensional parametrisation of the background with an analytical function, taking into account all dependencies is not feasible. The same approach is used as for the IRF export, providing the $γ$-like background to GAMMALIB for each run individually. The function describing the run-specific background rate still depends on three variables: the coordinates x and y in the detector system and the reconstructed event energy E.

Runs where no VHE signal is present in the FoV are used to study the $γ$-like background, The events collected during such runs are thought to be fully dominated by $γ$-like background. These observations (off-runs) are used to study and derive the background. A run is defined as off-run, if every known source or insignificant hotspot is offset from the pointing position by at least $3°.0$. For extended sources, the respective twofold extension is added to this minimum distance. The selected sample of off-runs comprises 5157 runs or $∼ 2300$ h of empty-field observations. This allows for detailed background studies with many accumulated events.

Having selected all available off-runs, they are condensed into 28 groups (bins) with different observational attributes. The binning definition is oriented on the spacing of MC simulation of zenith and azimuth. The bin boundaries are given in Table 5.1. In this binning, the

Table 5.1.: Off-run binning definition.

Parameter	Bin edges													
Zenith	0	18	26	32	37	41	46	50	53	57	60	63	67	70	90
Azimuth			0					180					360		

Notes. All values are given in degrees. The azimuth values are increased by $180°$ to simplify the linear representation.
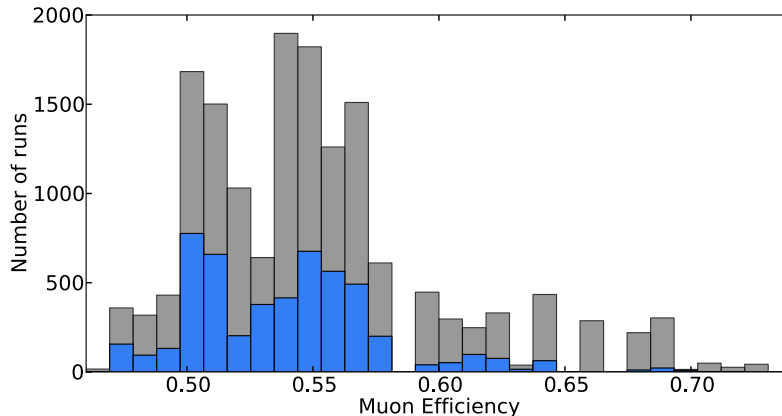
Figure 5.8.: Shown in grey are the abundance of muon efficiencies derived from all considered observational runs. In blue, the muon efficiencies for the selected off-runs are superimposed.

background neglects a possible dependency on the muon efficiency. The majority of muon efficiencies from all H. E. S. S. runs is rather constrained to a range of $0.5-0.6$ (Fig. 5.8), within which the shape of the background is assumed to stay constant. This range also corresponds to one set of MC simulations. Also shown in Fig. 5.8, the distribution of muon efficiencies from off-runs are well representative for the whole sample of observational runs. The off-run binning definition further ignores changes in the background, induced by a malfunctioning telescope. Roughly 20% of all considered runs were taken with three telescopes only. An additional subdivision of the off-runs by the number of telescopes was therefore tested. Apart from losing statistics in the individual bins, no significant change in the resulting background model can be found. The number of off-runs varies strongly between zenith angle bins. This can be attributed to the H. E. S. S. observing strategy, which generally prefers observations close to zenith at low energy thresholds. Table 5.2 shows the number of runs in each of the

Table 5.2.: Number of runs per observational bin

		Zenith bin													
		1	2	3	4	5	6	7	8	9	10	11	12	13	14
Azimuth bin	1	617	604	350	198	97	176	141	57	83	15	3	0	0	0
	2	1085	579	423	216	139	123	139	72	9	0	0	0	0	0

Notes. The bin numbers reflect the bin definition from Table 5.1. The zenith bin with number 1, e.g. corresponds to a range of $0° - 18°$ zenith angle. The entries represent the number of runs falling in the respective bin.

defined bins. Observation runs on VHE γ-ray sources with pointings where no corresponding off-run is available are skipped in the later source analysis. Since the distribution of off-run pointings are representative for all H. E. S. S. observations, the number of runs which cannot be used in the following is small. In total, only 104 runs from the exported sample have to be removed from analyses.

Each bin represents a specific range of observational attributes. From the binned off-runs, 28 independent models are created, which can be used to describe the γ-like background for each observational run with similar attributes, i.e. similar pointing in zenith and azimuth. All events from one specific off-run bin are filled into a 3D histogram, depending on (x, y, E). At this point, the energy threshold of each run (see Sect. 5.2.3) has to be taken into account.
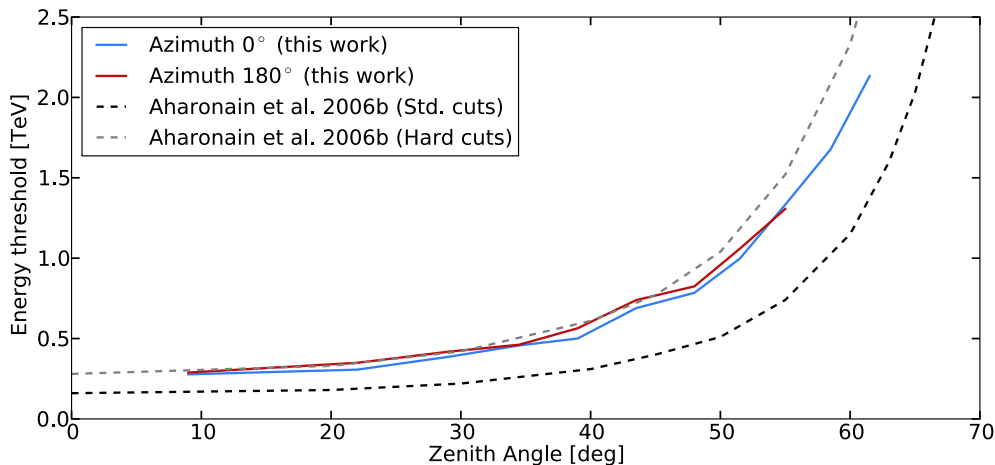
Figure 5.9.: Energy thresholds plotted against zenith angle. The blue and red lines denote the energy thresholds for two different azimuth bands. For comparison the energy thresholds given in Aharonian et al. (2006a) are shown as dashed black and grey lines.

A specific bin of off-runs exhibits many different energy thresholds, e.g. due to varying muon efficiencies. To avoid mixing of energy thresholds within an observational bin, the run with the highest energy threshold is conservatively chosen to dictate the minimum considered energy of an entire bin. Accordingly, the threshold for any other run in the respective bin is increased to that value. In this approach, the run-wise energy threshold based on the effective area, is further increased by the corresponding background model. The applied energy threshold is therefore only dependent on the run pointing position in the horizon system (zenith, azimuth). The dependence of this threshold with respect to the pointing is shown in Fig. 5.9. For higher zenith angles, the increasing atmospheric depth causes a loss in sensitivity to low energy air showers, resulting in a higher energy threshold. The influence of different azimuth pointings is much less than the zenith-angle dependence. For comparison, the energy thresholds presented in Aharonian et al. (2006a) are also shown. The choice of the definition of the energy threshold definition is very conservative. It is defined at 15% of the energy at the maximum effective area (see Sect. 5.2.3). Combined with applying the highest energy threshold of an observational off-run bin, this leads to rather high energy thresholds. Compared to previously published values, the energy threshold in this work resembles the hard cuts of Aharonian et al. (2006a).

Each of the 28 histograms, representing an observational bin, is binned adaptively according to the number of corresponding off-runs. An equal number of bins N_s in x and y ($N_s = N_x = N_y$) are used for the spatial binning. If the number of available off-runs exceeds 100, a fixed number spatial bins $N_s = 80$ and $N_E = 20$ energy bins (above the described threshold) are used. The binning is empirically coarsened according to the number of off-runs N_{off}. The applied relations, optimised for the available statistics are:

$$N_s = 80 - \begin{cases} 4 \cdot (10 - \lfloor N_{off}/10 \rfloor) & N_{off} < 100 \\ 0 & \text{else} \end{cases} \qquad (5.5)$$

$$N_{\mathrm{E}} \quad = \quad 20 - \begin{cases} 10 - \lfloor N_{\mathrm{off}}/10 \rfloor & N_{\mathrm{off}} < 100 \\ 0 & \text{else} \end{cases} \tag{5.6}$$

By reducing the number of bins for less off-runs, empty bins due to the lack of statistics are avoided. Bins without any event would indicate that no γ-like background is expected in the respective camera coordinate. To circumvent the problem of empty bins due to statistical fluctuations, the 3D histograms are smoothed while conserving the precedent integral over all bins. Translating the number of events per bin into a γ-like background rate which is independent of the binning definition, each bin content is divided by the accumulated observation time of the respective off-runs, by the spatial size of one bin and by the width of the respective energy bin. Accordingly, each bin represents an event rate in units of $\mathrm{s}^{-1}\,\mathrm{sr}^{-1}\,\mathrm{MeV}^{-1}$. The energy unit MeV is chosen to be consistent with the GAMMALIB internal convention.

The 3D histograms, stored in a ROOT format, are then exported to a 3D table using the FITS format. The eight empty histograms with no corresponding off-run (see Table 5.2) are dropped in the export. The presented approach describing the background from observational data results in 20 FITS files, requiring 8.1 MB disk space in total. These tables are used for the background modelling in GAMMALIB. Fig. 5.10 presents four snap shots of this background model, illustrating the variation of γ-like background across the FoV. The top two panels are representative for observations close to zenith. Depicting the energy dependence, the background model for this zenith band is shown for two energies, namely at 500 GeV (left) and 10 TeV (right). The shape of the spatial background distribution strongly varies with energy. While for lower energies the distribution looks similar to a Gaussian, the background at high energies has a central void, forming a ring-like structure. The latter shape can be attributed to an applied image selection cut (nominal distance cut, see de Naurois & Rolland 2009), which rejects high-energy showers images close to the camera center. The two lower panels show the model which is used to describe the background for zenith angles between $50° - 53°$. At such comparably high zenith angles, the reconstruction chain does not cause a central dip in the model for high energies (right). The spatial distribution, however, is much broader compared to model at lower energies.

The corresponding FITS file, containing the 3D background model is read into GAMMALIB for each run individually. The next Section summarises the technical implementation for the subsequent use of this background model in GAMMALIB.

Complex Background Modelling in GAMMALIB

To use a background model, which is not described by an analytical function, but a 3D map of intensities, the required functionality is implemented GAMMALIB. Each observational run has its own, individual background model. In contrast to a sky model, the background is given in instrument specific coordinates and must not be folded with the IRFs. A folding is not necessary since the model already represents the actual rate of events and should not describe a VHE γ-ray source in the sky. A background model is further strictly independent from other runs and should therefore only apply to the respective observation. To achieve such a requirement, the instrumental γ-like background model is treated like an additional IRF. Every run, loaded into memory, has its own model to describe the background, similar to the effective area and the PSF. Accordingly, it is important to keep track of the runs and the given corresponding models, which should be optimised. To load a H. E. S. S. run into GAMMALIB, the easiest way is to provide a file in an `xml` format, listing the corresponding
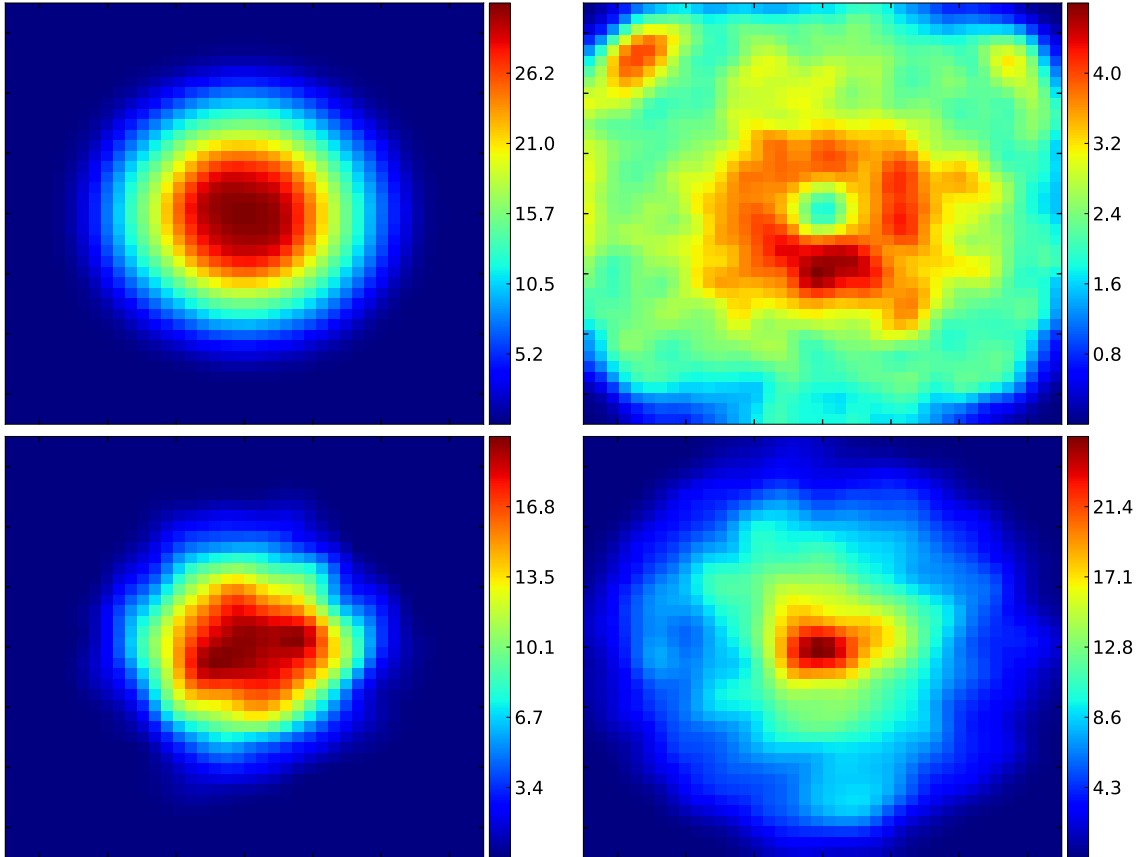
Figure 5.10.: Background models in detector coordinates for two different zenith angle bands (top panels: $[0°, 18°]$, bottom panels: $[50°, 53°]$). The azimuth is $0°$. The frame of each image corresponds to $8° \times 8°$ in the camera system which has its origin in the image center. The left panels show the respective background models for a reconstructed event energy of $500\,\text{GeV}$. The colour scales represent the background rate in units of $10^{-5}\,\text{s}^{-1}\,\text{sr}^{-1}\,\text{MeV}^{-1}$. In contrast, the right panels illustrate the background rate at a reconstructed energy of $10\,\text{TeV}$. Note that these colour maps are scaled by a factor of 100 compared to the scales for $500\,\text{GeV}$.

data and IRFs in FITS format. A unique run identifier should also be given. Such an `xml` file should look like the following:

```xml
<?xml version="1.0" encoding="UTF-8" standalone="no"?>
<observation_list title="observation list">
  <observation name="SourceOfInterest" id="21835" instrument="HESS">
    <parameter name="EventList" file="events_21835.fits" />
    <parameter name="EffectiveArea" file="Aeff_21835.fits" />
    <parameter name="PointSpreadFunction" file="psf_21835.fits" />
    <parameter name="EnergyDispersion" file="" />
    <parameter name="Background" file="bgd_21835.fits" />
  </observation>
</observation_list>
```

Note the given run identifier (id), "21835" in this case. GAMMALIB directly ties the loaded background information and the IRFs to this corresponding observation. In general, the analytical models are given in a separate file. This is completely analogous to the Fermi Science Tools, presented in Chap. 4. The file, listing all the required models is also given in the xml syntax. For the case of the presented background, a spectral model which scales the given 3D function is added:

```xml
<?xml version="1.0" encoding="UTF-8" standalone="no"?>
<source_library title="source library">
  <source name="Background" type="CTAInstBackground" instrument="HESS" id="21835">
    <spectrum type="ConstantValue">
      <parameter name="Value" value="1.0" scale="1" min="0.1" max="10" free="1"/>
    </spectrum>
</source_library>
```

In this definition, the model is connected to the provided background of the respective observation by assigning the same run identifier as above. The given model simply scales the background rate by a constant factor. Certainly, the energy dependence of the background model can be adjusted by more complex spectral models providing more flexibility. This is done in *Fermi*-LAT analyses where the Galactic diffuse model is scaled by a spectral power law. Fitting the normalising parameter, it is possible account for statistical and in particular systematic run-by-run variations in the background. Accordingly, the background model can be individually adjusted for each run. If the data can be well described by the given model, the normalisation parameter is expected to be around unity.

The background model is represented in GAMMALIB via the class `GCTABackground3D`. Evaluating this model for a specific event in the unbinned likelihood optimisation procedure, a 3D interpolation is induced. This interpolation is performed to derive the exact likelihood of the event with respect to the background model. To account for strong gradients in energy, an interpolate along the decadic logarithm of the event energy is performed. At the same time, a linear interpolation between the neighbouring spatial bins is conducted. Therefore, this class provides a continuous 3D function of the γ-like background rate.

The likelihood fit in GAMMALIB is implemented by means of the Levenberg-Marquardt algorithm (Levenberg 1944; Marquardt 1963). This algorithm uses the functional gradients to find the best-fitting parameters. For many models, the parameter gradients can be determined analytically, which significantly speeds up the computation. For the presented case of the background, where only a constant prefactor is fit, the gradient is also easily determined analytically. The framework, however, is flexible enough to also numerically derive the parameter gradients.

This Section presented a model to describe the shape of the irreducible γ-like background in each run. Having created and explained the necessary infrastructure to support this kind of background description in GAMMALIB, this work focuses on the verification of the presented model.

Background Model Verification

Each observational H. E. S. S. run can be assigned to a corresponding background model. Since no interfering VHE γ-ray source is present, the individual off-runs themselves are well suited to probe this background model. Therefore, the presented model is investigated whether it depicts an adequate description for every observation in the off-run sample. In particular, it has to be ensured that no artificial VHE γ-ray source is introduced due to an
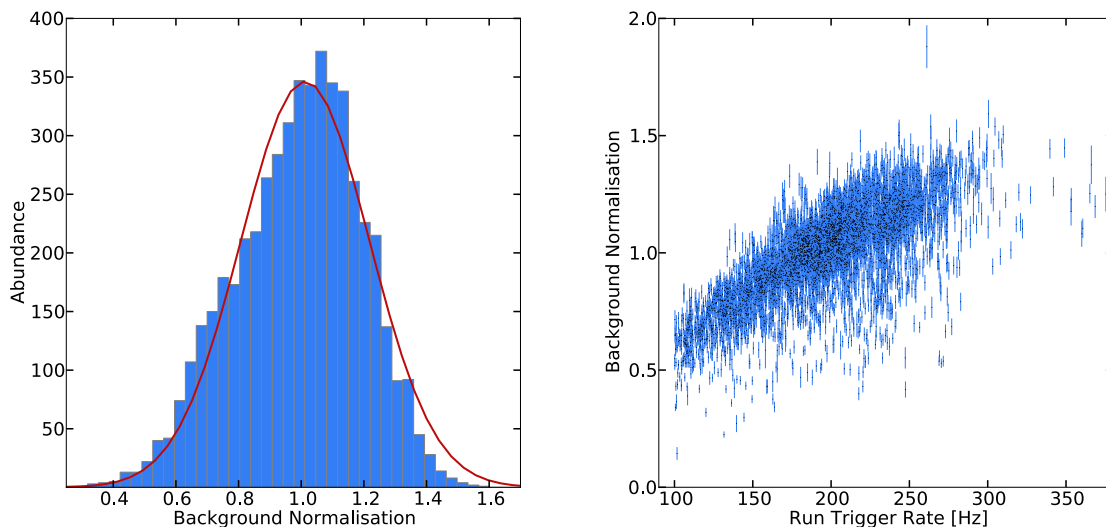
Figure 5.11.: *Left*: The distribution of the fitted scaling parameter of off-runs. The red line denotes a fit with a Gaussian function. *Right*: Background normalisation plotted versus the corresponding trigger rate of the run. The sudden cut at 100 Hz originates from the applied run selection.

insufficient background description. For this testing purpose, the likelihood framework of GAMMALIB is used. Each off-run is analysed separately using `ctlike`, which works almost analogously to `gtlike` from the Fermi Science Tools. For the likelihood optimisation of each off-run, a constant function is provided as spectral model (see above example), leading to one free parameter per run. This parameter allows for an absolute scaling of the model predicted rate of γ-like background. To be conform with the nominal H. E. S. S. FoV of 5°, the fit is constrained to events, which are reconstructed within a radius of 2°.5 around the pointing position. This criterion is also applied to all analyses presented later in this work. Optimising the normalising parameter in the unbinned likelihood framework takes less than one second on an current notebook[9] for an average run containing $1500 - 3000$ events.

From the performed optimisation, the best-fitting parameter for each background normalisation are obtained. The distribution of this parameter is shown in Fig. 5.11 (left). The mean of the fitted values is, by construction, close to unity ($\mu = 0.99$), while the distribution has an rms of $\sigma = 0.20$. Fitting a Gaussian curve to the distribution (red line) results in compatible parameters ($\mu_{\mathrm{gauss}} = 1.01 \pm 0.01$, $\sigma_{\mathrm{gauss}} = 0.21 \pm 0.01$). The Gaussian, however, is not a good description of the histogram, indicating that the scatter is not purely statistical. In conclusion, the mean background rate varies by $\sim 20\%$ on run-by-run basis. To reduce the number of free parameters in an analysis, one could try to predict the background rate for each run. Therefore, it is investigated whether the background normalisation is correlated to one or more observational parameters. In general, no clear correlation can be manifested (see Appendix A.2). A significant trend, however, can be seen in the trigger rate (right panel of Fig. 5.11). This trend is expected since a higher trigger rate leads to more events, which, in turn requires a higher background normalisation to explain the data. The relation of the

---

[9]MacBook Air, 1.8 GHz Intel Core i5, 8 GB 1600 MHz DDR3

trigger rate to background normalisation is almost linear. The scatter around this trend, however, is very large and not purely statistical. The main reason for this lies most certainly in the variation of the opacity of the atmosphere. Such variations might partly be reflected in the trigger rate, which, however, is influenced by many more variables, like the night sky brightness of the observed region. Predicting the background level to reduce the number free parameters in the fit would therefore introduce large systematic errors on individual runs. Consequently, the scaling parameter of the γ-like background is left free. The analyses presented later in this work make therefore use of the possibility to fit the background level for each run in GAMMALIB. This is not feasible with the traditional background modelling using the reflected regions method.

The likelihood optimisation does not provide a direct measure for the goodness of fit. To probe the fit quality of the background model a TS map is created for each off-run. The TS value is generally derived by a likelihood ratio test comparing the likelihood of two nested hypotheses. The log-likelihood of the null hypothesis, $\log \mathcal{L}_0$, is the fit of the background model alone. As alternative hypothesis, the log-likelihood $\log \mathcal{L}_1$ is computed by a fit of the background model with a VHE γ-ray point source at a certain position. The TS value at this position in the sky is then determined as

$$\mathrm{TS} = 2 \cdot (\log \mathcal{L}_1 - \log \mathcal{L}_0). \tag{5.7}$$

The putative point source requires an additional free parameter to the fit, namely the prefactor of its power law spectral model. For reasons of the fit stability, the spectral index of the hypothetical source is fixed to -2.5, which resembles an average in the VHE γ-ray regime. To calculate the complete TS map, the fit of the alternative hypothesis is repeated on a grid of positions in the sky. The resulting TS map is filled according to the position of the putative point source. To generally calculate TS maps later in this thesis, the tool `cttsmap` is created. This tool is flexible to calculate TS maps for various purposes. In general, the TS value represents the statistical significance of a VHE γ-ray source. In case the null hypothesis is valid, the distribution of TS values follows a χ^2-distribution for N degrees of freedom (Wilks' theorem, Wilks 1938). The number of degrees of freedom N is defined by the difference in free parameters between the null and alternative hypothesis. In the present case of one additional parameter, describing the spectral prefactor of the VHE γ-ray source, $N = 1$. The TS maps are generated for a region in the sky of $3°\!.5 \times 3°\!.5$ subdivided into bins of $0°\!.1$ length. The size of the map is the maximum which is fully contained in the $2°\!.5$ selection radius. To be sensitive to possible point sources, the bin size was chosen to coarsely reflect the angular width of the H. E. S. S. PSF. An example TS map is shown in the left panel of Fig. 5.12. The map corresponds to run 21835 which was already presented in Fig. 5.7. The colour scale of the map represents the TS value in each bin. The distribution of the TS values is shown in the right panel. Note that for less than 1% of the bins, GAMMALIB indicates a badly converged fit. The corresponding TS values, which are numerically compatible with zero, are not considered in the distribution. On top, the corresponding χ^2-distribution for one degree of freedom is overlaid. The TS distribution matches the function quite well.

To generally test the background models for the analysed off-runs, the distributions from the derived TS maps are accumulated. The resulting combined distribution is shown in Fig. 5.13. The expected χ^2-distribution matches the TS distribution well. The highest TS value of TS ≈ 27 results from a single bin. Taking into account the number of trials, the probability of one bin statistically fluctuating to that value is $\approx 72\%$. Therefore the distribution is completely compatible with statistical noise around the null hypothesis. In addition
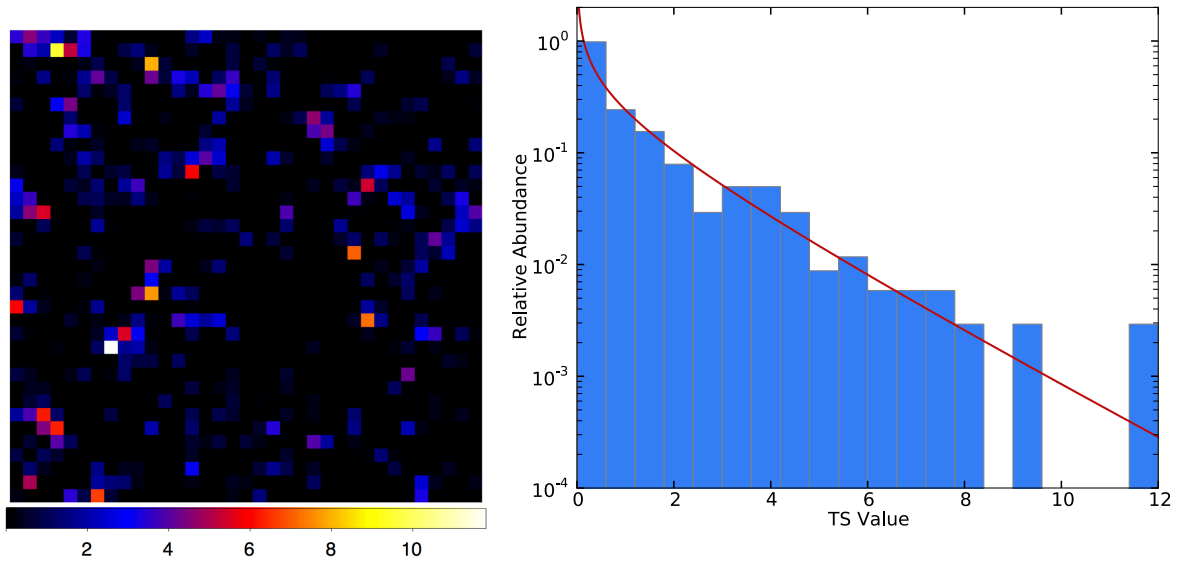
Figure 5.12.: Exemplary TS of an off-run (# 21835). The left panel presents the derived TS values, spatially distributed in the sky. The map is centred on the telescope pointing position. On the right panel, the distribution of TS values is shown. The red curve represents the expected χ^2-distribution.
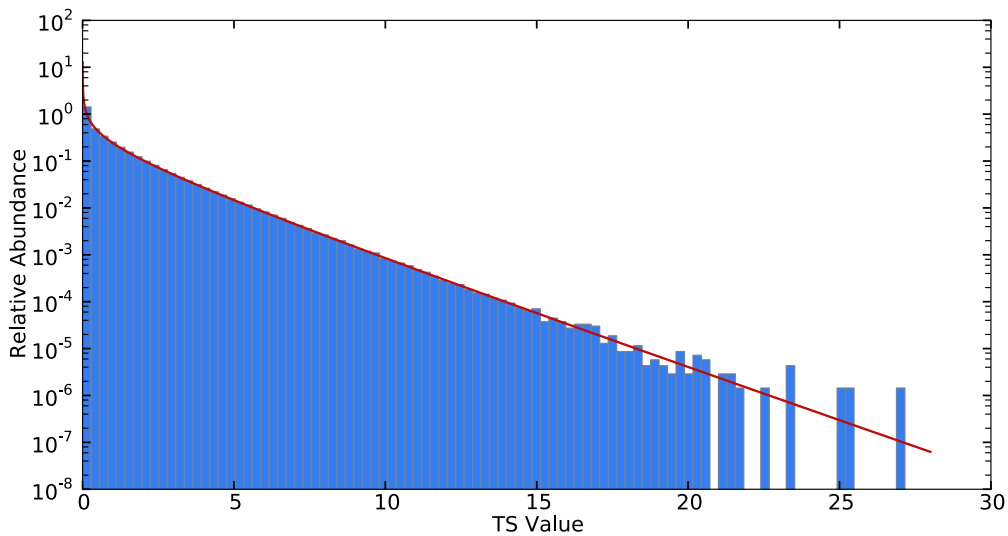

Figure 5.13.: TS distribution of all off-runs. The histogram is normalised to be compared to the expected χ^2-distribution (red solid line).

influences from the observational binning of the background model are studied, i.e. the TS distribution in each individual observational bin is inspected. There is no unexpected TS value showing up in either of the distributions (see Appendix A.3). Accordingly, the presented background model seems to be a sufficient description for each off-run. Transferring these findings to all observational runs, the background model at hand, can describe the

γ-like background in each run.

5.3. Analysis Examples

Having derived a functioning background model to describe the γ-like event distribution in each run, it is possible to start analysing VHE γ-ray sources. In this Section, examples indicating the powerful capabilities of the likelihood framework in GAMMALIB are presented. To conduct individual analysis steps, the following tools are used:

- **ctselect**: This tool is able to select events from the given dataset according to the required cuts. In the H. E. S. S. analyses presented in this work, it is applied to drop events which are reconstructed outside of the analysis range.

- **ctlike**: The main tool of the CTOOLS performing the likelihood optimisation of a given model, using the provided data.

- **ctbin**: Bins events into a sky map. To visualise an event list, this tool is flexible to apply a user-defined spatial and energy binning.

- **ctmodel**: Creates a sky map according to a given model and observation condition. Each bin of the sky map is filled by the number of expected events. The output of this tool can hence be compared to the sky map derived by **ctbin**.

The results, derived with **ctlike** are compared to analyses conducted with the H. E. S. S. software. To establish GAMMALIB as high-level analysis framework for the future CTA observatory, the results should exhibit compatibility with the current analysis approaches. The canonical way to test an analysis framework is to start with simple analyses and proceed to more challenging cases if the results are satisfying.

5.3.1. The Crab Nebula - an Isolated Point Source

The broadly discussed Crab Nebula is the strongest source in the VHE γ-ray sky, which makes it a good candidate for an initial test of the GAMMALIB likelihood framework. Due to its brightness, the source further provides the possibility to investigate systematic effects.

Run Selection and Model Generation

Every source analysis in GAMMALIB requires a model describing the emission in the RoI. Around the Crab Nebula, no region of VHE γ-ray emission is known. Therefore, the Crab Nebula is the only source in the RoI. Spatially, this source is modelled as a point-like, leaving the parameters of the source position free in the fit. As spectral part of the model, a log-parabola model (Eq. 4.7) is employed, which was implement into GAMMALIB to describe the curved IC spectra of PWNe. For the analysis, all runs pointing within 2.5 from the nominal position of the Crab Nebula are selected. Accordingly, the source of interest is required to be in the defined run-FoV of 2.5 radius. The selection results in 207 runs which can be accumulated in the analysis. For each run, the respective background model is used and assigned with the corresponding run number. As spectral model for the background in each run, a scaling function with one, normalising parameter is applied. The energy range resulting from the described cuts and threshold definitions is $[0.69, 64.5]$ TeV. The comparably high energy threshold is usual for analyses of the Crab Nebula with H. E. S. S.: due to the telescope
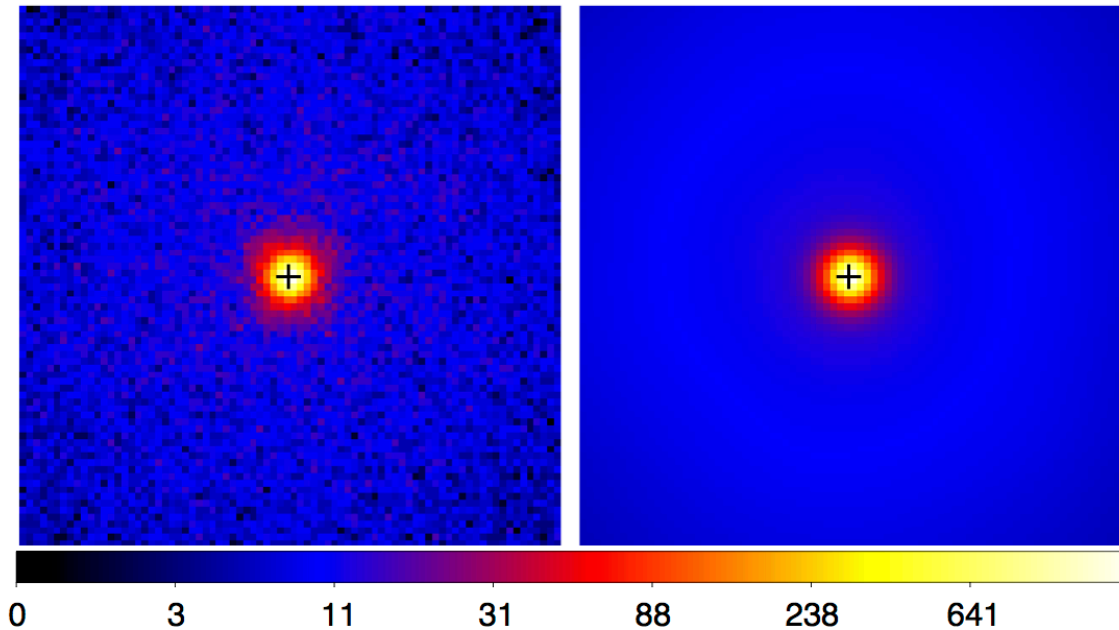
Figure 5.14.: *Left*: Count map of VHE γ-ray candidates filled from 207 runs. *Right*: Corresponding model map, representing the number of counts predicted by the best-fit model. Both maps show a $2° \times 2°$ region around the Crab Nebula position, which is marked by a black cross. To accommodate the strong source, the colour scale, depicting the number of VHE γ-ray candidates per bin, is logarithmically stretched.

location in Namibia the source culminates at a zenith angle of roughly 45°. According to Fig. 5.9, observations at such high zenith angles imply a high energy threshold.

Analysis with GAMMALIB

The data is analysed using unbinned `ctlike`. The resulting fit parameters are listed in Table 5.3. To search for possible spatial structures which are badly modelled, different types

Table 5.3.: Analysis of the Crab Nebula with `ctlike` and the H. E. S. S. software.

Analysis type	Φ	α	β	RA	DEC	TS
`ctlike`	4.57 ± 0.04	2.45 ± 0.02	0.14 ± 0.01	83.6295 ± 0.0003	22.0125 ± 0.0003	133259
`corr. ctlike`	4.28 ± 0.04	2.46 ± 0.02	0.14 ± 0.01	83.6297 ± 0.0003	22.0126 ± 0.0003	132989
H. E. S. S.	4.24 ± 0.04	2.53 ± 0.02	0.11 ± 0.01	83.6292 ± 0.0002	22.0123 ± 0.0002	$\sigma = 226$

Notes. The second row depicts the analysis results, derived with the corrected PSF (see text). Since the H. E. S. S. software uses a different approach, no TS value can be computed. Instead, the statistical significance of the Crab Nebula, derived with the described analysis, is listed.

of maps are created. As a first check, analogous to *Fermi*-LAT analyses, residual maps are computed. For this purpose, the existing tools `ctbin` and `ctmodel` are improved to support the map creation for the superposition of several runs. The resulting sky maps of the Crab Nebula region are presented in Fig. 5.14. The count map (left) and the model map (right) look quite similar, indicating that the fit converged successfully. To compare
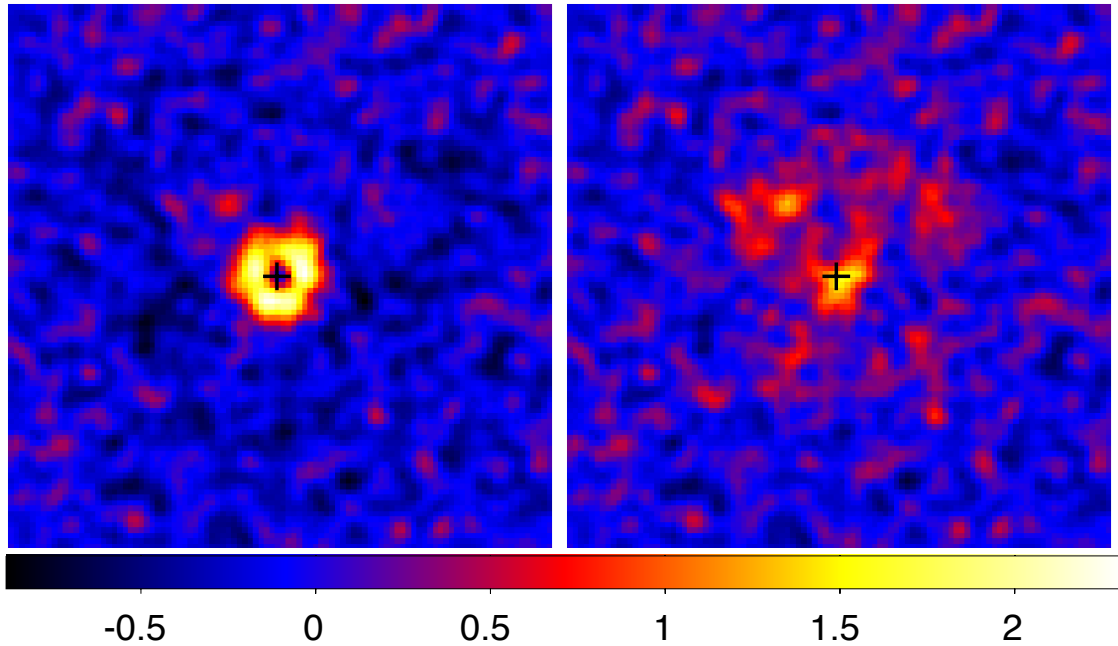
Figure 5.15.: *Left*: Residual significance map of the Crab Nebula, derived from the initial analysis in GAMMALIB. The PSF from MC simulations causes a ring-shaped structure. *Right*: Residual significance map of the same data, analysed with the empirically adjusted PSF (see text). The amplitude of the residuals is less compared to the left panel. The black cross indicates the nominal Crab Nebula position in both maps, which represent a $2° \times 2°$ region in the sky. Each map is smoothed with a Gaussian kernel of $0°06$ to visualise structures in the maps. Accordingly, the colour scale does not depict absolute significances.

the detected to modelled counts, a residual significance map is computed following (Eq. 4.8.) Note that this map is derived with a newly created tool `ctrescounts`. This tool takes into account run-wise differing energy thresholds and exposure variations. The resulting residual map is shown in (Fig. 5.15, left). There is a clear, ring-shaped structure around the source position. This feature can be explained by systematic errors in the H. E. S. S. PSF. Recent internal investigations revealed that the PSF derived from MC simulations is systematically too small. This problem is confirmed by the study of binary systems or active galactic nuclei (AGN), which are considered true point sources. Intense investigations are ongoing, which are not part of this thesis. To take into account this mismatch, the MC PSF is artificially increased. The parameters of the fitted King profile were adjusted by the following relations:

$$\gamma_{\text{new}} = \gamma_{\text{MC}} + \delta\gamma_{\text{corr}} \tag{5.8}$$

$$\sigma_{\text{new}} = \sqrt{\sigma_{\text{MC}}^2 + (\delta\sigma_{\text{corr}})^2}, \tag{5.9}$$

where γ_{MC} and σ_{MC} depict the originally derived values. To induce a residual map of the Crab Nebula with as few significant leftover structures as possible, the corrections $\delta\gamma_{\text{corr}} = 0.66$ and $\delta\sigma_{\text{corr}} = 0°018$ are empirically inferred for this work. The analysis of the Crab Nebula is repeated with the corrected PSF. The fit results are also listed in Table 5.3. The newly

created residual count map is presented in the right panel of Fig. 5.15. The residuals at the Crab position disappeared to a large extend. There are, however, still some remaining residuals in the image center. Most certainly, the global addition of correction terms might be a too simplistic approach for the complex PSF with all its dependencies. Since such residuals are only significant for the very bright sources like the Crab Nebula, this work continues using that approach. Since a small detectable extension of the Crab Nebula cannot be excluded, the inferred PSF correction was also checked for the AGN PKS 2155−304. The residual maps of this point-like source give consistent results.

The applied PSF correction is important to measure the proper extensions of PWNe, later in this thesis. Since GAMMALIB combines spectral and morphological analysis, the correct extension in turn is necessary to derive the spectra of interest.

To probe the results, derived with GAMMALIB/CTOOLS, a standard H. E. S. S. analysis is performed, using the same runs and the same energy threshold as above. Standard analysis in this case means that the reflected region method is employed to estimate the background. The usual definition of an on-region for a point source requires a sufficient understanding of the PSF to estimate the leakage out of that region. Since the PSF seems to be inconsistent with data, a larger on-region with radius $\theta = 0°\!.3$ is used to collect most of the photons from the source. At the same time, the leakage of the PSF out of this region is neglected, assuming the source is fully contained in this region. With this approach, the analysis philosophies between GAMMALIB and H. E. S. S. standard seem more compatible, since GAMMALIB also models the entire source emission. The drawback of increasing the on-region is a reduced significance of the source itself, due to a higher background level influencing the excess (Eq. 5.2). The slightly decreasing statistical significance, however, is not a problem for the analysis of the bright Crab Nebula. Table 5.3 lists the result of a spectral analysis applying the same spectral model as with `ctlike`. The derived parameters are statistically not perfectly compatible. Due to the different analysis approaches of the two frameworks, a perfect agreement is, however, not expected. By using a more realistic PSF in GAMMALIB, the flux normalisations Φ are nevertheless comparable. The different spectral index and consequently the slightly deviating curvature, can probably be attributed to not considered energy resolution in `ctlike`. Another reason might be that there could be still some minor leakage out of the $\theta = 0°\!.3$ region in the H. E. S. S. analysis. The relative deviation in the spectral index is of the order of 3%, which is well below the estimated systematic uncertainty for general H. E. S. S. analysis (Aharonian et al. 2006a). Therefore, the presented cross-checks are considered compatible.

As spectral and morphology analyses are strictly separated in H. E. S. S., the Crab Nebula position is derived by an additional step. Assuming a spectral index of 2.7, which was derived from a simple power law fit, the PSF from spectral MC simulations is used to fit the center of gravity of emission using the derived sky map. The results are also listed in Table 5.3. Despite a slight numerical deviation, the derived positions are satisfyingly compatible for the purpose of the analyses presented in this work.

Spectral Energy Distribution

The likelihood analysis philosophy of modelling the entire RoI in GAMMALIB resembles the one of *Fermi*-LAT analyses. For the computation of spectral points and a subsequent SED, the same approach as described in Sect. 4.2.1 is applied. Creating a tool which computes spectral data points is part of this thesis. The way it was implemented, the user has flexibility to provide an arbitrary energy binning for the points calculation. Since the Crab Nebula is significant with TS $> 10^5$, 40 spectral points are calculated in energy bins which are equally
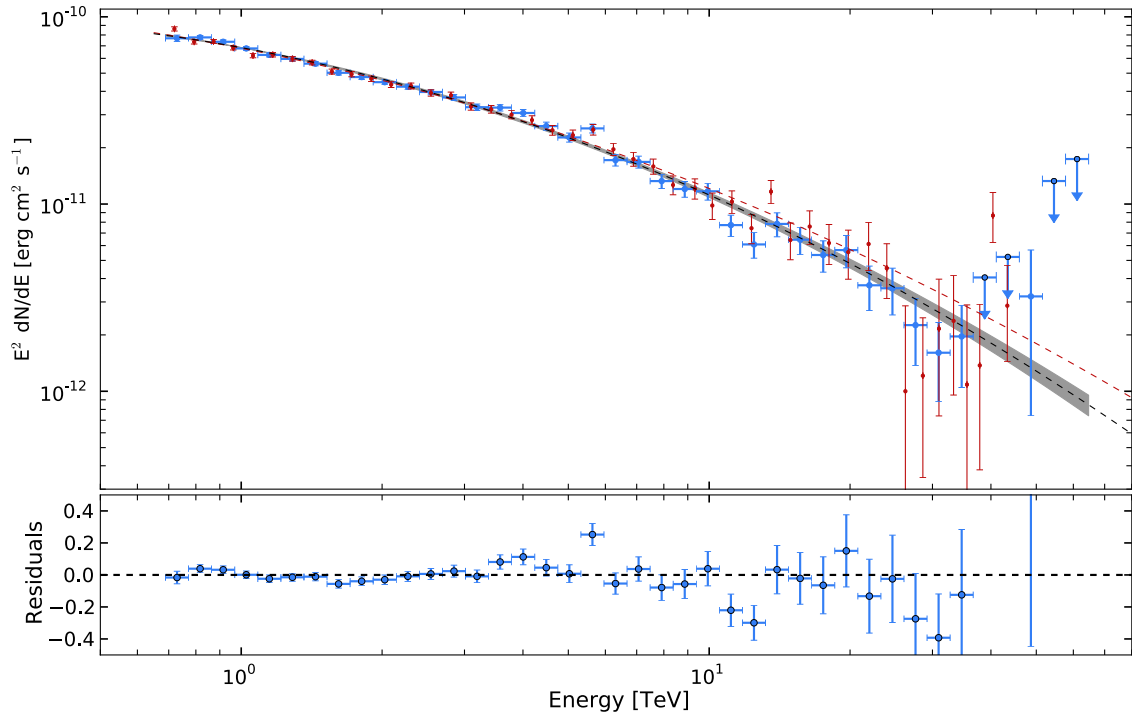
Figure 5.16.: SED of the Crab Nebula, derived with GAMMALIB and the H. E. S. S. software. The blue points denote the spectral points derived in the likelihood framework of GAMMALIB. The black-dashed line represents the corresponding best-fit model. The grey-shaded area depicts the corresponding 68% confidence region. The red-dashed line shows the best-fit model, derived with the H. E. S. S. software. The lower panel depicts the residuals from the data point with respect to the best-fit model.

spaced on a logarithmic scale. In each bin, the prefactor of the Crab Nebula spectrum is fitted using `ctlike`, leaving all other background parameters fixed to their optimised values. If the Crab Nebula cannot be detected in one bin with TS > 4, an upper limit (95% confidence) is calculated instead. Since the upper limit calculation is not available in GAMMALIB, another tool to compute the limit value is created. In this tool, the likelihood function is inspected for the limit estimation.

The approach to calculate spectral points in the H. E. S. S. analysis software is different. Usually, a minimum significance of 3σ is required to form a spectral point. The energy range of the spectral bin is increased until this condition is met. Therefore, the data points, derived by a forward-folding technique, are spaced unevenly. To compare these two analysis frameworks, the derived flux points are shown together in one SED. In Fig. 5.16, the resulting spectra from GAMMALIB (blue) and the H. E. S. S. software (red) are presented. The grey-shaded band shows the 68% confidence region of the spectral fit in GAMMALIB. This band is derived by Gaussian error propagation, taking into account the covariance matrix of the fit. Most spectral points agree quite well between the frameworks. Above $\sim 20\,\text{TeV}$, the derived spectral models (dashed lines) slightly deviate from each other. The reason for this might be, among others, the not considered energy resolution in GAMMALIB.

Run-by-Run Measurements and Systematic Estimates

Since the Crab Nebula is the brightest source in the VHE γ-ray sky, this object is used to estimate systematic uncertainties of the analysis. In the following, it is assumed that the Crab Nebula, intrinsically, has a timely constant flux in the considered VHE regime and that the detection of variability of the synchrotron component (Chap. 4) does not affect the IC component. Several approaches to model the flaring synchrotron emission of the Crab predict IC variability far above 100 TeV. In addition, the predicted amplitude is well below any detection threshold of current IACTs. Therefore, using the Crab as a calibration source with constant flux is justified.

To investigate possible systematic uncertainties, the Crab Nebula is analysed on a run-by-run basis. In each run, the Crab Nebula is modelled by a spectral power law. Obtaining a direct measurement of the photon flux of the Crab Nebula, a power law, taking the integrated flux as normalising parameter (see Eq. 4.6), is applied. The flux value is calculated in the energy range $[1, 100]$ TeV. The position of the point source is fixed to the best-fit values (Table 5.3). Accordingly, for each of the 207 selected runs, `ctlike` optimises three free parameters, namely the photon flux and spectral index of the power law model and the scaling factor of the background model. Deriving the mean parameters, the same model is fit to the whole dataset. The resulting mean flux is determined to be $(2.57\pm0.02)\cdot10^{-11}\,\mathrm{cm}^{-2}\,\mathrm{s}^{-1}$, while the spectral index is $-(2.73 \pm 0.01)$. To quantify the systematic uncertainty of the derived spectral parameters of the Crab, pull distributions of the run-by-run measured parameters are created. In general, the entries g_i of a pull distribution for each run i are determined by

$$g_i = \frac{x_i - \bar{x}}{\sigma_i},\tag{5.10}$$

where x_i and σ_i are the derived parameter and its uncertainty for each run, respectively. The mean value $\bar{x}$ is the above-derived result from the analysis of the complete dataset. In case the flux variations are purely statistical, the pull distribution is expected to follow a normal distribution with a mean of $\mu = 0$ and a rms of $\sigma = 1$. Fig. 5.17 shows the pull distributions of the photon fluxes and spectral indices. Both distributions are fitted with a Gaussian function. The characterising parameters of the fits (μ, σ) are indicated in the upper area of the panels. The spectral index distribution (right) is compatible with a Gaussian, which is why no systematic uncertainties on a run-by-run basis can be found. Therefore, the scatter seems to be purely statistical. In contrast, the pull distribution of the derived fluxes (left panel) strongly deviates from a normal distribution. Especially the long tail towards lower fluxes implies a large systematic uncertainty in the reconstructed flux. To obtain a rough estimate of the flux systematics, the parameters of the fitted Gaussian are compared to the expected normal distribution. Assuming the fitted pull distribution (σ_fit) represents the statistical plus an additional systematic uncertainty, an approximated systematic error σ_sys can be inferred as

$$\sigma_\mathrm{sys} = \sqrt{\sigma_\mathrm{fit}^2 - \sigma_\mathrm{stat}^2}.\tag{5.11}$$

The expected broadness of only statistical fluctuations is $\sigma_\mathrm{stat} = 1$. Therefore, evaluating Eq. 5.11 leads to $\sigma_\mathrm{sys} = 1.5$. This value implies that the systematic uncertainty is larger by a factor of 1.5 compared to the statistical errors. The mean statistical error of each run is of the order of 12%, indicating a systematic uncertainty of roughly 18% on the derived fluxes. This value is quite compatible with the run-by-run uncertainty of 15%, which is given in Aharonian et al. (2006a). The pull distribution of fluxes is rather asymmetric implying the
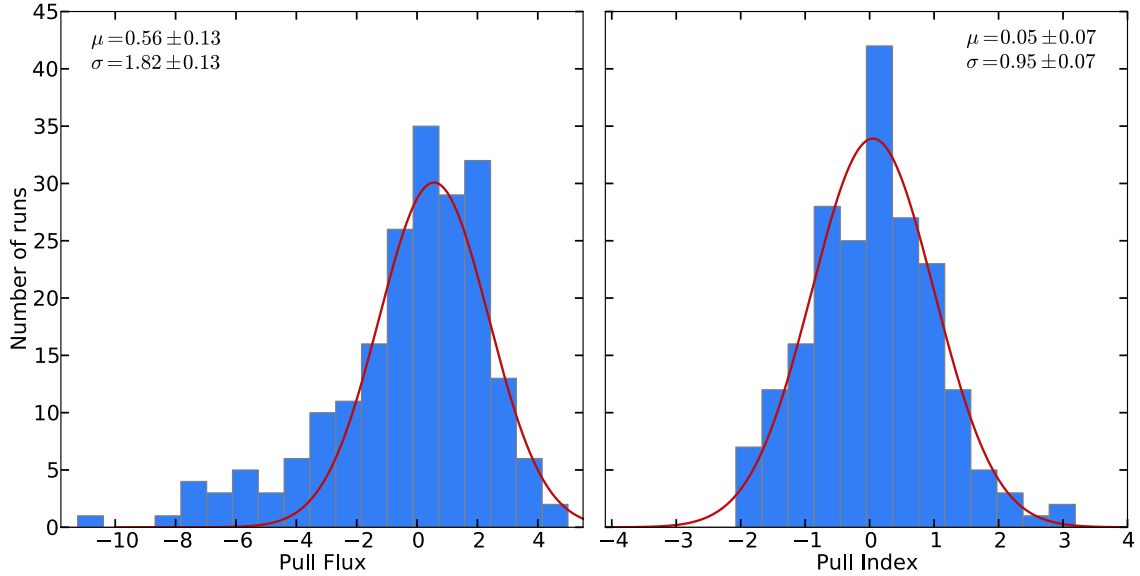
Figure 5.17.: Pull distributions of run-by-run measurements. The left panel shows the pull distribution of the fitted photon fluxes, while the right panel presents the same distribution of the measured spectral index. The red lines denote the best-fit Gaussian functions.

systematic uncertainties to be asymmetric.

The derived systematic error is similar to the 20% variation of the background, derived in Sect. 5.2.4. The background rate is probably subject to the varying opacity of the atmosphere. These variations should also affect the number of reconstructed VHE γ rays. As presented in the right panel of Fig. 5.11, the trigger rate, reflecting the transparency of the atmosphere, affects the rate of reconstructed γ-like events. Therefore, the rate of VHE γ rays, representing the flux of the Crab in this case, can also suffer from bad observation conditions. To illustrate this relation, the photon flux of the Crab Nebula is plotted against the background normalisation (see Fig. 5.18). The left panel presents run-by-run measurements. Assuming the background level to be rather constant during one observational night, the night-by-night measurements are shown in the right panel. For this purpose, all runs from a specific night are condensed to analyse the Crab Nebula flux. The shown background normalisation represents the mean fit value of the night-wise accumulated runs. The fitted background normalisation reflects the atmospheric conditions. A clear trend can be recognised: a high background rate, representing a transparent atmosphere also implies a higher reconstructed flux of the Crab Nebula. In contrast, if the background level is rather low, the Crab Nebula is also dimmer since e.g. a dusty atmosphere prevents the detection of all VHE γ rays. Due to smaller statistical uncertainties, this effect is enhanced in the panel showing the night-by-night fluxes. Therefore, the major cause of the systematic flux uncertainties can be identified. This problem may limit the measurement of all IACTs. By analysing H. E. S. S. data in the GAMMALIB framework using the presented approach, the origin of the flux systematic can be accessed directly. The fitted background normalisation might be a measure of the transparency of the atmosphere. Therefore, the analysis in GAMMALIB offers the potential to correct the derived fluxes depending on the fitted background normalisation.
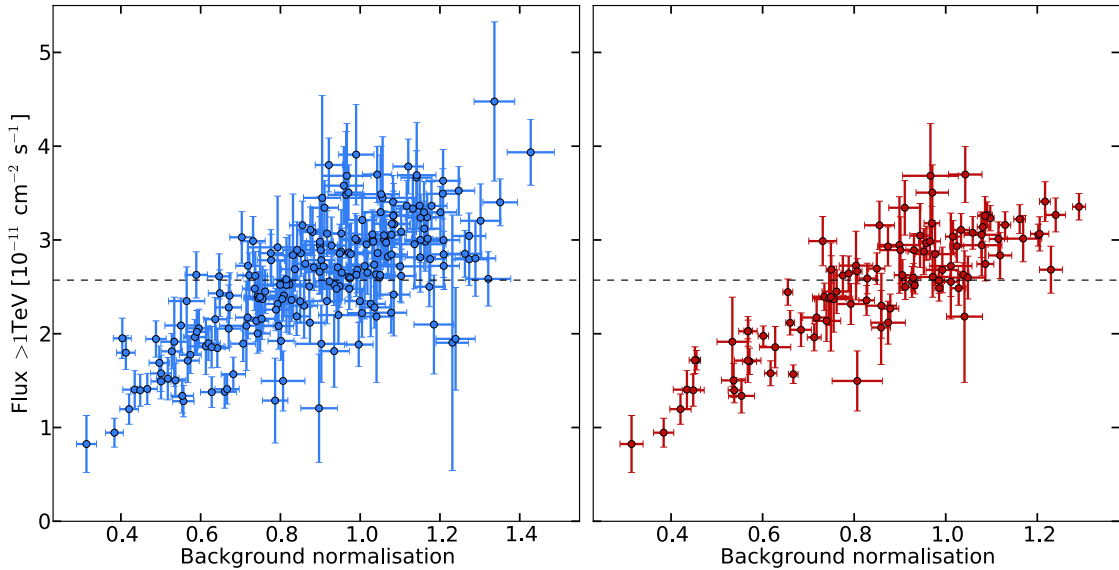
Figure 5.18.: *Left*: Run-by-run measured Crab Nebula flux, plotted versus the corresponding run background normalisation. *Right*: Night-by-night flux measurement of the Crab Nebula, shown against the mean background level in the corresponding night. The black-dashed line in both panels represents the average flux value, derived from all available runs.

One possibility to amend the fitted fluxes would be to scale the effective area depending on the background level. This approach is currently under investigation and development and is hence not used for the following analyses in this thesis. Further sources of systematic uncertainties, like applied cuts, reconstruction technique, or broken pixels in the camera are not studied in this thesis.

The analysis of the Crab Nebula with GAMMALIB and CTOOLS shows the limit and potential of this likelihood framework. The derived results sensitively depend on the proper knowledge of the IRFs. Accordingly, the PSF was adjusted by an empirical relation to obtain more consistent results. Apart from that, the presented approach provides the possibility to directly access flux systematics, which can be corrected for in the future. Since the RoI of the Crab Nebula is a rather quiet region in the sky, the following Section demonstrates the capability of GAMMALIB to analyse more complex regions.

5.3.2. N 157B - Overlapping Sources

The H. E. S. S. spectrum of N 157B presented in Sect. 3.1 is derived with the conventional approach using the H. E. S. S. software. Benefiting from the deep exposure on the LMC region, the corresponding analysis reveals an additional weak point source, very close to N 157B. This source is positionally coincident with the largest known X-ray emitting shell, the superbubble 30 Doradus C (30 DorC, Bamba et al. 2004). The physical interpretation of the detection of VHE γ rays from this object is not part of this work. Since the angular distance between 30 DorC and N 157B is rather small ($\approx 0°15$), the PSF tails of these point sources are overlapping. Especially, the weak source 30 DorC is strongly contaminated by spill-over events

from N 157B. The spectral analysis of these two overlapping sources is quite challenging when applying the conventional reflected region method in the H. E. S. S. analysis framework. The contribution of flux from N 157B in the on-region of 30 Dor C has to be estimated to derive a correct spectrum (and vice versa). For 30 DorC, this is achieved by placing putative on-regions around N 157B, which are at the same angular distance as 30 DorC. Consequently, the spill-over flux can be estimated by averaging the emission measured in the test regions. The derived flux is then subtracted in the spectral analysis. The separation of two overlapping sources to derive their energy spectra is a non-standard procedure and therefore requires quite manual effort. More details on this analysis are given in the upcoming publication (H.E.S.S. Collaboration, in prep.).

RoI Model

To probe the capabilities of GAMMALIB handling such a scenario, a corresponding analysis of the LMC region is conducted. Creating the required RoI source model, 30 DorC and N 157B are added. Both point-like sources are modelled by a power law in energy with the two free parameters Φ and Γ

$$\frac{\mathrm{d}N}{\mathrm{d}E} = \Phi \left(\frac{E}{1\,\mathrm{TeV}} \right)^{-\Gamma} . \tag{5.12}$$

To determine the centre of gravity of the respective emission, the position are left free in the likelihood optimisation, too. The likelihood framework naturally takes into account the PSF tails and resulting event spill-over between the sources. Accordingly, no flux correction has to be applied. Note that the adjusted PSF (Sect. 5.3.1) is used, implying smaller residuals for point-like sources.

Complementing the RoI model for the LMC region, this work follows the H. E. S. S. analysis result, which shows indications for an additional, even weaker point source. The VHE γ-ray excess leads to a statistical significance of 4.7σ. The source spatially coincides with the SNR N 132D, which is extremely bright in radio wavelengths (Dickel & Milne 1995). The marginal detection of this source completes the sample of extreme sources in the LMC: the IC bright PWN N 157B, the close-by superbubble 30 DorC and the most luminous SNR N 132D. For the analysis in GAMMALIB, N 132D is additionally included in the source model at its nominal position. The energy spectrum of this source is likewise modelled by a power law and position is left free to be optimised in the likelihood fit. For the background modelling approach, described in Sect. 5.2.4, a model with one free parameter is added, scaling the background rate for each considered run. In total, the analysis takes into account 486 runs on the LMC, leading to an accumulated observation time of 219 h.

Analysis Results

The analysis is conducted using `ctlike`, optimising the free parameters in the RoI model. The results are listed in Table 5.4. For comparison, the best-fit models from the H. E. S. S. software for each source are also listed. The derived spectral and positional parameters nicely agree on a statistical basis. Since both analyses, however, make use of the same dataset, a statistical comparison is not conclusive. Regarding the best-fit values, a slight systematic trend to higher flux normalisations Φ can be identified in GAMMALIB analyses. Nevertheless, by adding the required point sources in the RoI, GAMMALIB is able to fit all parameters of interest in one analysis to a satisfying result. As a further sanity check, the fitted normalisations of the run-wise background models are studied. The derived normalisations are found to be normally

Table 5.4.: Analysis of the LMC region

Source	Analysis	Φ	Γ	RA	DEC	Significance
	`ctlike`	13.23 ± 0.67	2.74 ± 0.06	84.4484 ± 0.0049	-69.1588 ± 0.0018	$\mathrm{TS} = 1616$
N 157B	H. E. S. S.	13.17 ± 1.01	2.77 ± 0.08	84.4468 ± 0.0016	-69.1596 ± 0.0014	$\sigma = 33$
	`ctlike`*	13.13 ± 0.67	2.74 ± 0.06	$-$	$-$	$\mathrm{TS} = 1578$
	`ctlike`	2.28 ± 0.41	2.51 ± 0.19	83.9544 ± 0.0170	-69.1824 ± 0.0058	$\mathrm{TS} = 90$
30 DorC	H. E. S. S.	2.18 ± 0.48	2.56 ± 0.20	83.9792 ± 0.0167	-69.1854 ± 0.0061	$\sigma = 8.8$
	`ctlike`*	2.18 ± 0.43	2.57 ± 0.20	$-$	$-$	$\mathrm{TS} = 78$
	`ctlike`	1.39 ± 0.34	2.20 ± 0.19	81.3126 ± 0.0230	-69.6483 ± 0.0080	$\mathrm{TS} = 50$
N 132D	H. E. S. S.	1.28 ± 0.48	2.44 ± 0.34	81.2792 ± 0.0208	-69.6416 ± 0.0068	$\sigma = 4.7$
	`ctlike`*	1.28 ± 0.34	2.21 ± 0.21	$-$	$-$	$\mathrm{TS} = 41$
Excess model	`ctlike`*	109.8 ± 7.7	2.19 ± 0.05	81.5000	-68.2667	$\mathrm{TS} = 713$

Notes. The flux normalisation Φ is given in units of $10^{-13}\,\mathrm{TeV}^{-1}\,\mathrm{cm}^{-2}\,\mathrm{s}^{-1}$. The sky coordinates right ascension (RA) and declination (DEC) are given in degrees. The analysis, marked `ctlike`*, represents the fit with the underlying broad Gaussian component LMC component in the RoI model.

distributed with $\mu = 0.93$ and $\sigma = 0.14$. These values are compatible with the distribution which is expected from off-runs, shown in Fig. 5.11. Therefore, the made assumption to transfer the background model from off-runs to observation runs is reasonable.

Sky Maps of the LMC with GAMMALIB

Visualising the sources in the LMC, TS maps of the chosen RoI in the LMC are computed. The left panel of Fig. 5.19 presents the TS map of the LMC region. To show all significant structures, the three point sources are removed from the RoI model. The map is centred on the position of N 157B. In order not to truncate the bright PWN N 157B, the colour scale, representing the TS value, is put logarithmically. The positions of the three point sources are highlighted in the map. For enhanced visibility, an arrow indicates the position of N 132D. The overlapping sources N 157B and 30 DorC (green and blue cross, respectively) are clearly visible. To emphasise the weak sources, the right panel shows a TS map of the same region, including the strong source N 157B in the source model. The model parameters are fixed to its best-fit values. Besides the two point-like source 30 DorC and N 132D, there seem to be still some residual TS values in the lower right part of the map. The overlaid contours represent the accumulated exposure from all available observations. Details about the exposure calculation can be found in the Appendix of this work (A.4). The exposure peak is slightly offset from N 157B and 30 DorC. The deepest exposure, i.e. the highest sensitivity is positionally coincident with the most left-over structures in the residual TS map. The origin of this excess is unclear. Possible systematic effects might accumulate for regions with deep exposure. Since the LMC is a region of many stars, the NSB level e.g. could create artificial γ-ray events which pass the selection cuts. Investigating the origin of this excess is beyond the scope of this thesis. Nevertheless, to account for this excess in the model, a broad 2D Gaussian is added. This spatial model is centred on $(\mathrm{RA}, \mathrm{DEC}) = (81°\!.50, 68°\!.27)$ with a Gaussian width of $1°\!.2$. The choice of this function is inspired by the detection of diffuse emission in the LMC (Abdo et al. 2010b). It should be stressed, however, that no physical statement about this excess is pursued in this thesis. As spectral part of the excess, a power law is assumed. The data is re-analysed using `ctlike` with the updated RoI model. To speed up the computation, the derived point-source locations are fixed to their best-fit values. Subsequently, the log-likelihood of the best-fit model is compared to the value derived in the above analysis. Applying Eq. 5.7 results in $\mathrm{TS}_{\mathrm{diffuse}} = 713$, implying a significant improvement of
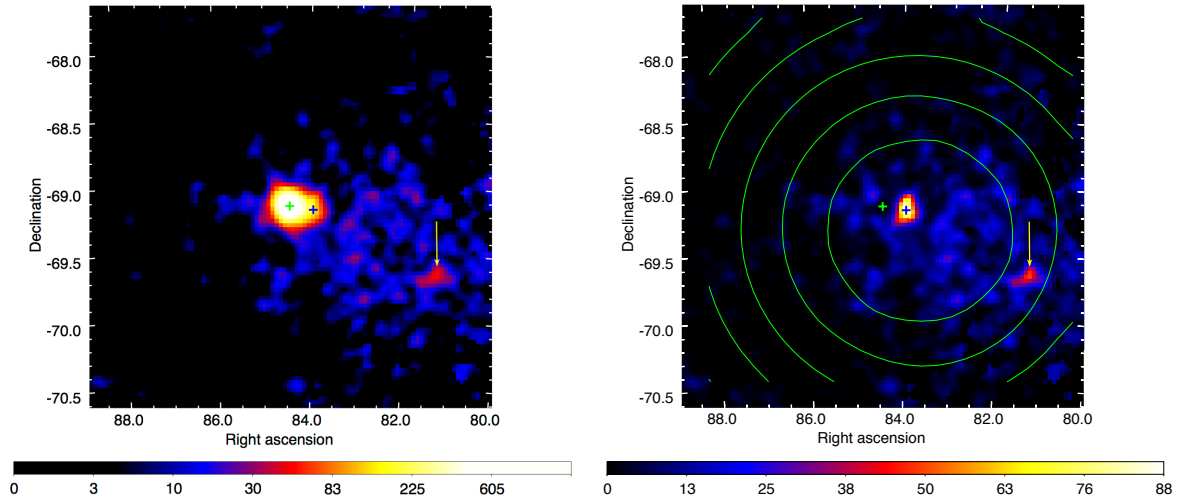
Figure 5.19.: Two TS maps of a $3° \times 3°$ region in the LMC. *Left*: TS map showing the distribution of all significant structures in the RoI. The three sources described in the text are highlighted by a green and blue cross (N 157B, 30 DorC), and a yellow arrow (N 132D). Note that the colour scale, indicating the TS value in each bin is logarithmically scaled. *Right*: TS map of the same region. The strong source N 157B is kept in the RoI model, fixed to the derived best-fit parameters. Its position is marked by a white cross. Consequently, the only two sources appearing in the map are 30 DorC (blue cross) and N 132D (yellow arrow). The colour scale can be kept linear in this case.

the fit. The spectra of the three sources are slightly affected when taking into account the underlying excess. The updated spectral parameters, along with the spectrum of the fitted Gaussian are listed in Table 5.4. Accounting for the excess in the model further approaches the best-fit parameters of the three point sources to the values provided by the H. E. S. S. analysis. The reason behind this might be the choice of the background regions required by the reflected background method. The off-regions are most certainly partly overlapping with regions of positive excess in the LMC. Accordingly, for the H. E. S. S. spectral analysis, this excess is subtracted, leading to a slightly lower flux.

GAMMALIB has proven to correctly handle overlapping sources. In addition, a broadly extended, underlying component is fitted, leading to consistent spectral results for the point sources compared to the H. E. S. S. software.

5.4. Fermi-**LAT** Analysis in GAMMALIB

Having demonstrated that GAMMALIB provides a suitable framework to conduct H. E. S. S. analyses, the software is also tested using *Fermi*-LAT data. The likelihood framework of GAMMALIB currently supports only binned analyses for *Fermi*-LAT data. An implementation of the corresponding unbinned analysis method is rather complex. After six years on orbit, *Fermi*-LAT has collected a large number of events, such that unbinned likelihood analyses for timely constant sources become unpractical. Therefore, *Fermi*-LAT data is analysed using

the binned framework.

To validate the *Fermi*-LAT analysis in GAMMALIB, the exemplary Crab Nebula is again used as test case. The binned framework in `ctlike` functions analogously to binned `gtlike` (see Chap. 4). As input, it makes use of the binned events, the exposure information, as well as the precomputed and averaged instrument response according to the chosen binning. Note that in the following analyses, P8 data is used as shown for previous *Fermi*-LAT analysis. So far, GAMMALIB has only been tested for P7Rep data[10]. This probes if GAMMALIB can handle other IRFs without any obstacle.

For the purpose of a quick verifying cross-check, the "off-pulse" dataset of the Crab Nebula, presented in Sect. 4.2.1, is used. The identical RoI model, with the same free parameters is also adopted. Running the corresponding analysis with `ctlike`, the fit parameters are obtained as listed in Table 5.5. For comparison, the previously derived `gtlike`-results are also shown. The best-fit parameters of both frameworks agree perfectly. This is expected

Table 5.5.: Re-analysis of the Crab Nebula (off-pulse)

Parameter	`gtlike`	`ctlike`	unit
F_{syn}	(7.46 ± 0.04)	7.46 ± 0.04	$10^{-7}\,\mathrm{cm}^{-2}\,\mathrm{s}^{-1}$
Γ	$-(3.49 \pm 0.03)$	$-(3.49 \pm 0.03)$	—
Φ_{IC}	(1.48 ± 0.28)	1.48 ± 0.29	$10^{-11}\,\mathrm{MeV}^{-1}\,\mathrm{cm}^{-2}\,\mathrm{s}^{-1}$
α	1.21 ± 0.07	1.21 ± 0.07	—
β	0.11 ± 0.02	0.11 ± 0.02	—
Φ_{gal}	0.929 ± 0.004	0.929 ± 0.004	—
Γ_{gal}	9.8 ± 6.5	9.8 ± 6.5	10^{-3}
N_{iso}	0.95 ± 0.01	0.95 ± 0.01	—

Notes. Parameters are labelled exactly like in Sect. 4.2.1. The values derived with the Fermi Science Tools (`gtlike`) are taken from Table 4.1.

since the exact same dataset is analysed with the same philosophy. The results show that the implemented functionality to analyse binned *Fermi*-LAT data works satisfyingly. Only very minor numerical differences can be found after some decimal places. The off-pulse analysis is repeated in energy bins to derive an SED for the Crab Nebula. The derived data points also fully agree with those from the Fermi Science Tools. Therefore, a graphical representation of the results is omitted in this case. A more extensive validation of *Fermi*-LAT data analyses is currently ongoing (Schulz in prep.). In conclusion, GAMMALIB is perfectly suited to analyse *Fermi*-LAT data. Consequently, this work proceeds to combine data from *Fermi*-LAT and H. E. S. S. to provide insights to the IC peaks of PWNe.

5.5. Exemplary Combination of Data from Fermi-LAT and H. E. S. S.

The structure of GAMMALIB is flexible enough to handle all kinds of observations. Regardless of instrument, or analysis mode (binned, unbinned), every observing unit of a detector is handled by the `GObservation` base class. The entirety of `GObservation`-objects are enclosed

---

[10]https://cta-redmine.irap.omp.eu/issues/1004

in the container class `GObservations`. The latter can hold all information of e.g. H. E. S. S. runs and *Fermi*-LAT observations. Consequently, it is possible to combine several observations independently. The RoI model has to comprise all necessary sources and components, which are required to explain the emission in the given observations. Each model can be assigned to a respective instrument for which it is valid. This is important e.g for the run-wise background model described in Sect. 5.2.4. The model to explain the γ-like background in each run is specific to the H. E. S. S. instrument and does not apply for *Fermi*-LAT observations. Similarly, the *Fermi*-LAT Galactic diffuse emission model should not be used for H. E. S. S. analyses. Although a simple extrapolation of this model is possible in GAMMALIB, the diffuse emission in the VHE regime is mostly unexplored and might differ quite severely from the extrapolated model. In contrast, if the assignment of an instrument to a specific model is omitted, it applies to all observations. Thus, the likelihood can be optimised by taking into account instrument-specific models as well as sky models, which are present for every instrument.

As a first and exemplary analysis the Crab Nebula is again used to demonstrate the capabilities of GAMMALIB to combine data and fit models over several decades of energy.

5.5.1. Data Preparation

Since for *Fermi*-LAT analyses, `ctlike` can only use the binned framework, the data has to be prepared for the use in GAMMALIB. For this purpose, the folding integrals of diffuse components with the IRF (Eq. 4.5) have to be precomputed. Therefore, it is not yet possible to directly fit morphological models for *Fermi*-LAT data in GAMMALIB. The precomputing task is performed by `gtsrcmaps`, which is part of the Fermi Science Tools. To parametrise the spectrum of the IC component of the Crab Nebula with one analytical model, the dataset is restricted to events above $1\,\text{GeV}$. This threshold is also chosen to circumvent uncertainties in the low energy range of the Galactic diffuse model which is especially important for PWNe which are located in the Galactic plane. Enabling a larger overlapping energy range with H. E. S. S., *Fermi*-LAT events up to $750\,\text{GeV}$ are taken into account. Complementing the event selection, the same cuts as presented in Sect. 4.1.2 are applied on the available *Fermi*-LAT dataset (MJD $54682.7 - 56456.8$). Subsequently, the events are binned into 15 sky maps with 80×80 spatial bins. Each bin has a size of $0°\!.15$, which is slightly less than the PSF above $1\,\text{GeV}$.

Considering data from *Fermi*-LAT and H. E. S. S. in GAMMALIB leads to a statistical combination of binned and unbinned analyses, respectively. Composing the global likelihood of both analysis types results in a weighting mismatch between both instruments. For the moment, it is not possible to circumvent this weighting problem, which is why all combined analyses are dominated by the unbinned H. E. S. S. data. Taking into account *Fermi*-LAT data, however, provides additional constraints on the low energy part of the spectrum.

5.5.2. Model Generation

To create a source model describing the RoI, all necessary models for H. E. S. S. and *Fermi*-LAT are superimposed. Starting with H. E. S. S., all run-specific background models are added. All of them have one free parameter and are assigned with their specific run number and the H. E. S. S. instrument name. As described above, no additional VHE γ-ray source is needed. For *Fermi*-LAT, all sources which are listed in the internal 4 yr catalogue (see Sect. 4.1.2) are added to the model. Each of the sources is considered specific to *Fermi*-

LAT, which is why they are not subject to the combined analysis. The IC component of the Crab Nebula is removed from this list, since it is added separately. Reducing the number of free parameters, the spectral models of the additional point sources are fixed to their best-fit values provided in the 4 yr catalogue. To describe the diffuse components, the Galactic diffuse model and the isotropic diffuse model are added with their usual free parameters. As templates for these two diffuse models, the same files, as described in Sect. 4.1.3, are used. Likewise, both models are exclusively valid for the *Fermi*-LAT data. They are therefore not used to evaluate the likelihood with H. E. S. S. data. Finally, the source of interest, the Crab Nebula, is added to the RoI model. Well-suited to parametrise the curved IC spectrum, the spectral part of this point-source is modelled by a log-parabola model (Eq. 4.7). The Crab Nebula model is not assigned with any observational identifier or instrument name, since it should apply to all observations.

In sum, the combined RoI model has 212 free parameters: three of them describing the Crab Nebula, one for the isotropic diffuse normalisation, two for the Galactic diffuse model, and 207 for the background model of each H. E. S. S. run.

5.5.3. Analysis and Results

Having defined the observations and the corresponding RoI model, the analysis is conducted with `ctlike`. The combined analysis of *Fermi*-LAT and H. E. S. S. data is still quite fast, requiring only $\sim 1\,\mathrm{min}$ of computation time. In general, the computational speed is very much dominated by the number of diffuse or extended components in the unbinned H. E. S. S. analysis. The fit reveals, for the first time, the spectrum of the Crab Nebula, obtained from a combined fit in the energy range between $1\,\mathrm{GeV}$ and $65\,\mathrm{TeV}$. The best-fit model is described by

$$\frac{\mathrm{d}N}{\mathrm{d}E} = (4.28 \pm 0.03) \cdot \left(\frac{E}{1\,\mathrm{TeV}}\right)^{-(2.53\pm0.01)-(0.10\pm0.00)\log 10(E/(1\,\mathrm{TeV}))} . \tag{5.13}$$

The resulting spectrum is given in units of $10^{-11}\,\mathrm{TeV}^{-1}\,\mathrm{cm}^{-2}\,\mathrm{s}^{-1}$. The fitted model is visualised in Fig. 5.20 as a black solid line. The corresponding 68% confidence region, is depicted as a grey-shaded area. In addition, SED data points of this first combined analysis are computed. For this purpose, *Fermi*-LAT data has to be precomputed in the respective slices of energy. Between $1\,\mathrm{GeV}$ and $750\,\mathrm{GeV}$, 15 bins are used, equally spaced on a logarithmic scale. Likewise, 15 additional energy bins from $750\,\mathrm{GeV}$ to $65\,\mathrm{TeV}$ are used for the H. E. S. S. data. Due to the high energy threshold of $680\,\mathrm{GeV}$ for Crab Nebula observations with H. E. S. S., there is only one energy bin where data from both instruments can be combined. To derive the spectral points, the prefactor of the log-parabola model is fitted in each energy bin, leaving all other parameters in the RoI model fixed. The spectral points in Fig. 5.20 nicely demonstrate the different sensitivities of the two instruments. Where H. E. S. S. data can be considered in one energy bin, the statistical errors shrink drastically. The energy bin, which combines data from both telescopes, is highlighted in red. The small energy range in which H. E. S. S. data can be considered within this bin ($680 - 750\,\mathrm{GeV}$), is sufficient to strongly decrease the statistical error.

The combined spectral fit with the log-parabola model leads to an estimate of the IC peak E_{peak}. This value is defined, where the log-parabola model is maximal in the SED:

$$\frac{\partial(E^2\mathrm{d}N/\mathrm{d}E)}{\partial E}\Big|_{E_{\mathrm{peak}}} \stackrel{!}{=} 0. \tag{5.14}$$
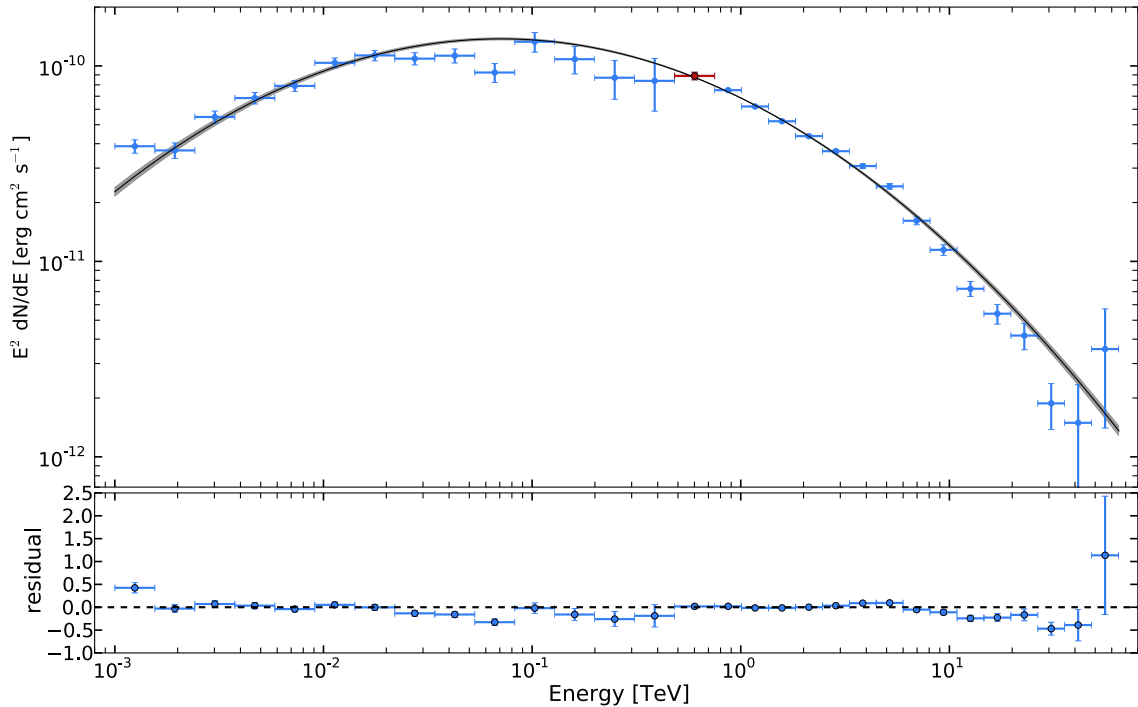
Figure 5.20.: The top panel presents the result of the first combined analysis of *Fermi*-LAT and H. E. S. S. data. The grey-shaded band depicts the 68% confidence region of the spectral fit with a log-parabola model over almost five decades in energy. The blue points result from spectral fits in energy bands. The data point highlighted in red depicts the one energy bin, where both instruments contribute. The bottom panel represents the residuals from the data points with respect to the best-fit model.

Accordingly, the IC peak can be determined to

$$E_{\text{peak}} = \exp\left(\frac{2 - \alpha}{2\beta}\right) \cdot E_0, \qquad (5.15)$$

where α and β derive from the likelihood fit. In the analyses, E_0 is usually fixed to 1 TeV. For the presented combined analysis of the Crab Nebula, the IC peak is computed to $E_{\text{peak}} = 70.8 \pm 5.8\,\text{GeV}$. This measurement confirms the value of $77 \pm 35\,\text{GeV}$, derived from MAGIC observations (Albert et al. 2008). A more recent MAGIC analysis, presented in Zanin (2011), revealed a slightly lower IC peak of $59 \pm 6\,\text{GeV}$. This value is nevertheless compatible with the presented analysis within two standard deviations.

The errors on the IC peak do not consider systematic uncertainties. For the presented combined analysis, the systematic uncertainties from both instruments would have to be considered, according to their weighting in the likelihood fit. Studying how systematic uncertainties of individual instruments are reflected in the IC peak energy is beyond the scope of this thesis.

The SED of the Crab Nebula indicates that the IC peak is intrinsically quite broad. The spectral data points suggest more a broad plateau between $20 - 750\,\text{GeV}$ than a shape following

the log-parabola function. There might be many reasons for this appearance. The radiation fields most certainly play an important role: each individual target radiation field produces a different spectral shape of the emitted photons. Since only the resulting superposition can be detected, a plateau could emerge from two close-by IC peaks (see, e.g., Fig. 2 in Meyer et al. 2010).

In previous Sections, a general scheme of analyses with GAMMALIB and CTOOLS was presented. The capabilities of this likelihood framework offers a reasonable alternative for the traditional high-level analysis methods of IACTs. Having prepared the infrastructure to conduct H. E. S. S. analyses, this work focuses on the application to PWNe. To complement the study, presented in Sect. 2.3, IC peaks are derived for the PWN sample. For this purpose, data from *Fermi*-LAT and H. E. S. S. is combined in GAMMALIB in the following.

5.6. IC Peaks of PWNe

In this Section, the IC peaks of PWNe are derived to further probe the capabilities of the software. This work emphasises on establishing GAMMALIB /CTOOLS as an alternative analysis framework for γ-ray astronomy. The obtained results are subsequently compared to model predictions and published values where available. Due to the large number of VHE detected PWNe, a semi-automated framework to derive the IC peaks is employed. The applied steps are explained in the following.

5.6.1. RoIs Definition and Data Selection

Initially, PWNe are selected to be considered in this study. The list of PWNe is mainly following Table 2.3. Due to the Northern location of CTA 1, H. E. S. S. cannot observe this source. Therefore, this PWN is removed from the sample. The resulting list of RoIs contains 24 PWNe. Each RoI depicts a circular region in the sky, centred on the position of the associated pulsar. Every region is chosen to have a radius of 3° from which H. E. S. S. runs are selected. In case of a point-like source at the RoI centre, some runs do not have exposure at the source position due to the applied FoV cut of 2°.5. Since many PWNe are extended, more runs can be accumulated to better measure the morphology.

For *Fermi*-LAT, the RoI radius is much larger. Events are filled in maps which comprise $12° \times 12°$ on the sky. Each map is subdivided into 80×80 spatial bins. In addition, the data are split in 15 energy bins between $1 - 750 \, \text{GeV}$. Having defined the data selection criteria for the chosen RoIs, this work proceeds to assemble the models describing the RoIs.

5.6.2. Towards an RoI Model for H. E. S. S.

To determine a suited RoI model for every PWN in the H. E. S. S. energy range, an iterative procedure is applied. The taken consecutive steps are presented in the following. Note that the subsequent analyses are conducted without data from *Fermi*-LAT since this Section is intended to create H. E. S. S. specific RoI models.

Initial Fit

As basis for an initial RoI model for H. E. S. S., a preliminary source catalogue (following Carrigan et al. 2013) is used. Data from this reference also served as basis to derive the
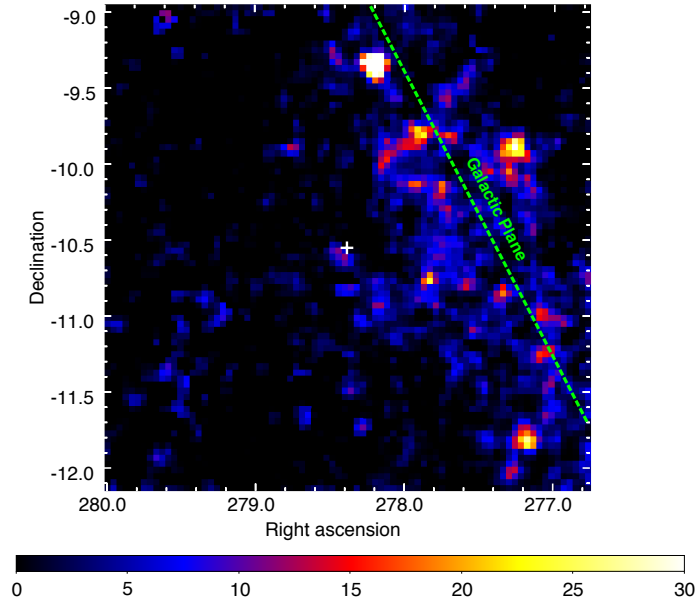
Figure 5.21.: Exemplary residual TS map of the RoI around HESS J1833−105, depicting the residual emission along the Galactic Plane. The position of the PWN in this region is marked by a white cross.

PWN properties in Sect. 2.3. For each RoI, all sources from this catalogue, which may contribute in the considered region, are added. The listed spectral and spatial models are adopted. For each source, the spectral normalisation parameter is left free. In case of an extended source, the parameter defining the size is also taken as free parameter. Note that due to the applied enlargement of PSF, extension measures might differ from the catalogue values. For the PWN of interest, a log-parabola with three free parameters is applied. Using the presented background model with one free parameter per run, the initial analysis is conducted in GAMMALIB. In general, the resulting quality checks are not satisfying, showing residual emission all across the Galactic plane (see Fig. 5.21).

Accounting for Large-Scale Excess

The residuals along the Galactic plane can be attributed to a large-scale excess, which was already presented by Egberts et al. (2013), who interpreted the signal as Galactic diffuse VHE γ-ray emission. A detailed investigation of this component, including systematic studies and physical interpretation of this excess is not part of this work. To properly analyse the population of VHE γ-ray emitting PWNe, however, the excess has to be taken into account. Therefore, a simplistic model to describe this component is included in the RoI models. As a first order approach, a Gaussian band model is used[11] in Galactic coordinates as spatial representation of the large-scale component. This model is constrained to the region of the

---

[11]R. Terrier: private communication

HGPS:

$$I(\lambda, \beta) \quad \propto \quad \begin{cases} \exp\left(-\frac{\beta^2}{2\sigma_\beta^2}\right) & |\lambda| < 80° \\ 0 & \text{else} \end{cases}, \tag{5.16}$$

where (λ, β) represent Galactic longitude and latitude, respectively. From the HGPS, the solution $\sigma_\beta = 0°\!.4$ is adopted. The resulting model, presented in Fig. 5.22, is included in
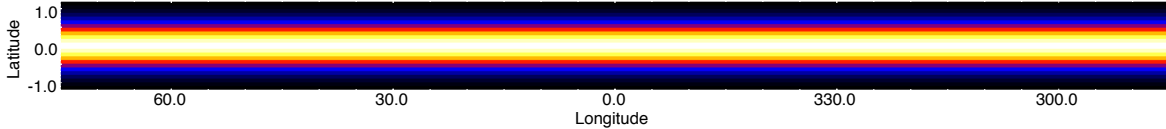
Figure 5.22.: Gaussian band model in Galactic coordinates, mimicking the Galactic diffuse emission in the H. E. S. S. energy range. The colour scale is linear from low intensities (dark) to high intensities (bright).

RoIs, which are located close to the Galactic plane.

As spectral part of this component, a power law is assumed. With the two additionally introduced parameters, the large-scale excess can be modelled. The derived fluxes represent the spectral appearance of this component excess under the assumption of the Gaussian band model.

Since adding the large-scale component might affect the spectra of VHE γ-ray sources, their spectral parameters are left free in the subsequent likelihood optimisations. The inclusion of the band model leads to significant improvements of the fit, varying between the RoIs from TS = 44 to TS = 6700. The fact that this excess is also seen in H. E. S. S. analyses, further verifies the analysis procedure in GAMMALIB. The analysis framework is able to detect large-scale emission, which is an important feature regarding the CTA observatory with its foreseen sensitivity.

Adding Newly Detected Sources

Inspecting the residuals TS maps for each RoI, three additional compact sources, which do not appear in the HGPS are found. In the residual TS maps they show up with TS > 50. Therefore, they are included into the models describing the respective RoIs. These sources are modelled point-like with a spectral power laws. Their best-fit positions along with their spectral parameters and significances are presented in Table 5.6. The sources are labelled following standard H. E. S. S. conventions. Two of the sources also appear in dedicated analyses

Table 5.6.: Sources not detected by the HGPS

Source	Φ	Γ	RA	DEC	Significance (TS)
HESS J1826−130*	1.63 ± 0.31	1.76 ± 0.13	276.501	−13.034	71
HESS J1828−100	2.64 ± 0.43	2.22 ± 0.19	277.225	−10.0203	58
HESS J1911+091†	2.81 ± 0.37	3.25 ± 0.27	287.769	9.10186	101

Notes. Parameter symbols and units are the same as in Table 5.4.
* This source, associated with the Eel nebula, has already been discovered by an independent analysis within the H. E. S. S. collaboration.
† The emission is positionally coincident with the SNR W49B, which was already announced as a H. E. S. S. detection (Brun et al. 2010).

from the H. E. S. S. collaboration. The reason why the HGPS could not re-associate these two sources is unclear. The emission region called HESS J1828−100 has no counterpart from earlier H. E. S. S. analyses or close-by *Fermi*-LAT sources. Including these three sources leads to an improvement of the fit, so they are subsequently fixed to their best-fit values.

Building Templates for Extended Sources with Complex Morphologies

The morphological analysis of IACT data in GAMMALIB is currently limited to few spatial models. Most of them are sufficient to describe the majority of PWNe in the Galactic plane. The available models are a symmetrical 2D Gaussian and a circular disk[12]. Applying these models leads to an extension fit of the respective source. However, there are few PWNe, which show clear asymmetric structure, which can not be described by these models. To provide more flexibility for the analysis, elliptical source models are currently being implemented into GAMMALIB[13] and are not ready to be used. In a more general approach, any sky model can be described by a sky map template, providing the spatial shape of the emission. The disadvantage of this type of spatial modelling is that morphological parameters cannot be optimised by the likelihood fit. Since the elliptical models are not ready to be used in analyses, such templates are created for sources which show a clear asymmetry.

In total, four PWNe cannot be well-described by symmetrical models. These objects are Vela X (Aharonian et al. 2006c; Abramowski et al. 2012), MSH15-5*2* (Aharonian et al. 2005b; Schoeck 2010), HESS J1303-631 (H.E.S.S. Collaboration et al. 2012b), and HESS J1825-137 (Aharonian et al. 2005c, 2006f; Brucker 2013). Starting from the best-fit morphologies from the latest references, the sky maps are iteratively adjust to match the observed emission profile. The sky maps are hence filled with a linear combination of the following analytical functions, representing the intensity I.

- Radial models:
  - Gaussian:

  $$I(r) \propto \exp\left(-\frac{R^2}{2\sigma^2}\right) \tag{5.17}$$

  - Disk

  $$I(r) \propto \begin{cases} 1 & r < R \\ 0 & \text{else} \end{cases} \tag{5.18}$$

  with R being the angular distance from the model centroid. The parameters σ and R represent the Gaussian width and the radius of the disk, respectively.

- Elliptical Models:
  - Asymmetrical Gaussian:

  $$\begin{aligned} I(x,y) \propto \exp\left(-\frac{((x-x_0)\cos y_0 \cos\phi + (y-y_0)\sin\phi)^2}{2\sigma_1^2}\right) \cdot \\ \cdot \exp\left(-\frac{(-(x-x_0)\cos y_0 \sin\phi + (y-y_0)\cos\phi)^2}{2\sigma_2^2}\right) \end{aligned} \tag{5.19}$$

---

[12]There is also the possibility to use a radial shell model, which, however does not apply for any of the considered PWNe

[13]`https://cta-redmine.irap.omp.eu/issues/754`

– Elliptical Disk:

$$I(r,\phi) \propto \begin{cases} 1 & r < \sqrt{(R_1 \cos \Delta\phi)^2 + (R_2 \sin \Delta\phi)^2} \\ 0 & \text{else} \end{cases} \tag{5.20}$$

where x_0, y_0 are the celestial coordinates of the model centroid, $R_{1,2}$ are the minor and major axis of the ellipse. The angle ϕ denotes the coordinate rotation angle, defined counter clockwise from North. $\Delta\phi$ denotes the difference in rotation angle between the input coordinate and ϕ.

All models are normalised in GAMMALIB, so the prefactors are omitted. To derive a sufficient morphological description for the four sources, the above functions are combined, each with an individual weighting factor. The best matching models are listed in Table 5.7. For visu-

Table 5.7.: Extended sources with complex morphologies

Source	Type	Weight	Parameters
Vela X	Asymm. Gaussian	0.5	RA $= 128°\!.75$, DEC $= -45°\!.58$, $\sigma_1 = 0°\!.48$, $\sigma_2 = 0°\!.36$, $\phi = 41°$
	Gaussian	1.0	RA $= 128°\!.07$, DEC $= -45°\!.50$, $\sigma = 1°\!.20$
HESS J1303$-$613	Asymm. Gaussian	1.0	RA $= 195°\!.70$, DEC $= -63°\!.18$, $\sigma_1 = 0°\!.19$, $\sigma_2 = 0°\!.15$, $\phi = 147°$
MSH15-5*2*	Asymm. Gaussian	1.0	RA $= 228°\!.51$, DEC $= -59°\!.17$, $\sigma_1 = 0°\!.12$, $\sigma_2 = 0°\!.07$, $\phi = 134°$
	Gaussian	0.3	RA $= 228°\!.59$, DEC $= -59°\!.15$, $\sigma = 0°\!.25$
HESS J1825$-$137	Asymm. Gaussian	1.0	RA $= 276°\!.42$, DEC $= -13°\!.84$, $\sigma_1 = 0°\!.26$, $\sigma_2 = 0°\!.23$, $\phi = 17°$
	Elliptical Disk	0.8	RA $= 276°\!.27$, DEC $= -14°\!.07$, $R_1 = 0°\!.90$, $R_2 = 0°\!.70$, $\phi = 40°$
	Radial Disk	0.5	RA $= 276°\!.54$, DEC $= -14°\!.22$, $R = 1°$

Notes. The parameter RA and DEC denote the centroid of each model

alisation of these four models, see Appendix A.5. Note that the applied spatial models are only intended to sufficiently derive the energy spectra of the respective sources. Accordingly, there is no underlying physical motivation for the choice of the superimposed functions and their relative weighting.

The described iterative process leads to RoI models for the H. E. S. S. analysis for each of the considered PWNe. It is known that some PWNe show energy-dependent morphologies (Aharonian et al. 2006f; H.E.S.S. Collaboration et al. 2012b). In general, GAMMALIB provides the structure to perform such a spatio-spectral modelling of this behaviour. A detailed model, describing the exact variation of the morphology with energy is required for this purpose. Creating such a complex model, however, does not fit into the scope of this work. Since morphological fits for *Fermi*-LAT data are currently not supported in GAMMALIB, it is inferred that the fitted morphological shapes of the H. E. S. S. PWNe are representative for the whole energy range of the combined analysis above 1 GeV. This might introduce some systematic uncertainties, since the exact shape for each energy is unknown. Accordingly, the combined spectra of the considered PWNe are derived under the assumption of a fixed spatial model.

5.6.3. Adding Fermi-LAT Models and the Source of Interest

To analyse all PWNe with a combined analysis, the RoI models derived from the above H. E. S. S. analyses, are complemented by *Fermi*-LAT sources. For each RoI, a list of sources is compiled from the 4 yr catalogue, which was used in Chap. 4. From this list, every source

closer than 17° from the respective RoI centre is added to the RoI model. To complete the required *Fermi*-LAT models, the Galactic and isotropic diffuse components are added as done in above analyses. These components are left free to vary in every RoI. All *Fermi*-LAT sources are fixed to their parameters provided in the 4 yr catalogue. In the GAMMALIB framework, these sources are considered specific to *Fermi*-LAT data. Therefore, they are not evaluated for H. E. S. S. data. A combined model fit is only conducted for the PWN in the RoI centre.

Finally, the source of interest is added to the respective RoI model. To obtain a combined analysis, this model is valid for both instruments, H. E. S. S. and *Fermi*-LAT. Every PWN is added with the best-fit morphology model from the H. E. S. S. analysis above. The spatial parameters are fixed to their best-fit shape, regardless of the model type. Due to the detected energy-dependent morphology of individual PWNe (Aharonian et al. 2006f; H.E.S.S. Collaboration et al. 2012c), a systematic uncertainty is introduced by assuming a fixed spatial model for almost five decades of energy. As spectral part, a log-parabola model is used to describe the combined energy spectrum for each PWN between 1 GeV and 80 TeV. By definition, this model provides direct access to the IC peak via Eq. 5.15. To avoid duplicate entries in the list of source models for each RoI, the corresponding *Fermi*-LAT source of the respective PWN is removed from the model. In many RoIs a clear *Fermi*-LAT counterpart of the H. E. S. S. PWN is missing. In such cases the closest point-source within 0.3 of the derived PWN position is removed. For four RoIs in total, a catalogue source is removed as possible PWN counterpart. These RoIs are HESS J1458−608, G0.9+0.1, HESS J1809−193, and HESS J1813−178. Since the association of the *Fermi*-LAT source with the respective PWN is uncertain, this might introduce further systematics for these RoIs.

5.6.4. Analysis Results

In each RoI, a combined analysis using the data from *Fermi*-LAT and H. E. S. S. is conducted. Probing the combined fits for convergence, the distributions of background parameters are inspected. In total, 4928 H. E. S. S. runs are used for the analysis of PWNe. The fitted background scaling factor for each of these runs is shown in the top left panel of Fig. 5.23. Their distribution is in full agreement with the expectation from off-runs (Fig. 5.11). Having a mean of $\mu = 1.0$ and an rms of $\sigma = 0.2$, the best-fit background models prove to be fitted correctly. For each RoI, the corresponding H. E. S. S. residual map is shown in the Appendix of this work (A.6).

For *Fermi*-LAT, the Galactic and isotropic diffuse components are also optimised in the likelihood fit. On the upper right panel of Fig. 5.23, the fitted normalisations of the latter component are presented. The distribution is slightly shifted with respect to the expected value of ≈ 1. Since most PWNe are along the Galactic plane, the isotropic diffuse component might only play a minor role in the fit. On the bottom right panel, the index, which scales the Galactic diffuse model shows a peaked distribution towards the expected zero. The normalisation of the Galactic diffuse model (bottom left), seems to have two peaks. Around half of the fits converge around unity, which is generally expected. For the other RoIs values around 0.5 are fitted. These values were cross-checked with the Fermi Science Tools, using the same RoI source model, however, leaving the normalisation parameters of the catalogue sources free. The derived values are compatible with those from the combined analysis. Inspecting the corresponding residual maps indicates an adequate RoI description. A possible reason could be the latest Galactic diffuse model, which is used in the analyses. Since the residual maps are satisfactory, the low Galactic diffuse normalisations should not
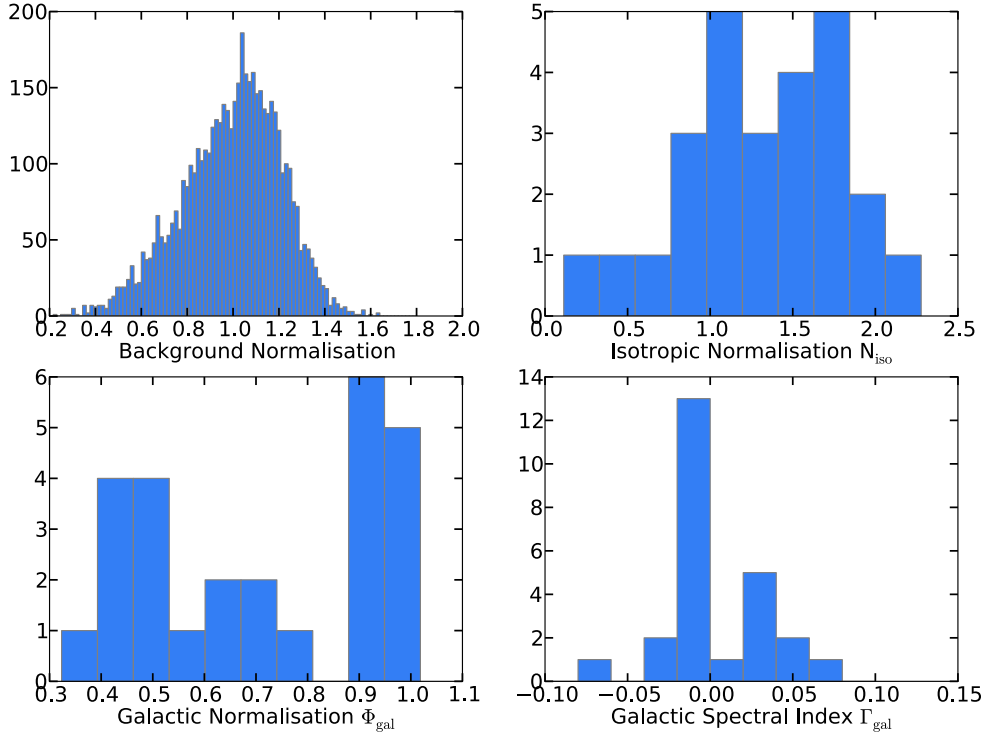
Figure 5.23.: The four panels represent the distribution of the background parameter, fitted in the combined analyses of PWNe. *Top left*: Background normalisation factor of all analysed H. E. S. S. runs. *Top right*: Normalisation of the *Fermi*-LAT isotropic diffuse component. *Bottom left*: The scaling prefactor of the Galactic diffuse model for *Fermi*-LAT. *Bottom right*: Distribution of the spectral index, which additionally scales the energy dependence of the Galactic diffuse model.

affect the measurements of the IC peaks. However, further studies are needed investigate this unexpected distribution.

The likelihood fit, conducted by `ctlike` further provides the best-fit parameters of the employed log-parabola model. The fit results for all PWNe along with their applied morphological models are presented in Table 5.8.

Table 5.8.: Analysis results

Source	Spatial Model	RA [°]	DEC [°]	Extension [°]	Φ [$10^{-12}\,\mathrm{cm}^{-2}\,\mathrm{s}^{-1}\,\mathrm{TeV}^{-1}$]	α	β	TS	E_{peak} [GeV]
Crab Nebula	Point	83.63	22.01	–	43.06 ± 0.36	2.52 ± 0.01	0.11 ± 0.00	137223	71 ± 6
N 157B	Point	84.43	−69.17	–	1.18 ± 0.07	2.22 ± 0.13	0.25 ± 0.07	1626	645 ± 243
Vela X	Template	–	–		32.11 ± 0.69	1.24 ± 0.04	0.34 ± 0.02	6910	3106 ± 95
HESS J1026−582	Gauss	156.66	−58.20	0.24	0.83 ± 0.17	1.13 ± 0.34	0.29 ± 0.13	131	4506 ± 1059
G292.2−0.5	Gauss	169.75	−61.46	0.12	1.63 ± 0.14	2.45 ± 0.14	0.29 ± 0.11	246	457 ± 198
HESS J1303−631	Template	–	–		7.08 ± 0.17	1.97 ± 0.05	0.23 ± 0.03	5465	1078 ± 102
HESS J1356−645	Gauss	209.00	−64.50	0.27	5.31 ± 0.51	1.89 ± 0.09	0.17 ± 0.04	267	1373 ± 339
Kookaburra (Rabbit)	Gauss	214.44	−60.97	0.11	3.60 ± 0.26	1.95 ± 0.09	0.17 ± 0.04	584	1172 ± 289
Kookaburra (PWN)	Gauss	215.06	−60.75	0.09	4.36 ± 0.27	2.01 ± 0.07	0.16 ± 0.03	924	955 ± 202
HESS J1458−608	Point	226.00	−60.94	–	0.84 ± 0.16	1.39 ± 0.39	0.32 ± 0.18	97	–
MSH 15−52	Template	–	–		8.44 ± 0.19	2.19 ± 0.02	0.09 ± 0.01	5840	339 ± 33
HESS J1616−508	Gauss	244.16	−50.91	0.23	12.19 ± 0.40	2.17 ± 0.03	0.03 ± 0.01	2218	77 ± 13
HESS J1708−443	Gauss	257.05	−44.33	0.45	6.06 ± 0.54	1.46 ± 0.15	0.22 ± 0.07	300	3438 ± 693
HESS J1718−385	Gauss	259.53	−38.55	0.14	0.50 ± 0.11	0.33 ± 0.34	0.58 ± 0.13	248	4230 ± 441
G0.9+0.1	Point	266.85	−28.15	–	0.74 ± 0.04	2.21 ± 0.06	0.20 ± 0.06	1261	601 ± 148
HESS J1809−193	Gauss	272.63	−19.30	0.33	3.17 ± 0.25	0.76 ± 0.17	0.66 ± 0.10	619	2552 ± 154
HESS J1813−178	Gauss	273.40	−17.84	0.06	3.19 ± 0.12	2.13 ± 0.03	0.02 ± 0.01	1797	–
HESS J1825−137	Template	–	–		23.46 ± 0.23	2.27 ± 0.01	0.13 ± 0.01	19871	338 ± 23
HESS J1831−098	Point	277.89	−9.87	–	0.25 ± 0.06	2.54 ± 0.37	0.62 ± 0.53	40	–
HESS J1833−105	Point	278.38	−10.55	–	0.64 ± 0.07	2.01 ± 0.15	0.30 ± 0.13	240	991 ± 247
HESS J1846−029	Point	281.60	−2.98	–	0.73 ± 0.05	2.34 ± 0.08	0.02 ± 0.01	416	–
IGR J18490−0000	Point	282.26	0.02	–	0.35 ± 0.05	1.55 ± 0.34	0.66 ± 0.30	93	1411 ± 258
HESS J1912+101	Disk	288.32	10.13	0.44	2.63 ± 0.17	2.27 ± 0.07	0.14 ± 0.04	365	388 ± 133
G54.1+0.3	Point	292.63	18.87	–	0.44 ± 0.09	2.22 ± 0.14	0.08 ± 0.04	75	–

Notes. The parameter symbols Φ, α, and β represent the best-fit log-parabola models (Eq. 4.7). The peak energies E_{peak} are calculated via Eq. 5.15. Note that for sources which are modelled by a spatial template, the extension cannot given unambiguously.
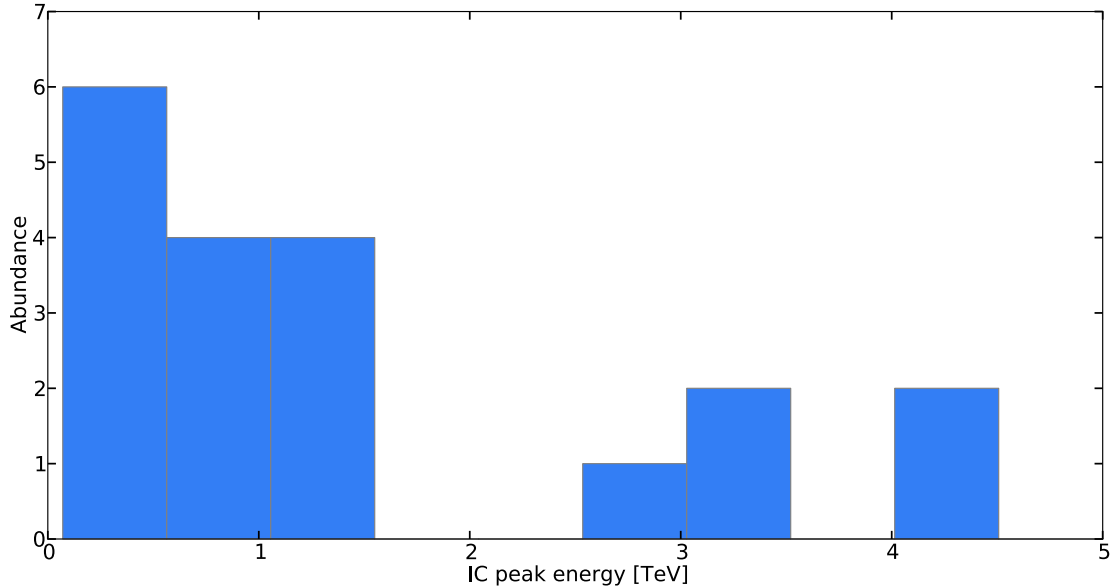
Figure 5.24.: Distribution of IC peaks derived with the combined analysis of *Fermi*-LAT and H. E. S. S. data in GAMMALIB.

The Table further lists the TS value, representing the statistical significance of the detection of each source. In addition, the energy of the IC peak is presented following Eq. 5.15. The uncertainty on this value is derived by Gaussian error propagation of the fitted spectral parameters.

Fig. 5.24 presents the distribution of derived IC peaks. Note that the peak energy is only given if the fitted curvature β significantly deviates from zero ($> 2\sigma$). Otherwise the detection of the spectral peak is considered insignificant. Most IC peak energies are determined below 1 TeV, with some outliers at much higher energies. For visualisation of the fitted energy spectra, along with the computed data points, the reader is referred to the Appendix A.7 of this work. The study of Acero et al. (2013), who determined the IC peak energy for PWNe and PWN candidates through *Fermi*-LAT analyses, serves as independent cross-check. Together with published H. E. S. S. data points, they derive the IC peak energy directly from the SED. Due to different selection criteria, the PWN sample presented in this thesis differs from Acero et al. (2013). In total, only six PWNe appear in both samples for which the measured IC peaks are compared. Fig. 5.25 presents the six objects for which the IC peak can be cross-checked. In general, the determined IC peaks are compatible with the study of (Acero et al. 2013). The statistical errors are smaller compared to the reference value. This can be attributed to the larger dataset and the combination of both instruments in one analysis. The cross-check further verifies the combined analysis of *Fermi*-LAT and H. E. S. S. data in the GAMMALIB framework. In the following, the analysis results are discussed from a technical and astrophysical point of view.

5.7. Technical Discussion

Using the analysis framework of GAMMALIB/CTOOLS, the energy spectra of PWNe can be constrained over almost five decades in energy. For the first time, data from *Fermi*-LAT
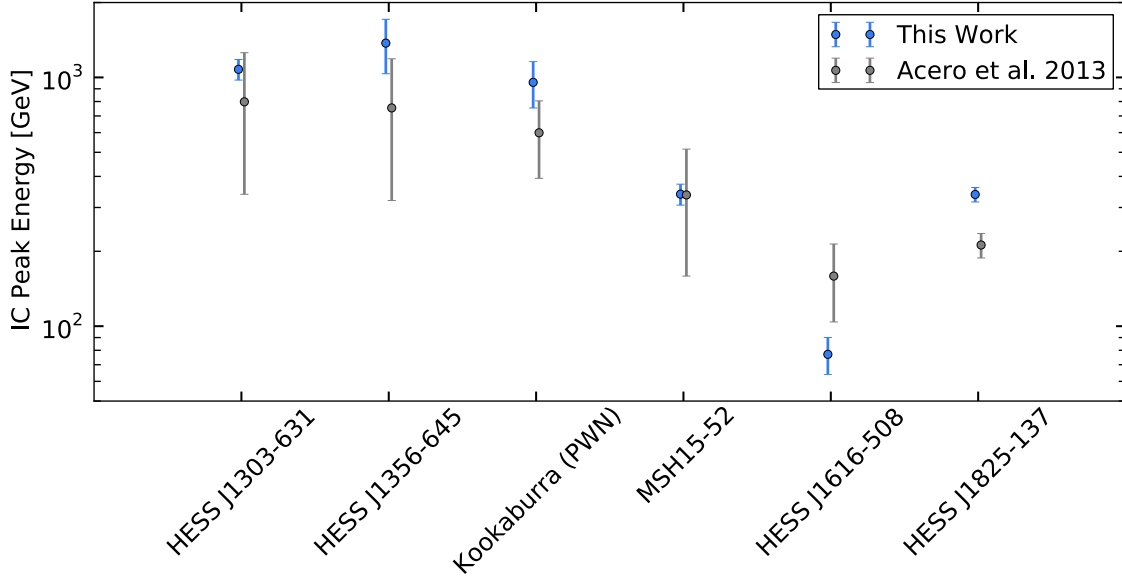
Figure 5.25.: Comparison of the measured IC peaks to the six PWNe which also appear in Acero et al. (2013). To enhance visibility, grey points are slightly shifted to the right with respect to the blue ones.

and H. E. S. S. is combined in one analysis framework to perform a uniform analysis of the population γ-ray emitting PWNe. In particular, this work presents a consistent approach to determine the energy of IC peaks. To achieve a uniform analysis in the likelihood framework of GAMMALIB, a new analysis philosophy is applied to VHE γ-ray data. The traditional, region-based approach to determine the underlying background level is replaced by a full description of the background in the FoV. The latter requires a model for the background events for each run. In the presented approach, this model relies on the basic assumption that the spatial distribution of γ-like background can be reasonably approximated.

Compared to the introduced background modelling, the advantage of the reflected region method is that the background level is determined from the same observational run as the VHE γ-ray signal. The current analysis frameworks of H. E. S. S. uses the determined background level as fixed underlying component. This method was developed in the beginning of VHE γ-ray astronomy, when only few sources of point-like nature were expected. Accordingly, the region-based technique is a reasonable approach in case the source of interest is small compared to the FoV. The sensitivity of current-generation detectors, however, reveals sky regions with many extended and overlapping VHE γ-ray sources, which might further be confused with large-scale diffuse emission. In such cases, the region-based approach to determine the background level reaches its limitation.

The likelihood in GAMMALIB provides much more flexibility to analyse crowded regions in the sky. Based on the model fitting approach from the Fermi Science Tools, GAMMALIB can analyse multiple, overlapping sources on top of large-scale structures. Further studies are ongoing to investigate the maximum level of source extensions which can be measured in GAMMALIB. The problem of a run-by-run varying background level is circumvented by handling the background as model which is free to adjust in the likelihood optimisation. Since the analysis in GAMMALIB starts from reconstructed event lists, this framework is not limited

to a specific instrument. GAMMALIB/CTOOLS has proven to be capable of combining data from several γ-ray detectors to gain a broader insight to a source of interest.

The presented likelihood approach provides the flexibility to combine spatial and spectral modelling, which is strictly separated in current IACT analysis frameworks. In one analysis run with `ctlike` the position, extension and spectrum of a γ-ray source can be determined by a global fit.

Current VHE γ-ray instruments have reached the sensitivity to detect and resolve a large number of sources. The likelihood framework of GAMMALIB provides a reasonable alternative for traditional analysis methods which reach their limit when it comes to crowded sky regions. This work presented an extensive scientific validation of the likelihood framework by deriving astrophysical results. In the following, these results are discussed.

5.8. Astrophysical Discussion

The IC peaks, measured by means of the GAMMALIB likelihood framework, show a rather broad distribution (see Fig. 5.24). The highest IC peak energy of $\sim 4\,\mathrm{TeV}$ originates from Vela X. This spectral maximum was already detected by Aharonian et al. (2006c) and is hence expected. As described in Sect. 2.3, Vela X is located at a distance of $290\,\mathrm{pc}$. Due to its large extension, H. E. S. S. only detects the innermost region of this PWN. Consequently, the spectral maximum derives from the freshly injected electrons exclusively. Since the detected *Fermi*-LAT source from Vela X is offset from the VHE centroid (Grondin et al. 2013), the relic PWN, consisting of older electrons is not considered in the conducted analysis. For this source, an analysis with a detailed, energy-dependent spatial template would be necessary for a sufficient description.

The Crab Nebula and N 157B belong to the PWNe with low energy peaks ($80\,\mathrm{GeV}$ and $300\,\mathrm{GeV}$, respectively). Regarding their IC peaks, however, these two exceptional PWNe do not significantly protrude from the PWN population. Although N 157B is not detected by *Fermi*-LAT, the corresponding data constrains the IC peak. Fig. 5.26 presents the derived SED of N 157B to illustrate the combination of upper limits from *Fermi*-LAT data with the firm H. E. S. S. detection. In blue, the spectral data points are shown. In case the source could not be detected with $\mathrm{TS} > 4$, an upper limit is derived, which is denoted by a downward arrow. In the *Fermi*-LAT range, two data points reveal an excess above the defined significances threshold. The data point at low energies is computed with $\mathrm{TS} \approx 12$, while for the measurement at $\sim 500\,\mathrm{GeV}$, the fit revealed $\mathrm{TS} \approx 22$. The derived significances indicate that, after $5\,\mathrm{yr}$ of data-taking, the sensitivity of *Fermi*-LAT approaches the flux level of N 157B.

To study the spectral evolution of PWNe, the measured IC peaks are inspected with respect to the characteristic age of the associated pulsar. The results are presented in Fig. 5.27, illustrating the large scatter of IC peaks between $40\,\mathrm{GeV}$ and $4\,\mathrm{TeV}$. In case of an evolutionary behaviour, a general correlation with the characteristic age should be visible. A dependency, however, can not be manifested. Nevertheless, a slight positive correlation can be recognised but the small number of considered PWNe prevents to draw firm conclusions. In the presented Figure, the broadly discussed Crab Nebula and N 157B are highlighted for comparison to the rest of the PWN population.

For comparison, the model presented in Sect. 2.2.3 is overlaid in Fig. 5.27. The solid black line represents the "mean model" from Table 2.1. Mimicking an intrinsic scatter, the shaded grey area is computed by varying the parameters in within the ranges listed in the same
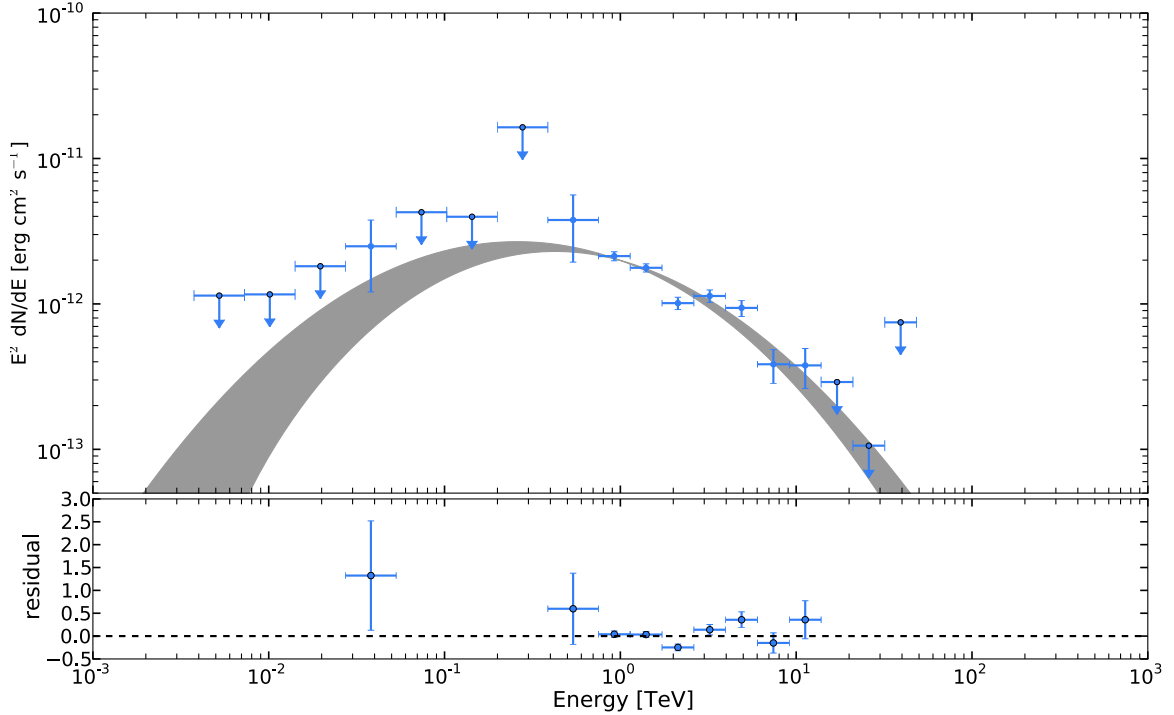
Figure 5.26.: Combined SED of N 157B. The blue data points represent the analysis result in energy slices. Downward arrows indicate an upper limit due to the lack of statistical significance. The shaded grey area depicts the 68% confidence region of the best-fit spectral model. In the lower panel, residuals from the data points to the best-fit model are shown.

Table. The time-dependent model predicts a significant shift of the IC peak towards lower energies for evolved PWNe. In contrast, the measured IC peak energies show a slight trend towards higher energies with increasing age. The data therefore contradicts the model prediction. Consequently, the evolutionary model might be too simplistic to describe the spectral evolution of the detected PWN population.

The large scatter of measured IC peaks implies that generalising PWNe by means of an evolutionary model is rather complex. The time-dependent model considers the evolution to be mainly dependent on the energy-providing pulsar , input magnetic field and dynamical expansion. As shown in Chap. 3, however, the unique environment of a PWN may play an important role regarding the evolutionary behaviour of PWNe. Therefore, a model to globally predict the spectral appearance of PWNe should also to take into account specific environmental conditions.

Interpreting evolutionary trends of the PWN population, one has to keep in mind that the characteristic age might deviate from the true pulsar age. One should further consider that the detected PWN population is subject to observational biases. The detection of PWNe with harder spectra, i.e. higher IC peak energies might be generally favoured by γ-ray detectors. In both cases of *Fermi*-LAT and H. E. S. S., this originates in the strongly decreasing background with energy. Sources of γ rays with hard spectra can be distinguished from the background much easier. In addition, the current understanding of expanding PWNe might
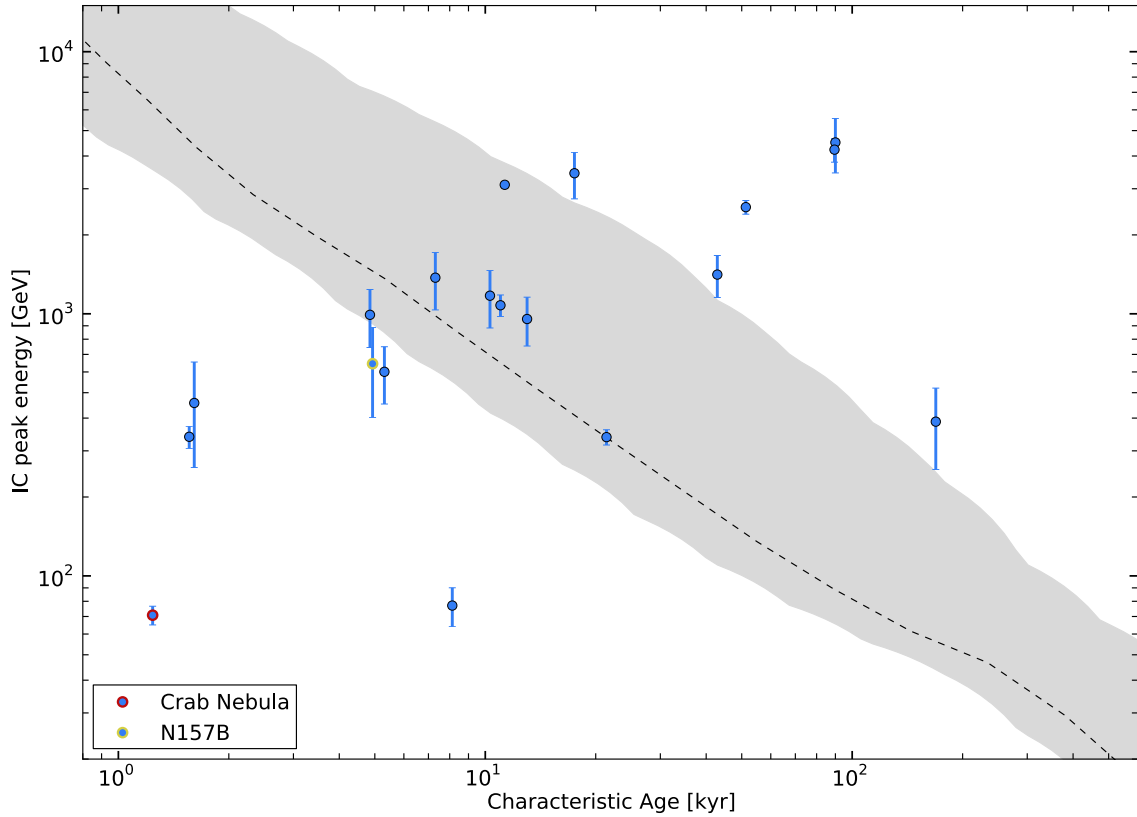
Figure 5.27.: IC peak energy plotted versus the characteristic age of the corresponding pulsar. The Crab Nebula and N 157B, which are discussed in detailed in this work, are highlighted in colours. The black dashed line represents the predicted evolution of the time-dependent model shown in Sect. 2.2.3. The grey-shaded band depicts the envelope of the model derived by the parameter scatter listed in Table 2.1.

lead to large γ-ray sources with low surface brightnesses. Therefore, evolved PWNe could reveal only their bright core with fresh injected electrons. This could lead to a similar effect as for Vela X.

In conclusion, the analysis in GAMMALIB/CTOOLS confirms the hypothesis of a diverse PWN population. The obtained results should however be taken with care due to pending investigations of the exact systematic uncertainty which is introduced with this framework. In addition, the observational bias should be quantified to draw conclusions. The main result of this Chapter is the functioning likelihood analysis framework, which can provide interesting physical results in the future.

6. Conclusion and Outlook

In this thesis, a detailed study of the population of γ-ray emitting PWNe was presented. The investigated sample of PWNe revealed a large diversity regarding their γ-ray emission. Generalising the evolution of PWNe with a time-dependent model makes us understand universal trends but also shows large deviations from the expectation for individual objects. This indicates that each PWN is unique and requires dedicated considerations to understand its particular properties. In this work, a stationary modelling was conducted for the exceptionally IC bright PWN N 157B in the LMC. This object, powered by the most energetic pulsar known, exhibits a rather low magnetisation of its particle wind. In contrast, the famous Crab Nebula with its likewise energetic pulsar, appears rather different. The pulsar wind of the Crab Nebula is much more magnetised compared to N 157B. Although their corresponding pulsars are quite similar in terms of energetics, this interesting difference of these two objects indicates that their surroundings could play an important role regarding the evolution and appearance.

Focusing on the Crab Nebula, this thesis investigated the unexpected flares of this PWN in the HE γ-ray regime. With an updated reconstruction method, the time-averaged spectra of pulsar and nebula were measured down to 50 MeV. In addition, this work presented the most up-to-date light curve of the Crab with roughly 5 yr of *Fermi*-LAT observations. Variability in the Crab flux could be measured on various time scales, while no indications for periodicity in the light curve was found. Investigations of the SEDs of the five major flares revealed a large diversity between the flares. The brighter ones tend to show evidence for a spectral cut-off. This work further presented a dedicated analysis of the Crab Nebula flare in March 2013, which revealed a rapidly varying synchrotron component. The time scale of this variability was determined to 6.5 h, which suggests the flaring origin to be very confined in the Crab Nebula. The currently most promising explanations for the flares are violent events of magnetic reconnection, which produce relativistic particles, boosted towards our line of sight. A possible site for these flares could be the "inner knot" which is suggested to be the projection along the wind termination shock.

As technical part of this thesis, a new likelihood framework to analyse γ-ray data was presented. This analysis software, named GAMMALIB, is currently being developed for the future CTA observatory. The planned detector system will provide a much higher sensitivity compared to current-generation, ground-based VHE γ-ray detectors such as the H. E. S. S. experiment. The large number of expected detections with CTA will complicate the data analysis procedure. The analysis philosophy of GAMMALIB is intended to model the entire FoV, similar to how satellite γ-ray data are treated. To analyse H. E. S. S. data within this framework, a model describing the cosmic-ray induced γ-like background was developed. The model was built from empty-field observations and could be statistically verified to function satisfactorily. Using the presented background model, the framework was shown to be capable of reproducing H. E. S. S. analysis results quite accurately. In addition, the FoV likelihood modelling depicts a simple and efficient way to separate overlapping γ-ray sources and derive their spectra without obstacles. The GAMMALIB analysis has also shown to properly handle

large-scale structures of excess, e.g. in the LMC and the Galactic plane. These structures might be associated with diffuse VHE γ-ray emission, or might turn out to be or contain a systematic effect of the data or analysis. Systematic studies are ongoing to investigate these results and investigate the origins of the measured large-scale structures.

Having proven that the likelihood framework depicts a good alternative for conventional H. E. S. S. analyses, the analysis of *Fermi*-LAT data was also positively tested in GAMMALIB. The structure of the introduced software framework further provides the possibility to analyse data from several instruments in one analysis. This feature was used in this thesis to measure IC peaks of PWNe combining the information from *Fermi*-LAT and H. E. S. S. data. The obtained peaks in this analysis were cross-checked against values from the literature which were available for six PWNe. The results confirm the capabilities of GAMMALIB to combine data from several instruments in one analysis framework. The IC peaks, measured with the presented likelihood framework, further support the hypothesis of the large diversity of PWNe. The diversity is hard to explain by the presented model, which describes the time evolution of PWNe. In conclusion, each γ-ray emitting PWN of the presented population is unique regarding its properties. An important factor, influencing the appearance of PWNe, might be their environmental conditions.

This thesis presented first results and extended scientific validation of the GAMMALIB framework. The likelihood analysis is perfectly suited to be applied to H. E. S. S. data. Accordingly, this thesis presented a pioneering analysis approach for IACTs, which provides more flexibility than traditional analysis methods. The likelihood framework of GAMMALIB may become especially important for the new $28\,\mathrm{m}$ telescope in the centre of the H. E. S. S. array. This telescope has a lower energy threshold ($\sim 30\,\mathrm{GeV}$), combined with a smaller FoV and a broader PSF. These settings complicate the application of e.g. the reflected region method, especially in regions where diffuse γ-ray emission is present. The GAMMALIB likelihood framework would provide a suitable alternative for the data analysis of this new telescope.

The future CTA observatory, for which the presented software is primarily designed, is expected to reveal a large number (> 1000) VHE γ-ray sources. Consequently, there will be many crowded sky regions with overlapping extended sources and large-scale diffuse components. The traditional region-based approach is unsuited for such challenging analyses. The presented GAMMALIB analysis framework already offers a good alternative for the high-level analysis of CTA data.

A. Supplementary Material for Chapter 5

A.1. Run Quality Selection Parameters

Runs that are selected for the analysis in GAMMALIB are required to pass certain criteria. The following Table list the applied selections. Parameter without a unit are calculated internally in the H. E. S. S. software. For documentation, these values are also listed here without explanation.

Table A.1.: Run quality selection criteria

Parameter	Minimum value	Maximum value
# Telescopes in run	3	4
Mean trigger rate [Hz]	100	500
Mean trigger stability	0	4
Broken pixels [%]	0	15
Relative Humidity [%]	0	90
Radiometer	-999	-20
Radiometer stability	0	3
Observation mode	Tracking	

A.2. Dependencies of the Fitted Background Model Normalisation

The background normalisation for each of the presented off-runs is checked for a dependency on run specific parameters. In each of the following Figures, the fitted background normalisation is plotted against a self-describing run variable.
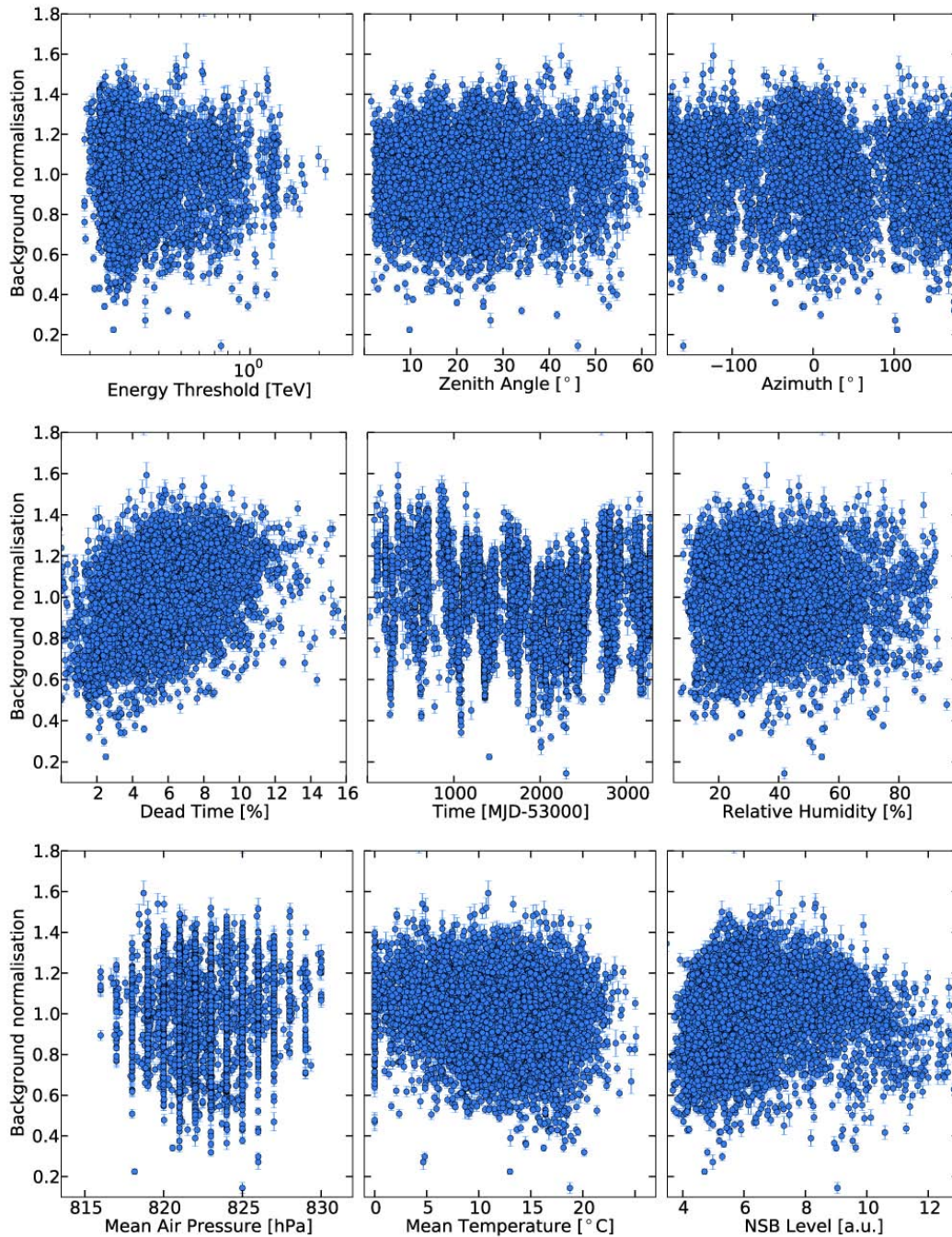
Figure A.1.: The fitted background normalisation, plotted against various run-specific parameters.

A.3. Verification of the Background Model in Observational Bins

In the main text, the accumulated TS distribution is shown for all off-runs. In this Section, the distribution is subdivided into the observational bins. The following Figures present the TS distribution from the TS maps derived from each bin individually. The respective bin is indicated on the top right of each panel.
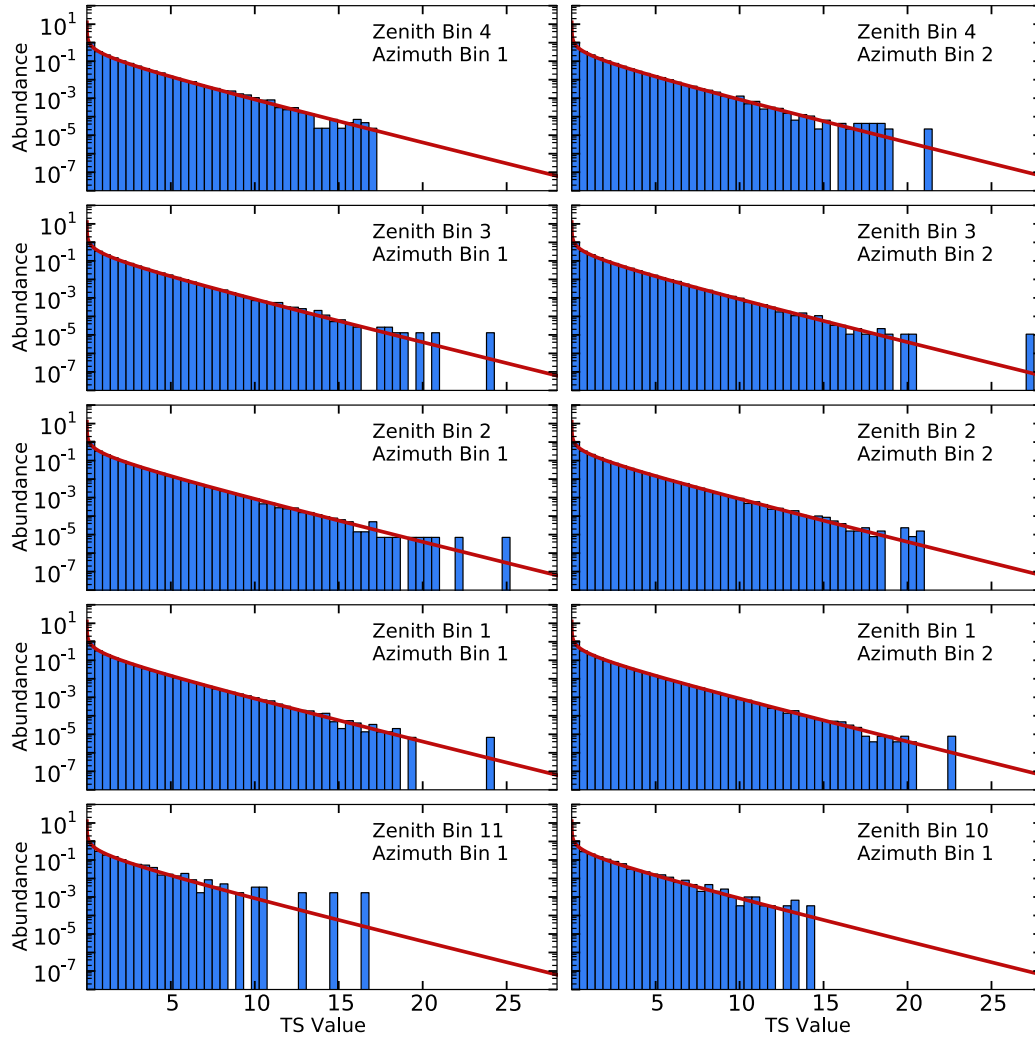
Figure A.2.: TS distributions derived from off-runs in each observational bin. The red line denotes the corresponding χ^2-distribution in each panel.
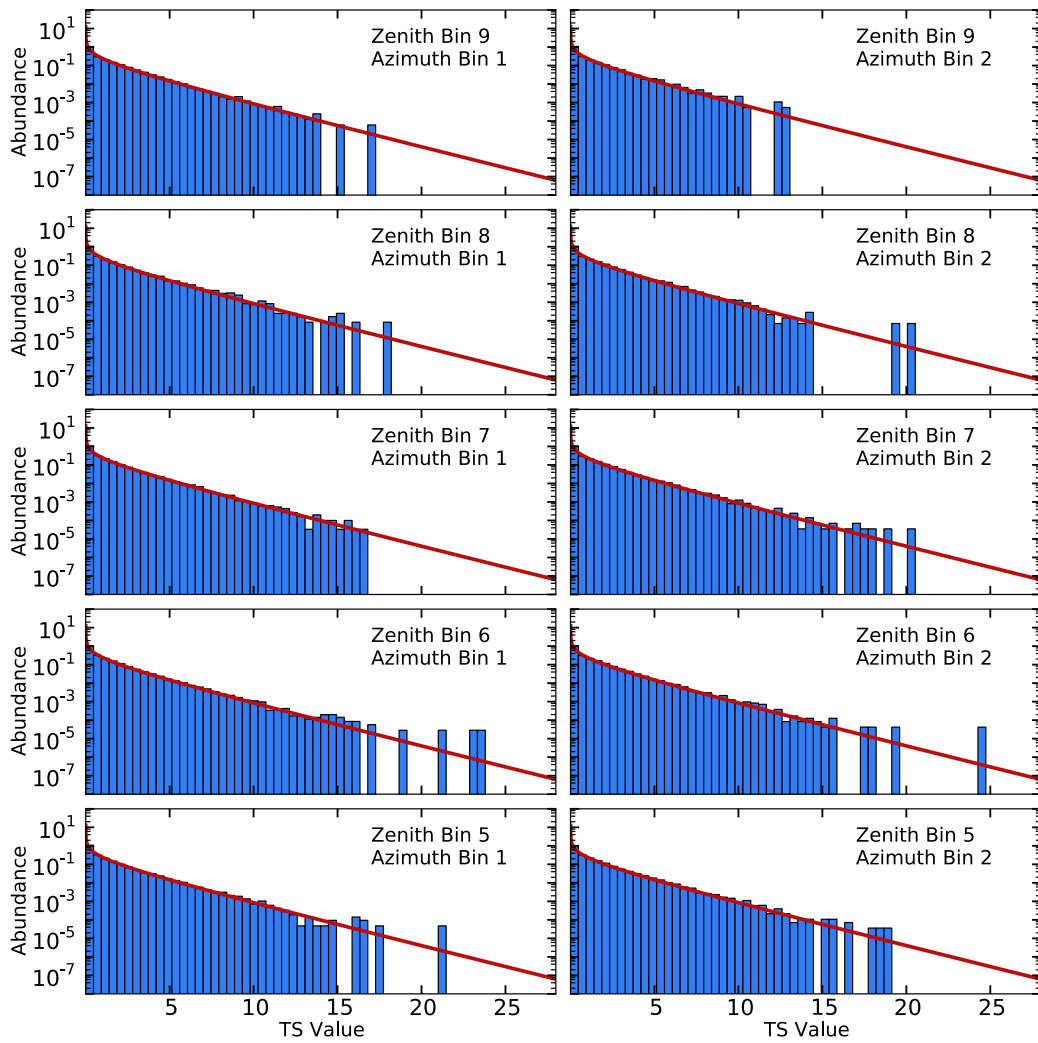
Figure A.3.: Second part of Fig. A.2.

A.4. γ-ray Exposure Calculation

To generate the contours shown in Fig. 5.19, an exposure map for all runs is calculated. The exposure represents the run-wise, energy-integrated effective area, multiplied by the observation time, for each position in the sky. To create a map for all available observations, all selected runs are accumulated to get the total exposure in each sky position. The unit of the exposure is $cm^2 s$. The exposure map of the LMC, from which the contours are derived is presented in Fig. A.4
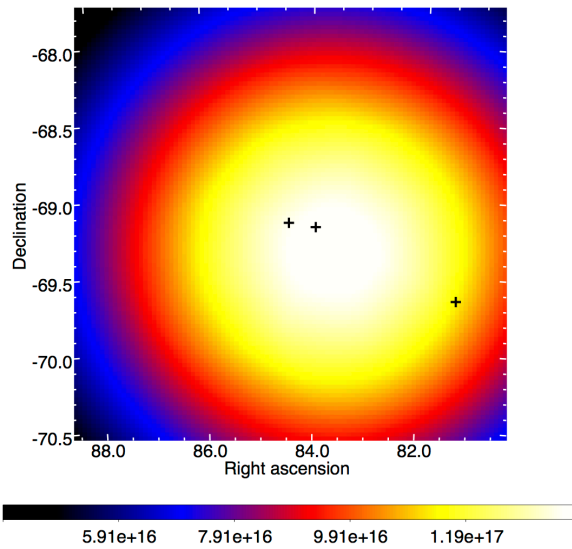
Figure A.4.: Exposure map of the LMC region accumulated from all available H. E. S. S. runs. The unit of the colour scale is $cm^2 s$. The black crosses represent the positions of the three sources in the RoI.

A.5. Complex Morphologies of Four PWNe

To obtain good spectra, the PWN morphology should match the observed ones. As presented in Table 5.7, four PWNe could not be modelled analytically. Empirical templates are built instead. The four templates are visualised in Fig. A.5.
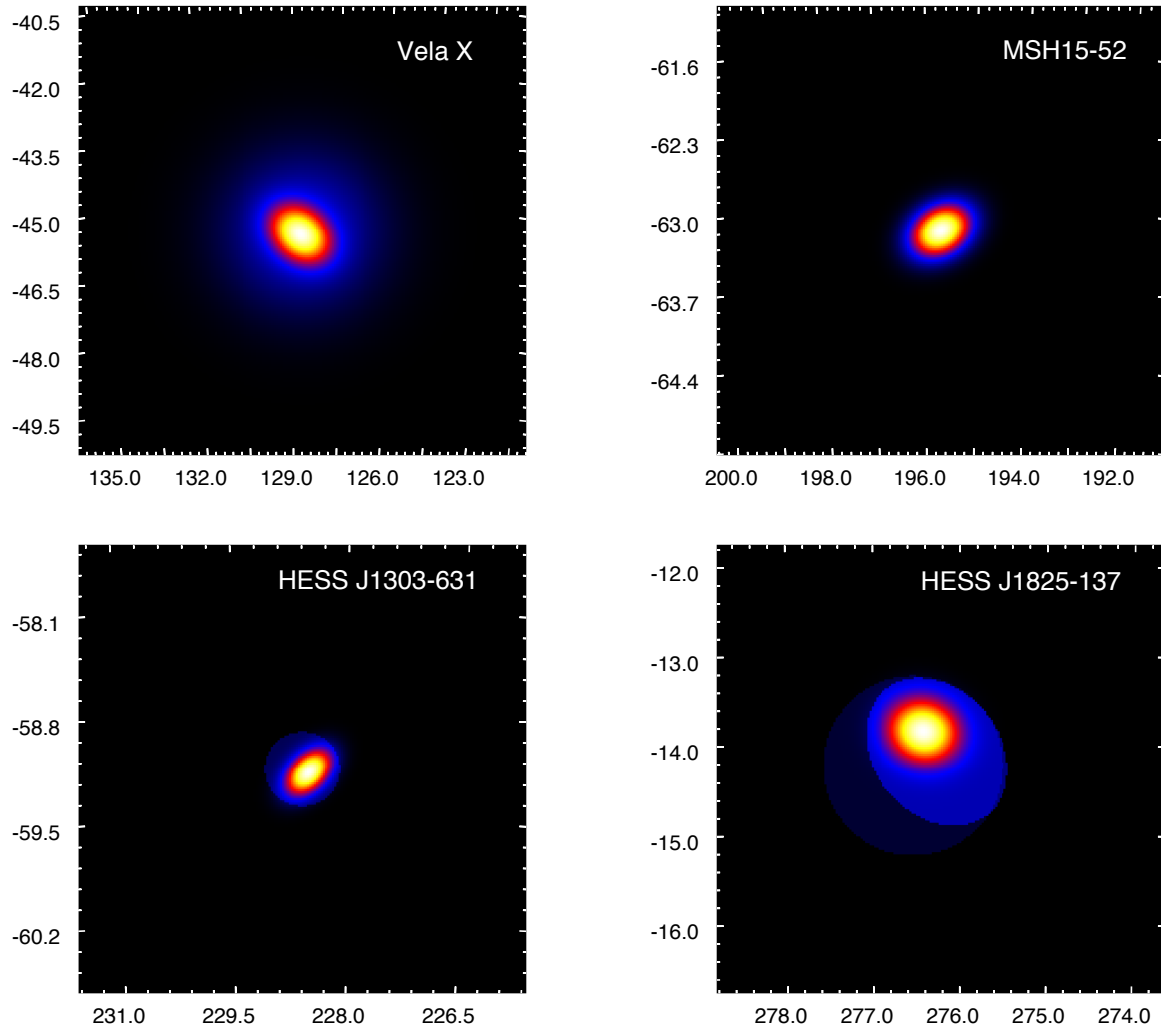
Figure A.5.: The templates used for PWNe with complex morphologies. Note that each map has a different size in the sky. The coordinates indicate Right Ascension and Declination in units of degrees.

A.6. Residual Maps of H. E. S. S. Analyses

To verify the correct fit convergence in the VHE γ-ray regime, model maps are created for each RoI using `ctmodel`. In the same spatial binning, all considered events are filled into a count map. This task is conducted with `ctbin`. Using Eq. 4.8, residual significance maps are computed (Fig. A.6-A.6). To illustrate possible structures, each map is smoothed with a Gaussian kernel of $0°\!.09$. Accordingly, the colour scale does not represent the absolute significance values. All maps are depicted in a tangential projection, covering a $2°\!.4 \times 2°\!.4$ region on the sky, which is centred on the best-fit position of the respective PWN Table 5.8. Three RoIs show evidence for left-over structures, which can be attributed to the complex sky region: HESS J1718$-$385 is located close to the shell-type SNR RX J1713.7$-$3946. The modelling of the latter would require more detailed considerations. G0.9+0.1 is located close to the Galactic Center region with strong contribution from diffuse emission. HESS J1825$-$137 has a complex morphology, which is difficult to account for. Still, the deviations from a flat residual distribution is relatively small even in those cases.

G292.2-0.5

HESS J1303-631

HESS J1356-645

Kookaburra (Rabbit)

Kookaburra (PWN)

HESS J1458-608

MSH15-52

HESS J1616-508

HESS J1708-433

HESS J1718-385

G0.9+0.1

HESS J1809-193

G0.9+0.1

HESS J1809-193

HESS J1813-178

HESS J1825-137

HESS J1831-098

HESS J1833-105

A.7. SEDs of PWNe Derived with the Combined Analysis in GAMMALIB

All spectra, derived in GAMMALIB, which were not shown in the main text are presented in this Section. For each PWNe, ten spectral bins are calculated with `ctspecpoints`. Since this tool is still in a preliminary testing phase, some data points could not be calculated due to technical problems, which are under investigations. The data belonging to these points were correctly used though in the unbinned fit.

List of Figures

List of Tables

Bibliography

Abdo, A. A., Ackermann, M., Ajello, M., et al. 2011, Science, 331, 739

Abdo, A. A., Ackermann, M., Ajello, M., et al. 2010a, ApJ, 708, 1254

Abdo, A. A., Ackermann, M., Ajello, M., et al. 2010b, A&A, 512, A7

Abdo, A. A., Ackermann, M., Ajello, M., et al. 2010c, Physical Review Letters, 104, 101101

Abdo, A. A., Ackermann, M., Ajello, M., et al. 2009, Phys. Rev. D, 80, 122004

Abdo, A. A., Ajello, M., Allafort, A., et al. 2013, ApJS, 208, 17

Abramowski, A., Acero, F., Aharonian, F., et al. 2012, A&A, 548, A38

Acero, F., Ackermann, M., Ajello, M., et al. 2013, ApJ, 773, 77

Ackermann, M., Ajello, M., Albert, A., et al. 2013, ApJ, 771, 57

Ackermann, M., Ajello, M., Albert, A., et al. 2012a, ApJS, 203, 4

Ackermann, M., Ajello, M., Atwood, W. B., et al. 2012b, ApJ, 750, 3

Aharonian, F., Akhperjanian, A., Beilicke, M., et al. 2004a, ApJ, 614, 897

Aharonian, F., Akhperjanian, A. G., Aye, K.-M., et al. 2005a, Science, 307, 1938

Aharonian, F., Akhperjanian, A. G., Aye, K.-M., et al. 2005b, A&A, 435, L17

Aharonian, F., Akhperjanian, A. G., Aye, K.-M., et al. 2004b, Astroparticle Physics, 22, 109

Aharonian, F., Akhperjanian, A. G., Barres de Almeida, U., et al. 2008, A&A, 477, 353

Aharonian, F., Akhperjanian, A. G., Bazer-Bachi, A. R., et al. 2006a, A&A, 457, 899

Aharonian, F., Akhperjanian, A. G., Bazer-Bachi, A. R., et al. 2006b, A&A, 448, L43

Aharonian, F., Akhperjanian, A. G., Bazer-Bachi, A. R., et al. 2006c, A&A, 448, L43

Aharonian, F., Akhperjanian, A. G., Bazer-Bachi, A. R., et al. 2006d, ApJ, 636, 777

Aharonian, F., Akhperjanian, A. G., Bazer-Bachi, A. R., et al. 2006e, Nature, 439, 695

Aharonian, F., Akhperjanian, A. G., Bazer-Bachi, A. R., et al. 2006f, A&A, 460, 365

Aharonian, F. A., Akhperjanian, A. G., Barrio, J. A., et al. 2000, ApJ, 539, 317

Aharonian, F. A., Akhperjanian, A. G., Bazer-Bachi, A. R., et al. 2005c, A&A, 442, L25

Aitchinson, J. & Brown, J. A. C. 1963, The Lognormal Distribution (Cambridge: Cambridge University Press)

Albert, J., Aliu, E., Anderhub, H., et al. 2008, ApJ, 674, 1037

Aleksić, J., Alvarez, E. A., Antonelli, L. A., et al. 2012, A&A, 540, A69

Aliu, E., Archambault, S., Arlen, T., et al. 2013, ApJ, 764, 38

Aliu, E., Archambault, S., Aune, T., et al. 2014, ApJ, 781, L11

Arons, J. 2012, Space Sci. Rev., 173, 341

Atoyan, A. M. & Aharonian, F. A. 1996, MNRAS, 278, 525

Atwood, W., Albert, A., Baldini, L., et al. 2013, ArXiv e-prints, 1303.3514

Atwood, W. B., Abdo, A. A., Ackermann, M., et al. 2009, ApJ, 697, 1071

Atwood, W. B., Bagagli, R., Baldini, L., et al. 2007, Astroparticle Physics, 28, 422

Auger, P., Ehrenfest, P., Maze, R., Daudin, J., & Fréon, R. A. 1939, Reviews of Modern Phyics, 11, 288

Baade, W. & Zwicky, F. 1934, Physical Review, 46, 76

Bai, X.-N. & Spitkovsky, A. 2010, ApJ, 715, 1282

Balbo, M., Walter, R., Ferrigno, C., & Bordas, P. 2011, A&A, 527, L4

Bamba, A., Ueno, M., Nakajima, H., & Koyama, K. 2004, ApJ, 602, 257

Bechtol et al., K. 2014, in American Astronomical Society Meeting Abstracts, Vol. 223, 426.08

Bednarek, W. & Idec, W. 2011, MNRAS, 414, 2229

Bennett, C. L., Halpern, M., Hinshaw, G., et al. 2003, ApJS, 148, 1

Berge, D., Funk, S., & Hinton, J. 2007, A&A, 466, 1219

Blondin, J. M., Chevalier, R. A., & Frierson, D. M. 2001, ApJ, 563, 806

Blumenthal, G. R. & Gould, R. J. 1970, Reviews of Modern Physics, 42, 237

Bogovalov, S. V. 1999, A&A, 349, 1017

Bouvier, A., Gebremedhin, L., Johnson, C., et al. 2013, in Society of Photo-Optical Instrumentation Engineers (SPIE) Conference Series, Vol. 8852

Brucker, J. 2013, Dissertation, Friedrich-Alexander-Universität, Erlangen, Germany

Brun, F., de Naurois, M., Hofmann, W., et al. 2010, in 25th Texas Symposium on Relativistic Astrophysics

Bucciantini, N., Arons, J., & Amato, E. 2011, MNRAS, 410, 381

Bucciantini, N., Thompson, T. A., Arons, J., Quataert, E., & Del Zanna, L. 2006, MNRAS, 368, 1717

Buehler, R., Scargle, J. D., Blandford, R. D., et al. 2012, ApJ, 749, 26

Bühler, R. & Blandford, R. 2014, Reports on Progress in Physics, 77, 066901

Bykov, A. M., Pavlov, G. G., Artemyev, A. V., & Uvarov, Y. A. 2012, MNRAS, 421, L67

Camus, N. F., Komissarov, S. S., Bucciantini, N., & Hughes, P. A. 2009, MNRAS, 400, 1241

Caraveo, P. A., De Luca, A., Mignani, R. P., & Bignami, G. F. 2001, ApJ, 561, 930

Carrigan, S. 2007, PhD thesis, Ruperto-Carola University of Heidelberg

Carrigan, S., Brun, F., Chaves, R. C. G., et al. 2013, ArXiv e-prints, 1307.4690

Carrigan, S., Hinton, J. A., Hofmann, W., & et al. 2008, in International Cosmic Ray Conference, Vol. 2, 659–662

Cash, W. 1979, ApJ, 228, 939

Cerutti, B., Uzdensky, D. A., & Begelman, M. C. 2012, ApJ, 746, 148

Cerutti, B., Werner, G. R., Uzdensky, D. A., & Begelman, M. C. 2013, ApJ, 770, 147

Cerutti, B., Werner, G. R., Uzdensky, D. A., & Begelman, M. C. 2014a, Physics of Plasmas, 21, 056501

Cerutti, B., Werner, G. R., Uzdensky, D. A., & Begelman, M. C. 2014b, ApJ, 782, 104

Chalme-Calvet, R., de Naurois, M., & Tavernet, J.-P. 2014, ArXiv e-prints, 1403.4550

Chen, Y., Wang, Q. D., Gotthelf, E. V., et al. 2006, ApJ, 651, 237

Chevalier, R. A. 1977, in Astrophysics and Space Science Library, Vol. 66, Supernovae, ed. D. N. Schramm, 53

Chiang, J. 2012, Automated Science Processing for the Fermi Large Area Telescope, ed. M. J. Way, J. D. Scargle, K. M. Ali, & A. N. Srivastava, 41–54

Chu, Y.-H., Kennicutt, Jr., R. C., Schommer, R. A., & Laff, J. 1992, AJ, 103, 1545

Clark, D. H. & Stephenson, F. R. 1977, The historical supernovae

Clausen-Brown, E. & Lyutikov, M. 2012, MNRAS, 426, 1374

Cocke, W. J., Disney, M. J., & Taylor, D. J. 1969, Nature, 221, 525

Collins, II, G. W., Claspy, W. P., & Martin, J. C. 1999, PASP, 111, 871

Commichau, S. C., Biland, A., Kranich, D., & et al. 2008, International Cosmic Ray Conference, 3, 1357

Compton, A. H. 1923, Phys. Rev., 21, 483

de Jager, O. C. & Djannati-Ataï, A. 2009, in Astrophysics and Space Science Library, ed. W. Becker, Vol. 357, 451

de Jager, O. C., Ferreira, S. E. S., Djannati-Ataï, A., et al. 2009, ArXiv e-prints, 0906.2644

de Jager, O. C. & Harding, A. K. 1992, ApJ, 396, 161

de Naurois, M. 2012, Habilitation, Universit Pierre et Marie Curie - Paris VI (13/03/2012), Pascal Vincent (Pr.), Paris, France

de Naurois, M. & Rolland, L. 2009, Astroparticle Physics, 32, 231

Dicke, R. H., Peebles, P. J. E., Roll, P. G., & Wilkinson, D. T. 1965, ApJ, 142, 414

Dickel, J. R. & Milne, D. K. 1995, AJ, 109, 200

Doering, M., Bernloehr, K., Hermann, G., Hofmann, W., & Lampeitl, H. 2001, ArXiv e-prints, 0107149

Dubus, G., Contreras, J. L., Funk, S., et al. 2013, Astroparticle Physics, 43, 317

Duyvendak, J. J. L. 1942, PASP, 54, 91

Edwards, R. T., Hobbs, G. B., & Manchester, R. N. 2006, MNRAS, 372, 1549

Egberts, K., Brun, F., Casanova, S., et al. 2013, ArXiv e-prints, 1308.0161

Fermi, E. 1949, Physical Review, 75, 1169

Fomin, V. P., Stepanian, A. A., Lamb, R. C., et al. 1994, Astroparticle Physics, 2, 137

Funk, S. 2005, Dissertation, Ruprecht-Karls-Universität, Heidelberg, Germany

Funk, S., Hinton, J., Hermann, G., et al. 2005, in American Institute of Physics Conference Series, Vol. 745, High Energy Gamma-Ray Astronomy, ed. F. A. Aharonian, H. J. Völk, & D. Horns, 753–757

Gaensler, B. M. & Slane, P. O. 2006, ARA&A, 44, 17

Galbraith, W. & Jelley, J. V. 1953, Nature, 171, 349

Gelfand, J. D., Slane, P. O., & Zhang, W. 2009, ApJ, 703, 2051

Goldreich, P. & Julian, W. H. 1969, ApJ, 157, 869

Grondin, M.-H., Romani, R. W., Lemoine-Goumard, M., et al. 2013, ApJ, 774, 110

Guilbert, P. W., Fabian, A. C., & Rees, M. J. 1983, MNRAS, 205, 593

Gvaramadze, V. V. 2001, A&A, 374, 259

H. E. S. S. Collaboration, Abramowski, A., Aharonian, F., et al. 2014, A&A, 562, L4

Helene, O. 1983, Nuclear Instruments and Methods in Physics Research, 212, 319

H.E.S.S. Collaboration,. in prep., Extremely energetic cosmic ray accelerators in the Large Magellanic Cloud

H.E.S.S. Collaboration, Abramowski, A., Acero, F., Aharonian, F., & Akhperjanian. 2012a, A&A, 545, L2

H.E.S.S. Collaboration, Abramowski, A., Acero, F., et al. 2012b, A&A, 548, A46

H.E.S.S. Collaboration, Abramowski, A., Acero, F., et al. 2012c, A&A, 548, A46

H.E.S.S. Collaboration, Abramowski, A., Acero, F., et al. 2011, A&A, 525, A46

Hester, J. J. 2008, ARA&A, 46, 127

Hester, J. J., Mori, K., Burrows, D., et al. 2002, ApJ, 577, L49

Hester, J. J., Scowen, P. A., Sankrit, R., et al. 1995, ApJ, 448, 240

Hewish, A., Bell, S. J., Pilkington, J. D. H., Scott, P. F., & Collins, R. A. 1968, Nature, 217, 709

Hillas, A. M. 1985a, International Cosmic Ray Conference, 3, 445

Hillas, A. M. 1985b, International Cosmic Ray Conference, 7, 231

Hobbs, G. B., Edwards, R. T., & Manchester, R. N. 2006, MNRAS, 369, 655

Homola, P., Engel, R., & Wilczyński, H. 2014, ArXiv e-prints, 1405.4671

Čerenkov, P. A. 1937, Phys. Rev., 52, 378

Indebetouw, R., de Messières, G. E., Madden, S., et al. 2009, ApJ, 694, 84

Jackson, B., Scargle, J. D., Barnes, D., et al. 2003, ArXiv Mathematics e-prints, 0309285

James, F. & Roos, M. 1975, Computer Physics Communications, 10, 343

Kalapotharakos, C. & Contopoulos, I. 2009, A&A, 496, 495

Kalapotharakos, C., Harding, A. K., Kazanas, D., & Contopoulos, I. 2012a, ApJ, 754, L1

Kalapotharakos, C., Kazanas, D., Harding, A., & Contopoulos, I. 2012b, ApJ, 749, 2

Kargaltsev, O. & Pavlov, G. G. 2010, in American Institute of Physics Conference Series, Vol. 1248, American Institute of Physics Conference Series, ed. A. Comastri, L. Angelini, & M. Cappi, 25–28

Kargaltsev, O., Rangelov, B., & Pavlov, G. G. 2013, ArXiv e-prints, 1305.2552

Kennel, C. F. & Coroniti, F. V. 1984, ApJ, 283, 694

King, I. 1962, AJ, 67, 471

Kirk, J. G. 2004, Physical Review Letters, 92, 181101

Klein, O. & Nishina, Y. 1929, Zeitschrift für Physik, 52, 853

Klepser, S., Carrigan, S., de Oña Wilhelmi, E., et al. 2013, ArXiv e-prints, 1307.7905

Knödlseder, J. 2012, in Astronomical Society of the Pacific Conference Series, Vol. 461, Astronomical Data Analysis Software and Systems XXI, ed. P. Ballester, D. Egret, & N. P. F. Lorente, 65

Knödlseder, J., Mayer, M., Deil, C., et al. 2013, ArXiv e-prints

Komissarov, S. S. 2013, MNRAS, 428, 2459

Komissarov, S. S. & Lyubarsky, Y. E. 2004, MNRAS, 349, 779

Komissarov, S. S. & Lyutikov, M. 2011, MNRAS, 414, 2017

Lazarian, A. 2005, in American Institute of Physics Conference Series, Vol. 784, Magnetic Fields in the Universe: From Laboratory and Stars to Primordial Structures., ed. E. M. de Gouveia dal Pino, G. Lugones, & A. Lazarian, 42–53

Lazarian, A., Kowal, G., de Gouveia Dal Pino, E., & Vishniac, E. 2011, in IAU Symposium, Vol. 274, IAU Symposium, ed. A. Bonanno, E. de Gouveia Dal Pino, & A. G. Kosovichev, 62–71

Lazendic, J. S., Dickel, J. R., Haynes, R. F., Jones, P. A., & White, G. L. 2000, ApJ, 540, 808

Levenberg, K. 1944, Quart. J. Appl. Maths., II, 164

Li, J., Spitkovsky, A., & Tchekhovskoy, A. 2012, ApJ, 746, 60

Li, T.-P. & Ma, Y.-Q. 1983, ApJ, 272, 317

Lobanov, A. P., Horns, D., & Muxlow, T. W. B. 2011, A&A, 533, A10

Lyubarsky, Y. E. 2003, MNRAS, 345, 153

Lyubarsky, Y. E. 2012, MNRAS, 427, 1497

Lyutikov, M. 2010, MNRAS, 405, 1809

Lyutikov, M., Balsara, D., & Matthews, C. 2012, MNRAS, 422, 3118

Macri, L. M., Stanek, K. Z., Bersier, D., Greenhill, L. J., & Reid, M. J. 2006, ApJ, 652, 1133

Magalhaes, N. S., Miranda, T. A., & Frajuca, C. 2012, ApJ, 755, 54

Manchester, R. N., Hobbs, G. B., Teoh, A., & Hobbs, M. 2005, VizieR Online Data Catalog, 7245, 0

Manchester, R. N. & Taylor, J. H. 1977, Pulsars.

Marandon, V. 2010, PhD thesis, Observatoire de Paris, Université Paris 7

Marquardt, D. 1963, Journal of the Society for Industrial and Applied Mathematics, 11, 431

Marshall, F. E., Gotthelf, E. V., Middleditch, J., Wang, Q. D., & Zhang, W. 2004, ApJ, 603, 682

Marshall, F. E., Gotthelf, E. V., Zhang, W., Middleditch, J., & Wang, Q. D. 1998, ApJ, 499, L179

Mattana, F., Falanga, M., Götz, D., et al. 2009, ApJ, 694, 12

Mattox, J. R., Bertsch, D. L., Chiang, J., et al. 1996, ApJ, 461, 396

Mayall, N. U. & Oort, J. H. 1942, PASP, 54, 95

Mayer, M. 2010, Diploma thesis, Friedrich-Alexander-Universität Erlangen-Nürnberg

Mayer, M., Brucker, J., Holler, M., et al. 2012, ArXiv e-prints, 1202.1455

Mayer, M., Buehler, R., Hays, E., et al. 2013, ApJ, 775, L37

Mellinger, A. 2009, PASP, 121, 1180

Meyer, M., Horns, D., & Zechlin, H.-S. 2010, A&A, 523, A2

Micelotta, E. R., Brandl, B. R., & Israel, F. P. 2009, A&A, 500, 807

Michel, F. C. 1974, ApJ, 187, 585

Migliazzo, J. M., Gaensler, B. M., Backer, D. C., et al. 2002, ApJ, 567, L141

Mizuno, Y., Lyubarsky, Y., Nishikawa, K.-I., & Hardee, P. E. 2011, ApJ, 728, 90

Morii, M., Kawai, N., Usui, R., et al. 2011, Journal of Physics Conference Series, 302, 012062

Nolan, P. L., Abdo, A. A., Ackermann, M., et al. 2012, ApJS, 199, 31

Nolan, P. L., Arzoumanian, Z., Bertsch, D. L., et al. 1993, ApJ, 409, 697

Ojha, R., Buehler, R., Hays, E., & Dutka, M. 2012, The Astronomer's Telegram, 4239, 1

Ojha, R., Buehler, R., Hays, E., & Dutka, M. 2013, The Astronomer's Telegram, 4855, 1

Pacini, F. & Salvati, M. 1973, ApJ, 186, 249

Pence, W., Blackburn, J. K., & Greene, E. 1993, in Astronomical Society of the Pacific Conference Series, Vol. 52, Astronomical Data Analysis Software and Systems II, ed. R. J. Hanisch, R. J. V. Brissenden, & J. Barnes, 541

Pence, W. D., Chiappetti, L., Page, C. G., Shaw, R. A., & Stobie, E. 2010, A&A, 524, A42

Penzias, A. A. & Wilson, R. W. 1965, ApJ, 142, 419

Porter, T. A. & Strong, A. W. 2005, in International Cosmic Ray Conference, Vol. 4, 77

Porth, O., Komissarov, S. S., & Keppens, R. 2014, MNRAS, 438, 278

Ray, P. S., Kerr, M., Parent, D., et al. 2011, ApJS, 194, 17

Reynolds, S. P. & Chevalier, R. A. 1984, ApJ, 278, 630

Rudy, A., Horns, D., DeLuca, A., et al. in prep., Characterization of the Inner Knot of the Crab: The Site of the Gamma-ray Flares?

Sandberg, A. & Sollerman, J. 2009, A&A, 504, 525

Scargle, J. D. 1998, ApJ, 504, 405

Schoeck, F. 2010, Dissertation, Friedrich-Alexander-Universität, Erlangen, Germany

Schulz, A. in prep., Dissertation, Universität Potsdam, Germany

Sironi, L. & Spitkovsky, A. 2011a, ApJ, 741, 39

Sironi, L. & Spitkovsky, A. 2011b, ApJ, 726, 75

Sironi, L. & Spitkovsky, A. 2014, ApJ, 783, L21

Sironi, L., Spitkovsky, A., & Arons, J. 2013, ApJ, 771, 54

Smith, D. A., Guillemot, L., Camilo, F., et al. 2008, A&A, 492, 923

Sollerman, J. 2003, A&A, 406, 639

Spitkovsky, A. 2006, ApJ, 648, L51

Spitkovsky, A. 2008, ApJ, 682, L5

Staelin, D. H. & Reifenstein, III, E. C. 1968, Science, 162, 1481

Stephenson, F. R. & Green, D. A. 2002, Historical supernovae and their remnants, by
F. Richard Stephenson and David A. Green. International series in astronomy and as-
trophysics, vol. 5. Oxford: Clarendon Press, 2002, ISBN 0198507666, 5

Stothers, R. 1980, PASP, 92, 145

Striani, E., Tavani, M., Piano, G., et al. 2011, ApJ, 741, L5

Striani, E., Tavani, M., Vittorini, V., et al. 2013, ApJ, 765, 52

Sturrock, P. A. 1971, ApJ, 164, 529

Tavani, M., Bulgarelli, A., Vittorini, V., et al. 2011, Science, 331, 736

Tchekhovskoy, A., Spitkovsky, A., & Li, J. G. 2013, MNRAS, 435, L1

Uzdensky, D. A., Cerutti, B., & Begelman, M. C. 2011, ApJ, 737, L40

van der Meulen, R. D., Bloemen, H., Bennett, K., et al. 1998, A&A, 330, 321

van der Swaluw, E., Achterberg, A., Gallant, Y. A., & Tóth, G. 2001, A&A, 380, 309

van der Swaluw, E., Downes, T. P., & Keegan, R. 2004, A&A, 420, 937

VERITAS Collaboration, Aliu, E., Arlen, T., et al. 2011, Science, 334, 69

Vernetto, S. 2014, Nuclear Instruments and Methods in Physics Research A, 742, 220

Vincent, P., Denanca, J.-P., Huppert, J.-F., et al. 2003, International Cosmic Ray Conference,
5, 2887

Wang, Q. D. & Gotthelf, E. V. 1998, ApJ, 509, L109

Weisskopf, M. C., Tennant, A. F., Arons, J., et al. 2013, ApJ, 765, 56

Wilks, S. S. 1938, The Annals of Mathematical Statistics, 9, 60

Yuan, Q., Yin, P.-F., Wu, X.-F., et al. 2011, ApJ, 730, L15

Zanin, R. 2011, International Cosmic Ray Conference, 7, 72

Zhang, L., Chen, S. B., & Fang, J. 2008, ApJ, 676, 1210

Acknowledgements/Danksagung

"Keine Schuld ist dringender als die, Danke zu sagen." *Cicero*

Das Gelingen dieser Arbeit wurde von vielen Menschen maßgeblich beeinflusst. Die große Unterstützung, die ich in den letzten Jahren erfahren habe, ist von unschätzbarem Wert. An dieser Stelle möchte ich versuchen alle zu nennen, ohne die diese Arbeit nicht möglich gewesene wäre.

- Mein erster Dank gilt meinem Betreuer und Doktorvater Christian Stegmann. Seine spannende Idee, Daten zweier Instrumente zu kombinieren, hat mich begeistert. Insbesondere sein gutes Auge für Details und die wegweisenden Ratschläge haben dieser Arbeit die entscheidende Richtung gegeben. Außerdem bedanken möchte ich mich für die Möglichkeit, meinen Arbeitsplatz während dieser Doktorarbeit nach Berlin verlagern zu können.

- Ich danke Stefan Klepser für den unermüdlichen Einsatz bei der Betreuung. Die tägliche Physikdiskussion hat diese Arbeit entscheidend vorangebracht. In jedem Bereich hat Stefan mir wertvolle Tipps und Ideen geben können, ohne die diese Arbeit nicht hätte wachsen können. Außerdem möchte ich mich für das intensive und aufmerksame Korrekturlesen bedanken.

- Besonders hervorzuheben ist auch die Betreuung von Rolf Bühler. Ich bedanke mich für die einzigartige Chance, die Crabflares zu analysieren. Ohne die andauernde Unterstützung und Hilfe in allen Bereichen wäre diese Arbeit nicht möglich gewesen. Seine Begeisterung für Astrophysik hat mich täglich neu inspiriert.

- Stefan Ohm gebührt ein großer Dank für das intensive Korrekturlesen, vor allem in den Anfangszügen meiner Arbeit. Seine Hilfestellung hat der Arbeit sowohl sprachlich als auch fachlich in vielerlei Hinsicht die Richtung vorgegeben.

- Die Grundprinzipien der Fermi-Analysen habe ich von Markus Ackermann gelernt. Ich danke für seine Betreuung und die spannenden Diskussionen während der Fermi-Gruppenmeetings.

- Ein besonderer Dank gilt Jürgen Knödlseder, der die GAMMALIB/CTOOLS Software geschrieben hat. Durch seine vielen nützlichen Tipps wurde ich an die Software herangeführt. Ohne die Infrastruktur dieser Analyseumgebung hätte meine Arbeit nicht gelingen können.

Darüber hinaus möchte ich mich bei einer Reihe von Menschen für die kollegiale, produktive und freundschaftliche Zusammenarbeit während der letzten Jahre bedanken. Dieser Dank gilt:

- Meiner ehemaligen Arbeitsgruppe, in Erlangen in der ich, im physikalischen Sinne, das Laufen gelernt habe: Anton, Constanze, Daniel, Fabian, Fidi, Ira, Julia, Kathrin, Peter, Philipp, Sebastian und Steffi.

- Peter Eger und Dan Parsons für die tolle Zeit während der Schicht in Namibia.

- Der Zeuthener und Potsdamer H. E. S. S. Gruppe für das hervorragende Arbeitsklima: Bev, Clemens, Gianluca, Kathrin, Matthias, Stefan K., Stefan O. und Valentin

Von der H. E. S. S. Gruppe möchte ich folgenden vier Menschen ganz besonders für die langjährige Freundschaft seit Beginn unseres Studiums danken:

- Anneli für die langen, ausführlichen und spannenden Gespräche bei und neben der Arbeit.

- Arnim für die große Unterstützung bei allem was Software angeht, aber vor allem für die schönen Zeiten in Erlangen, Berlin und Amsterdam.

- Kora für die vielen Tipps zur PSF Parametrisierung, aber vor allem für schönen Balkonfeste und ihre täglich gute Laune.

- Markus für die tolle Freundschaft seit dem F-Praktikum. Unser gleicher Humor und Filmgeschmack hat jede Kaffeepause zu einer willkommenen Abwechslung gemacht. Vor allem bedanken möchte ich mich für die inspirierende Zusammenschreibphase mit dem ein oder anderen nächtlichen Gedankenaustausch.

Ein besonders großer Dank gilt meinen Eltern und meinem Bruder, die mich unterstützt haben, wo es nur ging. Ihr ständiger Glaube in meiner Fähigkeiten hat mir besondere Motivation gegeben.

Zu guter Letzt, aber trotzdem immer an erster Stelle in meinem Leben, steht meine Verlobte Sabine. Ein nicht in Worte zu fassender Dank dafür dass sie alle Launen, Probleme, Erfolge und Geschichten über diese Arbeit ertragen und mich in sämtlichen Entscheidungen bestärkt und unterstützt hat. Ich freue mich auf ein langes glückliches Leben mit Dir.